Colección Documentos Ciemat

KINETIC MODELLING OF THE *ESCHERICHIA COLI* INACTIVATION IN WATER BY SOLAR RADIATION: APPLICATIONS TO SODIS

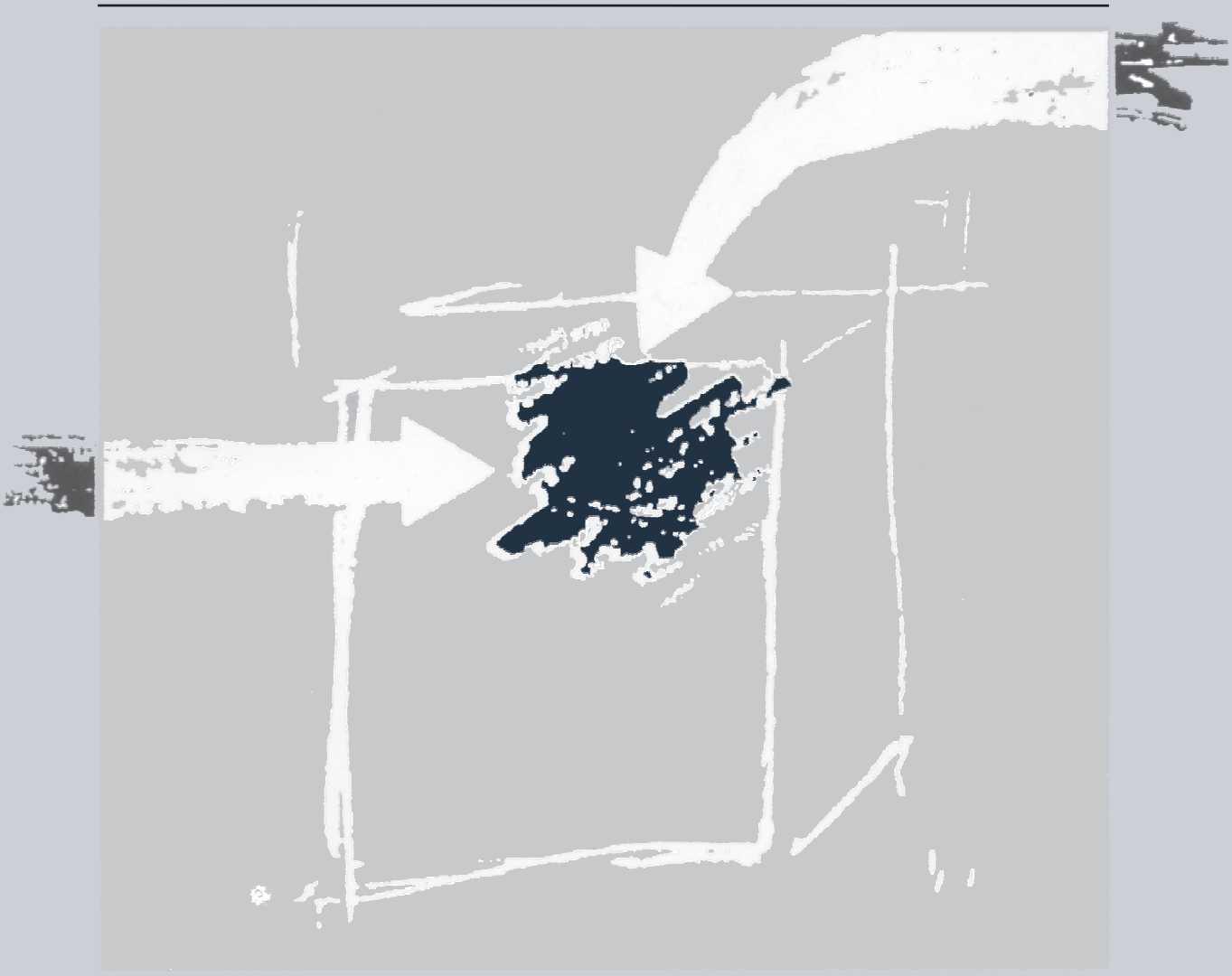

MARÍA CASTRO ALFÉREZ
PILAR FERNÁNDEZ IBÁÑEZ
MARÍA INMACULADA POLO LÓPEZ
JAVIER MARUGÁN AGUADO

GOBIERNO DE ESPAÑA
MINISTERIO DE ECONOMÍA, INDUSTRIA Y COMPETITIVIDAD
Ciemat
Centro de Investigaciones Energéticas, Medioambientales y Tecnológicas

KINETIC MODELLING OF THE *ESCHERICHIA COLI* INACTIVATION IN WATER BY SOLAR RADIATION: APPLICATIONS TO SODIS

MARÍA CASTRO ALFÉREZ

PILAR FERNÁNDEZ IBÁÑEZ

MARÍA INMACULADA POLO LÓPEZ

JAVIER MARUGÁN AGUADO

Es propiedad:

EDITORIAL CIEMAT
Avda. Complutense, 40
28040-MADRID
2017

Catálogo general de publicaciones oficiales
http://www.060.es

Depósito Legal: M-26081-2017
ISBN: 978-84-7834-778-0
NIPO: 058-17-037-3

KINETIC MODELLING OF THE *ESCHERICHIA COLI* INACTIVATION IN WATER BY SOLAR RADIATION: APPLICATIONS TO SODIS

Autores:

María Castro Alférez

Pilar Fernández Ibáñez

María Inmaculada Polo López

Javier Marugán Aguado

INDEX OF CONTENTS

INDEX OF FIGURES

INDEX OF TABLES

ABBREVIATIONS

Ahp	Alkylhydroperoxide reductase
ADP	Adenosine diphosphate
ATP	Adenosine triphosphate
B	Bacteria
BS	Borosilicate
CAT	Catalase
CFU	Colony-forming units
CoA	Coenzyme A
CPC	Compound Parabolic Collectors
CPD	Cyclobutane pyrimidine dimers
CPS	Counts per second
CyoABCD	Quinol oxidase
DCF	2,7-dichlorofluorescein
DCFH	2,7-dichlorodihydrofluorescein
DCFH-DA	2,7-dichlorodihydrofluorescein diacetate
DL	Detection limit
DMSO	Dimethyl sulfoxide
DO	Dissolved oxygen
DOC	Dissolved Organic Carbon
DOM	Discrete Ordinate Method
EPA	United States Environmental Protection Agency
ETC	Electron Transport Chain
FAD	Flavin adenine dinucleotide
FAO	Food and Agriculture Organization
FITC-A	Fluorescein isothiocyanate
Fur	Ferric uptake regulator

GDP	Guanosine diphosphate
GSH	Glutathione
HPI	Hidroperoxidase I
HPII	Hidroperoxidase II
HRP	Horseradish peroxidase
HWTS	Household Water Treatment and Safe Storage
IC	Inorganic Carbon
ID	Infective dose
IW	Isotonic water
LB	Luria-Bertani
LDPE	Low-density polyethylene
LRV	Log reduction value
LVRPA	Local volumetric rate of photon absorption
Q/QH_2	Quinone/quinol
MC	Methacrylate
Ndh	NADH dehydrogenase II
NDIR	Non-dispersive infrared detector
NAD^+/NADH	Oxidized/Reduced Nicotinamide Adenine Dinucleotide
NRMSLE	Normalized root mean squared logarithmic error
NTU	Nephelometric Turbidity Units
NuoA-N	NADH dehydrogenase I or NADH:quinone reductase
OM	Organic matter
PBS	Phosphate-buffered saline
PC	Polycarbonate
PDT	Photodynamic therapy
PET	Polyethylene terephthalate

PSA	Plataforma Solar de Almería
PTFE	Polytetrafluoroethylene
RNS	Reactive Nitrogen Species
ROS	Reactive Oxygen Species
rpm	Revolutions per minute
RTE	Radiative Transfer Equation
S	Photosensitizer
SFM	Six flux model
SOD	Superoxide dismutase
SODIS	Solar water disinfection
SSB's	Single strands breaks
TC	Total Carbon
U	Units
UNESCO	United Nations Educational, Scientific and Cultural Organization
WASH	Water, Sanitation and Hygiene
WHO	World Health Organization
WW	Well water

NOMENCLATURE

A	Area (m^2)
A	Pre-exponential factor (units depend on the specific reaction)
A_m	Specific mass activity of catalase (U mg^{-1})
A_v	Volumetric specific catalase activity (U L^{-1} or μM min^{-1})
B	Spectral radiance of a blackbody (W m^{-2} sr^{-1} m^{-1})
c	Speed of light in air ($3 \cdot 10^8$ m s^{-1})
c	Concentration of disinfectant in Chick-Watson model
$Dose$	Solar dose (J m^{-2})
e^a	Local volumetric rate of photon absorption (Einstein m^{-3} s^{-1})
E	Radiative energy (Einstein or J)
Ea	Activation energy (J mol^{-1})
f	Corrector factor of the turbidity (dimensionless)
g	Density function parameter (dimensionless)
G	Incident radiation (Einstein s^{-1} m^{-2} or W m^{-2})
h	Planck constant ($6.63 \cdot 10^{-34}$ J s^{-1})
I	Radiation intensity or irradiance (Einstein s^{-1} m^{-2} sr^{-1} or W m^{-2} sr^{-1})
k	Kinetic constant (units depend on the specific reaction)
k^*	Specific kinetic constant (units depend on the specific reaction)
k	Boltzmann constant ($1.38 \cdot 10^{-23}$ J K^{-1})
K_m	Michaelis constant (M)
l, L	Optical path length (cm)
m	Model parameter of Hom equation
M	Number of divisions of the radiation direction in the mesh created for the discrete ordinate method
n	Model parameter of Hom equation
n	Dilution coefficient in Chick-Watson model
N	Bacterial population (CFU mL^{-1})

N_A	Avogadro number (photon Einstein^{-1})
N_X, N_Y	Number of divisions of the X and Y axis in the mesh created for the discrete ordinate method
p	Phase function (dimensionless)
r	Radius (cm)
r, R	Reaction rate (mol L^{-1} s^{-1})
R	Ideal gas constant (8.314 J K^{-1} mol^{-1})
s	Directional spatial variable
S	Synergy term
S	Radiation source term (Einstein s^{-1} m^{-1} or W m^{-1})
t	Time (s)
T	Temperature (K or ºC)
T	Transmittance (dimensionless)
α	Mancini fit parameter
γ	Kinetic parameter of the *SODIS model* (units depend on the specific reaction)
δ	Kinetic parameter of the *synergistic SODIS-thermal model* (units depend on the specific reaction)
ε	Extinction absorption coefficient (M^{-1} cm^{-1})
η	Direction cosine of the direction of light propagation with respect to y axis
θ	Mancini fit parameter
θ	Angle of the radiation respect to the normal direction
κ	Absorption coefficient (cm^{-1})
κ^*	Specific absorption coefficient (M^{-1} cm^{-1})
λ	Wavelength (nm)
μ	Direction cosine of the direction of light propagation with respect to x axis
σ	Scattering coefficient (cm^{-1})
σ^*	Specific scattering coefficient (M^{-1} cm^{-1})
ω	Gaussian quadrature weighting factor
Ω	Direction of radiation propagation

Subscripts

0	Indicates initial condition
i	Relative to inactive bacteria
lag	Relative to lag phase in the inactivation process
model	Relative to modelled time predicted by the synergistic SODIS-thermal model to achieve a desired bacterial reduction
ox	Indicates oxidized condition of the organic matter
R	Relative to light resistant bacterial population
red	Indicates reduced condition of the organic matter
res	Relative to residual bacterial population
S	Relative to light sensitive bacterial population
safe	Relative to safe time required to achieve a desired bacterial reduction
v	Relative to viable bacteria
w	Relative to the wall of the photo-reactor

Special symbols

[ ]	Concentration of intracellular chemical species (M) or concentration of bacteria in the bulk (CFU mL^{-1})
‘	Different radiation direction to the propagation direction
-	Indicates and averaged value in the UVA range (320 – 400 nm)

SUMMARY / RESUMEN

SUMMARY

One of the most important problems worldwide is the scarcity of water. The lack of freshwater and its dissimilar distribution together with inadequate sanitation and hygiene in low-income areas makes that nowadays millions of people are drinking contaminated water with faecal contamination. A number of waterborne pathogens present in this water induce serious diseases that, in many cases could be lethal in the most vulnerable population.

In this context, the solar water disinfection technique, so-called SODIS is a low-cost intervention method used in communities with low resources and poor access to improved drinking water sources. For the last decades, the deployment of SODIS has reached ca. 5 million people around the world thanks to the work of Non-Governmental Organizations (NGOs) and scientists devoted to the dissemination of this technique in the communities to reduce the microbial load of drinking water. This simple method consists on the exposure of the contaminated water to direct sunlight for at least 6 hours under full sunshine within transparent containers. Typically, polyethylene terephthalate (PET) bottles are used as containers for SODIS. Although, the factors that affect the SODIS efficiency are well known and the technique has been proven to be suitable in diverse operational conditions, there are still some unknown aspects in this area, mainly those related with the understanding of the triggers of solar photo-inactivation of the living cells. The aim of this work is to model the mechanisms driving the interaction between cells and solar radiation to increase the knowledge on the microbial inactivation happening during SODIS under real conditions, i.e. solar mild heat, natural solar UVA irradiance, variable weather conditions, turbid water and PET irregularly shape bottles.

In particular, the mechanistic model has been developed with *E. coli* K-12 within isotonic water (distilled water added sodium chloride). Firstly the model considers that the bacterial inactivation during the solar exposure is due to the attack of Reactive Oxygen Species (ROS) to diverse intracellular targets. In the

literature, the hypothesis of the photo-generation of these intracellular ROS by the action of sunlight photons is widely accepted. For the first time, this work reports on the experimental determination of the intracellular ROS formed inside *E. coli* cells exposed to natural solar radiation. This observation has been essential to lay out this mechanistic model. The intracellular ROS detection was performed using a new experimental protocol different from the standard protocols reported for detect oxidative stress in eukaryotic cells by fluorescent ROS-probes. This new protocol was especially developed and validated in this work for the detection of ROS in *E. coli*. The 2,7-dichlorodihydrofluorescein diacetate (DCFH-DA) was used as probe, which was chemically hydrolysed prior to contact with the bacteria and the flow-cytometry as the fluorescence detection technique.

Then, a first novel kinetic mechanistic model that explains the bacterial inactivation during solar water disinfection was proposed. It is based on the photo-generation of intracellular ROS and the photo-inactivation of catalase (CAT) and superoxide dismutase (SOD) enzymes, which main functions are scavenging harmful ROS generated inside bacteria cells. To estimate the model parameters, a series of SODIS experiments at different values of UVA irradiance and initial bacterial concentration were conducted under controlled conditions of radiation and temperature in a lab-scale reactor. In addition, the kinetic constant of the photo-inactivation of catalase was experimentally determined under the same controlled conditions.

Continuing with this work, a modification of the first proposed model was developed to consider also the effect of solar mild temperatures reached during SODIS, which was mathematically formulated in the model. For this purpose, thermal inactivation experiments in the dark and SODIS experiments at different controlled temperature values were conducted in order to determine the relationship between water temperature and the bacterial inactivation during the cells exposure to sunlight. A clear synergistic effect between temperature and UVA radiation was experimentally observed, therefore this synergy was included

in the model using the Arrhenius parameters that were determined by the model regression.

Finally, the synergistic SODIS-thermal model obtained was validated under real conditions in a number of real cases, i.e. under natural sunlight in clear waters (isotonic and well water) and using PET bottles. Validation experiments were conducted with different climate conditions (sunny and cloudy days) and the simulations were performed taken into account the variable values of the solar irradiance and the water temperature during the disinfection process. In addition, a light transport model for the PET bottles was developed to determine the incident radiation inside the photo-reactor for the case of turbid water. The simulation results from the synergistic SODIS-thermal model described satisfactorily the bacterial inactivation in turbid water using two turbidity agents, natural red soil and kaolin, in the range from 5 to 300 NTU, taking into account the radiation depletion. The experimental results of bacterial photo-inactivation obtained for sevaral pilot solar photo-reactors previously developed and evaluated for this application using different materials and designed for larger output volumes were also successfully described by the synergistic SODIS-thermal model.

The synergistic SODIS-thermal model proposed in this work has promising applications for large scale photo-reactors design. It could be used as a tool to predict the efficiency of new reactor prototypes without the necessity of building and operating them. In this work, it was also introduced the 'safe treatment time' and the 'safe UVA dose' parameters as the physical parameters that indicate whether the treated water is safe for drinking in a certain photo-reactor. For this purpose, the synergistic SODIS-thermal model was used with the aim of comparing the efficiency of different reactors for solar water disinfection. In addition, these parameters could be used when SODIS process is operating in the real field in a photo-reactor. In these cases, the model takes into account the variability of the irradiance and the water temperature to predict the bacterial inactivation profiles and to determine the final point of the treatment to reach a certain bacterial reduction.

RESUMEN

Uno de los mayores problemas a nivel mundial es la escasez de agua que unida a la desigual distribución de agua dulce en el mundo y a la falta de higiene y sanidad adecuados en zonas con bajos ingresos económicos, provoca que actualmente millones de personas se vean obligadas a consumir aguas contaminadas. La carga fecal que presentan estas aguas genera serios problemas de salud a aquellos que las consumen, incluso pueden resultar letales para la población más vulnerable.

La técnica de 'desinfección solar de agua', más conocida como SODIS (acrónimo de la expresión inglesa 'solar water disinfection') se presenta como una solución de bajo coste para aquellas comunidades con accesos limitados a fuentes de agua potable y con bajos recursos económicos. En las últimas décadas, su uso se ha extendido a cerca de 5 millones de personas en todo el mundo gracias al trabajo realizado por las ONGs y científicos dedicados a la difusión del SODIS como método de tratamiento de agua. El funcionamiento es muy simple, consiste en exponer el agua contaminada en contenedores transparentes (normalmente botellas de tereftalato de polietileno, PET por sus siglas en inglés) a la luz solar directa durante al menos 6 horas. La eficacia de la técnica SODIS ha sido muy estudiada demostrando que es adecuada en diversas condiciones de operación y se han determinando cuáles son los factores que más influyen en la desinfección. Sin embargo, todavía hay algunos aspectos desconocidos en la técnica SODIS, principalmente aquellos relacionados con la comprensión de los mecanismos de la foto-inactivación solar de las células bacterianas.

El objetivo de este trabajo consiste en modelar los mecanismos por los que se produce la inactivación celular mediante su interacción con la radiación solar. En particular, se ha desarrollado un modelo mecanicista usando *E. coli* K-12 en agua isotónica (agua destilada con cloruro sódico). El modelo se basa en una de la hipótesis más aceptadas de la literatura, que afirma que la inactivación

bacteriana durante la exposición solar se debe al ataque a diversas dianas intracelulares por las Especies Reactivas de Oxígeno (ROS, por sus siglas en inglés) que se generan a nivel celular debido a la acción de los fotones de la luz solar. Por primera vez, este trabajo demuestra experimentalmente la presencia y acúmulo de ROS en el interior de las células de *E. coli* expuestas a radiación solar natural, lo que ha sido esencial para el desarrollo del modelo mecanicista de SODIS. La detección intracelular de las ROS se ha realizado mediante un protolocolo modificado para la medida del estrés oxidativo en células eucariotas mediantes sondas fluorescentes, usando el diacetato de 2,7-diclorodihidrofluoresceína (DCFH-DA), previamente hidrolizada químicamente y posteriormente detectada mediante citometría de flujo.

Como pilar de este trabajo, se ha propuesto un primer modelo mecanicista cinético que explica la inactivación bacteriana durante la desinfección solar del agua. El modelo se basa en la foto-generación de ROS intracelulares y la foto-inactivación de ciertas enzimas: la catalasa (CAT) y la superóxido dismutasa (SOD), cuyas funciones principales son la eliminación de las ROS generadas dentro de las células bacterianas. Para estimar los parámetros del modelo, se ha llevado a cabo una serie de experimentos de SODIS a escala de laboratorio con diferentes valores de irradiancia solar y diferentes valores de concentración inicial de bacteria en condiciones controladas de radiación y temperatura. La constante cinética de la foto-inactivación de la catalasa se determinó experimentalmente bajo las mismas condiciones controladas.

A continuación, se ha desarrollado una modificación del primer modelo propuesto para considerar también el efecto térmico que normalmente se genera en el proceso SODIS (30 – 55 ºC). Para ello, se realizaron experimentos de inactivación térmica en oscuridad y experimentos de SODIS a diferentes valores de temperatura controlada para determinar la relación entre la temperatura del agua y la inactivación bacteriana durante la exposición de las células a la luz solar. Se observó un claro efecto sinérgico entre la temperatura y la radiación UVA, que se incluyó en el modelo matemáticamente mediante los parámetros de Arrhenius obtenidos por regresión.

Finalmente, el modelo obtenido se ha validado en condiciones reales de iluminación solar natural en aguas claras (agua isotónica y de pozo) y en botellas PET, usando los valores cambiantes de la irradiancia solar y la temperatura del agua durante el proceso de desinfección. También se ha validado el modelo en aguas turbias en botellas PET, para lo que adicionalmente se ha desarrollado un modelo de luz que estima la radiación dentro del foto-reactor. El rango de turbidez validado ha sido de 5 a 300 NTU usando dos agentes de turbidez distintos, caolín y tierras rojas naturales. Además, el modelo se ha validado en diversos reactores solares a escala de planta piloto diseñados para obtener volúmenes de producción mayores y usando diferentes materiales. En todos los casos, los experimentos y las simulaciones se llevaron a cabo bajo diferentes condiciones climáticas (días soleados y días nublados).

El modelo de desinfección solar de agua propuesto en este trabajo presenta prometedoras aplicaciones para el diseño de foto-reactores solares a gran escala, como una herramienta para predecir la eficiencia de nuevos prototipos de reactores sin necesidad de construirlos y operarlos. Para ello, se han definido los parámetros de "tiempo seguro de tratamiento " y "dosis segura de UVA" que permiten comparar la eficiencia de diferentes reactores solares ante unas mismas condiciones climáticas. Además, estos parámetros podrían utilizarse para estimar los requisitos de tiempo y dosis de energía necesarios para proporcionar agua segura para consumo humano obtenida mediante el tratamiento SODIS en condiciones reales en un reactor solar que esté instalado y operando. En este caso, el modelo tiene en cuenta la variabilidad de la irradiancia y la temperatura del agua para predecir los perfiles de inactivación bacteriana y determinar el punto final del tratamiento para alcanzar una determinada reducción bacteriana.

CHAPTER 1
INTRODUCTION

1 INTRODUCTION

1.1 Water problematic

Water is essential for life. It is involved in several world aspects from food and energy security to human and environmental health, affecting the livelihoods of billions of people. In 2010, the UN General Assembly explicitly recognized the human right to water and sanitation: *everyone has the right to sufficient, continuous, safe, acceptable, physically accessible and affordable water for personal and domestic use*. In addition, improved global water supply and sanitation and better management of water resources is vital to realize living opportunities, generate income and contribute to economic productivity. Demand of freshwater is constantly growing; by 2050, the global water demand is expected to increase by

55 %, mainly due to growing demands from food manufacturing, thermal electricity generation and domestic use [UNESCO, 2015].

In this context, the availability of fresh water on the Earth has become a critical worldwide problem. Water distribution is not homogenous and most of the water sources are not available for human uses [Shiklomanov, 1993]. A 70 % of the Earth's surface is covered by water but only a 2.5 % is fresh water. This fresh water is distributed in different states, being around 80 % in glaciers, mountainous areas or periglacial floors and only around 20 % is present in lakes, streams, swamps, accessible wetlands and aquifers that are naturally renewed by precipitation. However, only a 1 % is available to the human use (Figure 1.1).

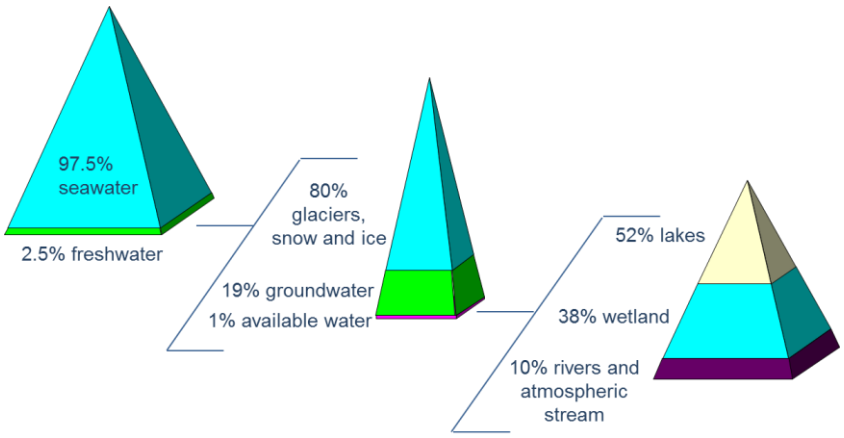

Figure 1.1. Global distribution of water.

Additionally, the available water is not distributed equally worldwide. Lots of campaigns and investment programs have been performed by international bodies such as World Health Organization (WHO), Food and Agriculture Organization (FAO) or United Nations Educational, Scientific and Cultural Organization (UNESCO) directed to improve the water, sanitation and hygiene (WASH) of many countries. It was reached for example an increase in the access to an improved drinking water source from 76 % in 1990 to 91 % in 2015, which means that 2.6 billion people have gained access to an improved drinking water sources over this period of 25 years. In the Table 1.1, several sources considered as improved and unimproved drinking water sources are listed.

Table 1.1. List of the "improved" and "unimproved" drinking water sources [WHO/UNICEF, 2015].

Improved drinking water	**Piped water on premises**: Piped household water connection located inside the user's dwelling, plot or yard. **Other improved drinking water sources**: Public taps or standpipes, tube wells or boreholes, protected dug wells, protected springs, rainwater collection.
Unimproved drinking water	**Unimproved drinking water sources**: Unprotected dug well, unprotected spring, cart with small tank/drum, tanker truck, bottled water (*). **Surface drinking water sources**: River, dam, lake, pond, stream, canal, irrigation channels.

(*)Bottled water is considered 'improved' for drinking only when an improved water source is used for refilling the bottles.

In spite of the big effort of the last decades to improve WASH services, nowadays 663 million people rely on unimproved drinking sources including 159 million people that use surface waters who suffer the greatest risk to contract waterborne diseases. Nearly half of all people using unimproved drinking water sources live in sub-Saharan Africa while one fifth live in Southern Asia (Figure 1.2). Significant proportions of the population in sub-Saharan Africa and Oceania are still using rivers, lakes, ponds and irrigation canals as their main source of drinking water [WHO/UNICEF, 2015].

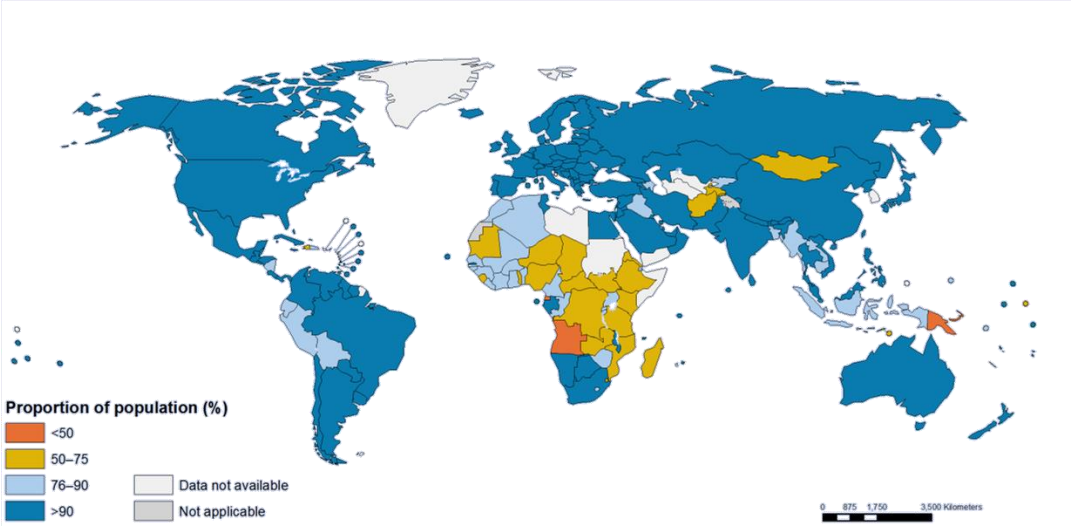

Figure 1.2. World map of the proportion of population using improved drinking water sources in 2015 [WHO, 2016a].

Disparities in the access to safe drinking water also exist between rural and urban areas. The 96 % of the global urban population uses improved drinking water sources, compared with the 84 % of the rural population. Eight out of ten people still without improved drinking water sources live in rural areas. In addition, rural populations account for the 93 % of the people using surface water.

Improved sources are not necessarily safe; at least 1.8 billion people use a drinking water source that is contaminated with faecal matter. The contamination could be produced at any point of the water cycle, from water source to transport or storage, especially in environments where sanitation is inadequate or where water supply is intermittent or the treatment is deficient. Contaminated water and poor sanitation are linked to the transmission of diseases such as cholera, diarrhoea, dysentery, hepatitis A, typhoid and polio. Diarrhoea is the most widely known disease linked to contaminated food and water. Around 842 000 people of which 361 000 are children aged under 5 years, are estimated to die each year from diarrhoea as a result of unsafe drinking water, sanitation and hand hygiene [WHO, 2016b]. In the Figure 1.3 it is shown an index of the mortality population attributed to the consumption of contaminated water, being again the African continent the most affected.

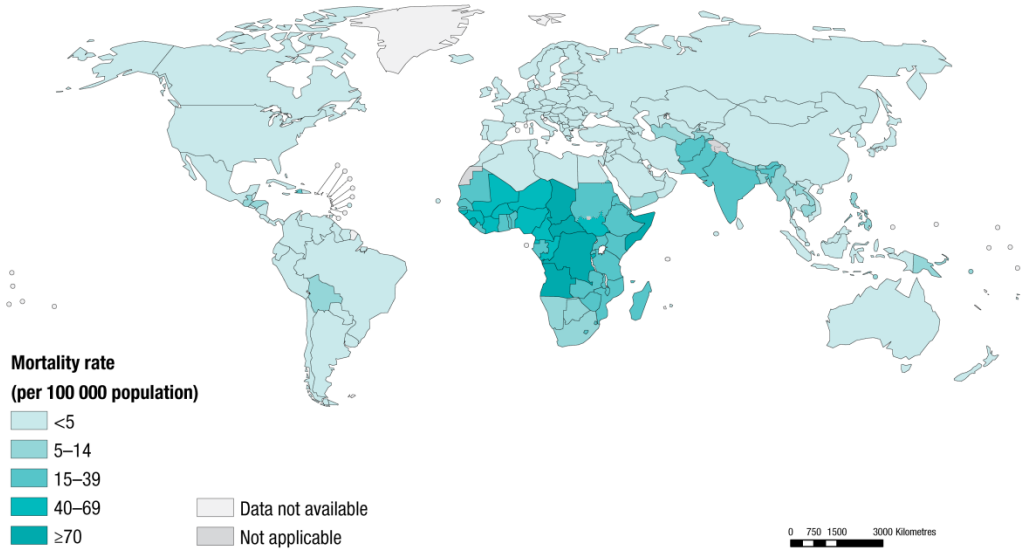

Figure 1.3. World map of the mortality rate attributed to unsafe WASH services in 2012 [WHO, 2016a].

Table 1.2 provides a list of several waterborne pathogens associated with unsafe drinking water sources. The effects on the host are diverse in characteristics, behaviour and resistance depending on the type of microorganism, the host or the environmental changes as fluctuations in human and animal populations, reuse of wastewater for human activities, population movement and travel, selective pressures for new pathogens and mutants or recombinations of existing pathogens. The most vulnerable population of contaminated drinking water are the elderly or very young people, patients with burns or extensive wounds, people undergoing immunosuppressive therapy or those with acquired immunodeficiency syndrome (AIDS).

Table 1.2. Pathogens transmitted through drinking water [WHO, 2011a].

Pathogen	Diseases and symptoms	Persist[a]	Cl resist[b]
Bacteria			
Burkholderia pseudomallei	Melioidosis (pneumonia, abscesses or ulcers, abscesses in internal organs and neurological illnesses)	May multiply	Low
Campylobacter jejuni	Abdominal pain, diarrhoea (vomiting, chills, fever), reactive arthritis and meningitis	Moderate	Low
Escherichia coli	Diarrhoea (colitis, vomiting, fever), haemolytic uraemic syndrome, infections (abdominal cramps, nausea)	Moderate	Low
Legionella spp.	Legionellosis (fever, headache, nausea, vomiting, aching muscles and coughing)	May multiply	Low
Leptospira	Infections (fever, headache, muscle & abdominal pain, chills, eyes-redness, jaundice, vomiting, diarrhoea, rash, skin and mucouses hemorrhages including pulmonary bleeding ending to leptospirosis)	Long	Low
Mycobacteria (no-tuberculous)	Pulmonary disease, Buruli ulcer, osteomyelitis, septic arthritis	May multiply	High
Salmonella spp.	Gastroenteritis (diarrhoea, nausea and vomiting), bacteraemia or septicaemia (fever)	Moderate	Low
Shigella spp.	Intestinal diseases, including bacillary dysentery (abdominal cramps, fever and watery diarrhoea)	Short	Low
Vibrio cholera	Diarrhoea (severe dehydration and loss of electrolytes)	Short to long	Low
Acinetobacter[c]	Urinary tract infections, pneumonia, bacteraemia, secondary meningitis and wound infections	Common and may multiply	Low
Aeromonas[c]	Infections including septicaemia, wound infections and respiratory tract infections; gastrointestinal illness	Common and may multiply	Low
Enterobacter sakazakii[c]	Sepsis, meningitis, cerebritis, necrotizing enterocolitis	Unlikely	Low
Helicobacter pylori[c]	Chronic gastritis, ending to peptic & duodenal ulcer and gastric cancer	Detected and short	Low
Klebsiella[c]	Infections, such as pneumonia	Can multiply	Low
Pseudomonas aeruginosa[c]	Destructive lesions or septicaemia and meningitis	Common and may multiply	Moderate
Staphylococcus aureus[c]	Skin sepsis, enteric infections, septicaemia, endocarditis, osteomyelitis, pneumonia, gastrointestinal disease	Common and may multiply	Moderate
Yersinia enterocolitica[c]	Gastroenteritis (diarrhoea, fever and abdominal pain) and ulcerations of the terminal ilium	Common and may multiply	Low
Helminths			
Dracunculus medinensis	Local eruption of the worm (urticaria, erythema, dyspnoea, vomiting, pruritus and giddiness)	Moderate	Moderate
Schistosoma spp.	Schistosomiasis (fever, chills, muscle pains and cough in allergic reaction; bloody diarrhoea, abdominal pains and hepatosplenomegaly in chronic infection)	Short	Moderate
Fasciola spp.[c]	Fascioliasis (dyspepsia, nausea and vomiting, abdominal pain and a high fever in the invasive phase; jaundice, chest pains, loss of weight and cholelithiasis in the chronic phase)	Detected	High
Free-living nematodes[c]	They could carry pathogenic bacteria in their gut such as enterobacteriaceae, *Nocardia* and *Mycobacterium*	Detected and may multiply	High

Pathogen	Diseases and symptoms	Persist[a]	Cl resist[b]
Protozoa			
Acanthamoeba spp.	Granulomatous amoebic encephalitis, acanthamoebic keratitis, acanthamoebic uveitis	May multiply	High
Cryptosporidium hominis/parvum	Diarrhoea (nausea, vomiting and fever)	Long	High
Cyclospora cayetanensis	Cyclosporiasis (watery diarrhoea, abdominal cramping, weight loss, anorexia, myalgia, vomiting, fever)	Long	High
Entamoeba histolytica	Amoebic dysentery (diarrhoea with cramping, lower abdominal pain, low-grade fever)	Moderate	High
Giardia intestinalis	Giardiasis (diarrhoea)	Moderate	High
Naegleria fowleri	Amoebic meningoencephalitis	May multiply	Low
Balantidium coli[c]	Intestinal infections (diarrhoea, nausea, vomiting, headache and anorexia)	Detected	High
Blastocystis hominis[c]	Intestinal infections (diarrhoea, abdominal pain, anal itching, weight loss and excess gas)	Unknown	High
Isospora belli[c]	Isosporiasis (low-grade fever, lassitude and malaise, mild diarrhoea and vague abdominal pain)	Unknown	High
Microsporidia[c]	Severe enteritis (chronic diarrhoea, dehydration, weight loss)	Detected and moderate	Moderate
Toxoplasma gondii[c]	Toxoplasmosis, disease in central nervous system and lungs, severe neurological disorders, pneumonia, chorioretinitis, cerebral calcifications, hydrocephalus, severe thrombocytopenia and convulsions	Long	High
Viruses			
Adenoviruses	Infections of gastrointestinal tract, respiratory tract, urinary tract and eyes	Long	Moderate
Astroviruses	Gastroenteritis, predominantly diarrhoea	Long	Moderate
Enteroviruses	Febrile illness, myocarditis, meningoencephalitis, poliomyelitis, herpangina, hand-footand-mouth disease and neonatal multi-organ failure	Long	Moderate
Hepatitis A/E virus	Infectious hepatitis (fever, malaise, nausea, anorexia, abdominal discomfort and jaundice)	Long	Moderate
Caliciviruses	Gastroenteritis (nausea, vomiting and abdominal cramps, diarrhoea, chills, headache and muscular pain)	Long	Moderate
Rotaviruses	Gastroenteritis (severe watery diarrhea, fever, abdominal pain and vomiting; dehydration, metabolic acidosis)	Long	Moderate

[a] Persistance in water supplies: detection period for infective stage in water at 20 °C: short, up to 1 week; moderate, 1 week to 1 month; long, over 1 month.

[b] Resistance to chlorination: when the infective stage is freely suspended in water treated at conventional doses and contact times and pH between 7 and 8. Low means 99 % inactivation at 20 °C generally in < 1 min, moderate 1–30 min and high > 30 min. It should be noted that organisms that survive and grow in biofilms, such as *Legionella* and mycobacteria, will be protected from chlorination.

[c] Pathogens that have been suggested as possible causes of waterborne disease but where evidence either is limited or indicates that transmission through drinking water supplies is unlikely.

Monitoring each pathogen is not a suitable option to assure a safe drinking water. There are several microbial guidelines that provide information about the target or indicator microorganisms more suitable to be monitored and removed to ensure safe drinking water. The most relevant water guidelines are established by the WHO, EPA (United States Environmental Protection Agency) and Australian guidelines (summarized in Table 1.3).

Table 1.3. Drinking water guidelines of WHO, EPA and Australia [WHO, 2011a; EPA, 2011; NHMRC, NRMMC, 2011].

Pathogens	WHO	EPA	Australia
Coliphages	Indicator for effectiveness of disinfection and physical removal processes[a]	99.99 % killed/inactivated	Undetectable in 100 mL
Escherichia coli or thermotolerant[b]	Must not be detected in 100 mL sample	-	Undetectable in 100 mL
Total coliform	Indicator for cleanliness and integrity of distribution systems	No more than 5.0 % samples total coliform-positive in a month[c]	-
Intestinal enterococci[d]	-	-	Undetectable in 100 mL
Heterotrophic plate counts	Indicator for effectiveness of bacterial disinfection process and of the cleanliness and integrity of distribution systems	No more than 500 bacterial colonies per mL	-
Clostridium perfringens	Indicator for effectiveness of viruses and protozoa disinfection and physical removal processes	-	-
Cryptosporidium	-	99 % killed/inactivated	-
Giardia lamblia	-	99.9 % killed/inactivated	-
Legionella	-	No limit[e]	-

[a] *Bacteroides fragilis* phages and enteric viruses could be also indicators.
[b] *E. coli* is the most common thermotolerant coliform present in faeces and is regarded as the most specific indicator of recent faecal contamination.
[c] Every sample that has total coliforms must be analysed for faecal coliforms that are no allowed.
[d] Intestinal enterococci are a functional group of organisms including the genes of the *Enterococcus* and *Streptococcus* that are excreted in human and animal waste, including the species *Enterococcus faecalis*, *E. faecium*, *E. durans*, *E. hirae*, *E. cecorum*, *E. columbae*, *E. avium*, *E. gallinarum*, *Streptococcus bovis*.
[e] EPA believes that if *Giardia* and viruses are inactivated, *Legionella* will also be controlled.

1.2 Household water treatment and safe storage (HWTS)

The household water treatment and safe storage (HWTS) are any of the devices or techniques addressed to improve and maintain the microbial quality of the water for drinking and thereby reducing waterborne diseases transmission. Some of the most common HWTS used in those areas with difficulties to find uncontaminated drinking water are summarized in Table 1.4. A brief description of the HWTS is presented below [WHO, 2002; WHO, 2016c] except for the solar disinfection process that is explained in detail in the next section as it is the focus of this research.

Table 1.4. Methods for drinking water treatment at household level [adapted from WHO, 2002].

Method	Availability and practicality	Technical difficulty	Cost[a]	Microbial efficacy[b]
Chlorination	High to moderate[c]	Low to moderate	Low	High
Filtration	Varies[d]	Low to moderate	Low to moderate[d]	Varies[d]
Flocculation	Moderate	Moderate	Low to moderate[e]	Varies[e]
Boiling	Varies[f]	Low to moderate	Moderate to high[f]	High
UV disinfection	Varies[g]	Low to moderate	High	High
Solar disinfection	High	Low to moderate	Moderate	Moderate

[a] Classification by unit price (euro m^{-3}): Low < 0.5; Moderate 0.5-2; High > 2 [NWP, 2010].
[b] Microbial efficacy estimates in order-of-magnitude or $\log_{10}$ reductions of waterborne pathogens: Low < 1 $\log_{10}$ (< 90 %); Moderate 1-2 $\log_{10}$ (90-99 %); High > 2 $\log_{10}$ (> 99 %).
[c] On-site generation of gas is difficult but chemical production by acidifying chlorate or chlorite is simple if measuring devices and instructions are provided.
[d] Practicality, availability, cost and microbial efficacy depend on the filter medium and its availability: granular, ceramic, fabric, etc. Microbial efficacy also depends on pore size (some are highly efficient, >> 99% or >> 2-$\log_{10}$ reduction).
[e] Depends on flocculants, dose, mixing, settling conditions and pH range.
[f] Depends on heating method and on the availability and cost of fuels.
[g] Depends on availability and cost of type of lamps, electricity, operation and maintenance needs (pumps and system cleaning methods).

1.2.1 Chemical disinfection

Chemical disinfection of drinking water is widely recognized as safe and effective. The chemical disinfectants alter (often oxidize) the biochemical building blocks and disrupting the surface attachment molecules and vital cell functions of the microorganisms. Drinking water chemical disinfection includes any chlorine- or iodine-based technologies, including chlorine dioxide, as well as ozone, some other oxidants and some strong acids and bases.

Among all the chemical disinfection methods, chlorination is the most used in emergencies because is affordable, low cost, easy to use and transport, and provides residual protection against recontamination during storage. It is effective against bacteria and some viruses, although is ineffective against protozoan cysts such as *Cryptosporidium parvum*. Turbidity or dissolved organic matter can affect to disinfection and form potentially hazardous by-products.

1.2.2 Filtration

Household filtration involves the physical removal of suspended solids (including microbes) from water by a combination of size exclusion and adsorption. Some of these filters may also employ chemically active antimicrobial agents such as silver nitrate solution or colloidal suspensions of silver, in order to inactivate microbes or at least not to multiply. Common media include cloth, sand, porous rock, unglazed ceramics. In addition, advanced membranes specially configured for gravity-pressure applications are also used, developing microfiltration, ultrafiltration, nanofiltration and reverse osmosis.

The filtration technique is effective against bacteria and protozoa, and also against viruses by membranes but it is limited to the pore size. It is a simple technology and has a visual improvement in treated water. Nevertheless, it requires maintenance by cleaning the filters and receptacles and it is lack of residual protection against recontamination when storage provided is not safe.

1.2.3 Flocculation

Flocculation is a method that employs natural or chemical elements to coagulate or precipitate suspended particles, including microbes enhancing their sedimentation. Normally, the reagent is provided in sachets that contain the flocculant to induce suspended and larger microorganisms such as protozoa to bind to each other and settle to the bottom of the water vessel, and the disinfectant to inactivate the smaller microorganisms such as bacteria and viruses. As natural flocculant agent, Moringa oleifera seeds have been used widely to improve the microbial remove [Ndabigengesere and Narasiah, 1998; Beltrán-Heredia and Sánchez-Martín, 2009].

Flocculation-disinfection provides residual protection against recontamination during storage and facilitates the reduction of some heavy metals (e.g. arsenic) and particle-associated pesticides.

This method often needs multiple steps. Typically, it employs a series of three pots, and daily, the water is carefully transferred by decanting from one container to another. The water of the third vessel has been sequentially settled and stored at least 2 days to reduce microbes load.

1.2.4 Boiling

Boiling or heating with fuel is the most common household drinking water disinfection technique, with an estimated 1.1 billion people reporting that they usually boil the water before drinking it [Rosa and Clasen, 2010]. It has been proven to be effective against all type of waterborne pathogens, even those bacterial spores and protozoan cysts that have shown resistance to chemical disinfection or viruses that are too small to be mechanically removed by filtration. Boiling could be used within turbid waters or with high content of diverse dissolved constituents.

The recommended procedure is raising the temperature to a rolling boil, removing from heat and allowing the water to cool naturally to room

temperature or below. This method provides more than enough time to inactivate pathogenic bacteria, viruses and protozoa because they are sensitive to inactivation at temperatures below 100 ºC.

1.2.5 UV disinfection

Strictly speaking, the process that is extended known as 'UV disinfection' must be named 'UVC disinfection' because it uses the germicidal effect of monochromatic radiation at 254 nm of wavelength and other close wavelengths [Meulemans, 1987; Hijnen *et al.*, 2006; Zhou *et al.*, 2017]. The UVC light inactivates microbial organisms by altering their nucleic acids and proteins, which impairs their cell binding and inhibit their ability to replicate. It is effective against viruses, bacteria and protozoa and is simple to use, although its efficiency strongly depends on the optical properties of the water to be disinfected. It only consists on the water exposure to the radiation of UVC lamps. For household- and small-scale, low-pressure mercury arc lamps are commonly used. It is a promising technology for treating household drinking water at the point of use [Brownell *et al.*, 2008].

Nevertheless, UV disinfection requires a professional maintenance and a reliable electricity supply, so its application in developing countries is limited. Turbid water needs a pre-treatment as filtration or flocculation and it is very common recontamination after the treatment unless the water is safely stored.

1.3 Solar water disinfection

Although, the sunlight bactericidal effect was firstly observed around 140 years ago [Downes and Blunt, 1877], it had to wait still 100 years for the first application of the sunlight as water disinfectant by the so-called SODIS process, where Acra and co-workers used solar radiation to inactivate pathogens in oral rehydration solutions [Acra *et al.*, 1980]. It simply consists in placing the contaminated water into transparent plastic or glass containers (normally 2 L polyethylene terephthalate beverage bottles) which are then exposed to the sun.

Depending of the sunlight irradiance and the sensitivity of the pathogens, exposure times required to achieve the desired level of disinfection may vary from 6 to 48 hours; it takes around 6 hours under full sunshine [McGuigan *et al.*, 2012]. Figure 1.4 outlines the steps of the solar water disinfection process.

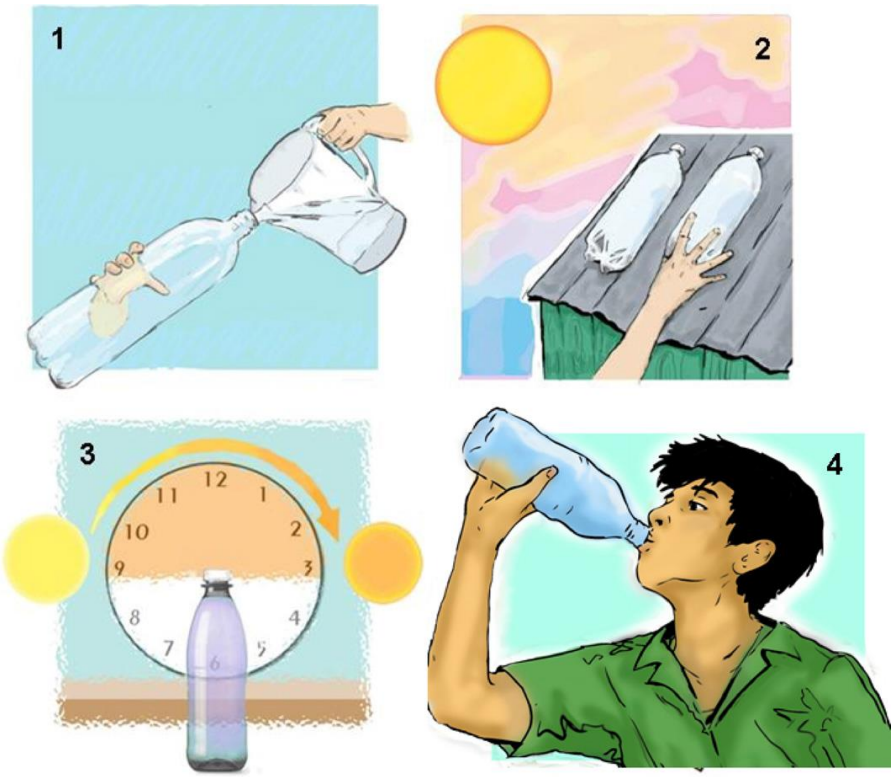

Figure 1.4. Graphical description of SODIS technique [McGuigan *et al.*, 2012].

The main effect of SODIS process is the reduction of the pathogens load in water achieved by the join effect of solar thermal heating and the action of UV-photons on microorganisms, which is recognized as a synergistic effect between both factors. The technique is very simple to use and low cost with minimal likelihood of recontamination. It is effective against viruses, bacteria, and protozoa, although it is strongly dependent on the weather conditions and nature of the microorganism. It is necessary a pre-treatment as filtration or flocculation for turbid waters and it is a relatively long process (i.e. few hours).

1.3.1 Solar radiation

The solar radiation acts as the main lethal agent in the solar water disinfection. In this section, the solar radiation is characterized in detail. Solar radiation is the set of electromagnetic waves emitted by the Sun. The Sun is a star where a series of nuclear fusion reactions are being taken place. These reactions generate a mass loss that is transformed to energy and transmitted outside of the Sun as solar radiation.

The average annual solar radiation arriving at the top of the Earth's atmosphere is around 1366 W m^{-2} (so-called 'solar constant') with a variation of ± 3 % due to the ellipse form of the Earth orbit. The global annual diurnal mean incoming solar radiation is one quarter of the total solar irradiance, or 342 W m^{-2} [Kiehl and Trenberth, 1997]. Nevertheless, the solar radiation is attenuated as the Sun's rays pass through the atmosphere as is shown in Figure 1.5. Some of the energy losses are due to the Earth's albedo that is the capacity of the surface to reflect solar energy. About 31.3 % (107 W m^{-2}) of this energy is scattered or reflected back to space by molecules, tiny airborne particles (known as aerosols) and clouds in the atmosphere (around 22.5 %, 77 W m^{-2}), or by the Earth's surface (8.8 %, 30 W m^{-2}). Also, the incoming solar radiation is absorbed by atmosphere particles and clouds (19.6 %, 67 W m^{-2}) so finally only a 49.1 % (168 W m^{-2}) is reaching the Earth's surface. This energy is given by two components:

- Direct radiation is constituted by the rays coming directly from the Sun.
- Diffuse radiation comes from different directions to direct. Light is scattered by atmosphere particles or Earth's surfaces that modify the original direction of sunlight.

The sum of both components (direct and diffuse) is the global radiation reaching the Earth's surface. Since Earth is continuously exposed to solar radiation, its intensity at each moment depends mainly on the incident angle of the sunlight that is determined by the latitude, the season and the hour of the day.

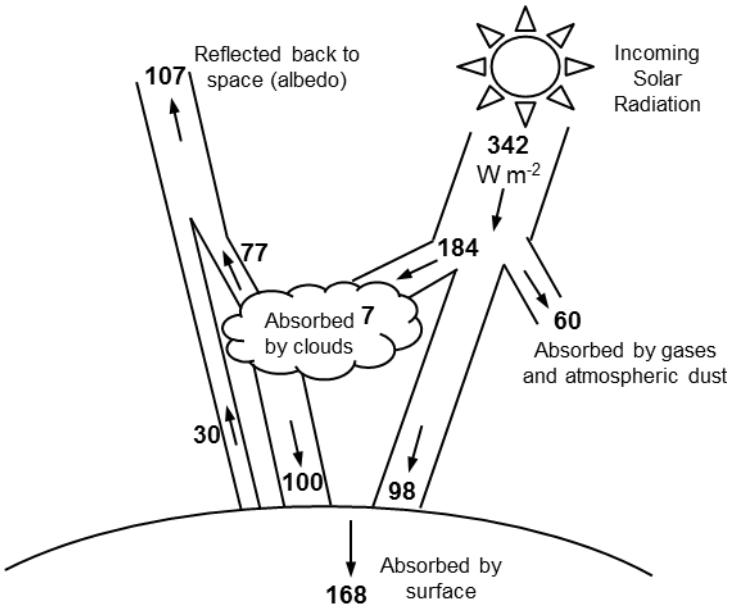

Figure 1.5. Global energy flows from solar radiation that is reflected and absorbed by atmosphere and Earth's surface. Data reported in terms of W m^{-2} [adapted from Trenberth and Stepaniak, 2004].

The solar radiation is distributed across the electromagnetic spectrum as shown in Figure 1.6. The distribution of solar radiation is ranged from 300 nm to approximately 3000 nm. It overspreads the UV range (UVB from 280 to 320 nm and UVA from 320 to 400 nm), visible range (from 400 to 800 nm) and infrared range (from 800 onwards). Most of the irradiance is received in the visible and infrared ranges (54.3 and 41.1 %, respectively) while the most energetic part of the spectrum is mostly absorbed by the atmosphere, reaching the Earth's surface only a 4.6 % of UV (distributed around 3 % of UVB and 97 % of UVA).

The Sun could be considered as a blackbody so its spectral density is given by Planck's law at a given temperature T. The spectral radiance of a blackbody, B_λ, describes the amount of energy emitted by radiation of different wavelengths λ. It is measured in terms of the power emitted per unit area of the body, per unit solid angle that the radiation is measured over, per unit wavelength (W m^{-2} sr^{-1} m^{-1}):

$$B_\lambda = \frac{2hc^2}{\lambda^5} \cdot \frac{1}{e^{\frac{hc}{\lambda kT}} - 1} \tag{1.1}$$

where h is the Planck constant ($6.63 \cdot 10^{-34}$ J s^{-1}), c is the speed of light in air ($3 \cdot 10^{8}$ m s^{-1}) and k is the Boltzmann constant ($1.38 \cdot 10^{-23}$ J K^{-1}). The spectral radiation of a blackbody at a temperature of 6000 K and assuming a solid angle of $6.8 \cdot 10^{-5}$ steradian for the source (the solar disk) is shown in Figure 1.6.

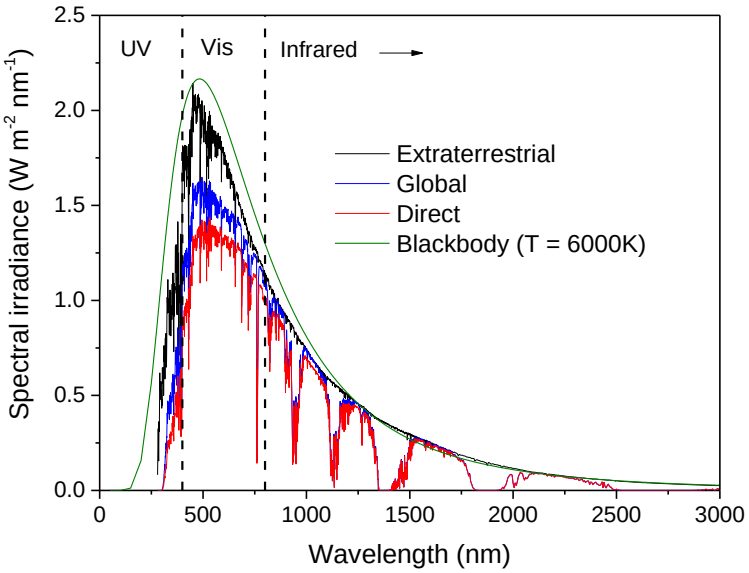

Figure 1.6. Reference solar spectral irradiance (ASTM G-173) at the top of Earth's surface (extraterrestrial) and at sea level (global and direct). Sun's spectrum considered it as a blackbody at 6000 K is also plotted.

1.3.2 Cells damages induced by sunlight

The first evidence of the bactericidal effect of sunlight was reported by Downes and Blunt in 1877 [Downes and Blunt, 1877]. It is commonly attributed to the synergistic effect of solar UV photons and mild-thermal heating produced during solar exposure. Nevertheless, each UV range may generate different injuries into cells according to their wavelength, as represented in Figure 1.7. The details of different ranges of radiation damages are explained below.

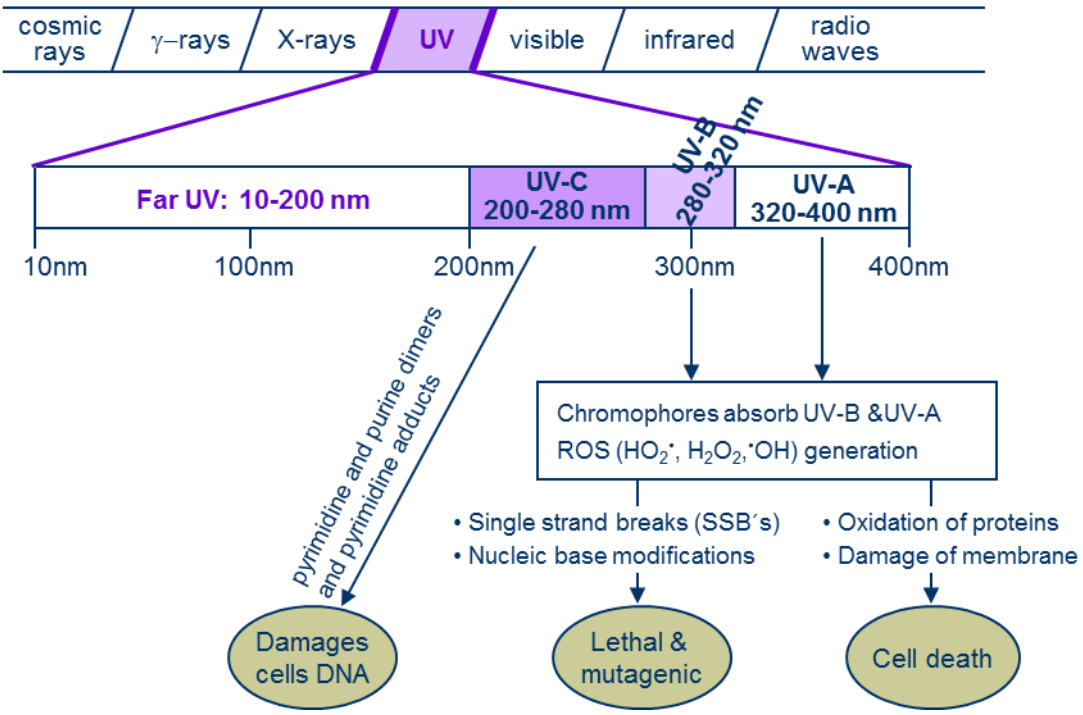

Figure 1.7. Main damages in cells caused by UV radiation [Malato *et al.*, 2009].

1.3.2.1 UVC (200 – 280 nm)

UVC is the most energetic and cell lethal UV radiation due to the maximum absorption of DNA, approximately at 260 nm. Cells radiated by UVC generate pyrimidine and purine dimers and pyrimidine adducts in DNA that eventually lead to later cells inactivation. In addition, UVC also generates protein damages, as they absorb light mainly at 190 nm, tailing up to 220 nm, mostly due to the presence of the peptide bond [–C(O)–NH–]. However, UVC does not reach the Earth's surface because is mostly absorbed in the atmosphere by ozone.

1.3.2.2 UVB (280 – 320 nm)

The shortest wavelengths of UVB are also absorbed in the atmosphere by ozone, reaching Earth's surface only a very small percentage of this radiation. This is strongly dependent on cloud cover and atmospheric conditions.

The UVB spectrum overlaps with the tail of DNA absorption, so that, the UVB radiation may lead to DNA alterations [Giannakis *et al.*, 2016]. The main DNA photo-products generated by the UVB light absorption are:

- Cyclobutane pyrimidine dimers (CPDs) formed by the excitation of pyrimidine bases (cytosine or thymine) to a triplet state and the further reaction with other pyrimidine bases.
- Pyrimidine (6-4) pyrimidone dimers formed by the excitation of pyrimidine bases to singlet triplet state and the reaction with other pyrimidine bases. Further absorption of UV light (A or B) could generate Dewar valence isomers that inhibit the DNA replication.
- Monomeric cytosine photoproducts formed by the excitation of monomeric cytosine compounds to singlet state and a nucleophilic addition of water.
- Purine base photoproducts. Purine bases (adenine or guanine) could absorb UVB light in a similar way as pyrimidine bases generating Dewar adducts.

In addition, some proteins can absorb UVB light, although their maximum absorbance belongs to the UVC region. Some of the amino acids that absorb UVB light are tryptophan (Trp), tyrosine (Tyr), phenylalanine (Phe), histidine (His), cysteine (Cys) and cysteine residues. Another important target is the enterobactin. It is a powerful iron-chelating agent which peak absorption occurs at 316 nm that results in an iron concentration increase under UVB light.

1.3.2.3 UVA (320 – 400 nm)

UVA also can damage directly DNA chain although the mechanism differs from UVB action. UVA is involved in the formation of CPD and Dewar valance isomers. The wavelengths that can induce the CPD formation tail up to 365 nm with simultaneous formation of (6-4) photo-products. In the case of Dewar valance isomers formation, the peak absorption for its formation is around 320 nm [Giannakis *et al.*, 2016].

In addition, UVA induced the reactions called Type I and Type II by the absorption of light of chromophores o photosensitizers as porphyrins, flavins, quinones, NADH/NADPH, among others. The Type I reactions are one-electron oxidation processes in which DNA bases are the electron donors, mainly guanine. This reaction induces the formation of Reactive Oxygen Species (ROS) by the generation of superoxide radicals that is the promoter of hydrogen peroxide and hydroxyl radicals. The Type II reactions involve the formation of singlet oxygen and the transformation of DNA bases to unstable stereoisomers. In the next section a detailed description of the formation of ROS is presented. Accumulated damages induced by ROS are considered as a main agent of damage produced by solar radiation. These species have been proven to induce lipids peroxidation, proteins oxidation, DNA damages by formation of pyrimidine dimers, or generation of single strands breaks (SSB's) [Goodsell, 2001]. Additionally, sunlight can also be absorbed by natural exogenous photosensitizers present in waters (i.e. humic acids and chlorophyls) and produce ROS by the reaction with dissolved oxygen.

UVA light could also alter the functionality of diverse intracellular compounds with important consequences in the cell survival. Catalase enzyme is one of this species that is affected by UVA light. Its main function is to decompound the hydrogen peroxide and to maintain it below the lethal doses to cells. Another vital and photo-sensitive compound is the dihydroxy acid dehydratase (DHAD). It is an iron-sulfur molecule that could be inactivated by UVA light. Further details on the importance of catalase and iron-sulfur cluster in cells are explained in the following sections.

Exposed cells have a series of DNA repair mechanisms that can restore dimers or remove the affected bases and nucleotides. This matter is particularly important for bacterial regrowth during storage. Repairing processes could probably come into action after the sunlight exposure. Nevertheless, if the UVA dose is sufficiently high, the repair mechanisms are overwhelmed [Ubomba-Jaswa *et al.*, 2009a].

1.3.3 Water pathogens

Bacteria, viruses, protozoa and fungi are waterborne vehicles agents (Table 1.2). Although *Escherichia coli* is the most studied microorganism, several pathogens have been object of study related to their resistance to solar radiation. Commonly, *E. coli* is used as a model target because it is a very well-known bacterium from all points of view: DNA metabolism, structure and composition, morphology, behaviour under different nutrient media, pathogenicity, types, strains, etc. The inactivation of *E. coli* cells are due to the disruption of the normal cellular functions as the ATP synthesis and the efflux pump. It was also observed loss in the membrane potential, a reduction of the glucose uptake and an increase in the permeability of the cytoplasmic membrane when the cells are exposed to sunlight [Berney *et al.*, 2006a].

Gill and McLoughlin performed an analysis of the kinetic rate k of the solar inactivation of different pathogens in comparison with *E. coli* using the ratio $k_{E.coli}/k$ as the relative solar disinfection resistance of each pathogen (Figure 1.8) [Gill and McLoughlin, 2007]. The relative resistance in many cases is provided in a range of values due to it is the result of diverse contributions. The diagram shows that the Gram-negative bacteria have similar sensitivity to *E. coli* with the exception of *Vibrio cholera*, which is much more resistant. Gram-positive bacteria (*Enterococci* sp., *Enterococcus faecalis* and *Bacillus subtilis*), are more difficult to disinfect. Although some of them are more resistant than *E. coli*, all the classically defined waterborne pathogenic bacteria have been found to be inactivated after 6 h of sunlight radiation [McGuigan *et al.*, 2012].

Protozoa (*Acanthamoeba polyphaga*, Figure 1.8) is quite resistant under normal conditions of irradiance and temperature; only when temperature exceeds 40 ºC any inactivation was observed. Other protozoa such as *Giardia lambia*, *Cryptosporidium* spp. or amoebae also show more resistance to SODIS than bacteria due to the thick-walled, chitinous cysts or oocysts forms of protozoa.

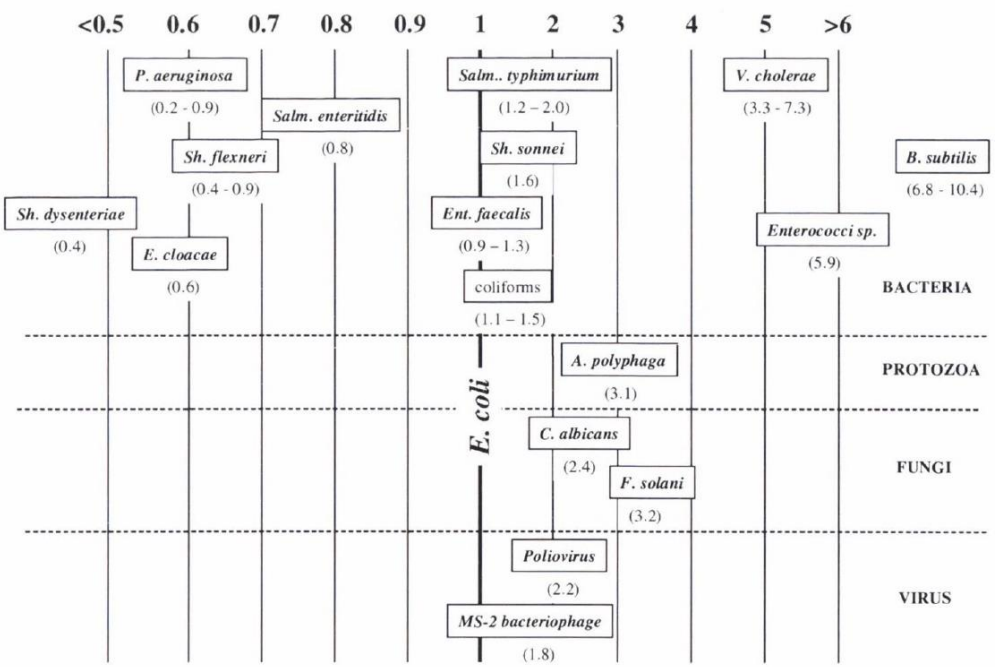

Figure 1.8. Relative solar radiation resistance of various microorganisms in comparison to *E. coli* [Gill and McLoughlin, 2007].

Fungal pathogens (*Candida albicans* and *Fusarium solani*, Figure 1.8) are more resistant than *E. coli* although their main route of infection is not via water, but via soil. Sichel and co-workers developed a comparison of the resistance to the action of sunlight of the genus *Fusarium*: *Fusarium oxysporum* > *Fusarium solani* > *Fusarium verticillioides* > *Fusarium anthophilum* > *Fusarium equiseti* [Sichel *et al.*, 2007b].

Finally, the viruses (bacteriophage Poliovirus and MS-2, Figure 1.8) present double resistance to solar radiation than *E. coli*. Nevertheless, the general resistance of the viruses against SODIS varies significantly from species to species. Somatic phage, bacteriophage f2 and bovine rotavirus are less resistant than bacteriophage Poliovirus or encephalomyocarditis virus [McGuigan *et al.*, 2012].

1.3.4 Common SODIS reactors

The concept "SODIS" is generally associated to the use of the typical plastic bottles of polyethylene terephthalate (PET) of 1 – 2 L. Recent research in the field was focused on overcoming the limitations of SODIS by the design of new reactors. The high treatment time (at least 6 hours) required to reach certain bacterial reduction, the low effectiveness in cloudy days or with turbid waters, the low volumes of treated water, limited to maximum capacity of the used bottles (2 L), the potential bacterial regrowth after the treatment time, the high user and weather dependency or the high resistance of some pathogens as spores, parasites, phages or virus to the solar exposure are some of the SODIS obstacles to be improved [McGuigan *et al.*, 2012].

Although, some interesting proposals to enhance SODIS efficiency and to increase the water out-put have been reported, not all the limitations have been overcome up to now and SODIS compliance is still limited. Keane and co-workers have reviewed the state-of-the-art of design and materials used for improved solar water disinfection [Keane *et al.*, 2014]. Some of these enhancements are (i) the substitution of PET material to acrylic bottles that obtain better inactivation results, (ii) photo-catalysts coated cylinders (typically TiO_2 or doped TiO_2) on bottles to reduce the treatment time and to assure no bacterial regrowth, and (iii) the substitution of small bottles by 19-L polycarbonate containers that permits treating larger volumes of water at a time [Keogh *et al.* 2015; Borde *et al.*, 2016].

On the other hand, photo-reactors with low-cost solar collectors designed for solar disinfection proposes have been demonstrated to be a promising choice. The main advantage of this type of reactors is the increase of the inlet photon flux in the water sample resulting in a reduction of the treatment time of larger volumes of water [Ubomba-Jaswa *et al.*, 2010]. Nonetheless, it is necessary to remember that SODIS is considered as an intervention technique to provide safe drinking water to little communities in low-income areas, thus materials and operational costs of the reactors should be maintained as cheap and robust as

possible. This requirement is accomplished by Compound Parabolic Collectors (CPC) reactors, which become a good candidate for SODIS implementation, and have successfully proven for solar disinfection [Navntoft *et al.*, 2008; Nalwanga *et al.*, 2014], photo-catalytic disinfection [Byrne *et al.*, 2011], and decontamination of polluted water [Malato *et al.*, 2009; Spasiano *et al.*, 2015]. Although photo-reactors have several advantages against bottles such as higher solar photon flux in water or exploitation of both direct and diffuse radiation leading to a higher efficiency in cloudy days, the photo-reactors take also some aspects into account that affect the disinfection performance. Re-circulatory flow systems generate dark areas delivering the solar dose in an interrupted manner to the water. Both, the ratio of illuminated/total volume and the way of delivering solar radiation dose affects significantly to the disinfection performance [Ubomba-Jaswa *et al.*, 2009a]. In line with this, the design of a different type of reactor was presented, like a 25-L batch reactor made of borosilicate glass placed in the focus of a CPC mirror that achieved good disinfection results against *E. coli* [Ubomba-Jaswa *et al.*, 2010].

In spite of the efforts done to design new SODIS reactors based on previous knowledge on photo-catalytic applications, there are still not any tailor-made design for SODIS efficient and inexpensive photo-reactors to conduct solar water disinfection at large scale for further implementation in developing countries or isolated communities.

1.3.5 Thermal effect during SODIS

Several factors affect the efficiency of disinfection by SODIS, lengthening or shortening the required solar exposure time to achieve a certain log-reduction. Solar irradiance and energy dose, wavelength, water temperature during treatment, water turbidity, salt concentration, dissolved oxygen, dissolved organic matter in the contaminated water and nature of the microorganisms are the most important factors that alter SODIS efficiency [Webb and Brown, 1979; Moss and Smith, 1981; Reed, 1997; McGuigan *et al.*, 1998; Ubomba-Jaswa *et al.*, 2009a; Ubomba-Jaswa *et al.*, 2010].

Regarding the temperature effect, Solic and Krstulovic studied the separated and combined effect of solar radiation and temperature on the survival of faecal coliforms in seawater [Solic and Krstulovic, 1992]. In the combined experiments, the temperature ranged from 14.5 to 24.9 ºC and the solar irradiance from 510 to 830 W m^{-2} (not named the range of wavelengths). An ANOVA analysis concluded that the effect of solar radiation is much important that temperature and the effects of temperature and solar radiation are not simply additive but are synergistic in their effect. In a later work, it was observed that water temperature between 20 and 40 ºC did not affect the inactivation of bacteria by UVA and visible light radiation. However, a beneficial effect at a threshold water temperature of 50 ºC was observed, since at this temperature or above, the required fluences to inactive *E. coli* were three times smaller compared to lower water temperatures [Wegelin *et al.*, 1994]. To support these results, Berney and co-workers studied the thermal effect on *E. coli* in the dark and observed at slight rate of inactivation even at 48 ºC [Berney *et al.*, 2006b]. Due to this strong synergy, a number of enhancement methods have been proposed to reach this water temperature value for SODIS acceleration. Some techniques used for increasing the water temperature are: (i) to use black paint over some sections of the bottles; (ii) to use absorptive materials, (iii) to circulate the water over a black surface in an enclosed container transparent to UVA light; (iv) to use solar collectors or solar reflectors [McGuigan *et al.*, 2012].

The beneficial effect of higher temperatures on solar water disinfection was experimentally demonstrated but it was directly attributed to a synergy with any comparison with the single effects addition. It was not until 1998, when McGuigan and co-workers reported the evidence of the synergy developing empirical models that predicted the inactivation curves of *E. coli* by thermal effect, by solar water disinfection with no dependence of temperature, and by the combined effect of both actions [McGuigan *et al.*, 1998]. Thermal inactivation was modelled with first order kinetics equation using a kinetic thermal constant as a function of temperature using the Mancini equation:

$$N(t) = N_0 \cdot e^{-k_T \cdot t}; \quad k_T = \theta^{(T-\alpha)} \tag{1.2}$$

where $N(t)$ and N_0 are the instantaneous and initial bacterial population respectively, k_T is the thermal constant, t is the time, T is the temperature and θ and α are the Mancini fit parameters. Optical inactivation, with no dependence of temperature, was modelled assuming two groups of bacterial population, light resistant and light sensitive bacteria:

$$N(t) = N_S \cdot e^{-k_S \cdot t} + N_R \cdot e^{-k_R \cdot t} \tag{1.3}$$

where N_S and N_R are the initial light sensitive and light resistant bacterial population respectively and k_S and k_R are the decay constants for light sensitive and resistant population. The combined effect between radiation and temperature was initially modelled as the additive of the single effects:

$$N(t) = N_S \cdot e^{-(k_S + k_T) \cdot t} + N_R \cdot e^{-(k_R + k_T) \cdot t} \tag{1.4}$$

However, they observed that this model underestimates the measured inactivation, demonstrating that the relationship between optical and thermal inactivation mechanisms is more than the addition of the combined simulations. To model the synergistic relationship they used a 'synergy term', S that takes values larger than 1 when synergy occurs:

$$N(t) = N_S \cdot e^{-S \cdot (k_S + k_T) \cdot t} + N_R \cdot e^{-S \cdot (k_R + k_T) \cdot t} \tag{1.5}$$

The equation that includes the synergy terms fitted accurately the experimental inactivation at different temperatures. This fact demonstrates that the optical and thermal effects modify the efficiency of the solar water disinfection synergistically.

1.4 Intracellular Reactive Oxygen Species in *E. coli*

1.4.1 Respiration of *E. coli*

E. coli is classified as a facultative anaerobic bacterium so it is able to extract energy from substrates both aerobically and anaerobically, although its aerobic energy production is far more efficient than the anaerobic metabolism. The bacterial aerobic respiration is represented in the Figure 1.9 and it is divided in four phases: glycolysis, pyruvate decarboxylation, Krebs cycle and electron transport chain. The oxygen can diffuse freely through the cellular membrane into the interior of the cytoplasm where respiration is taken place. In the process, the pyruvic acid produced by the glycolysis decomposes into carbon dioxide and water, generating the high-energy compounds adenosine triphosphate (ATP). The glucose is used as source of fuel and oxygen as the final acceptor of electrons.

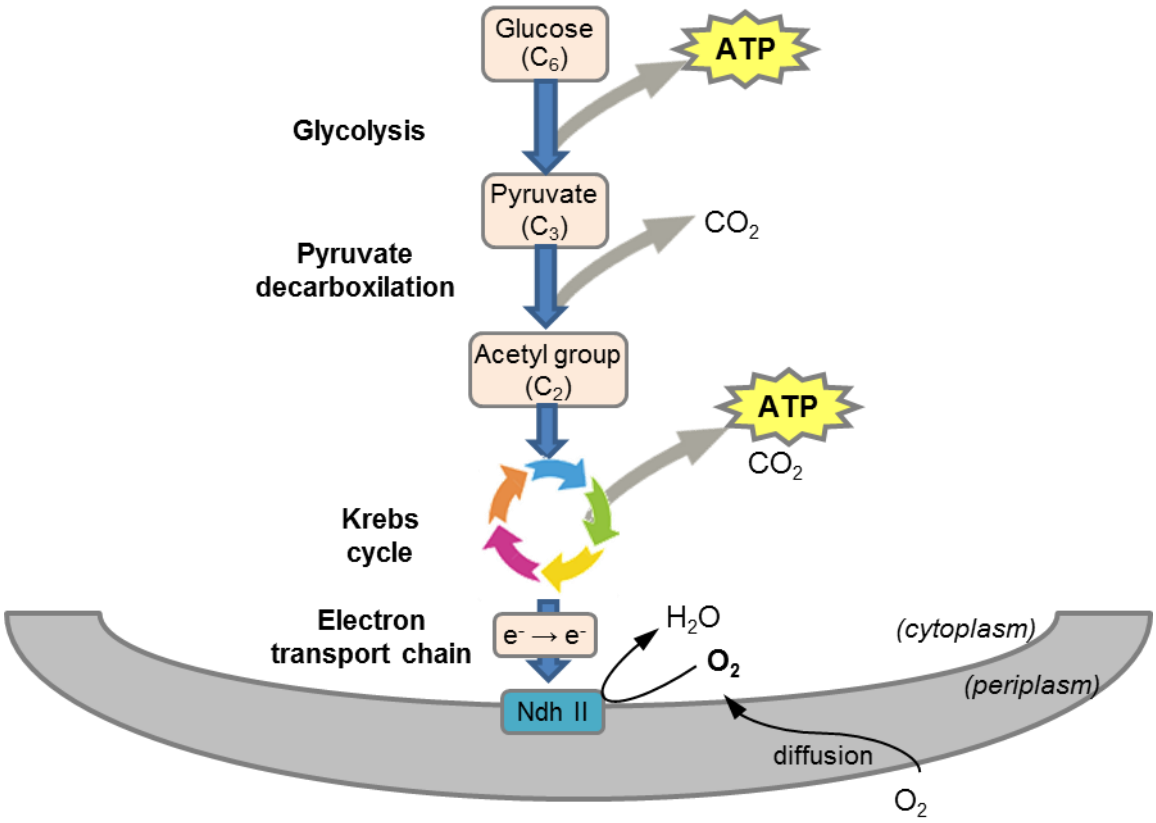

Figure 1.9. Scheme of the aerobic respiration process in cells.

1.4.1.1 Phases prior to electron transport chain

The first step of the respiration process is the **glycolysis** (Figure 1.9) that is the metabolic pathway that converts glucose ($C_6H_{12}O_6$) into pyruvate ($C_3H_3O_3^-$) and energy in form of ATP (2 molecules per 1 of glucose) by the following global reaction:

$$C_6H_{12}O_6 + 2NAD^+ + 2ADP + 2HPO_4^- \rightarrow 2C_3H_3O_3^- + 2NADH + 2H^+ + 2ATP + 2H_2O \quad (1.6)$$

where NAD^+ and NADH are the oxidized and reduced forms of the nicotinamide adenine dinucleotide and ADP is the adenosine diphosphate. It is an oxygen-free stage that occurs with some variations in nearly all organisms, aerobic and anaerobic; 10 different enzymes are involved on it [Tortora *et al.*, 2007].

The next stage of the respiration process is the **pyruvate decarboxylation** (Figure 1.9). It consists on the pyruvate oxidation to acetyl coenzyme A (acetyl-CoA), one molecule of NADH and one molecule of CO_2. The global reaction is:

$$C_3H_3O_3^- + NAD^+ + CoA \rightarrow \text{acetyl-CoA} + NADH + H^+ + CO_2 \quad (1.7)$$

The pyruvate dehydrogenase complex located in the cytosol, catalysed this reaction. The CoA is a compound that contains a high electronegative sulfur-based functional group that binds to a carbon in the acetyl group generating the very reactive acetyl-CoA.

The last step of the respiration process before the electron transport chain is the **Krebs cycle** (Figure 1.9) that is also known as the citric acid cycle or the tricarboxylic acid cycle. The Krebs cycle involves a total of nine reactions involving different enzymes and co-enzymes. It is a sequential cycle, in which the reagents are the products of the previous reaction. Some of the metabolic reactions require electron transfer in which the coenzymes NAD^+, GDP (guanosine diphosphate) and FAD (flavin adenine dinucleotide in the oxidized form) are involved as the electron donors.

1.4.1.2 Electron transport chain

The electron transport chain (ETC) is the last step of the respiration process. This phase has special interest from the point of view of the mechanistic model of bacterial inactivation presented in this work, thus it is explained in more detail.

The ETC results in the pumping of H^+ across the inner membrane (plasma or cytoplasmic membrane) creating a proton gradient from the cytoplasm to the periplasm. The protons are used by ATP synthase (located on the membrane) to generate ATP. Electrons involved in the process are finally transferred to exogenous oxygen forming water by the addition of two protons. Several transmembrane enzyme complexes that catalysed the redox reactions, co-enzymes that act as electron carriers and electron acceptors and donors, drive the process. In bacteria cells, the ETC is a very complex process since they have several electron donors, enzymes and electron acceptors that can operate simultaneously, generating a large number of respiratory pathways that can be established by different combinations of the compounds involved. *E. coli* have 10 different electron donor substrates and 8 different electron acceptors [Unden *et al.*, 2014].

Mainly, two types of enzymes are acting during the ETC: the dehydrogenases or quinone reductases and the terminal reductases or quinol oxidases. There are several types of both enzymes that are active depending on the cells conditions, i.e. aerobic or anaerobic [Unden *et al.*, 2014].

1. Dehydrogenases. The function of this enzyme is to oxidize the NADH formed in the Krebs cycle and to pump the H^+ forming by the redox reaction to the periplasm space. *E. coli* have 15 different primary dehydrogenases but NADH dehydrogenase I (NADH:quinone reductase, or NuoA-N) appears to be the only H^+-pumping dehydrogenase of the respiratory chain (Figure 1.10 (a)). The process is described by the reaction:

$$NADH + H^+ + Q + 4H^+_{in} \rightarrow NAD^+ + QH_2 + 4H^+_{ex} \quad (1.8)$$

During the oxidation of NADH, 4 H^+ are pumping across the cytoplasmic membrane per molecule of NADH (transfers 2 e^-) and the quinone (Q) is reduced to quinol (QH_2).

In aerobic respiration, the NADH dehydrogenase II (Ndh) is the major enzyme that has the same function of NuoA-N but without any gradient of H^+ (Figure 1.10 (a)).

2. Terminal oxidases. The function of this enzyme is to reduce an electron acceptor (mainly O_2) and to pump the H^+ to the periplasm. *E. coli* contains at least 14 different terminal membrane-bound reductases for the oxidation of quinol and the reduction of 8 different electron acceptors (oxygen, nitrate, nitrite, fumarate, trimethylamine N-oxide, dymethil sulfoxide, tetrathionate and thiosulfate). The terminal enzyme activated under aerobic conditions that reduces oxygen is the quinol oxidase CyoABCD (or quinol oxidase *bo*$_3$). It couples the redox reaction of quinol to H^+ pumping (Figure 1.10 (b)). The subunit CyoA catalyses the oxidation of quinol to quinone and the subunit CyoB transfers electrons from CyoA to oxygen [Schultz and Chan, 1998]. The global reaction is:

$$2\,QH_2 + O_2 + 8H^+_{in} \rightarrow \; 2Q + 2H_2O + 8H^+_{ex} \qquad (1.9)$$

CyoAB subunits are similar to the alternative quinol oxidase CydAB (used under microaerobic conditions, Figure 1.10 (b)) and contain the redox groups (heme *a*, heme *o*$_3$, Cu_B) required for intramolecular electron transfer, reduction of O_2 and H^+ pumping. The small accessory subunits CyoC and CyoD are not involved in catalysis.

Generally, the reactions could be classified in two redox reactions or two redox loops. In the first half-loop, 2 e^- are transferred from an electron donor at the periplasm (positive side) to the cytoplasm (negative side) where a quinone is reduced consuming 2 H^+ and forming a quinol. In the second half-loop, the quinol crosses the membrane to the periplasm, where it is oxidized and releases protons. Therefore, the complete redox loop generates a proton potential by the

transfer of e^- from the periplasm to the cytoplasm and a gradient of H^+ in the opposite sense. Although, the main function of the enzymes is to pump H^+ through the membrane, there are also some enzymes that act as redox half-loops or electron sinks without generating a proton potential directly.

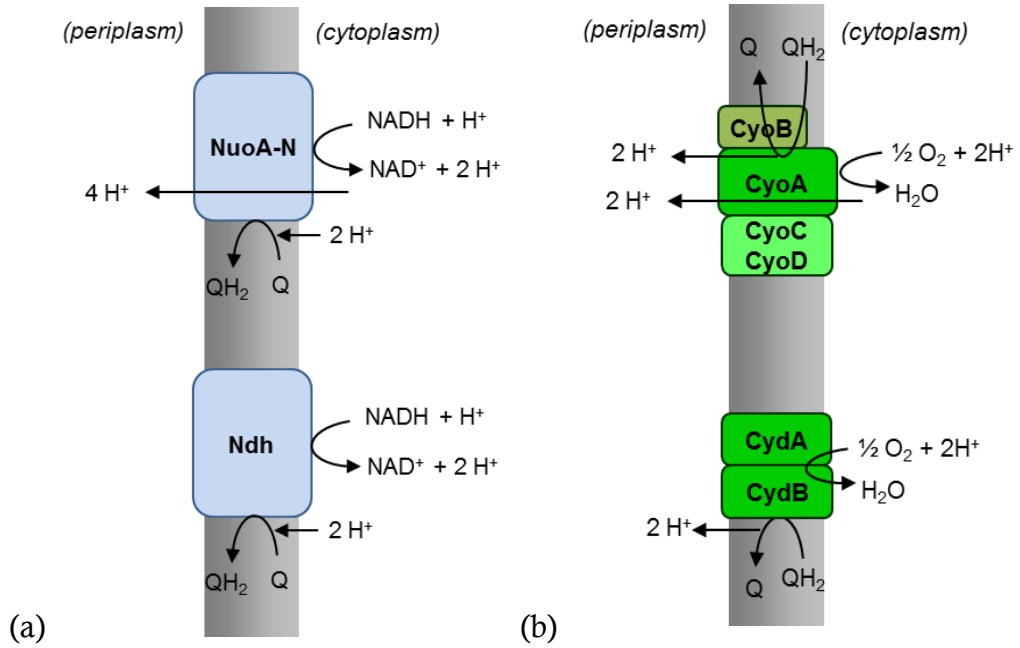

Figure 1.10. Scheme of the ETC in *E. coli*: (a) NADH oxidation by NuoA-N and Ndh and (b) e^- transfer to O_2 by CyoABCD and CydAB [adapted from Unden *et al.*, 2014].

1.4.2 Endogenous oxidative stress in *E. coli*

In aerobic organisms, molecular oxygen can free diffuse inside cells, so the intracellular concentration is similar as the immediately outside the cell [Imlay, 2008]. Intracellular O_2 can be reduced by one-electron steps (Figure 1.11) generating partially reduced oxygen species that are more reactive than molecular oxygen itself and are well-known as Reactive Oxygen Species (ROS). The evidence of the presence of oxygen free radicals in cells was firstly reported by Rebeca Gerschman *et al.* in 1954 while studying the toxic effects of high O_2 pressures and X-ray irradiation in mice [Gerschman *et al.* 1954].

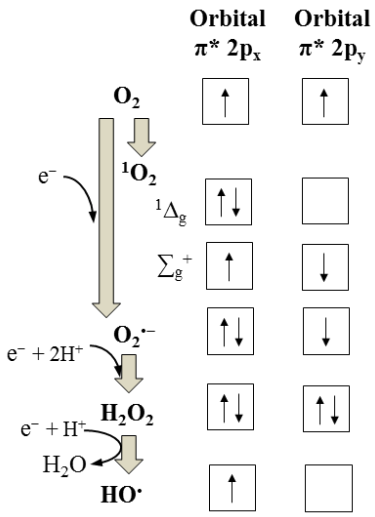

Figure 1.11. Oxidation states of oxygen.

ROS are characterized by having a highly positive redox potential. The standard reduction potential is defined relative to a reference electrode of hydrogen which is arbitrarily given a potential of 0.00 V. It is a measure of the tendency of a chemical species to acquire electrons, reducing its oxidation state and acting as an oxidizing agent. Each species has its own intrinsic reduction potential. The higher the reduction potential, the greater the species' strength is as oxidizing agent. Table 1.5 shows a list of the redox potentials of some ROS and other reactive species.

Several natural intracellular mechanisms result in the formation of the internal ROS in cells. The natural formation of intracellular ROS in aerobic cells leads to the necessity to maintain a strong defence activity against them. *E. coli* responds to oxidative stress by modifying the expression of many genes and activating more than 80 proteins. The best-characterized regulators of the antioxidant responses are the OxyR and SoxRS proteins, both activated in cells under specific types of oxidative stress. Their activation results in the expressions of a large variety of genes (regulons) showing a wide variety of cellular defence mechanisms against oxidative stress and includes: scavenging of reactive species, synthesis of reducing species, repairing of oxidative damages, drug efflux, reduction of cell permeability and replacement of redox-sensitive isozymes by

redox-resistant isozymes [Pomposiello *et al.*, 2001]. The most important mechanism to protect cells against the effects of oxidant species is to scavenge them using the enzymes superoxide dismutase and catalase that remove superoxide radical and hydrogen peroxide, respectively. Figure 1.12 shows the main natural pathways of generation of ROS in a bacterial cell, the most likely injuries caused by ROS and the mechanisms to scavenge some of these ROS. All the information summarized in the figure is explained in detail in next sections.

Table 1.5. Standard reduction potentials for biologically relevant molecules and reactive species [Vatansever *et al.*, 2013].

Half reaction	Reduction Potential (*)
$HO^{\bullet} + e^{-} + H^{+} \rightarrow H_2O$	+2.31 V
$O_3 + 2e^{-} + 2H^{+} \rightarrow H_2O + O_2$	+2.08 V
$O_3^{\bullet-} + e^{-} + 2H^{+} \rightarrow H_2O + O_2$	+1.90 V
$Co(III) + e^{-} \rightarrow Co(II)$	+1.82 V
$CO_3^{\bullet-} + e^{-} \rightarrow CO_3^{2-}$	+1.80 V
$H_2O_2 + 2e^{-} + 2H^{+} \rightarrow 2H_2O$	+1.76 V
$RO^{\bullet} + e^{-} + H^{+} \rightarrow ROH$	+1.60 V
$O^{\bullet-} + e^{-} + 2H^{+} \rightarrow H_2O$	+1.46 V
$N_3^{\bullet} + e^{-} \rightarrow N_3^{-}$	+1.30 V
$^1\sum_g O_2 + e^{-} \rightarrow O_2^{\bullet-}$	+1.27 V
$N_2O_4 + e^{-} \rightarrow NO^{\bullet} + NO_3^{-}$	+1.20 V
$HOCl + 2e^{-} + H^{+} \rightarrow H_2O + Cl^{-}$	+1.08 V
$Fe(III)(1,10\text{-phen})_3 + e^{-} \rightarrow Fe(II)(1,10\text{-phen})_3$	+1.06 V
$HO_2^{\bullet} + e^{-} + H^{+} \rightarrow H_2O_2$	+1.06 V
$O_3 + e^{-} \rightarrow O_3^{\bullet-}$	+1.03 V
$ROO^{\bullet} + e^{-} + H^{+} \rightarrow ROOH$	+1.00 V
$NO_2^{\bullet} + e^{-} \rightarrow NO_2^{-}$	+0.99 V
$O_3(g) + e^{-} \rightarrow O_3^{\bullet-}$	+0.91 V
$^1\Delta_g O_2 + e^{-} \rightarrow O_2^{\bullet-}$	+0.81 V
$N_2O_3 + e^{-} \rightarrow NO^{\bullet} + NO_2^{-}$	+0.80 V
$^1\Delta_g O_2(g) + e^{-} \rightarrow O_2^{\bullet-}$	+0.64 V
$SO_3^{\bullet-} + e^{-} \rightarrow SO_3^{2-}$	+0.63 V
$O_2^{\bullet-} + e^{-} + 2H^{+} \rightarrow H_2O_2$	+0.36 V
$H_2O_2 + e^{-} + H^{+} \rightarrow H_2O + HO^{\bullet}$	+0.32 V
$ONOO^{\bullet} + e^{-} \rightarrow ONOO^{-}$	+0.20 V
$Cu(II) + e^{-} \rightarrow Cu(I)$	+0.16 V
$2H^{+} + e^{-} \rightarrow H_2$	+0.00 V
$O_2 + e^{-} \rightarrow O_2^{\bullet-}$	−0.18 V
$O_2(g) + e^{-} \rightarrow O_2^{\bullet-}$	−0.33 V
$NAD^{+} + e^{-} + H^{+} \rightarrow NADH^{+}$	−1.58 V
$H_2O + e^{-} \rightarrow e_{aq}^{-}$	−2.87 V

(*) In aqueous solution (pH = 7), unless otherwise stated (g), at 25 °C and 1 M concentration.

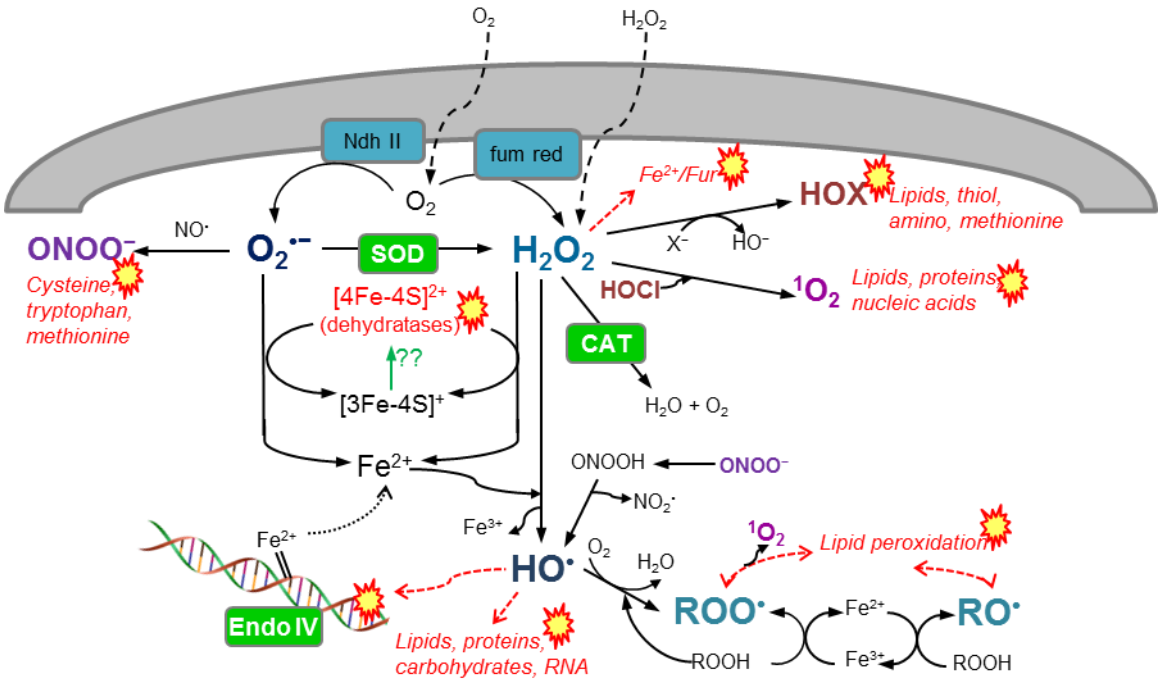

Figure 1.12. Scheme of the naturally formation of intracellular ROS that induce some biomolecules damages (in red) and the defensive response (in green).

1.4.2.1 Superoxide radical, $O_2^{\bullet-}$

The respiratory chain was proven to be the major source of $O_2^{\bullet-}$ formed in the cytoplasm and then released into the periplasm [Korshunov and Imlay, 2006] with a production rate of about 5 μM s^{-1} [Imlay, 2008]. The formation mechanism is driven during the ETC mainly by the Ndh [Messner and Imlay, 1999] and the terminal enzymes, fumarate reductase, succinate dehydrogenase and D-lactate dehydrogenase [Messner and Imlay, 2002]. The glutathione reductase was found one of the main cytosolic enzymes that catalyse the electron transfer from NADH to oxygen [Imlay *et al.*, 1988]. The endogenous redox compounds that provide the electrons to the final acceptor are typically flavins, viologens, phenazines, thiols or quinones [Imlay, 2008]. Oxygen is in theory the last acceptor of electrons to generate water but in reality, partially reduced oxygen species are produced as 'by products'. Thus, leakage of electrons from the electron transport chain is the source of hydroperoxyl radical $HO_2^{\bullet}$ that further dissociate to generate superoxide radicals, $O_2^{\bullet-}$ [Vatansever *et al.*, 2013]:

$$O_2 + e^- + H^+ \rightarrow HO_2^{\bullet} \quad (1.10)$$

$$HO_2^{\bullet} \rightarrow H^+ + O_2^{\bullet -} \quad (1.11)$$

Superoxide radical could be considered as an activator factor since is the precursor of other reactive radicals, but it could be toxic to certain biological structures itself. Also, $O_2^{\bullet -}$ permits splitting various C-O and C-halogens bounds. The main reactions in which $O_2^{\bullet -}$ is involved could be classified in six groups [Afanas'ev, 1989]:

1. Protonation to form the hydroperoxyl radical using organic compounds (alcohols, carboxylic acids, phenols, hydrocarbons,…) as the proton donor or directly with a free proton:

   $$O_2^{\bullet -} + HX \leftrightarrows HO_2^{\bullet} + X^- \quad (1.12)$$

   $$O_2^{\bullet -} + H^+ \leftrightarrows HO_2^{\bullet} \quad (1.13)$$

   The reaction (1.13) follows a second-order kinetics with a rate constant higher at acidic pH due to the increase in the concentration of $HO_2^{\bullet}$ (pKa = 4.8). [Augusto and Miyamoto, 2011].

2. Nucleophilic substitution with alkyl halides, sulfonates and phosphates (reaction (1.14)) or esters, acyl halides and acyl anhydrides (reaction (1.15)):

   $$O_2^{\bullet -} + AX \leftrightarrows AO_2^{\bullet} + X^- \quad (1.14)$$

   $$O_2^{\bullet -} + RCOX \leftrightarrows RC(O)O_2^{\bullet} + X^- \quad (1.15)$$

3. Electron transfer with quinones, cuprous complexes, ferrous complexes or sulfur dioxide:

   $$O_2^{\bullet -} + Q \leftrightarrows O_2 + Q^{\bullet -} \quad (1.16)$$

   Specifically, the reaction with iron-sulfur clusters has important implications on the oxidative stress. $O_2^{\bullet -}$ causes one-electron oxidation of the [4Fe-4S] clusters to form H_2O_2 and an unstable intermediate that decomposes releasing free iron. The importance of this reaction will be discussed below.

$$[4Fe\text{-}4S]^{2+} + O_2^{\bullet -} + 2H^+ \rightarrow H_2O_2 + [4Fe\text{-}4S]^{3+} \rightarrow [3Fe\text{-}4S]^{+} + Fe^{2+} \quad (1.17)$$

4. Addition with a metal ion or metal complex:

$$O_2^{\bullet -} + M^+ \leftrightarrows MO_2 \quad (1.18)$$

5. Radical-radical reactions of $O_2^{\bullet -}$ are additional reactions. One of these reactions that have received special attention, is the one with nitric oxide ($NO^{\bullet}$), that it is extremely fast ($k = 4 - 6 \cdot 10^9$ M^{-1} s^{-1}) and generates the peroxynitrite ($ONOO^-$) that is considered a strong biological oxidant [Winterbourn and Kettle, 2003]:

$$O_2^{\bullet -} + NO^{\bullet} \rightarrow ONOO^- \quad (1.19)$$

6. Deprotonation-oxidation:

$$O_2^{\bullet -} + RH \leftrightarrows HO_2^{\bullet} + R^- \quad (1.20)$$

$$R^- + O_2 \leftrightarrows R^{\bullet} + O_2^{\bullet -} \quad (1.21)$$

7. Dismutation:

$$O_2^{\bullet -} + O_2^{\bullet -} + 2H^+ \rightarrow H_2O_2 + O_2 \quad (1.22)$$

   The dismutation of $O_2^{\bullet -}$ occurs spontaneously at a slower rate ($k = 5 \cdot 10^5$ M^{-1} s^{-1}) but it is also catalysed by the superoxide dismutase enzyme ($k = 1.6 \cdot 10^9$ M^{-1} s^{-1}) [McCord and Fridovich, 1969]. The main function of this enzyme is to scavenge this toxic radical, naturally formed in the cells, and to maintain it at low or non-lethal concentrations, approximately 10^{-10} M, [Gort and Imlay, 1998].

Superoxide radicals are a very power oxidant that can cause several damages in bacterial cells by different routes. Firstly, $O_2^{\bullet -}$ is able to directly inactivate a family of dehydratases. This may affect to the efficiency of the routes in which those enzymes are involved, i.e. the branched-chain biosynthetic pathway (dihydroxyacid and isopropylmalate dehydratases) and the Krebs cycle (aconitase B and fumarases A and B) [Imlay and Hassett, 2011]. These enzymes

contain [4Fe-4S] clusters that are inactive by the reaction (1.17). Nevertheless, the bacterial cells could handle these enzymes damages because they are continuously reactivated by a repairing mechanism that still remains unknown [Djaman *et al*. 2004].

Indirectly, the inactivation of the iron-sulfur cluster also accelerates the rate of DNA damage due to the iron free release that act as a catalyst in Fenton reaction generating hydroxyl radicals (explained in detail below). Another metabolic routes affected by $O_2^{\bullet-}$ are the aromatic amino acids synthesis and the assimilation of sulfur atoms from sulfate [Imlay and Fridovich, 1992].

Nevertheless, as it was previously explained, bacterial cells count with cellular defences against $O_2^{\bullet-}$. In *E. coli*, two proteins govern the cell response against $O_2^{\bullet-}$, SoxR, which is a sensor protein that detects redox stress, and SoxS that is a transcriptional activator. SoxR contains a $[2Fe\text{-}2S]^{+}$ cluster that is oxidized to a +2 state when cells are exposed to redox-cycling agents. The oxidation of this homodimer protein generates a conformational change in the protein that is transmitted to the bound promoter region inducing the binding of a RNA-polymerase [Imlay, 2008] and the transcription of *soxS* that active the SoxS. This protein regulates the expression of a broad number of genes. When redox-cycling are removed, SoxR reverts to its reduced form, and then SoxS suffers a rapid turnover of by proteases ending the response [Imlay, 2008]. Figure 1.13 shows the genes expressed when cells are expose to high amounts of $O_2^{\bullet-}$.

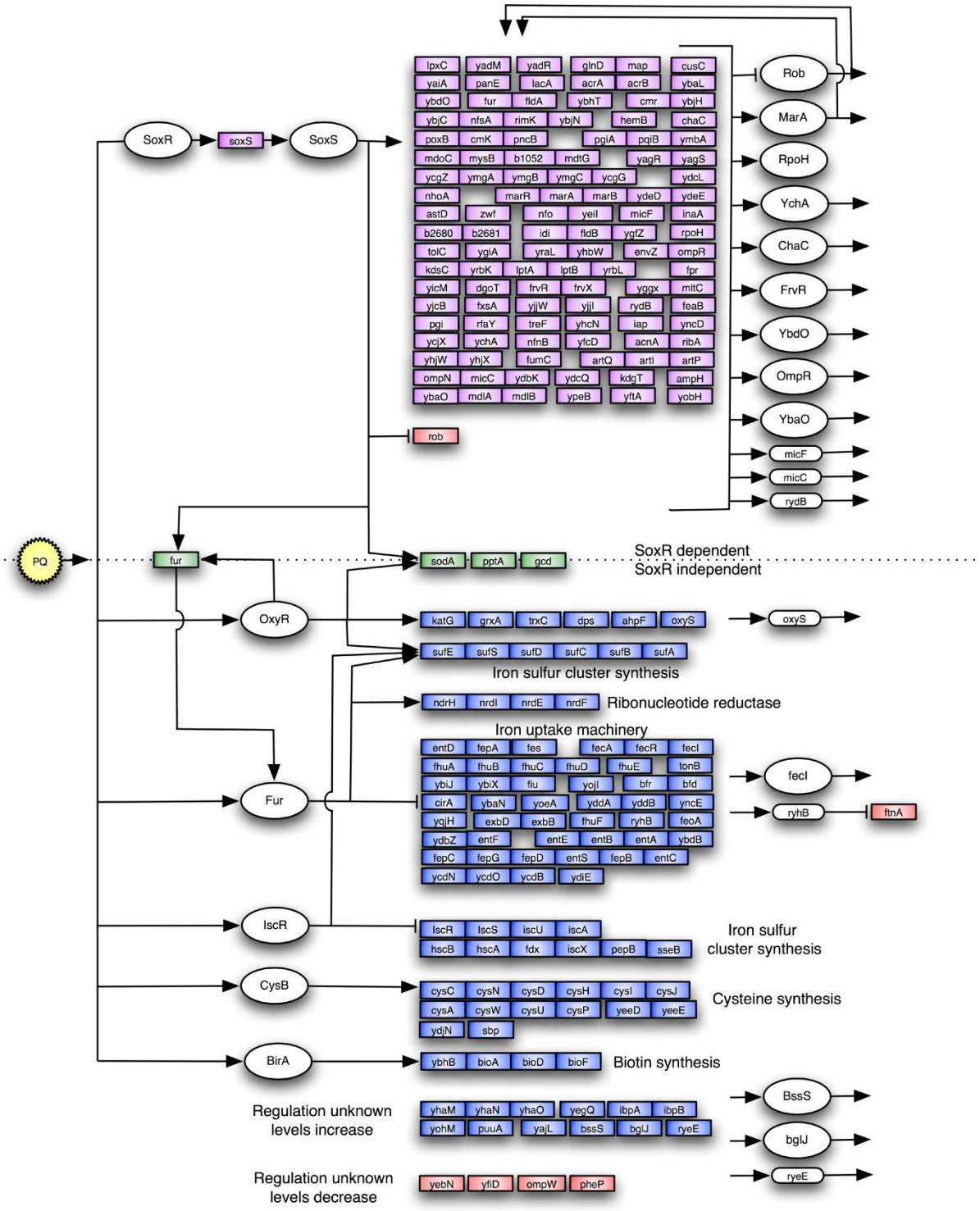

Figure 1.13. *E. coli* response against superoxide radicals generated by paraquat (PQ) [Blanchard *et al.*, 2007].

The main enzyme protecting cells against the levels of $O_2^{\bullet-}$ is the superoxide dismutase (SOD). Gram-negative bacteria commonly synthesize both cytoplasmic and periplasmic isozymes of SOD. At physiological state, $O_2^{\bullet-}$ do not cross membranes, so both compartments are considered separately. *E. coli* contains two cytoplasmic enzymes that are the MnSOD (encoded in *sodA*) and the FeSOD (*sodB*) and one periplasmic, CuZnSOD (enconded in *sodC*). The activation of MnSOD or FeSOD is dependent on the iron levels, being MnSOD the most synthesized at low iron concentrations. FeSOD is synthesized when iron is available and also in anaerobic conditions, apparently in preparation for entry into aerobic habitats [Massé and Gottesman, 2002]. The role of the periplasmic SOD is unclear since no periplasmic molecule has been identified as vulnerable to $O_2^{\bullet-}$ [Imlay and Hassett, 2011].

The amount of cytoplasmic SOD in exponential growth of *E. coli* was determined to be around 20 μM achieving levels of $O_2^{\bullet-}$ below 10^{-10} M [Gort an Imlay, 1998]. Considering that the formation rate of the radical is about 5 μM s^{-1}, the enzyme content is almost five orders of magnitude higher than the substrate. This fact is explained by the capacity of $O_2^{\bullet-}$ to oxidize [4Fe-4S] clusters in a very rapid reaction, $10^6 – 10^7$ M^{-1} s^{-1}. To avoid it, cells must synthetize high amounts of SOD, i.e. with less than 10 μM of SOD, the half-time of dehydratase inactivation will be less than an hour [Imlay, 2008]. In mutants of *E. coli* that lacked SOD (*E. coli sodA sodB*), it was found that the concentration of endogenous $O_2^{\bullet-}$ may be elevated $2.5 \cdot 10^3$-fold over that in aerobically growing wild-type cells [Farr and Kogoma, 1991].

1.4.2.2 Hydrogen peroxide, H_2O_2

Approximately 15 μM s^{-1} H_2O_2 is formed in well-fed cells. The mechanism of formation of the intracellular H_2O_2 has been largely studied [Messner and Imlay, 1999; Korshunov and Imlay, 2006]. Surprisingly in *E. coli*, the predominant sources of cytoplasmic H_2O_2 must lie outside the respiratory chain but the main source is still unknown [Seaver and Imlay, 2004]. It could be formed from the dismutation of superoxide radicals (reaction (1.22)) or from direct reduction of

oxygen by the action of the enzymes fumarate reductase and aspartate oxidase [Messner and Imlay, 2002].

External cellular H_2O_2 can freely diffuse across membranes due to the small size, reaching toxic levels inside cells. Millimolar doses of exogenous H_2O_2 are quite toxic to cells, but these doses are far beyond physiological concentration estimated to be around 10^{-7} – 10^{-8} M [Imlay, 2008]. Although H_2O_2 has a high reduction potential, its real power of oxidation for diverse biological molecules is low because of the high activation energy of these reactions [Augusto and Miyamoto, 2011]. The potential toxic effect of H_2O_2 is explained because it is the precursor of several radical species, which are more reactive, such as hydroxyl radical ($HO^{\bullet}$) and nitrogen dioxide ($NO_2^{\bullet}$), and non-radical species, including hypochlorous acid (HOCl) and related species.

H_2O_2 directly oxidizes unincorporated intracellular ferrous iron by the well-known Fenton reaction generating the powerful oxidant $HO^{\bullet}$:

$$Fe^{2+} + H_2O_2 \rightarrow Fe^{3+} + OH^- + HO^{\bullet} \quad (1.23)$$

The capacity of H_2O_2 to oxidize the ferrous ion affect to numerous pathways in the cells. Some of them are:

a. The oxidation of DNA-bound iron that could be mutagenic and lethal if the damages are abundant. At intracellular concentrations of H_2O_2 up to 1 μM, it is observed a large number of DNA damages while above 10 μM the rate of DNA injury becomes independent of H_2O_2 concentration [Park *et al.*, 2005] due to the lack of free ferrous iron.

b. The inactivation of [4Fe-4S] clusters of dehydratases that lead to the dysfunction of both the branched-chain biosynthetic pathway and the Krebs cycle [Imlay and Hassett, 2011]:

$$[4Fe\text{-}4S]^{2+} + H_2O_2 \rightarrow [4Fe\text{-}4S]^{3+} + OH^- + HO^{\bullet} \quad (1.24)$$

$$[4Fe\text{-}4S]^{3+} \rightarrow [3Fe\text{-}4S]^{+} + Fe^{2+} \quad (1.25)$$

c. The inactivation of some mononuclear enzymes as ribulose-5-phosphate epimerase [Sobota and Imlay, 2011]. The iron of the active enzyme binds to the substrate to prepare it to the epimerization.

d. The oxidation of the complex Fe^{2+}/Fur (ferric uptake regulator) that is the main regulator of the levels of iron in the cells. The mechanism of action of this regulator is quite simple: when the cell iron levels are acceptable, the ferrous ion of this complex binds to the DNA to repress the transcription of iron import systems. However, when it is oxidized, the repression is inhibited generating an increase in iron that can lead to lethal levels for DNA damages [Varghese *et al.*, 2007].

In addition, H_2O_2 is capable to react with some biological structures that have no transition metals. Two of the main targets of H_2O_2 are the thiols and the keto acids. Among the thiols, the cysteine reacts with a rate of 2 M^{-1} s^{-1}, and regarding keto acids, the pyruvate has a similar reaction rate of 2.2 M^{-1} s^{-1} [Winterbourn, 2013].

Regarding the intracellular levels of H_2O_2 in *E. coli*, recently Adolfsen and Brynildsen have been developed a very rigorous kinetic model of the reactions that determine the H_2O_2 concentration in cells [Adolfsen and Brynildsen, 2015]. The reactions are displayed in the Figure 1.14 that also includes the reactions by which H_2O_2 is scavenged to maintain low concentration inside bacteria.

Scavenger of hydrogen peroxide in biological systems consists mainly on the action of peroxidases (reaction (1.26)) and catalases (reaction (1.27)):

$$RH_2 + H_2O_2 \rightarrow R + 2H_2O \quad (1.26)$$

$$2H_2O_2 \rightarrow O_2 + 2H_2O \quad (1.27)$$

The primary scavenger in *E. coli* is an alkylhydroperoxide reductase (Ahp) which kinetic constant $k_{cat}/K_m = 4 \cdot 10^7$ M^{-1} s^{-1} was determined as a Michaelis-Menten kinetic (k_{cat}: kinetic constant; K_m: Michaelis constant) [Imlay, 2008].

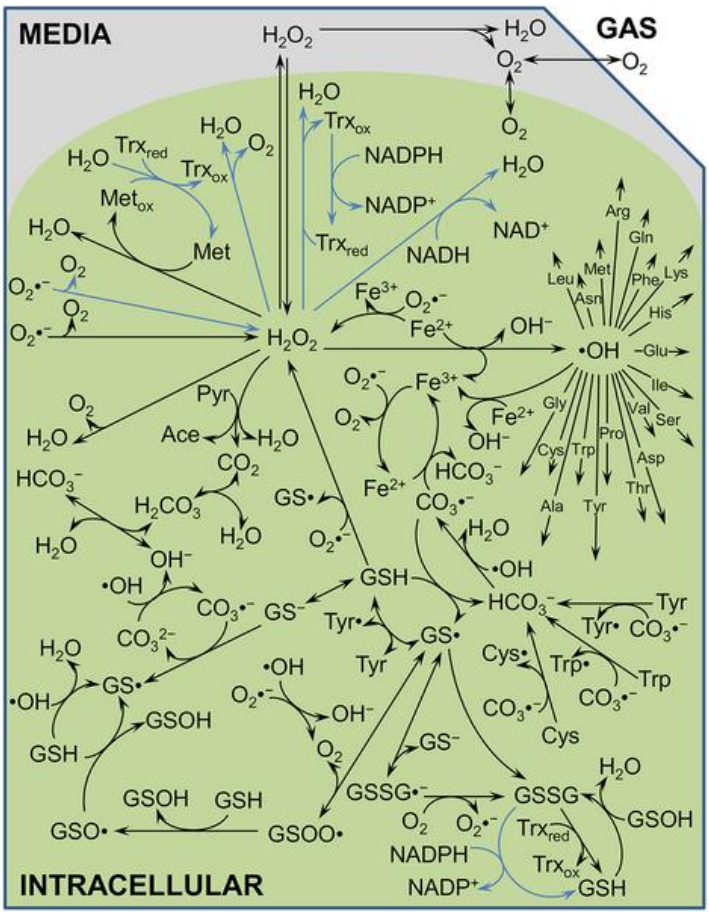

Figure 1.14. H_2O_2 intracellular reactions [Adolfsen and Brynildsen, 2015].

The high activity of the Ahp permits to maintain intracellular H_2O_2 below 20 nM, although the rate formation endogenously in aerobic cells is about 15 μM s^{-1}. Nevertheless, when the intracellular concentration of H_2O_2 is above 0.1 μM the Ahp enzyme is saturated and it cannot deal with the oxidant species. Upon this concentration, the response regulated by OxyR protein is activated. This protein acts as sensor stress and a transcription factor. OxyR has a cysteinyl residue (Cys199) that is oxidized by H_2O_2 to form a sulfenic acid that is quickly conversed to disulfide bond by the addition of other cysteinyl residue (Cys208). The bridge creates a conformational change in the protein that activates its transcription activity. When H_2O_2 stress is removed, the disulfide bond is reduced by glutaredoxins ending the response [Imlay and Hassett, 2011]. OxyR expressed the gene *katG* that strongly induces the activity of catalase

(hidroperoxidase I, HPI), and it becomes the primary scavenging enzyme during the exponential phase. The Michaelis kinetic constant of enzymatic decomposition of H_2O_2 is $k_{cat}/K_m = 9 \cdot 10^5\ M^{-1}\ s^{-1}$ [Seaver and Imlay, 2001a]. In the stationary-phase a second catalase (hidroperoxidase II, HPII) is activated (encoded by *katE*). This gene is induced by the protein RpoS [Loewen and Hengge-Aronis, 1994].

Although H_2O_2 can passively diffuse across bacterial membranes, internal and external H_2O_2 concentrations do not equilibrate due to the action of Ahp and/or catalase that maintain a ratio extra-/intracellular of 10/1 [Imlay, 2008].

1.4.2.3 Hydroxyl radical, $HO^{\bullet}$

Other ROS formed inside the cells is the hydroxyl radical $HO^{\bullet}$, usually in the presence of transition metal ions. This radical has the strongest oxidant potential produced in biological systems. It gains importance because it reacts very rapid with most biological targets with near diffusion-limited rates. The biomolecules that are susceptible to be oxidized by $HO^{\bullet}$ include lipids, proteins, carbohydrates, DNA and RNA. Cells do not have any scavenger system against the damage cause by hydroxyl radicals.

The main reactions that generate $HO^{\bullet}$ are the Fenton reaction catalysed by free iron (reaction (1.23)) or copper and the decomposition of peroxynitrite [Augusto and Miyamoto, 2011]:

$$ONOO^- + H^+ \leftrightarrows ONOOH \rightarrow 0.3\ HO^{\bullet} + 0.3\ NO_2^{\bullet} \qquad (1.28)$$

Reactions with hydroxyl radicals can be classified into three main types:

1. Hydrogen abstraction from organic compounds producing H_2O and a peroxyl radical ($ROO^{\bullet}$) in presence of O_2.
2. Addition with aromatic compounds to produce hydroxylated radical adducts.
3. Electron transfer reactions with anions.

The major cellular defences against the hydroxyl radicals is the prior scavenge of the H_2O_2 by the catalase enzyme to avoid the formation of the radical.

1.4.2.4 Hypohalous acids, HOX

The hypohalous acids with a moderately strong oxidative capacity in biological systems are the hypochlorous acid (HOCl), hypobromous acid (HOBr) and hypothiocyanous acid (HOSCN). Significant amounts of these acids are formed under physiological conditions by peroxidase-catalysed reactions of pseudohalide ions with H_2O_2 [Augusto and Miyamoto, 2011]:

$$H_2O_2 + Cl^- \rightarrow HOCl + OH^- \quad (1.29)$$

$$H_2O_2 + Br^- \rightarrow HOBr + OH^- \quad (1.30)$$

$$H_2O_2 + SCN^- \rightarrow HOSCN + OH^- \quad (1.31)$$

Amino, thiol and methionine groups are the most important targets to be oxidized by hypohalous acids that lead to an increased oxidative damage to biomolecules. HOX also affect to the integrity of lipids reacting by addition in carbon-carbon double bonds in fatty acids [Imlay and Hassett, 2011].

Cells present specific enzymatic defences against the hypohalous acids, nevertheless the main protective action is to avoid their formation by the decomposition of the H_2O_2 by catalase enzyme.

1.4.2.5 Peroxynitrite, $ONOO^-$

The formation of the peroxynitrite was described above by the reaction (1.19) between $O_2^{\bullet -}$ and $NO^{\bullet}$. The peroxynitrite is a potent oxidative agent with a similar reactivity than hypochlorous acid. It is capable to react with some amino acids such as cysteine, methionine or tryptophan [Koppenol, 1998].

In addition, the protonation of the peroxynitrite generates hydroxyl radicals and peroxynitrous acid by homolytic cleavage (reaction (1.28)).

1.4.2.6 Peroxyl (ROO•) and alkoxyl (RO•) radicals

These organic radicals are moderately strong oxidants and they can be generated from organic hydroperoxide (ROOH) decomposition induced by heat or radiation and by ROOH reaction with transition metal ions and other oxidants capable of abstracting hydrogen [Augusto and Miyamoto, 2011]:

$$ROOH + Fe^{2+} \rightarrow RO^{\bullet} + HO^{-} + Fe^{3+} \quad (1.32)$$

$$ROOH + Fe^{3+} \rightarrow ROO^{\bullet} + H^{+} + Fe^{2+} \quad (1.33)$$

Both radicals could be also generated from the oxidation of lipids, proteins and nucleic acids or in processes involving carbon-centered radicals.

The main reaction in which these radicals are involved is in hydrogen-abstraction for biomolecules as lipids, thiols or several chain-breaking antioxidants. Lipids are particularly susceptible to the attack of $RO^{\bullet}$ and $ROO^{\bullet}$ participating in the propagation of the lipid peroxidation chain reactions.

1.4.2.7 Singlet oxygen, $^1O_2$

$^1O_2$ is seemed to be one of the most damaging ROS in bacterial cells. It is a derivative of molecular oxygen in which all valence electrons are opposite spin while in the molecular oxygen (triplet state, O_2) the electrons are in the same direction (see Figure 1.11). Singlet oxygen exists in two forms, $^1\Delta_g$ and a higher energy form $\sum_g^+$ that decays to the $^1\Delta_g$ configuration immediately upon formation, and is thus thought to be irrelevant to biological systems.

The major pathway of singlet oxygen formation is the photo-excitation by the reactions Type II ((1.34) and (1.35)) that require the exposure to UVA light. Endogenous photosensitizer in the ground state (S^0) such as flavins, porphyrins and quinones absorbs light to attain an excited singlet state (S^1), which may spontaneously assume an excited triplet state (S^3) by electron spin inversion. Then, by Type II reaction, singlet oxygen is generated by the energy transfer from the triplet sensitizer to the molecular oxygen:

$$S^0 \xrightarrow{h\nu} S^1 \rightarrow S^3 \quad (1.34)$$

$$S^3 + O_2 \rightarrow {}^1O_2 + S^0 \quad (1.35)$$

The excited triplet photosensitizer (S^3) participates in several competing reaction pathways: it may decay back to S^0, react by a Type I reaction (without oxygen) or by Type II mechanism [Ryter and Tyrrell, 1998].

In addition, singlet oxygen is formed in absence of light in living organisms. It could be generated through the reaction between H_2O_2 and HOCl (reaction (1.36)) or by the membrane lipid peroxidation that is formed as a by-product of the disproportionation of organic peroxyl radicals (reaction (1.37)) [Ryter and Tyrrell, 1998]:

$$H_2O_2 + HOCl \rightarrow {}^1O_2 + H_2O + Cl_2 + H^+ \quad (1.36)$$

$$2ROO^{\bullet} \rightarrow {}^1O_2 + RO + ROH \quad (1.37)$$

Singlet oxygen is capable to react with organic molecules, including nucleic acids, proteins and lipids, generating damages in biomolecules. The common reaction mechanism is the addition to π-bonds [Augusto and Miyamoto, 2011].

1.4.3 Cellular damages and repair mechanisms

During a constant exposure of oxidative stress, bacteria cells usually are adapted rapidly. Even, if the stress has low intensity, the cells become more resistant to higher oxidation conditions. Oxidative stress may generate some mutagenic and non-lethal damages, i.e. modifications in nitrogenous bases of DNA, specific aminoacids of proteins and lipid peroxidation.

1.4.3.1 Iron-sulfur cluster repair

Cells count with the capacity of repair the iron-sulfur cluster recovering the iron-containing enzymes when the oxidative stress ends. For example, dehydratase activity of *E. coli* SOD mutants is rapidly removed when they are exposed to air due to the oxidation of iron-sulfur clusters by $O_2^{\bullet -}$ (reaction (1.17)) and H_2O_2

(reactions (1.24) and (1.25)). Nevertheless, it is fully recovered in less than 40 min, when cells are returned to anaerobic conditions [Djaman *et al.*, 2004]. The recovery process is still unclear but iron cycle must follow the next steps:

$$[3Fe\text{-}4S]^{+} + e^{-} \rightarrow [3Fe\text{-}4S]^{0} \quad (1.38)$$

$$[3Fe\text{-}4S]^{0} + Fe^{2+} \rightarrow [4Fe\text{-}4S]^{2+} \quad (1.39)$$

One of the electron donors compounds identify for the reaction (1.38) is the NADPH:ferredoxin/flavodoxin oxidoreductase but also an unidentified electron donor have to suffice the reaction [Djaman *et al.*, 2004]. The proteins Isc and Suf that are the responsible for the *de novo* assembly of clusters, are also involved in the repair process.

1.4.3.2 DNA repair

Aerobic conditions are a source of DNA damage and mutagenesis in cells. It was observed that mutants that lack both base excision repair and recombinational repair functions such as *recA xthA* and *polA recB* strains, are only viable in anaerobic conditions. This means that DNA repair systems are essential for the aerobic lifestyle.

The rate of natural mutations of DNA is increased by the action of intracellular ROS. H_2O_2 reacts directly with the Fe^{2+} that is binding to DNA by Fenton reaction (1.23) that oxidizes the iron to a 3+ stage and generates hydroxyl radicals. The action of $HO^{\bullet}$ is directed to purines, pyrimidines and deoxyribose and also generate DNA ruptures. One of the main targets of ROS ($HO^{\bullet}$ and $^1O_2$) is the guanine that is converted to 8-hydroxyguanine. These types of changes in the bases are very important when the DNA is replicated because they could lead to mutations. For example, the 8-hydroxyguanine could generate hydrogen bridges with an adenine instead of cytosine. *E. coli* has the enzyme formamidopyrimidine DNA glycosylase (Fpg, also known as MutM) that excises oxidized purines prior to replication [Imlay, 2008].

Due to the broad variety of damages in DNA chain, one of the most important repair pathways is not for specific lesions but for the absence of duplex integrity chain. In this sense, in *E. coli*, the endonucleases III and IV play a very important role in the recognition of the disruption, and then endonuclease IV and exonuclease III complete the repair process [Imlay, 2008].

1.4.3.3 Proteins damage

In bacteria, proteins are the responsible for the major cellular functions and are the main biological targets for oxidative damage. Some of the tasks that are altered are the reception and signal transmission, the ions transport, the DNA duplication and repair and the transcription and translation.

The proteins damages involve cleavage of the polypeptide chain, modification of amino acid side chains and conversion of the protein to derivatives that are highly sensitive to proteolytic degradation [Vatansever *et al.*, 2013].

Hydroxyl radical is one of the major species that generates the proteins injuries. It reacts with the amino acids that are placed where the radical is formed, usually where a transition metal is settled. In this sense, $^1O_2$ is more selective, reacting with amino acids of tryptophan, tyrosine, histidine, lysine, methionine and cysteine and also with catalases [Hansberg, 2002]. The products are peroxides which may decompose themselves into reactive intermediates.

The polyunsaturated fatty acids of the phospholipids in the membrane are susceptible to be oxidized by $HO^{\bullet}$ and $HO_2^{\bullet}$, initiating a self-propagating chain reaction because of the formation of a lipid peroxyl radical and generating a significant damage in the membranes [Hansberg, 2002].

Furthermore, inactivation of cellular enzymes could result by proteins' modification by aldehydes and ketones that are generated during the reaction between ROS and lipids and glycated proteins [Vatansever *et al.*, 2013].

1.4.4 Intracellular ROS detection

The capacity of ROS and RNS (Reactive Nitrogen Species) to cause mutagenic and lethal injuries in cells, has been widely investigated before in different medical fields such as cancer therapy, infections treatment or phototherapy because of their crucial role in oxidative stress. Furthermore, big efforts to detect ROS and RNS in cells tissues have been done, reporting a number of contributions on oxidative stress detection and determination in eukaryotic cells [Vatansever *et al.* 2013].

The most common method to determine the presence of those reactive species is the use of specific molecules (probes) with a relative selectivity to ROS generating fluorescent products that could be detected by fluorescent spectroscopy techniques. Fluorescence may be measured or observed with a fluorimeter, a microtiterplate reader, a microscope or a flow-cytometer. Although there is a wide range of fluorescent probes, the selection of one compound to detect a specific ROS is not an easy task. Some of the limitations of the probes are: (i) the interaction with other compounds, (ii) the low stability of some probes and/or products formed, (iii) problems with probes accessing cellular sites of ROS production, (iv) extracellular export of probes and/or products, (v) production of ROS by the probes themselves, (vi) membrane disruptions could alter the diffusion of the probes and (vii) cells' conformational changes that could affect to the fluorescence intensity [Bartosz, 2006; Imlay, 2015].

Very few organic molecules react stoichiometrically with radicals and oxidant species to form detectable intracellular fluorescent products. Main fluorescence probes are classified as a function of the species to which they are more reactive. A list of some of the most common probe used in cells and tissues ROS detection is summarized in Table 1.6.

Table 1.6. Summary of most common probes, detected ROS, excitation/emission wavelengths and main applications.

Probe	ROS and RNS	$\lambda_{ex}/\lambda_{em}$ (nm)	Observations	Ref[a]
Scopoletin (7-hydroxy-6-methoxy-coumarin)	**H_2O_2**/HRP[b]	360/460	Interferences in biological samples; low fluorescent power	[1, 2]
Amplex red (*N*-acetyl-3,7-dihydroxyphenoxazine)	**H_2O_2**/HRP[b]	563/587	High sensibility; resorufin (fluorescent product) is auto-oxidable	[1, 2]
HVA (homovanillic acid or 4-hydroxy-3-methoxy-phenylacetic acid)	**H_2O_2**/HRP[b]	312/420	Interferences with mitochondria constituents	[1, 2]
p-Hydroxyphenylacetic acid	**H_2O_2**/HRP[b]	300/400 (pH>10)	Interferences in biological samples	[2]
Dihydrotetramethylrosamine	**H_2O_2**/HRP[b]	550/574	Tested in vivo for *Amoeba proteus*	[2]
DCFH (2,7-dichloro-dihydrofluorescein)	**H_2O_2**; $HO^{\bullet}$; $ROO^{\bullet}$; $ONOO^-$; $NO^{\bullet}$	498/522	Indicator of cellular oxidative stress; cell-permeable; interference with others	[1, 2]
HPF and APF (2-[6-(4'-hydroxy/amino) phenoxy-3H-xanthen-3-on-9-yl]benzoic acid)	**H_2O_2**/HRP[b]; $HO^{\bullet}$; $ONOO^-$; HOCl	500/520	High resistance to auto-oxidation; suitable for enzymatic and cellular systems	[1, 2]
DHR123 (dihydrorhodamine 123)	**H_2O_2**/HRP[b]; HOCl; $ONOO^-$	505/529	Cell-permeable	[1, 2]
Boronate probes such as derivates of 7-aminocoumarin	**H_2O_2**; HOCl; $ONOO^-$	348/440	ROS reaction slow at physiological pH	[3]
HE (hydroethidine or dihydroethidium)	**$O_2^{\bullet-}$**	520/610	Interferences with H_2O_2 (which product is also fluorescent); cell-permeable	[1, 2]
2-(2-pyridil)-benzothiazoline	**$O_2^{\bullet-}$**	377/528	High selectivity; tested in vegetables	[4]
DPBF (1,3-diphenylisobenzofuran)	**$O_2^{\bullet-}$**; $^1O_2$	410/455	Detection in phospholipid liposomes	[1]
DMA (9,10-dimethylanthracene)	**$^1O_2$**	375/436	High selectivity; not located in a preferential depth in the membrane	[1]
DPAX & DMAX 9-[2-(3-carboxy-9,10-diphenyl/dimethyl)anthryl]-6-hydroxy-3H-xanthen-3-ones	**$^1O_2$**	495/515	High selectivity; cell-permeable	[1]

Probe	ROS and RNS	$\lambda_{ex}/\lambda_{em}$ (nm)	Observations	Ref[a]
4-(9-Anthroyloxy)-2,2,6,6-tetramethylpiperidine-1-oxyl and **CHD** (1,3-Cyclohexanedione)	**HO$^{\bullet}$**	377/427 and 400/452	Indirect detection (based in the reaction by HO$^{\bullet}$ and DMSO)	[1]
Sodium terephthalate	**HO$^{\bullet}$**	310/430	High selectivity	[1]
Coumarinsuch as **3-CCA** (coumarin-3-carboxylic cid) and **SECCA** (N-succinimidyl ester of coumarin-3-carboxylic acid)	**HO$^{\bullet}$**	350/430 and 395/430	High selectivity; highly sensible to pH	[1]
FL (fluorescein)	**HO$^{\bullet}$**; ROO$^{\bullet}$	495/515	Low selectivity	[1]
Dipyridamole	**HO$^{\bullet}$**; $O_2^{\bullet-}$; ROO$^{\bullet}$	415/480	Highly sensible to pH; chemical stability	[1]
cis-PnA or cis-Parinaric acid ((18:14):9,11, 13,15-cis-trans-trans-cis-octadecaenoic acid	**ROO$^{\bullet}$**	320/432	To evaluate lipid peroxidation; require extraction; air sensitive and photolabile	[1]
C11-BODIPY$^{581/591}$ (4,4-difluoro-5-(4-phenyl-1,3-butadienyl)-4-bora-3a,4a-diaza-s-indacene-3-undecanoic acid	**ROO$^{\bullet}$**; RO$^{\bullet}$; HO$^{\bullet}$; $ONOO^{-}$	510/595	Useful to evaluate lipid peroxidation	[1]
Lipophilic fluorescein derivatives such as 5-(N-dodecanoyl) aminofluorescein	**ROO$^{\bullet}$**	495/515	Useful to evaluate lipid peroxidation; tested for erythrocytes	[1]
DPPP (diphenyl-1-pyrenylphosphine)	**ROO$^{\bullet}$**	351/380	Reacts stoichiometrically; useful to evaluate lipid peroxidation	[1]
β-Phycoerythrin	**ROO$^{\bullet}$**	520/580	Evaluation of the antioxidant capacity	[1]
Diaminofluoresceins such as **DAF-2** (4,5-diaminofluorescein) and **DAF-FM** (4-amino-5-methylamino-2',7'-difluorofluorescein)	**NO**	490/515 and 495/515	Nanomolar detection limits	[2]

[a] [1]: Gomes *et al.*, 2005; [2]: Bartosz, 2006; [3]: Lo and Chu, 2003; [4]: Tang *et al.*, 2004

[b] Reaction catalyzed by HRP (horseradish peroxidase)

The most commonly used probe as indicator of intracellular oxidative stress is 2,7-dichlorodihydrofluorescein (DCFH) that is normally used in the diacetate form (DCFH-DA) because has a higher chemical stability. It diffuses through the cellular membrane and it could be naturally hydrolysed by endogenous cell esterases removing diacetate groups obtaining the DCFH. Then, non-fluorescent DCFH originates 2,7-dichlorofluorescein (DCF) by indirect reactions with iron, heme proteins, $GS^{\bullet}$, $CO_3^{\bullet -}$, $NO_2^{\bullet}$, $HO^{\bullet}$, and H_2O_2 (Figure 1.15). DCF is a fluorescent compound that can be detected by absorbance spectroscopy (ε_{500nm} = 59500 M^{-1} cm^{-1}) and fluorescence spectroscopy ($\lambda_{emission}/\lambda_{excitation}$ = 522/498 nm) [Crow, 1997].

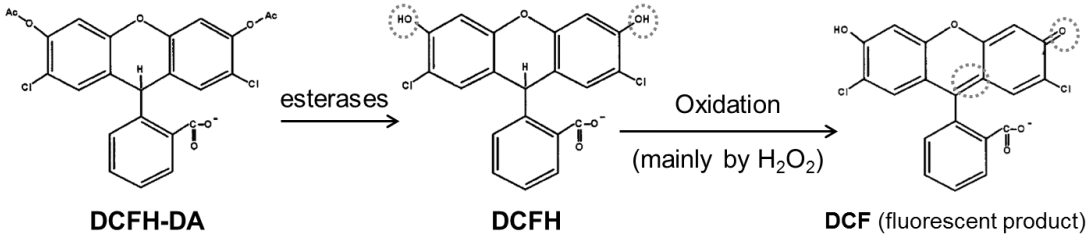

Figure 1.15. DCFH-DA molecule oxidation to the final product DCF.

Although, DCFH-DA was widely used to measure intracellular H_2O_2 or other ROS and RNS, it is better to consider it as an indicator of cellular oxidative stress [Kalyanaraman *et al.*, 2012; Dikalov and Harrison, 2012] due to DCFH-DA intracellular redox chemistry obeys to a very complex group of reactions that generate intermediates like $DCF^{\bullet}$, $DCFH^{\bullet}$, $DCF^{\bullet -}$ and $(DCF)^{*}$ (Figure 1.16). The main steps of these reactions are:

- DCFH formed by the hydrolysis of DCFH-DA, could be oxidized by several one-electron-oxidizing species. H_2O_2 does not directly react with DCFH, although it is required for the oxidation mediated redox-active metals (e.g., Fe^{2+}), heme protein (such as cytochrome c) or heme peroxidases. Other oxidants like $CO_3^{\bullet -}$, $NO_2^{\bullet}$ (formed from the myeloperoxidase/H_2O_2/NO_2^{-} system), $ONOO^{-}$, $NO^{\bullet}$ (from the peroxynitrite decomposition) and $HO^{\bullet}$ are able to react with DCFH forming the intermediate $DCF^{\bullet -}$.

- The intermediate radical $DCF^{\bullet-}$, formed from the oxidation of DCFH, rapidly reacts with O_2 to generate $O_2^{\bullet-}$ and the fluorescent product DCF. The dismutation of the superoxide radical yields additional H_2O_2 that may lead to an amplification of the fluorescence signal intensity.

- The final product DCF is also susceptible to be oxidized by the same one-electron-oxidizing species previously named. The intermediate $DCF^{\bullet}$ formed could be reduced by NADH or glutathione (GSH), that generate higher amounts of $O_2^{\bullet-}$ in the presence of O_2 causing the amplification of the fluorescence signal.

- Light also modify the fluorescence signal due to its interaction with DCF generating the intermediate $(DCF)^{*}$, that is finally reduced to $DCF^{\bullet-}$ by the action of NADH and GSH.

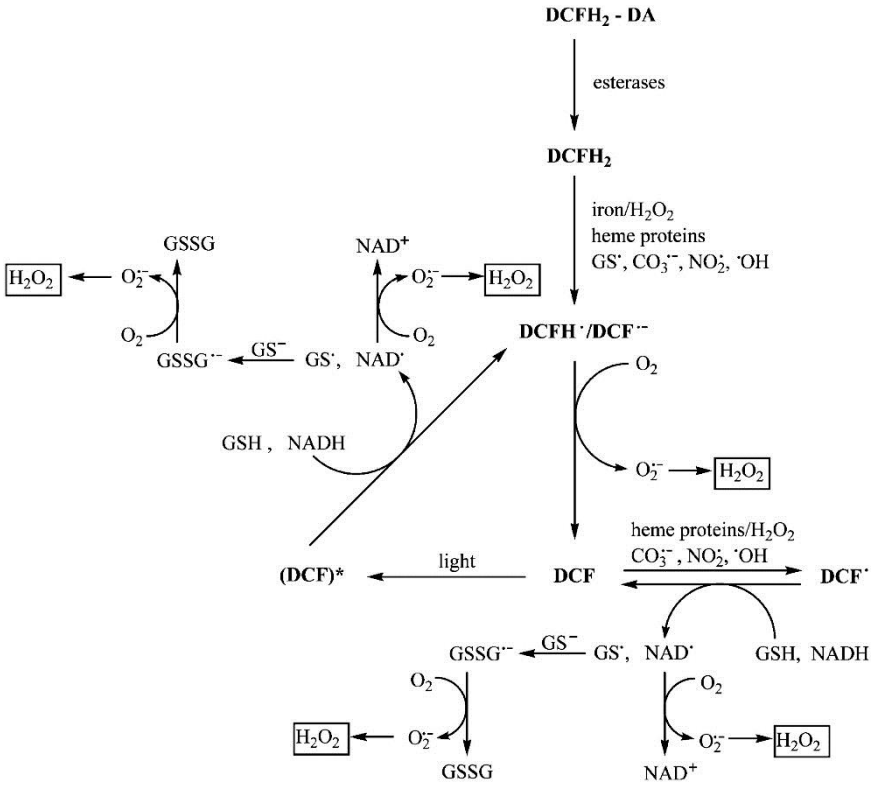

Figure 1.16. Complex group of reactions for the DCF formation from DCFH-DA that involve ROS and others intermediates generation [Kalyanaraman *et al.*, 2012].

1.5 Modelling

1.5.1 Disinfection models

The bacterial inactivation during the disinfection processes could be modelled and hence later predicted by empirical or mechanistic models. The empirical models are obtained by the fit of the experimental data to an equation whose parameters have commonly any physical meaning. On the contrary, the mechanistic models are based on the mechanisms that lead to the inactivation.

1.5.1.1 Empirical models

The most used disinfection models are empirical equations based on Chick's law and its modifications to fit the different inactivation curves behaviour [Chick, 1908]. The simplistic formulation of Chick's law is based on a first-order reaction:

$$N = N_0 \cdot e^{-k \cdot t} \tag{1.40}$$

For water disinfection with chemicals, it is presented the Chick-Watson model that incorporates the concentration-time concept [Watson, 1908], modifying the Chick's law as follow:

$$N = N_0 \cdot e^{-k \cdot [c]^n \cdot t} \tag{1.41}$$

where c (concentration of disinfectant) and n (dilution coefficient) are constants parameters, assuming no disinfectant demand.

Some disinfection processes present an initial delay at the beginning due to the existence of a lag stage in the inactivation of the bacteria ('shoulder' of the curve, Figure 1.17). The empirical model used to fit these inactivation profiles is the delayed Chick-Watson model with a lag parameter (t_{lag}):

$$N = \begin{cases} N_0 & \text{for } t \le t_{lag} \\ N_0 \cdot e^{-k\cdot[c]^n\cdot(t-t_{lag})} & \text{for } t > t_{lag} \end{cases} \quad (1.42)$$

In other cases, the disinfection rate remains constant from the beginning of the reaction until a certain moment (t_{res}) that the bacteria concentration keeps constant at a residual value, N_{res}, showing a 'tail' in the curve (Figure 1.17):

$$N = \begin{cases} N_0 \cdot e^{-k\cdot[c]^n\cdot(t-t_{lag})} & \text{for } t < t_{res} \\ N_{res} & \text{for } t \ge t_{res} \end{cases} \quad (1.43)$$

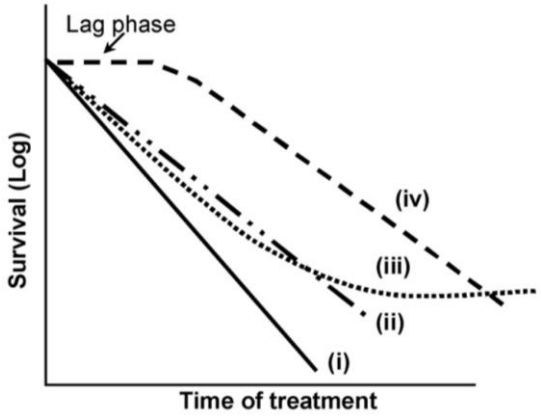

Figure 1.17. Microorganism's inactivation profiles of different types of bacterial populations [Malato *et al.*, 2009].

The duration of the beginning phase ('shoulder') and the 'tail' of these typical disinfection curves are corresponding to resistant populations. The population of resistant pathogens or microbes highly protected by other additional factors, is divided into subgroups with different resistant against the disinfection treatment, generating different levels of survival. Other authors agree that the 'shoulder' and 'tail' shapes are mainly due to grouping process of microorganisms [Malato *et al.*, 2009].

Another empirical model is described by the Hom equation [Hom, 1972] and its modifications to describe 'shoulder', linear and 'tail' regions:

$$N = N_0 \cdot e^{-\frac{k \cdot [c]^n \cdot t^m}{m}} \tag{1.44}$$

where *m* and *n* are the parameter of the model.

Although, these models have been used in several applications due to its simplicity, they have some limitations, mainly that the parameters have not real physical meaning, so they do not provide any information about the mechanisms of the disinfection process. In addition, the field experiences with real waters show deviation of the first-order kinetic and it is observed a dependency on the resistance of each microorganism and the heterogeneity of the existing population in the treated water.

1.5.1.2 Mechanistic models

Mechanistic models are more robust than empirical because are expected to be more accurate for complex situations that arise in practice due to variations in experimental conditions (temperature, irradiances sources, water quality, etc.).

One of the most important mechanistic disinfection models is the series-event [Severin *et al.*, 1983]. It assumes a series of discrete damage levels which correspond to a unit of damage that occurs in a stepwise manner until the organism reaches a threshold level of damage. It is supposed that the bacteria survive if the damage is below the threshold injury. The model could be represented as follows:

$$C_0 \xrightarrow{k_1} C_1 \xrightarrow{k_2} C_2 \ldots \xrightarrow{k_i} C_i \ldots C_{n-1} \xrightarrow{k_n} C_n \tag{1.45}$$

The model justified the presence of the 'shoulder' in the inactivation profiles by the need of an accumulative damage rather than an instantly lethal action. Nevertheless, the assumptions of the model could be disadvantageous due to the large requirement of damage levels to an accurately description of the inactivation. By assuming that the kinetic constant is the same at each level and first-order, the general expression for the bacterial concentration could be obtained:

$$\log\left(\frac{N}{N_0}\right) = -k \cdot t + \ln\left(1 + \sum_{i=1}^{n} \frac{(k \cdot t)^i}{i!}\right) \quad (1.46)$$

The assumption of the series-event has been used in several mechanistic models in disinfection: photo-catalysis with TiO_2 [Marugán *et al.*, 2008a], UVC disinfection [Labas *et al.*, 2006], H_2O_2 disinfection [Labas *et al.*, 2008] or the combined H_2O_2-UVC treatment [Labas *et al.*, 2009].

In line with this, some stochastic models have been presented to describe the inactivation processes [Jensen 2010; Fan and Argoti, 2012]. The main characteristics of this type of models are the use of probabilistic assumptions and the non-consideration of complexes intracellular processes as responsible for the inactivation.

In addition, several rigorous kinetic modelling were developed for disinfection processes. The TiO_2-photocatalytic disinfection was modelled for *E. coli* [Marugán *et al.*, 2011] and *Bacillus subtilis* [Zacarías *et al.*, 2010] by the assumption of bacterial inactivation due to the damages generated by hydroxyl radicals. The *E. coli* inactivation was also modelled for the disinfection by the addition of H_2O_2 to the contaminated water [Flores *et al.*, 2012]. As the TiO_2 disinfection models, the inactivation is assumed to be caused by the interaction of $HO^{\bullet}$ with the bacteria cells. In this model, the membrane disruption is also taken into account.

1.5.2 Light models

In the solar water treatment, the light is one of the main agents that affect to the efficiency of the process. The definition and the estimation of the light are essential to include the solar effect into the disinfection models.

1.5.2.1 Light parameters definition

The fundamental property for the characterization of the radiation field is the spectral specific intensity I_λ that could be defined as the amount of radiative

energy streaming through a unit area perpendicular to the direction of propagation Ω, per unit of solid angle about the direction Ω, per unit wavelength λ and per unit time. In photo-reactor engineering, the usual units for I_λ are Einstein s^{-1} m^{-2} sr^{-1} nm^{-1}.

I_λ could be estimated in a point P (Figure 1.18) located over an arbitrarily orientated small area dA about the space coordinate **x** being **n** the normal to the area at point P. At a given time, the rays will travel through this area in all directions. Considering the direction **Ω** that makes an angle θ to the normal **n**, all elementary solid angles corresponding to rays parallel to the direction **Ω** passing through dA define a truncated semi-infinite cone dω, whose cross-sectional area perpendicular to **Ω** at the point P will be dA cos θ. Considering dE_λ the total amount of radiative energy passing through the area dA inside the cone dω in the time dt and with and energy in the wavelength range between λ and λ+dλ. The spectral specific intensity is defined as:

$$I(\mathrm{x},\Omega,t,\lambda) = \lim_{\mathrm{d}A,\mathrm{d}\Omega,\mathrm{d}t,\mathrm{d}\lambda\to 0}\left(\frac{\mathrm{d}E_\lambda}{\mathrm{d}A\cdot\cos\theta\cdot\mathrm{d}\Omega\cdot\mathrm{d}t\cdot\mathrm{d}\lambda}\right) \tag{1.47}$$

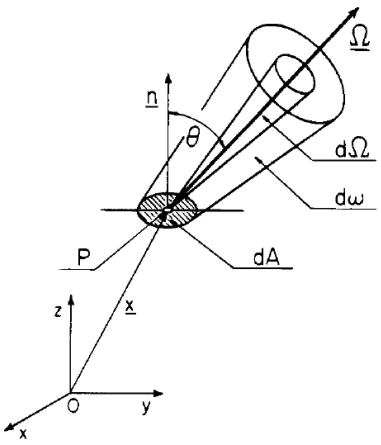

Figure 1.18. Characterization of the radiation field [Cassano *et al.*, 1995].

Incoming radiation from all directions must be absorbed by an elementary reacting volume. The spectral incident radiation G_λ is defined as the energy per

unit time and unit area from all directions and is commonly measured in terms of Einstein s^{-1} m^{-2} nm^{-1}:

$$G_\lambda(\mathrm{x},t) = \int_\Omega I_\lambda(\mathrm{x},t)\,\mathrm{d}\Omega \tag{1.48}$$

In the case of considering an elementary volume of radiation, the parameter used to characterize the light absorption is the local volumetric rate of photon absorption (LVRPA or e^a), expressed in terms of Einstein m^{-3} s^{-1}.

$$e^a_\lambda(\mathrm{x},t) = \kappa_\lambda(\mathrm{x},t)\cdot G_\lambda(\mathrm{x},t) \tag{1.49}$$

κ_λ is the volumetric absorption coefficient that is always a function of the concentration of the absorbing species. For polychromatic radiation the LVRPA could be calculated by the following equation:

$$e^a = \int_{\lambda_1}^{\lambda_2} \kappa_\lambda \cdot G_\lambda \mathrm{d}\lambda \tag{1.50}$$

1.5.2.2 Radiative Transfer Equation (RTE)

The Radiative Transfer Equation (RTE) describes the transport of photon in a medium that absorbs and scatters light. It is obtained from the radiation balance that could be translate, considering no emission, as the variation of the radiation intensity along the directional spatial variable *s* in a differential elementary volume that is equal to the intensity losses due to the medium absorption, the losses by the scattered light that fly out the volume element and the intensity gains due to the scattered light that comes from every directions (4π sr). Mathematically:

$$\frac{\mathrm{d}I_{\lambda,\Omega}(x)}{\mathrm{d}s} = -\underbrace{\kappa_\lambda \cdot I_{\lambda,\Omega}(x)}_{\text{ABSORPTION}} - \underbrace{\sigma_\lambda \cdot I_{\lambda,\Omega}(x)}_{\text{OUT-SCATTERING}} + \underbrace{\frac{\sigma_\lambda}{4\pi}\cdot \int_{\Omega'=4\pi} p(\Omega'\to\Omega)\cdot I_{\lambda,\Omega'}(x)\,\mathrm{d}\Omega'}_{\text{IN-SCATTERING SOURCE TERM}} \tag{1.51}$$

where σ_λ is the scattering coefficient and p ($\Omega'\to\Omega$) is the phase function that describes the spatial scattering distribution. Professors Cassano and Alfano have

published a large number of scientific contributions using the RTE to estimate the radiation fields for different reactors configurations. They also developed useful reviews about the fundamentals and applications of the light modelling and photo-reactor design [Cassano *et al.*, 1995; Cassano and Alfano, 2000].

The rigorous solution of the integro-differential equation could be achieved by two procedures: (i) probabilistic models as Monte Carlo simulations [Imoberdorf *et al.*, 2008] and (ii) discretization models such as the Discrete Ordinate Method (DOM). The last one has been applied widely in the photo-catalysis field for one-dimensional simplifications [Alfano *et al.*, 1995; Labas *et al.*, 2006] and two-dimensional problems [Marugán *et al.*, 2006; Marugán *et al.*, 2008b].

Other light model was developed through the solution of differential photon balances, with a simple procedure to solve the RTE considering probabilities for the photon scattering directions. Initially, the 'two-flux' model was proposed [Brucato and Rizzuti, 1997] and a later enhancement of the model that considers six directions of light was introduced and successfully applied to different reactors that was named 'six-flux' model (SFM) [Li Puma *et al.*, 2004; Brucato *et al.*, 2006].

CHAPTER 2

OBJECTIVES AND EXPERIMENTAL PLAN

2 OBJECTIVES AND EXPERIMENTAL PLAN

2.1 Objectives

The lack of access to improved drinking sources in many developed countries forced to millions of people to use contaminated water for domestic purposes with the risk to contract waterborne diseases. The WHO has promoted many campaigns to use Household Water Treatment and Safe Storage (HWTS) including the solar water disinfection (SODIS) among them. SODIS has been extensively used in the last decades because is presented as an effective low-cost technique against several types of water pathogens. Nevertheless, there are still many scientific questions surrounding the SODIS technique.

A better understanding of the SODIS mechanisms process is essential in order to design more efficient photo-reactors to reduce treatment times, ensure good disinfection results with no dependence of the radiation variability and water quality, scale them to higher treatment volumes without the necessity of increase cost, complexity, nor operational and maintenance tasks.

Solar water disinfection is a well-studied process in which several factors affected its efficiency: UV dose, water temperature, dissolved oxygen, flow-rates, etc. Nevertheless, in the literature there is no mechanistic model that explains the processes taking place during SODIS. The models that have been previously reported on SODIS are empirical models without physical parameter meaning but just fit the experimental data [Jensen, 2010; Fan and Argoti, 2012; Haider *et al.*, 2014].

The objective of this work is to develop a kinetic mechanistic model of the solar water disinfection process that explains the interactions between sunlight photons and bacterial cells. The model is intended to simulate the bacteria behaviour under different operational conditions and to be used as a tool in the reactor design field to predict the efficiency of new reactor prototypes without the necessity of building and testing them experimentally. For this work, *E. coli* K-12 has been selected as model bacterium.

The specific objectives in this work are:

1. To detect experimentally the presence of intracellular photo-generated ROS involved in the bacterial inactivation during solar water disinfection.

2. To develop a kinetic model that considers the mechanisms acting during the solar water disinfection process, where the interaction between solar radiation and bacteria promotes the intracellular ROS formation and hence generates oxidative damages that induce cell-death. This model is the pillar of this work and other modifications will be done to extend its applicability for practical utilisation of SODIS reactors.

3. To study experimentally the effect of water temperature during solar water disinfection discriminating between separated and simultaneous effects of radiation and temperature.

4. To modify the primary kinetic model to include the synergistic effect between temperature and UV radiation to develop a more complete SODIS mechanistic model with consideration of the thermal effects within the range of temperatures commonly reached during SODIS.

5. To validate the kinetic model in several photo-reactors including the commonly used PET bottles and several solar reactors at pilot scale designed for solar water disinfection under real field conditions of irradiance, temperature and turbidity.

2.2 Experimental plan

The experimental plan developed in this work accomplishes the specific objectives and it is explained below.

Objective 1: To detect experimentally the presence of intracellular photo-generated ROS involved in the bacterial inactivation during solar water disinfection. Chapter 4 explains in detail the experimental study performed to reach this objective. In summary it consisted on:

(i) Selecting the most commonly used fluorescent ROS–probe in oxidative eukaryotic cells detection, i.e. 2,7-dichlorodihydrofluorescein diacetate (DCFH-DA) to be applied for the particular case of solar water disinfection.

(ii) Studying the experimental procedure for the analysis of ROS in *E. coli* with DCFH-DA, performing the following steps:

- Analysis of the photo-stability of DCFH-DA under simulated sunlight using absorbance measurements.

- Assessment of the chemical hydrolysis of DCFH-DA with H_2O_2 as ROS positive control of the reaction between DCFH hydrolysed and ROS determined by absorbance (10 μM of DCFH with 0.01, 0.1, 1 mM of H_2O_2) and fluorescence spectroscopy (5, 10 μM of DCFH with 0.01, 0.1, 0.2, 0.3, 0.5, 1 mM of H_2O_2).

- Study of the incubation time between *E. coli* and DCFH by loading the cells with the ROS-probe and incubating during 5, 15, 30 and 60 min at 37 ºC.

(iii) Definition and validation of a new protocol for the detection of ROS in *E. coli* using additions of H_2O_2 (0, 0.1, 0.5, 0.75, 1, 1.5 mM) as the oxidative stress to the bacterial suspension and the flow-cytometry for the detection of the cells fluorescence.

(iv) Measurement of the intracellular ROS in *E. coli* during their exposure to natural sunlight using the proposed protocol and flow-cytometry. For this purpose, it will be used isotonic water contained in 200 mL borosilicate batch reactor in SODIS experiments.

Objective 2: To develop a kinetic model that considers the mechanisms acting during the solar water disinfection process, where the interaction between solar radiation and bacteria promotes the intracellular ROS formation and hence generates oxidative damages that induce cell-death. This model is the pillar of this work and other modifications will be done to extend its applicability for practical utilisation of SODIS reactors. Chapter 5 explains the whole model scheme and the experimental study performed to realise the objective 2, briefly:

(i) Revision of the scientific literature to select the most representative intracellular reactions involved in solar water disinfection and to collect their reported kinetic constants.

(ii) Experimental determination of the kinetic constant of the catalase photo-inactivation by the exposure of 30 mg L^{-1} of catalase to simulated sunlight

(30, 40, 50 W m^{-2} of UVA). Previously, the protocol to measure the catalase activity will be optimized by several tests using different concentrations of catalase (5, 10, 30, 50, 70 mg L^{-1}) and H_2O_2 (10, 20, 50, 70, 100 mM).

(iii) Performance of a series of solar water disinfection experiments using simulated light in a 700 mL open batch reactor and isotonic water with (a) 10^6 CFU mL^{-1} at different irradiances (0, 25, 30, 40 W m^{-2} of UVA) and (b) 30 W m^{-2} of UVA and different initial bacterial concentration (10^3, 10^4, 10^5, 10^6 CFU mL^{-1}).

(iv) Determination of the kinetic model constants still unknown (not previously reported neither experimentally determined) to complete the formulation of the SODIS model. The kinetic parameters will be obtained by error minimization between modelled and experimental data by a Monte Carlo search and a parameter optimization.

Objective 3: To study experimentally the effect of water temperature during solar water disinfection discriminating between separated and simultaneous effects of radiation and temperature. The modelling and experimental study performed to achieve this objective is shown in chapter 6, briefly:

(i) Experimental study of the thermal effect on bacterial viability by the exposure of 10^3 and 10^6 CFU mL^{-1} of *E. coli* suspensions to different temperatures (10, 20, 30, 37, 40, 42, 45, 50, 55 ºC) in the dark. From this study, the Arrhenius parameters of the *E. coli* thermal inactivation are obtained.

(ii) Performance of SODIS experiments using artificial solar spectrum in an 700 mL open batch reactor in isotonic water and 10^6 CFU mL^{-1}, 30 W m^{-2} of UVA and different temperatures (30, 40, 50 ºC) to investigate the synergy between thermal and photo-activated inactivation phenomena.

(iii) Analysis of the experimental results obtained for the effect of simulated solar UVA radiation (UVA effect), the effect of mild-heating (thermal

effect) and both factors at the same time under specific conditions. The analysis of these results and the comparison with simulations runs performed with the *SODIS + thermal model* that consists on the combination of the SODIS model reactions and the thermal inactivation reaction in dark.

(iv) Analysis of the contribution of the catalase inactivation to the solar water disinfection due to the mild-heat and the action of the UV radiation.

Objective 4: To modify the primary kinetic model to include the synergistic effect between temperature and UV radiation to develop a more complete SODIS mechanistic model with consideration of the thermal effects within the range of temperatures commonly reached during SODIS. The modelling and experimental study performed to achieve this objective is shown in chapter 6, briefly:

(i) Development of a new kinetic model (*synergistic SODIS-thermal model*) based on the synergy between photons and temperature observed (objective 3). The unknown kinetic parameters of this model will be estimated by minimizing the errors obtained from the comparison between model simulations and experimental data.

(ii) Experimental validation of the synergistic SODIS-thermal model with *E. coli* under simulated sunlight and 700 mL batch reactor. Two operational conditions will be conducted: (a) constant temperature of 30 ºC and different irradiances (30, 40, 50 W m^{-2} of UVA) and (b) increasing temperatures from 30 to 50 ºC and constant irradiances (30, 40 W m^{-2} of UVA).

Objective 5: To validate the kinetic model in several photo-reactors including the commonly used PET bottles and several solar reactors at pilot scale designed for solar water disinfection under real field conditions of irradiance, temperature and turbidity. In chapter 7, the validation modelling and experimental study performed was described, briefly:

(i) Solar water disinfection experiments will be performed in PET bottles in isotonic and well water under natural sunlight with increasing values of irradiance (20 – 35 W m^{-2} of UVA) and water temperature (20 – 45 ºC). The inactivation profiles obtained will be compared with the simulations results from the synergistic SODIS-thermal model.

(ii) Determination of the incident radiation available for the SODIS intracellular reactions in turbid water by the development of a light model in the PET bottle. The light model will be developed by solving the Radiative Transfer Equation using a 2-dimensional and 2-directional discrete ordinate method.

(iii) The synergistic SODIS-thermal model for turbid waters (estimating the incident radiation with the previous light model) will be applied to predict the inactivation of *E. coli* in turbid water containing red soils (5, 100 and 300 NTU) and kaolin (100 NTU). Furthermore, these simulations will be compared with experimental results obtained under different climate conditions (cloudy and sunny days) in PET bottles.

(iv) The synergistic SODIS-thermal model simulations with different photo-reactors will be compared with the results obtained experimentally under different climate conditions (cloudy and sunny days). It will be used photo-reactors made of different materials (polyethylene terephthalate, polycarbonate, borosilicate and methacrylate) and different volumes (2, 2.5, 19, 20 and 22.5 L).

CHAPTER 3
MATERIALS AND METHODS

3 MATERIALS AND METHODS

In this chapter, the materials and procedures used to obtain all the experimental results of this work are presented. Most of the experimental works have been performed at Plataforma Solar de Almería (PSA) facilities, where there is a biosecurity II lab for microbial analysis of water samples and different solar pilot reactors for conducting solar water disinfection experiments, as well as the equipment required for the appropriate solar radiation assessment in the solar UV range and for the evaluation of experimental results. In addition, several collaborations with other research centres like CIESOL (joint research centre formed by University of Almería and CIEMAT) and NIBEC (Nanotechnology and Integrated Bioengineering Centre) has permitted to enhance and complete this experimental work thanks to the access to other sophisticated equipment, which will be also described along this chapter.

This experimental work has been performed with suspensions of bacterium *E. coli* in water under sterile conditions to avoid microbial contamination. The water samples handling were done inside a laminar flow cabinet (Telstar Bio-II-A), and all the materials, culture media and solutions were autoclaved during 15 min at 121 ºC prior to use. Waste materials and solutions after each experiment were also autoclaved before disposal for security reasons.

3.1 Chemicals

The list of all the chemicals used in this work is detailed below:

- Sodium chloride (NaCl, Sigma Aldrich) was used as received to prepared isotonic water.
- Luria-Bertani nutrient medium (LB broth, Panreac) and Luria-Bertani agar (LB agar, Panreac) were used for bacterial growth and quantification.
- Phosphate-buffered saline (PBS, Oxoid) was used as isotonic medium for bacterial suspension and was also used in the DCFH-DA hydrolysis experiments.
- Potassium buffer, pH 7.0 prepared using 4.08 g L^{-1} KH_2PO_4 and 3.48 g L^{-1} K_2HPO_4 was used for catalase measurements.
- 2,7-dichlorodihydrofluorescein diacetate (DCFH-DA, Sigma Aldrich) was dissolved in dimethyl sulfoxide (DMSO, Sigma Aldrich) that was used as received. DCFH-DA was used as a ROS-probe for all experiments related with intracellular detection of ROS.
- Sodium hydroxide (NaOH, J. T. Burker) was used for the DCFH-DA hydrolysis.
- Hydrogen peroxide (H_2O_2, 35 %w/v, Sigma Aldrich) was used as received for positive control tests on ROS detection experiments, and it was also used in solution, 50 mM potassium buffer, for catalase measurements.
- Bovine liver catalase (Sigma-Aldrich, USA) was used as received and dissolved in 50 mM potassium buffer.
- Kaolin powder (Millipore Corporation, Germany) was used as received from the manufacturer and used for preparation of turbid solutions.

3.2 *Escherichia coli*

E. coli is a Gram negative bacterium that inhabit in the gastrointestinal tract of humans and other mammals. It is the most frequently studied microbial species in the area of water disinfection, among others, due to the entirety of its genome mapping and it is also considered a suitable faecal indicator organism.

3.2.1 Stock preparation

E. coli strain K-12 was obtained from the Spanish Culture Collection (CECT 4624) as a freeze-dried culture. The pellet was rehydrated and handled according to manufacturer. Briefly, dried pellet was rehydrated with 0.2 – 0.3 mL of LB broth using a Pasteur pipette. 100 μL of the suspension was transferred into a 5 mL tube of LB broth and incubated in a rotary shaker (Heidolph Unimax 1010) coupled to an incubator (Heidolph Inkubator 1000) at 100 rpm (revolutions per minute), 20 h at 37 ºC. Afterwards the solution became turbid due to the bacterial growth. Then, the sterile vials of cryobeads (Deltalab) were filled with the liquid inoculum for long term storage in the freezer at -5 ºC.

For recovering the stock, the vial was slowly unfreeze up to reach room temperature (25 ºC). One bead was streaked onto a Petri dish of LB agar and incubated for 20 h at 37 ºC to obtain isolated bacteria colonies. This dish was conserved during 1 week in the refrigerator to prepare a fresh *E. coli* culture for every experiment.

3.2.2 Inoculum preparation

Fresh liquid cultures were prepared taking one colony from the refrigerated stock in the Petri dish using a loop, transferred into 14 mL of liquid LB broth placed in a larger volume flask (≥ 50 mL) and incubated in a rotary shaker at 100 rpm, during 20 h at 37 ºC to get the bacterial stationary phase concentration (10^9 CFU mL^{-1}). Bacterial suspensions were harvested by centrifugation at 900 × *g* for 10 min. Then, the pellet was re-suspended in PBS solution and diluted directly

into the selected water matrix for each experiment to reach the required initial concentration (10^3 – 10^6 CFU mL^{-1}).

3.2.3 Bacterial enumeration

The samples taken during the experiments were enumerated using the standard plate counting method using LB agar Petri dishes. Serial 10-fold dilutions in PBS were performed and then three 20 µL drops of each dilution were placed in the Petri dish reaching a detection limit of 17 CFU mL^{-1}. Colonies were counted after incubation for 20 h at 37 °C (Figure 3.1).

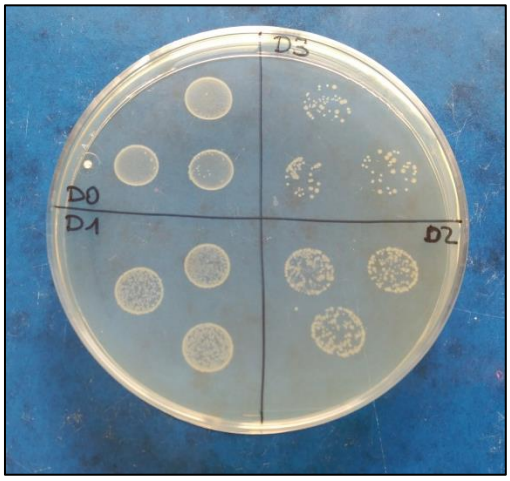

Figure 3.1. Photograph of *E. coli* colonies cultivated in a LB agar Petri dish placing drops of 10-fold dilutions (D0, D1, D2, and D3) of a 10^6 CFU mL^{-1} sample.

3.3 Water matrixes

3.3.1 Isotonic water

The reference water matrix used in this work was an isotonic medium prepared with sterilized distilled water with NaCl 0.9% (w/v); the presence of salt was necessary to avoid osmotic bacterial stress [Sichel *et al.*, 2007a]. This water is used for many experiments in the absence of interferences caused by inorganic and organic compounds that are naturally presented in other water matrixes.

Distilled water was obtained from an osmosis plant located at PSA facilities which operation is explained below:

- Silex filter to remove the solid particles of the raw water.
- Pre-treatment with dosages of hypochlorite, sodium bisulfite (to control chlorine), hydrochloric acid (to control pH) and anti-fouling (to avoid calcification in the membranes) followed by a 5 μm filtration.
- Inverse osmosis that takes place in three modules with 3 semi-permeable polyamide membranes each module. Two modules work in parallel and the third one uses the rejection of the other two modules. The flow production is around 1400 L h^{-1} with a rejection of 700 L h^{-1}.
- Electro-deionization to retain the salts that were not retained in the inverse osmosis. The plant uses ion exchange resins and electric currents to regenerate the resins. The flow production is around 1000 L h^{-1} with a rejection of 150 L h^{-1}.

The conductivity of distilled water was < 10 mS cm^{-1}, the pH was around 5.5, the dissolved organic carbon was < 0.5 mg L^{-1} and the main ions were Cl^- (0.7 – 0.8 mg L^{-1}) and NO_3^- (0.5 mg L^{-1}).

3.3.2 Well water

Well water used in this work was collected from a bore-hole well located on the PSA site with depth of approximately 200 m. Physico-chemical characteristics of the well water are shown in Table 3.1.

Experiments with turbid water were prepared with kaolin or red soils. Kaolin experiments were run with 100 Nephelometric Turbidity Units (NTU) turbid solution. 10 g of kaolin powder was added to 1000 mL of distilled sterile water to achieve a concentrated stock of 10 000 NTU. This solution was kept in constant agitation at 400 rpm during 24 hours [Keogh *et al.*, 2015]. Appropriate dilutions were carried out to achieve an initial turbidity of 100 NTU in the solar reactors.

Table 3.1. Average physical and chemical characteristics of natural well water.

Chemical and biological characteristics			
Cl^-	561.8 ± 2.0 mg L^{-1}	K^+	3.7 ± 0.1 mg L^{-1}
NO_3^-	53.9 ± 0.6 mg L^{-1}	Na^+	387.8 ± 1.6 mg L^{-1}
NO_2^-	1.3 ± 0.1 mg L^{-1}	Mg^{2+}	87.1 ± 1.6 mg L^{-1}
SO_4^{2-}	500.0 ± 1.9 mg L^{-1}	Ca^{2+}	139.3 ± 2.7 mg L^{-1}
HCO_3^-	495.0 ± 48.0 mg L^{-1}	Bacteria	0 ± 2 CFU mL^{-1}
Physical characteristics			
pH	7.57 ± 0.01	DOC	1.7 ± 1.4 mg L^{-1}
Conductivity	3215 ± 1 μS cm^{-1}	TC	89.6 ± 2.5 mg L^{-1}
Turbidity	0.2 ± 0.1 NTU	IC	87.9 ± 2.5 mg L^{-1}

DOC = Dissolved Organic Carbon
TC = Total Carbon
IC = Inorganic Carbon

Red soils are formed mainly by illite and halloysite minerals and also contain calcite. The granulometric analysis without the destruction of carbonates reported a 33 % of sand, 9 % of fine silt, 13 % of thick silt and 44 % of clay. Experimental data used in this work for solar water disinfection in waters added with red soils were previously published. The protocol of turbid solutions were also reported [Ubomba-Jaswa, 2009b]. Briefly, for 5, 100 and 300 NTU turbidity levels, 0.3, 7 and 13 g of soil was measured out respectively and added to 500 mL of well water. For the 5 NTU sample, this mixture was agitated every 10 min during a 0.5 h period and then left to stand for 1 h. The solution above the sediment was then pipetted off and measured to ensure correct turbidity. For 100 and 300 NTU, this mixture was agitated every 2 min during a 0.5 h period and left to stand for an hour. After sedimentation, the solution was then pipetted off, and measured to ensure correct turbidity.

3.4 Analytical techniques

3.4.1 Water characterization

3.4.1.1 pH, temperature, dissolved oxygen and conductivity

pH and dissolved oxygen were measured directly in the reactors with a multi-parametric sensor WTW multi720. Temperature was also measured directly in the reactors by a temperature sensor Checktemp (Hanna Instruments). Conductivity was measured using a conductivity meter GLP31 CRISON.

3.4.1.2 Turbidity

The turbidity is a measurement of the light scatter and absorption at 90º with respect to the incoming direction of light. Water samples become turbid (scatter and absorb light) by the presence of dissolved matter or suspended particles within a size ranged from colloidal to macroscopic. The most common units of turbidity used are the arbitrary NTU (Nephelometric Turbidity Units). The equipment used in this work was a turbidity meter Hach 2100AN model in which the samples are irradiated. It measures the light scattered by the samples that reached a detector located at 90º from the source of light.

Samples are located in a cylindrical glass cuvette that is carefully cleaned and homogenized just before sample measurement. The calibration was done once a year by the calibration kit Hach 2100AN (IS Stablcal® Stabilized Formazin standars) that contain a mix of hydrazine sulphate and hexamethylenetetramine ranging from 0.1 to 4000 NTU.

3.4.1.3 Dissolved organic carbon

Dissolved organic carbon (DOC), inorganic carbon (IC) and total carbon (TC) were analysed using a Shimadzu TOC-V-CSN and an auto-sampler ASI-V.

The TC of the samples is catalytically oxidized to CO_2 by combustion at 680 ºC that takes place by platinum supported on alumina spheres. The CO_2 formed is carried by air to a non-dispersive infrared detector (NDIR). Samples are taken to

reaction with phosphoric acid (25 % w/v) and air to permit the decomposition of carbonates and bicarbonates (IC) to CO_2. Again, the gas is carried to the NDIR detector. The detector sends the peak signals to a data analyser in which calibrations curves were previously introduced. DOC is estimated as the difference between the TC and the IC values.

Samples were filtered with a 0.22 μm polytetrafluoroethylene (PTFE, Millipore Millex® GN) before their injection into the equipment. The calibration was performed periodically with potassium hydrogen phthalate in Milli Q water for TC and a sodium carbonate / sodium bicarbonate (1:1) for IC. Five calibration straight lines are estimated for the following ranges of TOC concentration: 0-10, 10-50, 50-250, 250-1000, 1000-2500 mg L^{-1}.

3.4.1.4 Ion chromatography

Ion chromatography separates ions and polar molecules based on their affinity to the ion exchanger. It works on almost any kind of charged molecule such as large proteins, small nucleotides and amino acids. A sensor is coupled to the columns that allow the detection of anions and cations of water samples.

A sample is introduced into a sample loop and is carried by a buffered aqueous solution (mobile phase) onto a column that contains the stationary phase material. This is typically a resin or gel matrix consisting of agarose or cellulose beads with covalently bonded charged functional groups that interact with the target analytes (anions or cations). The mobile phase drags the analytes at different times depending of their affinity with the functional groups of the stationary phase that finally are detected by conductivity or UV/vis light absorbance.

The equipment used in this work to analyse anions and cations in water samples was an 850 Professional IC – Cation coupled to Metrohm 872 Extension Module. Samples were filtered with a 0.22 μm PTFE filters before injection into the equipment. The calibration was checked before the samples measurements by standard solutions of 10 mg L^{-1} of each anion and cation analysed.

3.4.2 UV spectra

The UV spectra of diverse solutions and different concentrations were measured by a spectrophotometer (Unicam-II) with the aim of estimate the specific absorption or scattering coefficients. The solutions measured were:

- *E. coli* solution of 10^2, 10^3, 10^4, 10^5, 10^6, 10^7 and 10^8 CFU mL^{-1}.
- Catalase solution of 1, 10, 100 and 500 mg L^{-1}.
- Kaolin solution of 10, 50, 100 and 300 NTU.
- Red soils solution of 5, 100 and 300 NTU.

3.4.3 Catalase quantification

Catalase activity was measured in the solutions with catalase dissolved in potassium buffer, pH 7.0. It was done by an indirect measurement following the reaction of H_2O_2 decomposition catalysed by this enzyme (reaction (1.27)) using a spectrophotometry method.

Catalase activity is expressed in terms of units (U) that is equal to the μmol of H_2O_2 decompound by catalase in one minute (μmol min^{-1}). The volumetric specific activity (A_v) of catalase is expressed in terms of U L^{-1} that is equal to μM min^{-1}, so it is a measurement of the H_2O_2 decomposition rate (R).

The volumetric specific activity or H_2O_2 decomposition rate of catalase was experimentally determined testing several concentrations of catalase (5 to 70 mg L^{-1}) and H_2O_2 (10 to 100 mM). 50 mM of H_2O_2 was detected as the optimal concentration of H_2O_2 for the catalase concentration range investigated. Once established this optimized concentration, their reaction with several concentrations of catalase permitted the experimental determination of the volumetric specific activity parameter (these results are presented and discussed in chapter 5).

The main steps of the protocol used are summarized as follow [Visick and Clarke, 1997]. Note that this description includes specifically the volume of reagents used in the case of 50 mM-H_2O_2 tests as an example:

1. A concentrated H_2O_2 solution of 1750 mM was prepared in 50 mM potassium buffer, pH 7.0. 100 µL of this solution were added to a quartz cuvette of 1 cm of path length containing 3.4 mL of a catalase samples. No dilution effect on catalase and H_2O_2 concentration was considered due to the low H_2O_2 volume added to the catalase samples.

2. Immediately, a rapid mix of the sample was done by pipetting and absorbance at 240 nm (A_{240nm}) was monitored every 10 seconds by a spectrophotometer (Unicam-II). The A_{240nm} is proportional to the H_2O_2 concentration therefore absorbance decreased over time as shown in Figure 3.2 (a), while O_2 concentration increased which was obvious by the formation of gas bubbles in the samples (Figure 3.2 (b)).

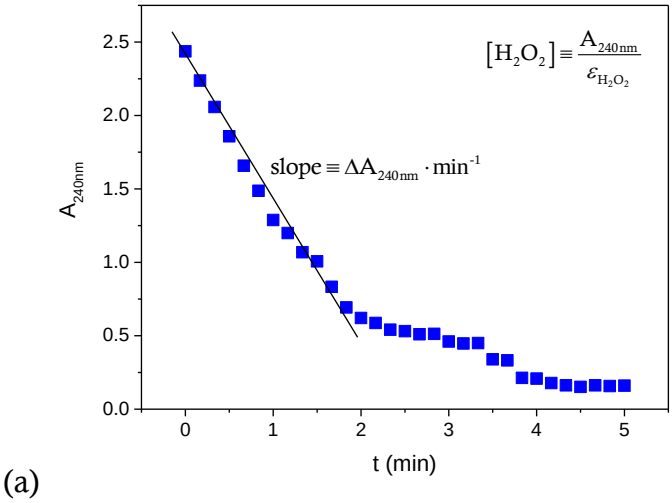

(a)

(b)

Figure 3.2. Decomposition of H_2O_2 catalysed by catalase (a) time-profile of the absorbance at 240 nm and (b) photograph of quartz cuvette in which the reaction was conducted (oxygen bubbles could be observed).

3. The slope of the curve absorbance versus time was calculated ($\Delta A_{240nm}\ min^{-1}$). Catalase A_v expressed as U L^{-1} was obtained according to the equation (3.1), where the ε_{H2O2} is the extinction absorption coefficient of H_2O_2 (43.6 $M^{-1}\ cm^{-1}$) and l is the optical path length given in terms of cm.

$$A_v = \frac{\text{slope} \cdot 10^6}{\varepsilon_{H2O2} \cdot l} \tag{3.1}$$

3.4.4 Fluorescence detection

The fluorescence phenomenon takes place when a compound absorbs light at a given wavelength and emits light at another wavelength. Due to the light absorption, an electron is excited to a higher and more unstable energy state. Then, the electron relaxes to its ground state inducing the emission of a photon in a different wavelength. Fluorescence emission wavelength has longer wavelength, and hence lower energy and different colour than the light responsible for excitation.

In this work, different types of fluorescence techniques were used for DCF fluorescent signal detection:

3.4.4.1 Fluorimetry

The basis of a fluorimeter consists on the irradiation of the sample and the detection of the fluorescence light emitted by the sample. Light filters are used to irradiate the sample at a specific wavelength and also for the detection of the fluorescence emission, minimizing the background ('noise') signal. The sensor is usually located perpendicularly to the light beam direction.

The fluorimeter used in this work is a Spectrafluor Plus (Figure 3.3) belongs to the research centre of CIESOL, located at University of Almeria (Spain). The wavelengths excitation/emission of 497/520 nm was used for specific detection of DCF fluorescence in water samples. The equipment provides the fluorescent

signal in terms of CPS (counts per second). The samples were placed in a quartz cuvette of 1 cm of path length with rounded borders.

(a) 

(b) 

Figure 3.3. (a) Spectrafluor Plus Fluorimeter and (b) its sample chamber.

3.4.4.2 Fluorescence microscopy

The principle of fluorescence microscopy is shown in Figure 3.4. Light that is provided by a xenon lamp is directed through an exciter filter, which selects the excitation wavelength. Then, light is reflected towards the sample by a dichroic mirror, designed to reflect light only at the excitation wavelength. The reflected light passes through the objective where it is focused onto the fluorescent sample. The emissions from the fluorescent species passed back up through the objective, the dichroic mirror and the barrier filter. The function of this filter is to avoid light contamination from other sources. Finally, the filtered fluorescent emission signal is received by a detector where the image can be either analysed, or transmitted to the lens for optical viewing.

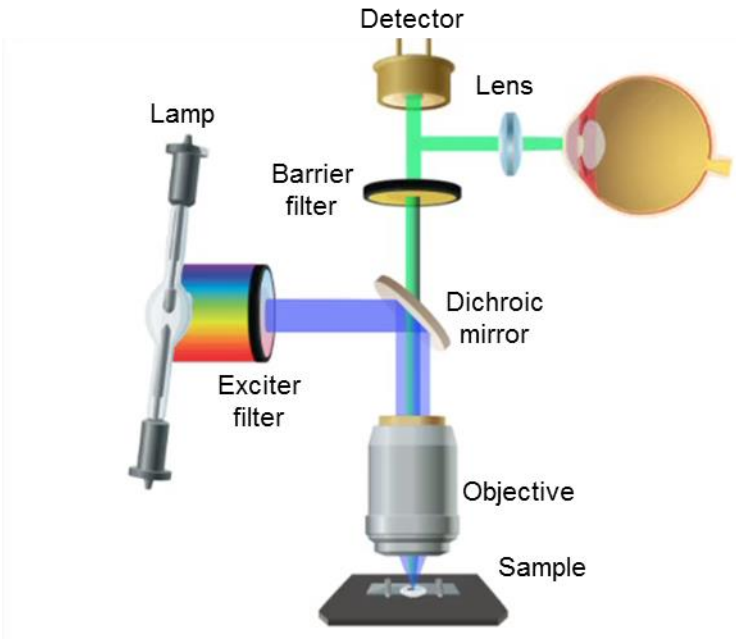

Figure 3.4. Components of a fluorescence microscopy [JoVE, 2016].

The fluorescence microscope used in this work is a Leica DM 2500 with excitation filters of 480/40 and emission filters of 585/40 coupled to a DFC365 FX camera (Figure 3.5 (a)). The samples were placed in a slide and a cover slip was placed over the sample. The objective was focused in bright field and then the excitation light was switched on and the sample was observed and photographed in five different points of the cover slip: near the four corners and in the middle (Figure 3.5 (b)). Cells counting of the five pictures were performed using the Leica Application Suite software [Arif *et al.*, 2016]. The estimation of the fluorescent cells concentration *C,* was done using the average of the total counting of 5 areas of the lid randomly selected $\bar{x}$, the picture area A_p ($9.44 \cdot 10^{-4}$ cm^2), the increases I (40x), the cover slip area A (4.84 cm^2) and the sample volume V (25 μL):

$$C = \frac{\bar{x} \cdot A}{A_p \cdot I \cdot V} \tag{3.2}$$

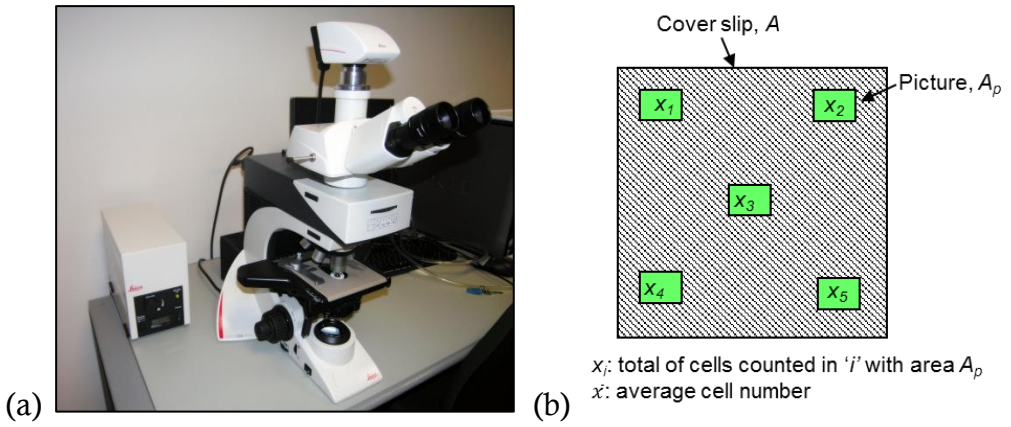

Figure 3.5. (a) Fluorescence microscope Leica DM 2500 and (b) diagram of the cover slip area.

3.4.4.3 Flow cytometry

Flow cytometry is an analytical technique that allows the rapid measurement of light scattered and fluorescence emission signals produced by a set of illuminated cells that are in a liquid suspension. The equipment permits the flow of cells one by one, detecting the signals when they pass individually through the beam of light. Therefore, the results represent the cumulative signal of individual fluorescence characteristics. The most common application of flow cytometry is the characterization of a cellular suspension as a function of size, volume, density, optical properties, membrane potential or pH.

The basis of a flow cytometer is shown in Figure 3.6. To get the suspension into a stream of cells in a single file, the method of hydrodynamic focusing (or laminar flow) is used. It consists on the flow of a sheath fluid at constant velocity a pressure in the outer layer. At the same time, the cellular suspension is passing through the laminar tube at a higher pressure to assure that cells defile one by one. Then, the cells are irradiated and the scatter is detected in two positions: in front of the light beam to measure the forward scatter (FS) and at 90º to measure the sides scatter (SS). FS correlates with cell size and SS is proportional to the granularity of the cells. Fluorescence detectors are also located at 90º to measure the fluorescence of the stained cells. The fluorescence sensors are photomultiplying tubes (PMTs) that detect, amplify and send the fluorescence

signal to a computer processing unit. The fluorescent light is filtered so that each sensor will detect fluorescence only at a specified wavelength.

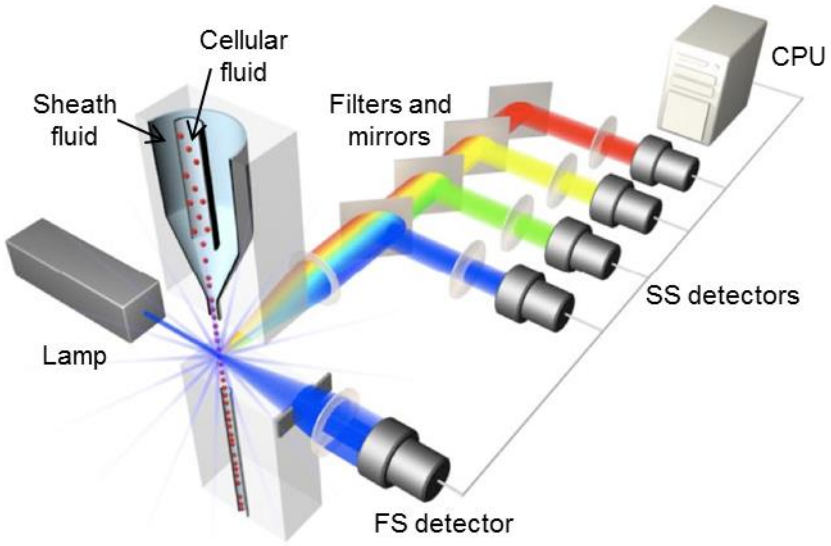

Figure 3.6. Basis of a flow cytometer.

The flow cytometer used in this work is FACSCANTO II (Figure 3.7) and belong to 'Centro de Investigaciones Biomédicas (CIBM)', University of Granada (Spain). It has a blue light that excites the samples (488 nm) and detection filters LongPass LP502 and Bandpass 530/30. The equipment gives the fluorescent signal of ca. 50 000 bacteria cells in terms of FITC-A signal. FITC-A (Fluorescein isothiocyanate) is a very well-known fluorescent probe used in cytometric assays and whose signal is used as arbitrary units as reference to other probes that emits in the same wavelength. The analysis of the data was performed by Flowing Software 2.

(a)  (b) 

Figure 3.7. (a) FACSCANTO II flow cytometer and (b) detail of its sample injection.

3.4.4.4 Non fluorescence detection: spectrophotometry

The DCF property of light absorption at 500 nm was used to detect and measure the conversion from DCFH to DCF. A spectrophotometer (Unicam-II) was used to perform spectral scanning in the range of wavelength of 300 – 800 nm with a quartz cuvette of 1 cm of path length.

3.5 Solar reactors

In this work different solar reactors were used depending of the conditions required for each experiment. All the experiments were performed using batch reactors to SODIS purposes. Different configurations were selected depending on the application.

3.5.1 200 mL-Batch reactor

Solar disinfection at natural solar light was done in bottles of 250 mL DURAN-glass (Schott, Germany) (Figure 3.8) as in other similar works [Sichel *et al.*, 2007a; Polo-López *et al.*, 2011; Helali *et al.* 2014]. It is made of borosilicate that permits the transmission of 90 % of UVA range. Although the geometry of the bottles is not optimized to performed solar water treatment, the photons income is enough for this experimental work. In addition, they present some advantages:

- Experiments are performed using small water volume, which implies reduction of the consumption of water, reagents and nutrient mediums.
- Replicates can be performed simultaneously under the same weather conditions avoiding differences in irradiance and temperature values.
- Bottles do not present dark spaces when they are exposed to sunlight, permitting the irradiation of the entire water volume in an interrupted manner during the experiment.

The total volume used in the bottles was 200 mL with an illuminated area cross surface of 95 cm^2 calculated as the cylindrical lateral area: $2\pi \cdot r \cdot h$, where the internal radius r is 2.75 cm and the water high h is 5.5 cm. Glass covers (Schott, Germany) were used instead of plastic lids, to allow the solar radiation to enter the bottle reactor from all directions (Figure 3.8). The reactors were placed on a magnetic agitator to keep a homogenous suspension during the experiments. Therefore, all the points of the solution received the same photon flux at each instantaneous moment and had a homogeneous bacterial concentration through the whole volume. The agitation was set at 100 rpm.

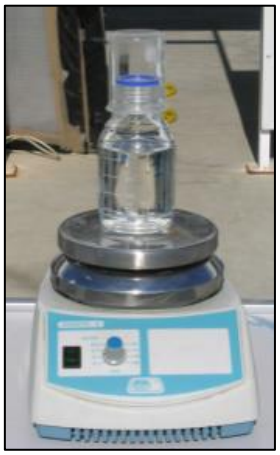

Figure 3.8. 200 mL-Batch reactor exposed to natural sunlight.

3.5.2 700 mL-Batch reactor

Solar disinfection experiments and catalase photo-inactivation performed to determine the kinetic parameters were run under controlled conditions of irradiance in a solar simulator system (explained below). The reactor used for these experiments was an open glass vessel of 19 cm of diameter and total volume of 700 mL, with an irradiated surface of 0.0284 m^2 (Figure 3.9). Water was stirred at 100 rpm during the experiments to assure that all the points of the solution received the same photon flux at each instantaneous moment and have homogeneous concentration of bacteria. The radiation came from the top, therefore direct radiation entered the water volume without alterations in direction being the entire volume illuminated. The system was selected because its size is large enough to neglect any radial profiles and to consider a one-dimensional radiation gradient. Samples were taken with a syringe and a sterilized flexible tube from the outside of the simulator system.

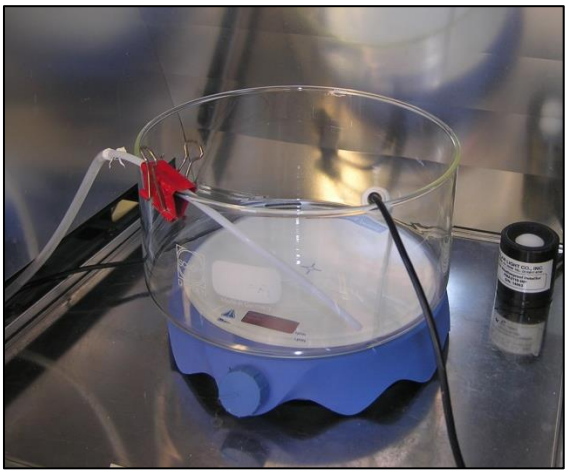

Figure 3.9. 700 mL-Batch reactor placed on the chamber of the solar simulator system.

3.5.3 Batch reactors used for model validation

Solar disinfection experiments under natural solar light for the model validation were done in diverse batch reactors, some of them commonly used for SODIS applications and research (Figure 3.10).

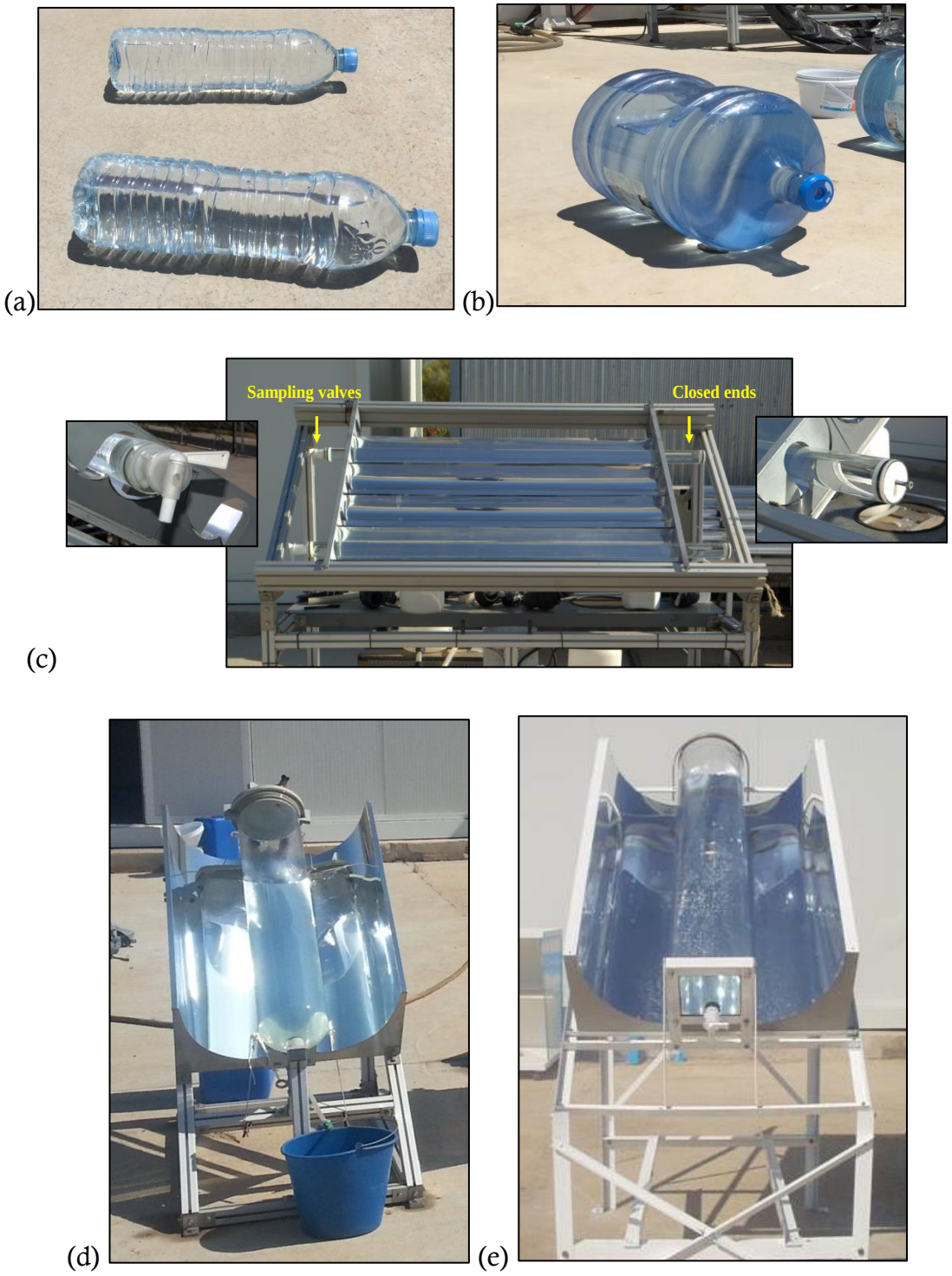

Figure 3.10. Batch solar reactors used for model validation: (a) 2 L-PET, (b) 19 L-PC, (c) 2.5 L-BS, (d) 20 L-BS and (e) 22.5 L-MC.

The solar reactors used for the validation of the model developed in this work were all batch reactors that were operated without any agitation. They have been previously used and described in other research SODIS contributions and applications. Their main characteristics are summarized in the Table 3.2 and explained below:

(i) **2 L-PET batch reactor**: typical bottles of polyethylene terephthalate (PET) using for SODIS application in the field [Ubomba-Jaswa *et al.*, 2010; McGuigan *et al.*, 2012].

(ii) **19 L-PC batch reactor**: typical water dispenser container for public places, made of polycarbonate (PC). It was previously used for SODIS studies with the aim of overcoming the volume limitations of PET bottles [Keogh *et al.*, 2015].

(iii) **2.5 L-BS batch reactor**: borosilicate (BS) glass tube which were closed at both ends and fitted in the linear focus of a horizontal compound parabolic collector (CPC). This type of reactor was previously used for the study of its SODIS efficiency under ideal conditions of materials composition, water illumination, and geometrical design [Ubomba-Jaswa *et al.*, 2010].

(iv) **20 L-BS batch reactor**: borosilicate glass container placed on a vertical CPC. This type of reactor was previously used for the study of its SODIS efficiency in static batch conditions, with improved solar collection, optimized materials selection and with a volume larger than typical SODIS compliance volumes [Nalwanga *et al.*, 2014].

(v) **22.5 L-MC batch reactor**: methacrylate (MC) photo-reactor placed on a vertical CPC. This type of reactor was previously used for the study of its SODIS efficiency in static batch conditions and large volume, decreasing the cost of the materials, augmenting its robustness and sacrificing its radiation transmission properties [Ubomba-Jaswa *et al.*, 2010].

The CPC reflectors used were all adapted to the dimensions of each reactor diameter. They were fitted to a metal frame inclined at 37º from the horizontal. This inclination was selected to match with the local latitude and recover the maximum UV radiation during the year [Ubomba-Jaswa *et al.*, 2010]. The CPC was made of highly reflective anodized aluminum sheet (MIROSUN® Aluminium GmbH) with a concentration factor of 1 and a UVA reflectivity of 87 %.

Table 3.2. Physical characteristics of the solar reactors used in the validation of the mechanistic model of solar water disinfection.

Reactor	2 L-PET	19 L-PC	2.5 L-BS	20 L-BS	22.5 L-MC
Volume	2 L	19 L	2.5 L	20 L	22.5 L
External diameter	8.5 cm	27 cm	5 cm	20 cm	20 cm
Length	0.29 m	0.48 m	1.3 m	1 m	1 m
Wall thickness	0.5 mm	1.4 mm	1.8 mm	10 mm	10 mm
Material	Polyethylene terephthalate	Polycarbonate	Borosilicate	Borosilicate	Methacrylate
UVA-transmittance	52 %	33 %	90 %	90 %	19 %
Position	Horizontal (resting on its side)	Horizontal (resting on its side)	On a horizontal CPC	On a vertical CPC	On a vertical CPC
Concentration factor of the CPC	-	-	1	1	1
Irradiated length of the CPC	-	-	148 cm	92.5 cm	92.5 cm
Irradiated width of the CPC	-	-	14.2 cm	62.5 cm	62.5 cm
Aperture area of the CPC	-	-	0.21 m^2	0.58 m^2	0.58 m^2

3.6 Irradiance measurement

3.6.1 UV radiometer

Solar global UV radiation was measured with a pyranometer Model CUV4, Kipp & Zonen (Netherlands) that has a spectral response ranged from 305 to 385 nm. It has an excellent linearity and directional response with a fast measurement (less than 1 second) and high sensitivity (1 mV W^{-1} m^2). It is suitable for outdoor measurements and the operation temperature ranged from -40 to +80 ºC. It has a semi-sphere that receives both diffuse and direct radiation.

The PSA counts on two UV radiometers at 3 m of high (Figure 3.11), one located horizontally and the other inclined 37º that are cleaned every day to assure good measurements. The majority of the pilot plants are inclined at 37º to receive the maximum solar UV dose energy along the year due to the location of PSA is 37.0ºN, 2.3ºW. Both equipments are connected by a data logger to a computer that registers the sensor measurements during the day in terms of incident irradiation (W m^{-2}), i.e. solar radiant energy rate incident on a surface per unit area. Data from the inclined pyranometer were used for reactors inclined 37º and data recorded from the horizontal pyranometer were used for horizontally placed systems (PET and PC batch reactors).

Figure 3.11. UV radiometer Model CUV4, Kipp & Zonen located in PSA facilities.

3.6.2 Portable UVA radiometer

Solar Light Co., Inc (Philadelphia), model PMA2111 was used as UVA detector (Figure 3.12). It provides fast and accurate irradiance measurement in the UVA

region (320 to 400 nm). The resolution of the measurement is 0.01 W m^{-2}. It is suitable for outdoor operation since the detector is enclosure hermetically and is able to work in extreme thermal conditions, from -40 to +50 °C.

Figure 3.12. Portable UVA radiometer (Solar Light Co., Inc).

It has a Teflon diffuser that assure an angular response close to a cosine function (Lambertian response) making the detector suitable for measuring diffused radiation or radiation from extended sources.

The portable UVA radiometer was used to measure the irradiance received in the 700 mL-batch reactor during experiments performed in-door with artificial light.

3.6.3 Spectrometer

AvaSpec-ULS2048 Spectrometer (Figure 3.13) was used to measure the spectral radiation. It has a sensitivity of 310 000 counts μW^{-1} ms^{-1} and provides spectral data in the range of 200 - 1100 nm in terms of W m^{-2} nm^{-1}. The connection with a computer is done via USB2-connection, delivering a scan every 1.8 ms. The integration time ranges from 1.1 ms to 10 minutes.

The radiation sensor is a cosine corrector CC-UV/VIS that collects light from an angle of 180°. It is made of Teflon, which is especially suited for measurements in the 200 – 800 nm range.

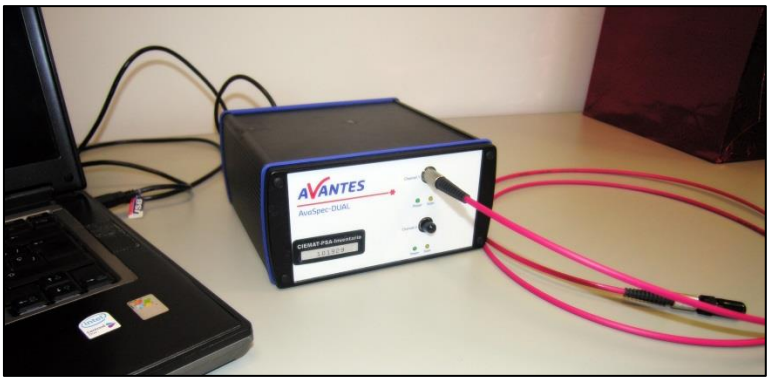

Figure 3.13. AvaSpec-ULS2048 Spectrometer used to spectral radiation measurements.

3.7 Sources of light

3.7.1 Natural sunlight

Experiments under natural sunlight were performed at PSA (37.0ºN, 2.3ºW) facilities. The weather of the location is usually sunny with very few cloudy days. Global irradiance is measured continuously from 7 am to 10 pm every day providing data every second and averaged values at desired periods of time (1 min, 5 min, etc.) by the UV radiometers explained above. Figure 3.14 (a) shows the monthly horizontal irradiance averaged of the year 2016. 10 am to 4 pm is the time frame with the highest UV irradiance whose values depend on the month of the year, ranging from 15 and 50 W m^{-2}. The period of the year with the less irradiance is from November to February. In this time, UV doses lower than 150 J m^{-2} in the central hours of the day (10 am to 4 pm, see Figure 3.14 (b)) are registered.

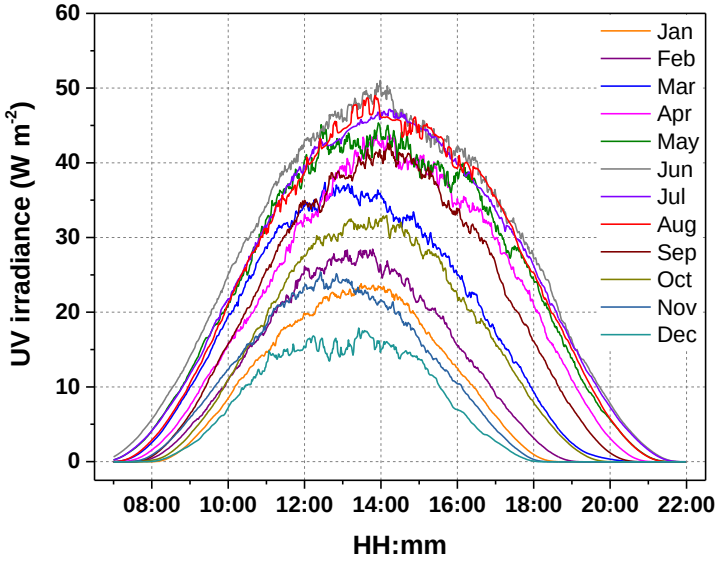

(a)

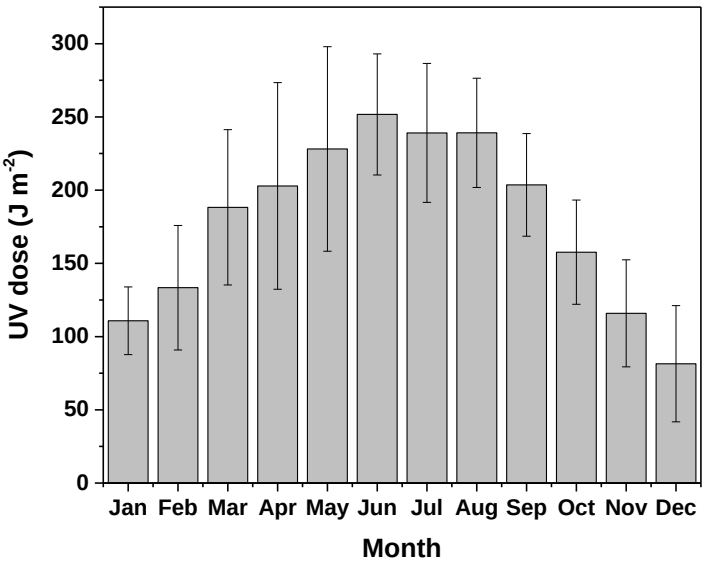

(b)

Figure 3.14. Monthly horizontal average radiation data of 2016 year (registered in the PSA facilities by CUV4 Kipp & Zonen pyranometer) (a) UV irradiance and (b) UV energy dose between 10 am and 4 pm.

3.7.2 Artificial sunlight

Artificial solar radiation was provided by a solar simulator equipment SUNTEST XLS+ (Atlas Material Testing Solutions) (Figure 3.15 (a)). The table chamber's dimensions are 330 x 330 mm and the walls of the chamber are

covered by reflectors to re-direct the radiation to the table samples. The distance from the floor to the lamp is 26 cm. The shape and configuration of the chamber are shown in the Figure 3.15 (b).

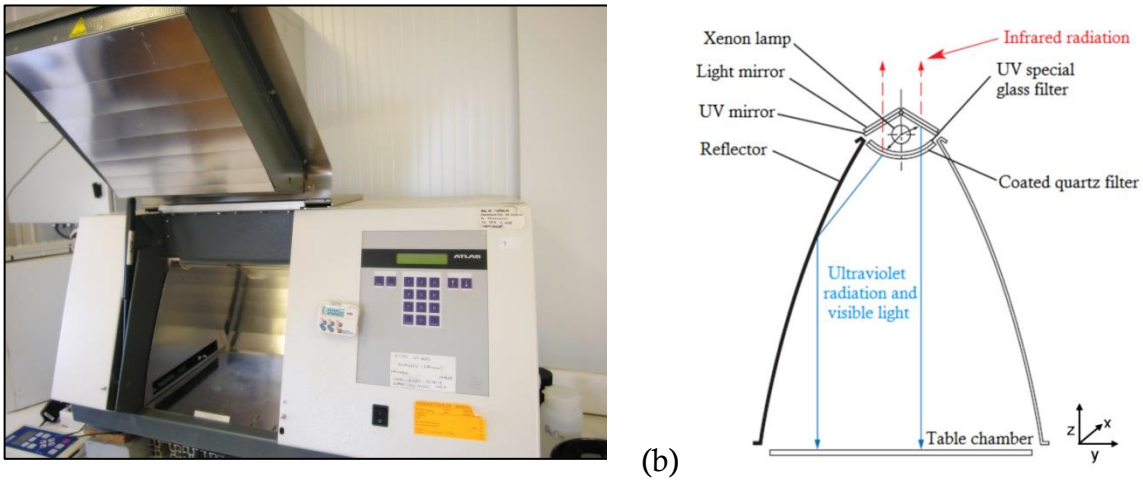

Figure 3.15. Solar simulator system: (a) SUNTEST XLS+ and (b) diagram of the interior of the chamber.

It has a xenon lamp, an UV mirror and a light mirror to reflect UV light upper the lamp and an optical UV special glass filter segment with a coated quartz filter (Figure 3.15 (b)). This combination of filters simulates the solar global radiation outdoors spectrum (daylight) avoiding elevated temperatures inside the chamber. A comparison with natural solar radiation can be made using the density function parameter, g_λ that it is expressed by the following equation:

$$g_\lambda = \frac{E_\lambda}{\sum_{\lambda_i} E_{\lambda_i}} \tag{3.3}$$

where E_λ is the power of light per unit of surface area (in terms of W m^{-2}) at a given wavelength λ. Figure 3.16 shows the spectrum of the artificial light in comparison with the natural solar spectrum. The shapes of both profiles are very similar from 300 nm to 600 nm. Beyond 600 nm, xenon lamp emits peaks of high intensities at certain wavelengths, while natural sunlight presents a smoother profile and higher values of the density function.

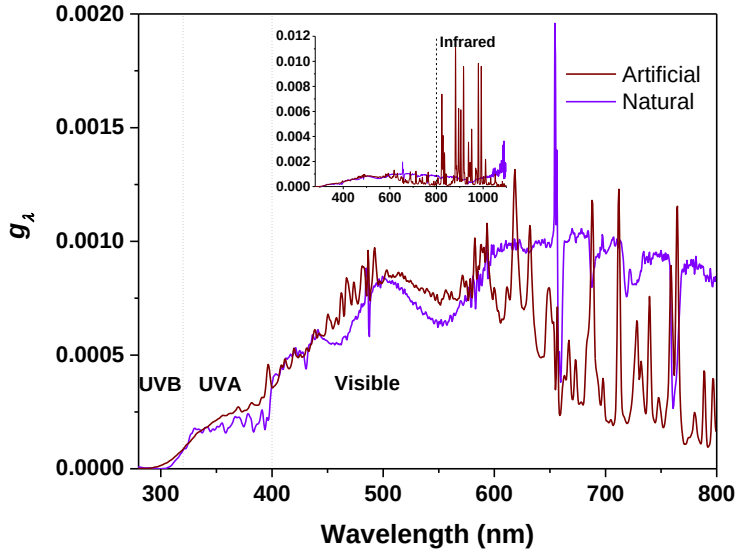

Figure 3.16. Density functions of natural and artificial sunlight radiation in UV, visible and infrared (inlet graph) ranges. Artificial irradiance was measured in the centre of the chamber at 10 cm height.

Table 3.3 shows the irradiance values measured in a certain time instant of a typical sunny day (natural sunlight) and at a specific height at the solar simulator system directly obtained with the spectrometer. The height of the measurement in the simulator system was selected in order to have similar irradiance values in the range of the 305 – 385 nm (considered as the reference range in this work), which was 11.4 ± 0.2 W m^{-2}. It is observed that both light sources present similar irradiance values in the UVB and UVA (and hence UV) ranges of the spectrum. Nevertheless, the visible range of natural sunlight has irradiance values significantly higher than the artificial one, i.e. ~ 300 vs 200 W m^{-2}. The ratio visible/UV for natural sunlight is 20.6 while for artificial sunlight is 12.4. In conclusion, the solar simulator system used in this work is an accurate source of UV photons that simulates the real UV sunlight.

Table 3.3. Comparison of instantaneous irradiance values of natural and artificial solar light measured by the spectrometer (AvaSpec-ULS2048).

	Natural sunlight		Artificial sunlight	
Range of wavelength	**Irradiance (W m^{-2})**	**Ratio Vis/Range**	**Irradiance (W m^{-2})**	**Ratio Vis/Range**
Reference: 305 – 385 nm	11.24	26.6	11.59	16.9
UVB: 280 - 320 nm	0.57	524.2	0.82	239.5
UVA: 320 - 400 nm	13.92	21.5	15.04	13.1
UV: 280 – 400 nm	14.49	20.6	15.86	12.4
Visible: 400 - 800 nm	298.79	1.0	196.4	1.0

The lamp provides constant irradiance value established as the set point in the equipment in the range of 300 to 800 nm. However, immediately after switched on, a peak of irradiance (2 orders of magnitude higher than the set point) of 9 – 10 seconds is observed. Then the selected irradiance is provided with a coefficient of variation of 5 %. If the door of the chamber is opened the lamp is switched off automatically. Due to this fact, and for avoiding interferences of the incident of radiation peaks on bacteria viability, all experiments were performed without opening the chamber. Samples were taken with a flexible tube and a syringe from the outside of the simulator system.

Figure 3.17 shows the irradiance measured by the UV radiometer (305 – 385 nm) when the solar simulator set point is 300 W m^{-2} in the range of 300 – 800 nm, at two different heights with respect to the table, z = 6.5 and 9 cm (19.5 and 17 cm from the lamp, respectively). At 9 cm high, a homogeneous radiation region of 2 cm is created in the middle of the chamber of around 31.5 W m^{-2} of UV intensity. The diameter of the homogenous region increases as the height decreases although the irradiance value decreases, i.e. at a height of 6.5 cm there is a 4 cm-wide homogenous region of UV intensity of around 29 W m^{-2}.

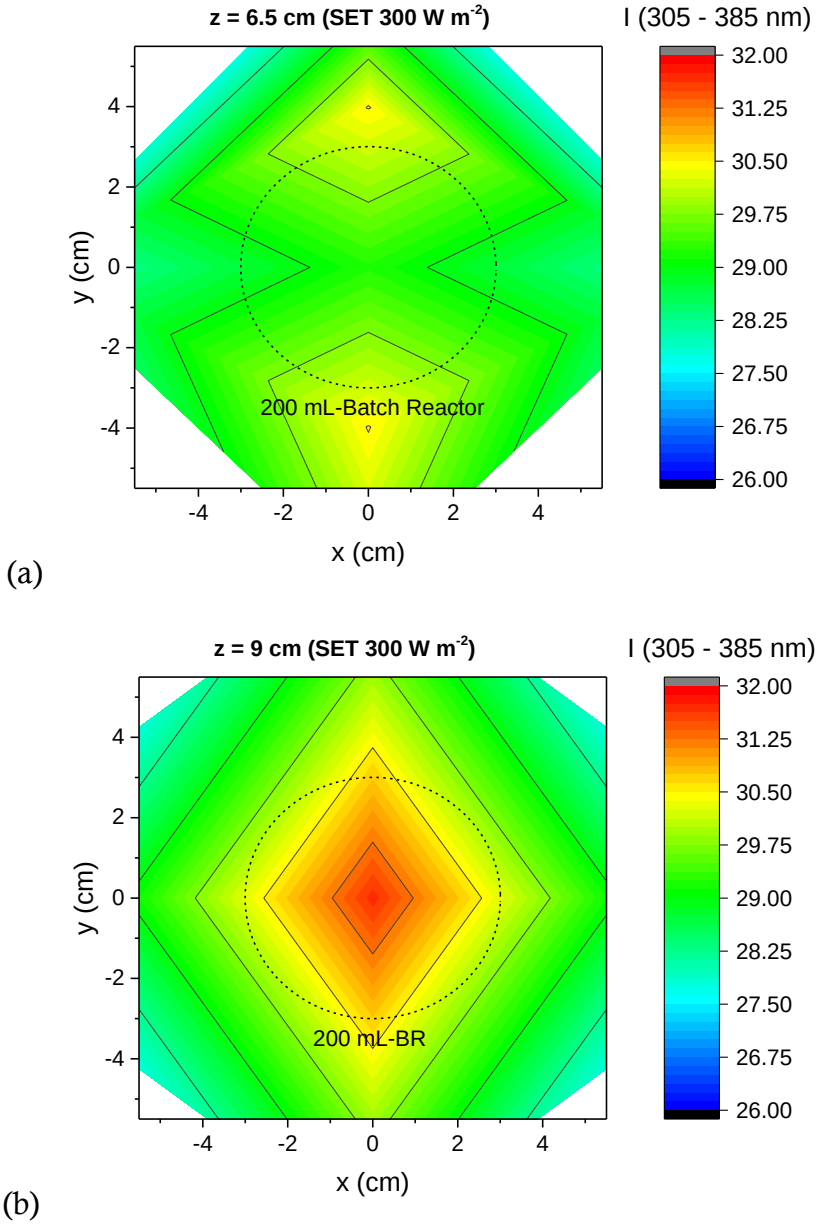

Figure 3.17. UV map in the SUNTEST XLS+ in the centre of the chamber at (a) 6.5 and (b) 9 cm high with a lamp radiation set point of 300 W m^{-2} (300 – 800 nm).

Figure 3.18 shows the gradient of UV radiation in the Z axis (height). The radiation decreases approximately 3.5 % per cm away the lamp. Although the irradiance is not homogeneous in the entire chamber, the radiation income of one reactor in continuous agitation located in the centre of the chamber, could be assumed as the average in all the points of the reactor.

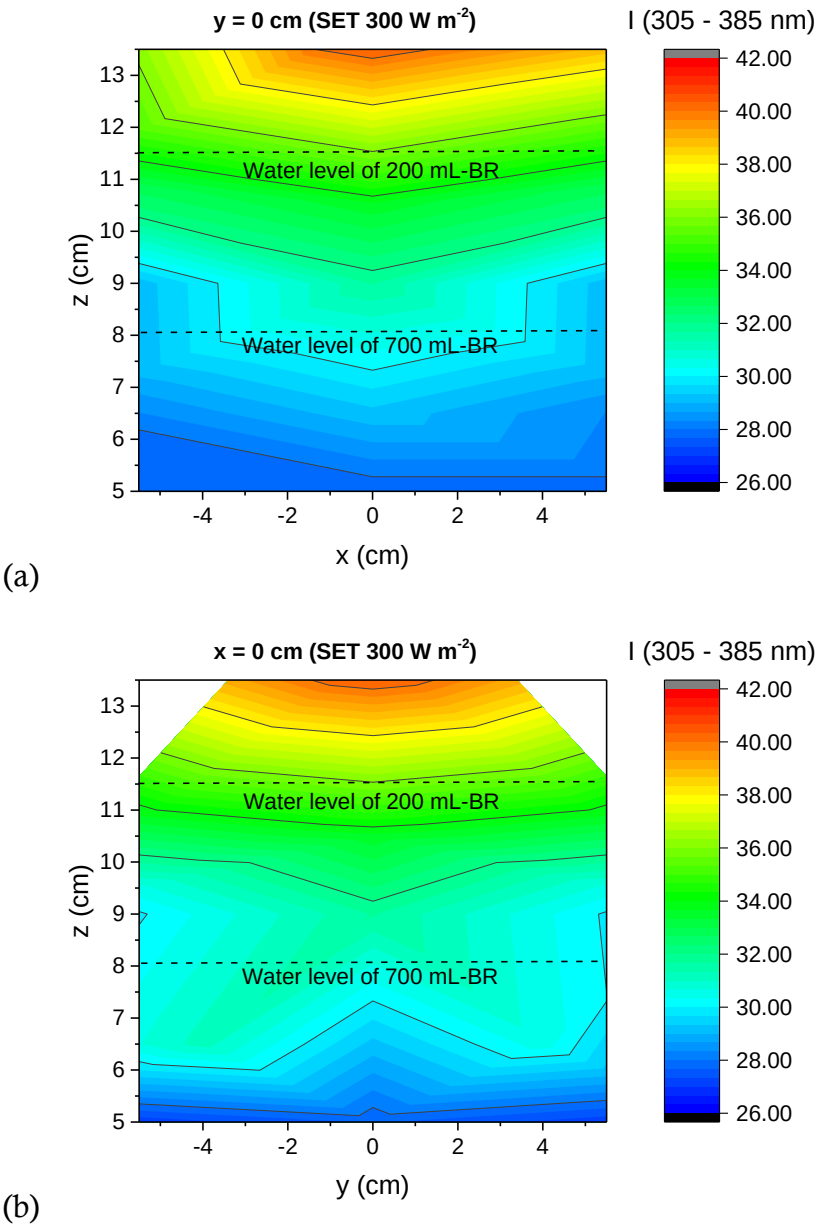

Figure 3.18. UV map in the SUNTEST XLS+ in the chamber at (a) y = 0 (XZ plane) and (b) x = 0 (YZ plane) with a lamp radiation set point of 300 W m^{-2} (300 – 800 nm).

3.8 Temperature control devices

The experimental studies of the thermal effect on the viability of *E. coli* were performed using several devices that permit to keep the temperature constant and controlled.

1. The experiments in the dark with controlled temperature were run in a cool-hotter dry bath incubator (UniEquip GmbH) (Figure 3.19). It permits to maintain the temperature constant in a range from -10 to + 100 ºC with an accuracy of ± 0.2 ºC.

   The equipment holds 1.5 mL sterile containers ('eppendorf' type). 3 replicates of each sampling time were filled with the bacterial suspension at the beginning of the experiment and introduced into the bath incubator. The samples were taken at predetermined times for bacterial enumeration.

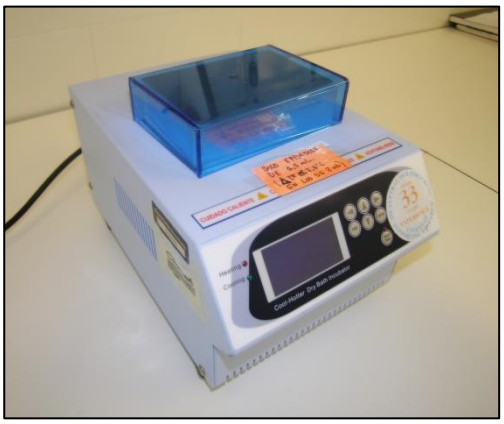

Figure 3.19. Cool-hotter dry bath incubator (UniEquip GmbH).

2. Solar water disinfection experiments with controlled temperature were performed in the solar simulator system using a thermostatic recirculation bath (Frigiterm-TFT-10, Selecta). The equipment permits to adjust bath water temperature in a range of -10 to +100 ºC with a tolerance of ± 0.1 ºC.

   The thermostatic bath (secondary bath) were placed outside the solar simulator system and connected by flexible tubes and a pump with a water container (primary bath) acting as jacketed of the 700 mL-batch reactor located inside the solar simulator system (Figure 3.20).

Figure 3.20. Thermostat recirculation bath (Frigiterm-TFT-10, Selecta) using as secondary thermal bath for solar disinfection experiments with controlled temperature.

Prior to start irradiation, the water under assessment was heated to reach the desired temperature with a stirred hotplate. Then the reactor was filled with the bacterial suspension and placed into the primary bath that was connected with the secondary bath. Due to the ventilation in the solar simulator chamber, and due to the lamp heating, water temperature was continually monitored and secondary bath set point was adjusted manually during experiments with the aim of reaching the temperature desired in the reactor (Figure 3.20).

3.9 Experimental procedure

In this work, several types of experiments were performed. They can be classified as water irradiation exposure or radiation experiment and water thermal exposure tests or thermal experiments. In addition, radiation experiments were performed with both natural and artificial sunlight. Nevertheless, the protocol for all the experiments followed almost the same scheme:

1. Filling the reactor with the desired water volume and adding turbidity source (kaolin and red soil) when required.

2. Controlling the water temperature until a certain value is reached and stable (only for those experiments in which constant temperature was required).

3. Adding a specific volume of *E. coli* suspension or chemicals (in the studies of DCFH-DA and catalase photo-stability tests) to achieve the initial concentration required.

4. Agitating the suspension during 5 min to assure homogenous conditions and take the initial sample in the dark (lamp off or using an opaque cover over the reactor).

5. Expose the reactor to solar radiation (natural or artificial) or thermal treatment (in dark).

6. Taking several samples during the experiment (samples timing depended on the total treatment time and the type of experiment) and performing the sample analysis required (dilution followed by plating, incubation and counting).

7. Cleaning the reactor at the end of each experiment using a diluted solution of H_2O_2 (approximately 20 mM) as disinfectant reagent, followed by rinsing out with distilled water three times.

8. Analysis of results. All the results showed in this work are the average of at least three replicated experiments per each experimental condition, with corresponding error bars calculated as standard deviation of the data.

3.10 Modelling

In this work two kinetic models are presented. The first one is explained in detailed in chapter 5 (*Mechanistic model of solar water disinfection: effect of solar UVA*) that has 5 unknown parameters; the second one is explained in chapter 6 (*Mechanistic model of solar water disinfection: synergistic effect of solar UVA and mild-heat*) and has only 3 model parameters. The parameters estimation was done by MATLAB® software by three search methods [Cabrera, 2013]:

- Sequential search to determine the magnitude order of the parameters.

- Monte Carlo method to attune the values of the parameters.
- Regression to optimize the parameters' values.

The search was done minimizing an objective function that is defined as the normalized root mean squared logarithmic error (NRMSLE) of the experimental and predicted viable bacteria concentration:

$$\mathrm{NRMSLE}_j = \frac{\sqrt{\frac{1}{n}\cdot\sum_i^n\left[\left[\log\left(m_i+1\right)-\log\left(e_i+1\right)\right]^2\right]}}{\frac{\sum_i^n\log\left(e_i\right)}{n}}\cdot 100 \tag{3.4}$$

$$\mathrm{NRMSLE} = \frac{\sum_j^N \mathrm{NRMSLE}_j}{N} \tag{3.5}$$

where NRMSLE_j is the error of one experiment *j*, NRMSLE is the average error of all experiments, *n* is the number of experimental points of the experiment *j*, *N* is the total number of experiments, *m* is the modelled predicted value and *e* the experimental value of viable bacteria concentration.

Both models present a system of differential (that define the H_2O_2 and bacteria concentration) and algebraic equations (that define the enzymes concentration) that must be solved simultaneously. All the variables of the model were normalized to avoid computing numerical problems as no solution convergence. Differential equations were solved using the solver module '*ode45*' that is commonly used for nonstiff problems. This solver is based on an explicit Runge-Kutta formula for fourth and fifth order solution that is part of the Dormand-Prince method. It is a single-step solver, i.e. to get the point $y(t_n)$, it is only needed the solution at the immediately preceding time point, $y(t_{n-1})$.

The MATLAB® codes for the two model of this work are summarized in the appendix section (Appendixes A and B).

3.10.1 Sequential search

The first stage of the optimization process was performed to determine the order of magnitude of each parameter. The procedure followed in this work is shown in Figure 3.21. The first step is to define a parameter vector with different values of magnitude orders for each parameter. A combination of the parameter vector was taken to solve the differential equations of the model in a specific operational condition, i.e. irradiance, temperature and initial bacterial concentration. Then the simulated values of the bacteria concentration were compared with the experimental data by the objective function. The combination of the parameters that reached minimum error was selected.

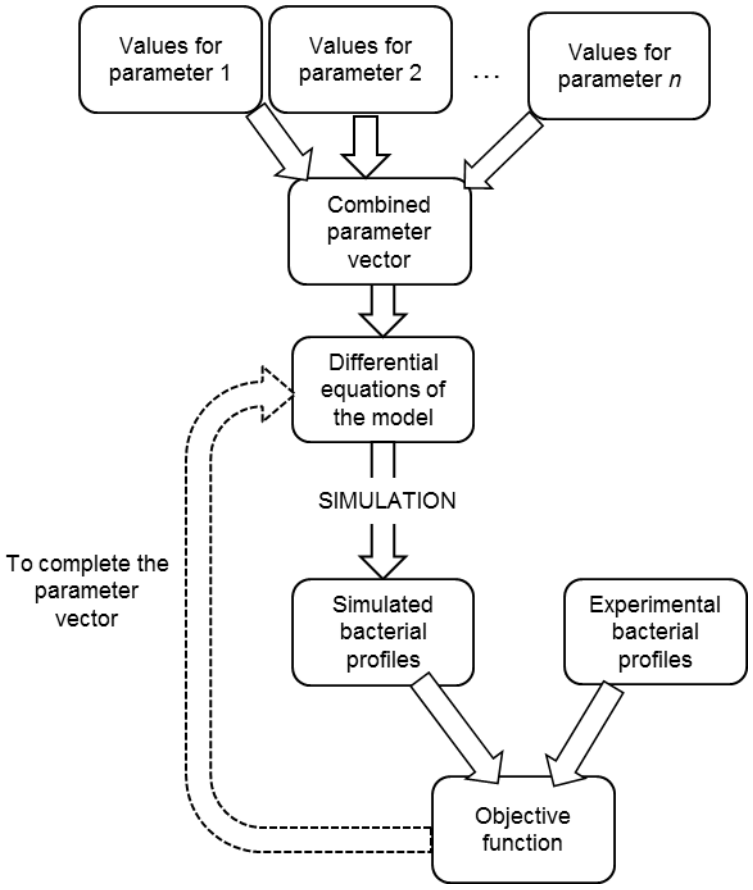

Figure 3.21. Sequential search as the first step for determining model parameters.

3.10.2 Monte Carlo

Monte Carlo methods are a broad class of computational algorithms that rely on repeated random sampling to obtain numerical results. The procedure of Monte Carlo search used in this work is shown in Figure 3.22. Firstly, intervals of parameters searching are defined with values determined by the 'sequential search'. Then, a vector of random values in the defined intervals is generated and it was introduced in the model to solve the differential equation. Simulated and experimental data are compared and the objective function is finally calculated. To speed up the search process, each run of the MATLAB® program define a big number of iterations (50 – 100) testing a matrix of random parameters instead of a vector. The procedure was repeated but using new parameter intervals for each run as function of the best set of parameters obtained, i.e. those that achieve the minimum NRMSLE. This step was considered concluded when the NRMSLE obtained was lower than 10 %.

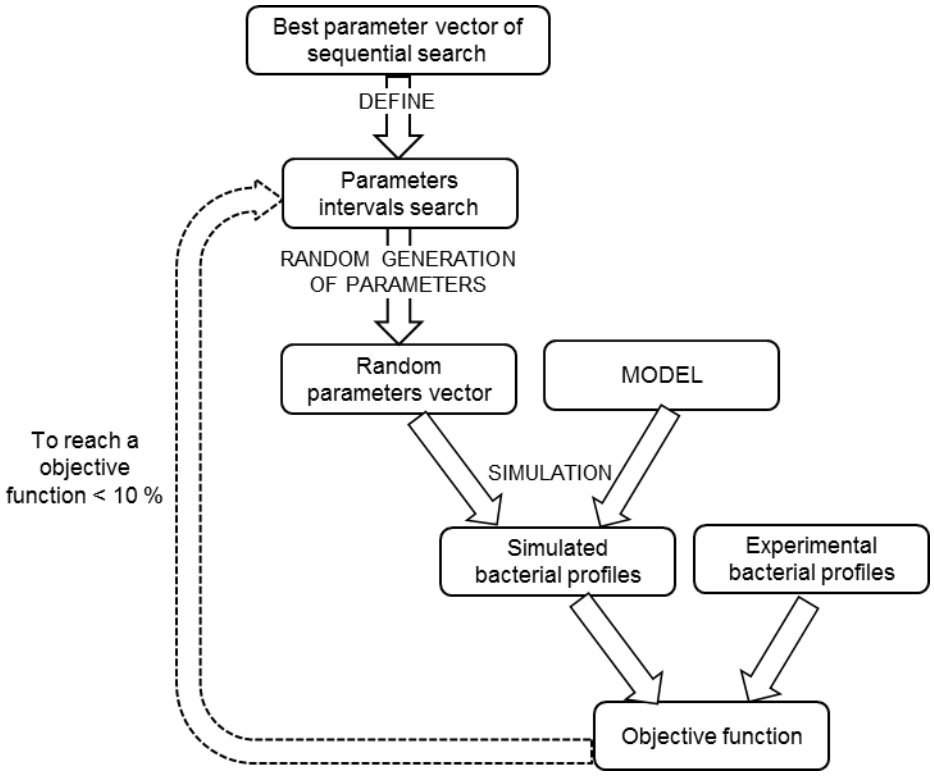

Figure 3.22. Monte Carlo search as the second stage for determining model parameters.

3.10.3 Optimization

The last step was the use of the 'Optimization toolbox' of the MATLAB® software. The objective function was a smooth nonlinear type with bounds constraints so the solver selected was '*fmincon*' (find minimum of constrained nonlinear multivariable function). This solver finds the minimum of a problem specified by:

$$\min_x f(x) \text{ such that} \begin{cases} c(x) \le 0 \\ ceq(x) = 0 \\ A \cdot x \le b \\ Aeq \cdot x = beq \\ lb \le x \le ub \end{cases} \tag{3.6}$$

where *lb* (lower bound) and *ub* (upper bound) are the restrictions in this problem and it could be a vector or a matrix.

The regression of the model was solved by the interior-point algorithm that was presented for the first time by Karmarkar in 1984. The main ideas of this algorithm are to obtain a feasible solution in the interior of the feasible region and move in the direction that minimizes the objective function as fast as possible. The algorithm is changing the feasible region of the solution each iteration to place the solution of the previous iteration in the centre of the region.

CHAPTER 4

INTRACELLULAR REACTIVE OXYGEN SPECIES DETECTION

4 INTRACELLULAR REACTIVE OXYGEN SPECIES DETECTION

In this chapter, the steps followed to detect intracellular ROS in *E. coli* cells after their exposure to solar radiation are explained. Firstly, a protocol to detect oxidative stress generated by ROS in *E. coli* cells using DCFH-DA as fluorescent probe has been developed. Several aspects related to the use of this probe such as its chemical stability under solar radiation, hydrolysis, suitable concentration and reaction time to favour optimal response between probe and bacteria were investigated. As a result, a new protocol for intracellular ROS detection in solar irradiated *E. coli* in water was proposed and validated. This protocol was eventually used to evaluate and detect the photo-induced generation of internal ROS in *E. coli* cells exposed to solar radiation.

4.1 Accepted protocol for intracellular ROS detection

Intracellular ROS detection is a common analysis in other research fields like photodynamic therapy, used for cancer therapy or antimicrobial infections that have provided a number of contributions on oxidative stress determination by ROS. Because of this application, the standardized ROS detection protocols using fluorescent probes are designed to eukaryotic cells. The few works related with the intracellular measurements of ROS in prokaryotic cells have used those protocols directly without any optimization for their purposes [Kramer and Muranyi, 2013; Wang *et al.*, 2014].

The ROS-probe protocol accepted to detect ROS inside eukaryotic cells (Figure 4.1) consists firstly on the addition of the probe to the cellular suspension and then the exposure to the oxidative conditions. Then, after an incubation period at optimum growth temperature, the fluorescent signal is measured by an accurate technique.

It is necessary to analyse some of the steps of the mentioned protocol when it is applied to the detection of ROS formed in *E. coli* cells during the exposure of solar radiation using the DCFH-DA as ROS-probe (Figure 4.1). According to this protocol, DCFH-DA should diffuse easily into cells and it is converted to DCFH by the intracellular and biological esterases action. After that, bacterial cells must be exposed to solar radiation that photo-induces the formation of ROS, which entail that the ROS-probe is also exposed to sunlight. This could be problematic for the stability of the probe that is highly affected by light [Gomes *et al.*, 2005; Dikalov and Harrison, 2012]. For this reason, it is necessary to modify the protocol and optimize it for the specific application of this work.

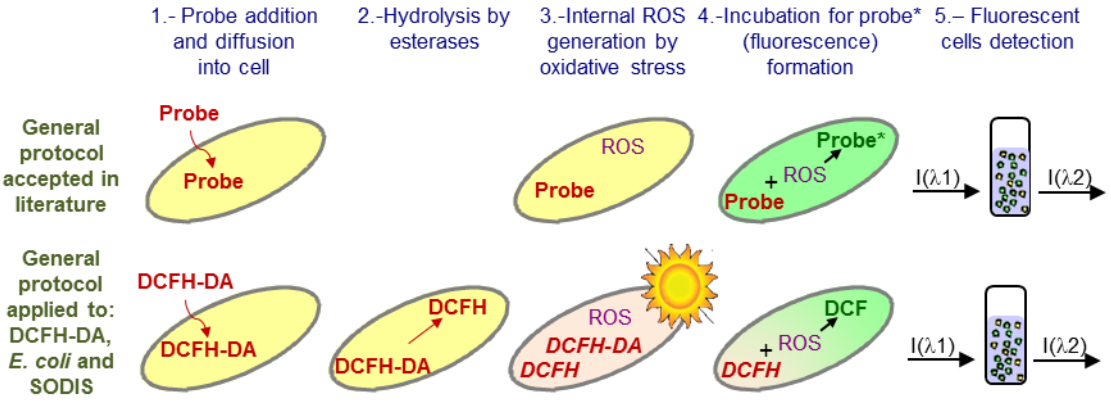

Figure 4.1. General protocol for intracellular ROS detection accepted in the literature and in a specific case, using DCFH-DA as the fluorescent probe to detect ROS formation in *E. coli* cells due to the exposure to solar radiation. Yellow colour indicates unaltered cell, orange indicates solar radiated cell and green indicates fluorescent cell.

4.2 Photo-chemical stability of DCFH-DA

Commonly, DCFH-DA protocols proposed a prior incubation period with cells before to the exposure to the oxidative stress under assessment to assure the conversion of DCFH-DA into DCFH [Cai *et al.*, 2007]. In the case of bacteria exposed to solar radiation, the oxidative stress is produced by continuous income of solar UV photons over bacteria. Initially, exposure of DCFH-DA to solar radiation was considered, and therefore its photo-chemical stability was tested.

A suspension of 50 μM DCFH-DA (without bacteria) was exposed to sunlight in the solar simulator system to a constant irradiance of solar 30 W m^{-2} of UVA. Absorbance spectrum of irradiated DCFH-DA was measured at different times of solar exposure, from 0 to 90 min (Figure 4.2). The absorbance increased in the range of 400 – 500 nm, suggesting the formation of photo-transformation compounds. Similar observation was published previously in cell-free samples containing DCF, DCFH and horseradish peroxidase when irradiated by UVA [Chignell and Sik, 2003]. This can be attributed to the photo-reduction of DCF, involving (DCF)* and $DFC^{\bullet-}$ generation [Dikalov and Harrison, 2012]. The formation of these photo-products could also alter the ROS levels due to the high reactivity of $DFC^{\bullet-}$ with oxygen, generating $O_2^{\bullet-}$ and consequently H_2O_2.

Hence, given the photo-transformation of DCFH-DA under sunlight, its addition to *E. coli* should be done only after solar exposure of bacteria in water. Although some researchers used the probe prior to cellular oxidative stress [Herrera *et al.* 2002, Karlsson *et al.* 2010] to incubate together and assure the probe diffusion into cells, alternatively the probe might be used after stress if ROS generation is an UV photo-induced process, as reported for cyanobacterium *Anabaena* sp. under UVB [He and Häder 2002, Rastogi *et al.* 2010].

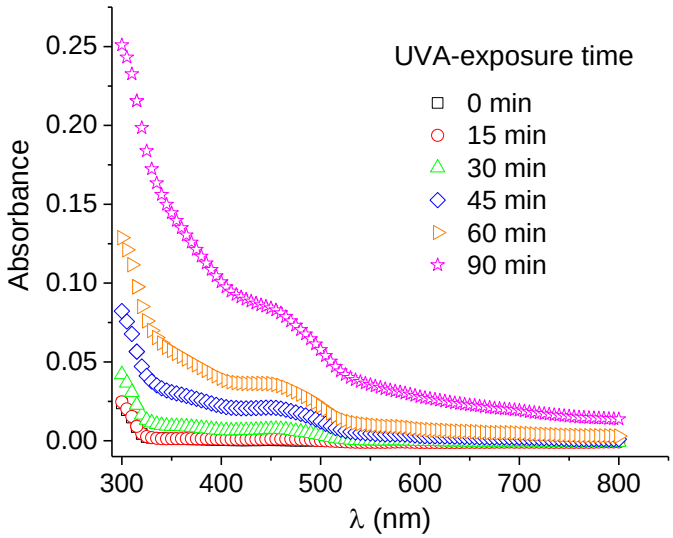

Figure 4.2. Absorbance spectrum of a 50 µM DCFH-DA solution at 0, 15, 30, 45, 60 and 90 min of simulated solar radiation (30 W m^{-2} UVA).

4.3 Hydrolysis of DCFH-DA

The proposal of adding the probe after solar radiation lead to a modification of the protocol as is shown in Figure 4.3, by the performance of the hydrolysis step after the solar exposure. However, under irradiation, it is expected that many intracellular molecules are modified or even inactivated [McGuigan *et al.*, 2012; Abdelsalam *et al.*, 2014; Baliza *et al.*, 2012]. It is also assumed that esterase may be altered by solar radiation, and therefore it may be working with lower efficiency than in unaltered cells. Therefore, solar irradiated cells could be affected at esterase level, so that proper hydrolysis of DCFH-DA is not optimal.

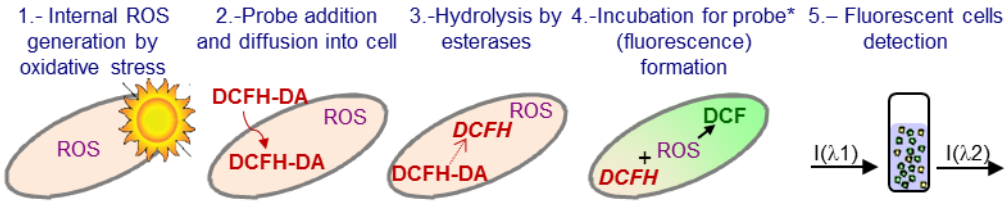

Figure 4.3. Modification of the accepted protocol for oxidative stress detection by the addition of the probe after ROS generation. Orange colour indicates radiated cell and green indicates fluorescent cell.

To avoid the uncertain state of the probe and consequently its reaction with intracellular ROS, an alternative chemical hydrolysis procedure is proposed to load the cells with DCFH instead of DCFH-DA. The advantage of pre-hydrolysis is not only to avoid potential esterases degradation, but also to permit ROS reaction with hydrolysed DCFH-DA immediately after added to bacteria, avoiding longer periods of intracellular reactions.

Hydrolysis of DCFH-DA was done adding 0.01 N of NaOH to 50 µM of DCFH-DA and incubated 30 minutes in dark. Then, the probe was neutralized with PBS 0.1 M to obtain the hydrolysed form, DCFH [Foucaud *et al.*, 2010].

4.3.1 DCFH-H_2O_2 reaction: H_2O_2 concentration dependence

The capability of the chemically hydrolysed DCFH as an indicator of ROS concentration was tested using H_2O_2 as a positive control of ROS. H_2O_2 was chosen due to its capability to react with DCFH and to penetrate easily into bacteria cells. Furthermore, H_2O_2 is commonly accepted as one of the ROS that are generated inside bacteria under light stress [Giannakis *et al*. 2016].

Reaction between 10 µM DCFH and H_2O_2 (0.01 to 1 mM) was done in the absence of bacteria in the dark. The H_2O_2 concentrations were selected to ensure good measurements of absorbance and fluorescent signals, and to check if the hydrolysed probe was reactive to H_2O_2. Further experimental work will optimize DCFH concentration to measure ROS at intracellular levels in *E. coli*.

Figure 4.4 shows that DCF formation is H_2O_2-concentration dependent; the higher H_2O_2 concentration, the higher DCF concentration was observed for both, absorbance and fluorescence peak values. This confirms that the chemical hydrolysis of DCFH-DA can be used to remove the diacetate groups of the probe avoiding the action of esterases. In addition, DCFH is demonstrated to be a good indicator of H_2O_2 concentration.

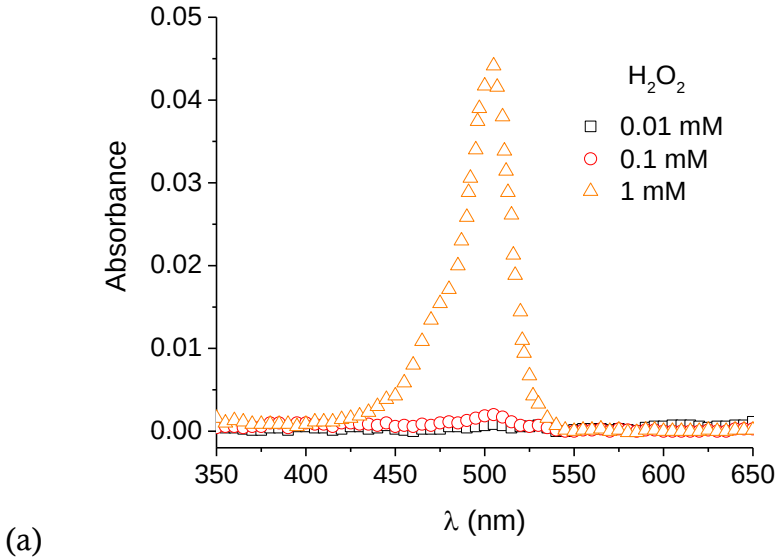

(a)

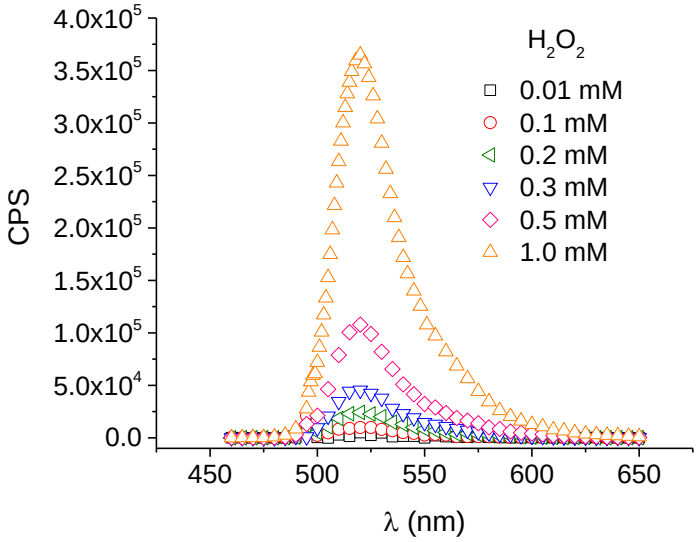

(b)

Figure 4.4. (a) Absorbance spectrum and (b) fluorescence emission signal of the formed DCF product from the reaction between DCFH (10 μM) and H_2O_2.

4.3.2 DCFH-H_2O_2 reaction: DCFH concentration dependence

In order to determine the saturation concentration of DCFH for a certain amount of H_2O_2, and to avoid DCFH overload which may give undesired fluorescence background signal, several reactions of DCFH and H_2O_2 at variable concentrations of both, were carried out in absence of bacteria and measured with the fluorimeter. Concentrations of DCFH tested were 1, 5, 10, 15, and 20 μM and the concentrations of H_2O_2 were 0.01, 0.1, 0.2, 0.3, 0.5 and 1 mM. At view of first results, 1, 15 and 20 μM-DCFH were discarded, as the signal was too low for 1 μM, while it was unstable at 15 and 20 μM, probably caused by the effect of ambient light and oxygen. Therefore, 5 and 10 μM were selected and two replicates of reactions at 5 and 10 μM of DCFH with all concentrations of H_2O_2 were done, and resulted highly reproducible (confidence level > 99 %). Average values of the maximum signal of fluorescence emitted by the samples are shown in Figure 4.5.

At low H_2O_2 concentrations, the fluorescence signal for both, 5 and 10 μM of DCFH, led to very similar values, while at higher H_2O_2 concentrations (> 0.3 mM) 10 μM of DCFH showed higher values than 5 μM, being 10 μM more precise to detect differences in fluorescence measurements. Due to the stability of the measurements at all H_2O_2 concentrations tested, both DCFH concentrations (5 and 10 μM) could be a good option to determine the internal ROS in *E. coli*. In this work, 10 μM of DCFH was selected for further experiments to detect fluorescence signal caused by intracellular generated ROS in solar exposed *E. coli*.

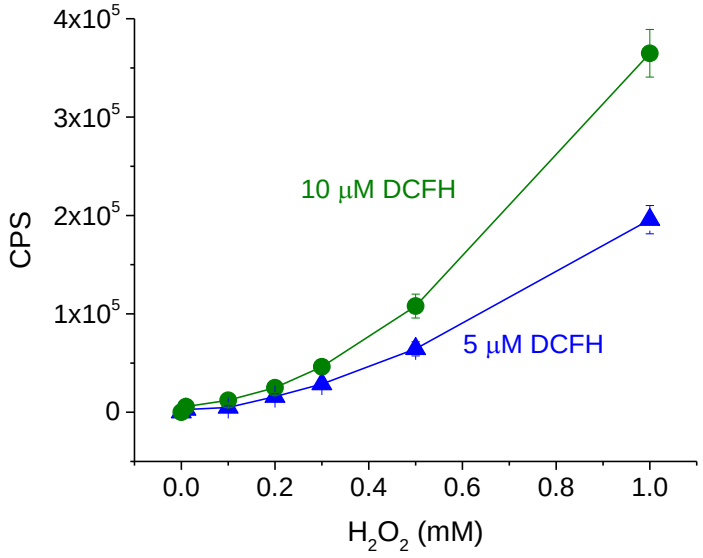

Figure 4.5. Maximum fluorescence emission signal of DCF product formed from the reaction between 5 and 10 μM (chemically hydrolysed) DCFH with H_2O_2 (0.01, 0.1, 0.2, 0.3, 0.5, and 1 mM).

Although, *E. coli* intracellular ROS values are expected to be very low as compared to this previous calibration; for instance 0.01 μM H_2O_2 intracellular concentration was reported [Imlay, 2008], it is more accurate to work in excess of DCFH by the following reasons: i) DCFH is expected to react with not only H_2O_2 but with all ROS generated after the stress-generating process, and ii) the addition of the DCFH is done to samples with a high bacterial concentration (10^6 CFU mL^{-1}) and not for a single cell.

4.4 DCFH - *E. coli* incubation

According to the literature, *E. coli* cells incubation time at 37 ºC in presence of DCFH-DA should range between 30 and 60 minutes, to permit the probe diffusion inside cells and the hydrolysis by endogenous esterase [Kramer and Muranyi, 2013; Wang *et al.*, 2014]. Nevertheless, these incubation times for samples containing solar irradiated *E. coli* may lead to modifications of physiological state of the cells, including ROS levels, due to metabolic activities during the incubation period. Therefore, a large incubation period could lead to

false-positive or higher signal detection by an increment of ROS concentration that does not represent the real state of the cells under evaluation. In this sense, the proposal of using the chemical hydrolysed DCFH-DA (in form of DCFH) permits decreasing incubation times with bacteria, since esterase internal step is skipped.

With the aim of determine if shorter periods are adequate for incubation of DCFH and *E. coli*, preliminary experiments were done using unaltered *E. coli* suspensions and a fluorescence microscope, for direct counting of fluorescent bacteria. This will also give an idea of the baseline fluorescence signal of non-altered bacteria and its stability over time.

High concentration of *E. coli* was used to permit the cell observation with the fluorescence microscope. 10^9 CFU mL^{-1} of *E. coli* were incubated in the dark with 10 μM of DCFH at 37 ºC for different times, 5, 15, 30, and 60 min and the samples were observed and counted using the fluorescence microscope. It was observed that all cells are dyed for all incubation times (5 to 60 min), as it is shown in the microscope view (Figure 4.6 (a)). Cell counting was done immediately after the tested incubation times; additionally each sample was re-numbered at different post-incubation times to confirm the stability of the measurements (Figure 4.6 (b)). Immediately after the incubation (time 0 in Figure 4.6 (b)), the cell counting resulted in the same concentration of fluorescent bacteria, 10^9 CFU mL^{-1}, which was the expected initial concentration of alive bacteria in the suspension. These results confirm that diffusion of DCFH inside bacteria and further reaction with intracellular ROS is very fast, for 5 and 15 min incubation, and it does not change over time (up to 60 min incubation). Nevertheless, longer incubation periods, 30 and 60 min, generated an increment in the number of counted florescent cells over post incubation time. This confirms the hypothesis that longer incubation times could lead to modifications in cells states (like changes of the bacterial state due to the cellular cycle) and in intracellular ROS levels (like possible accumulative fluorescence by probe reaction with new ROS generated during the aerobic metabolism).

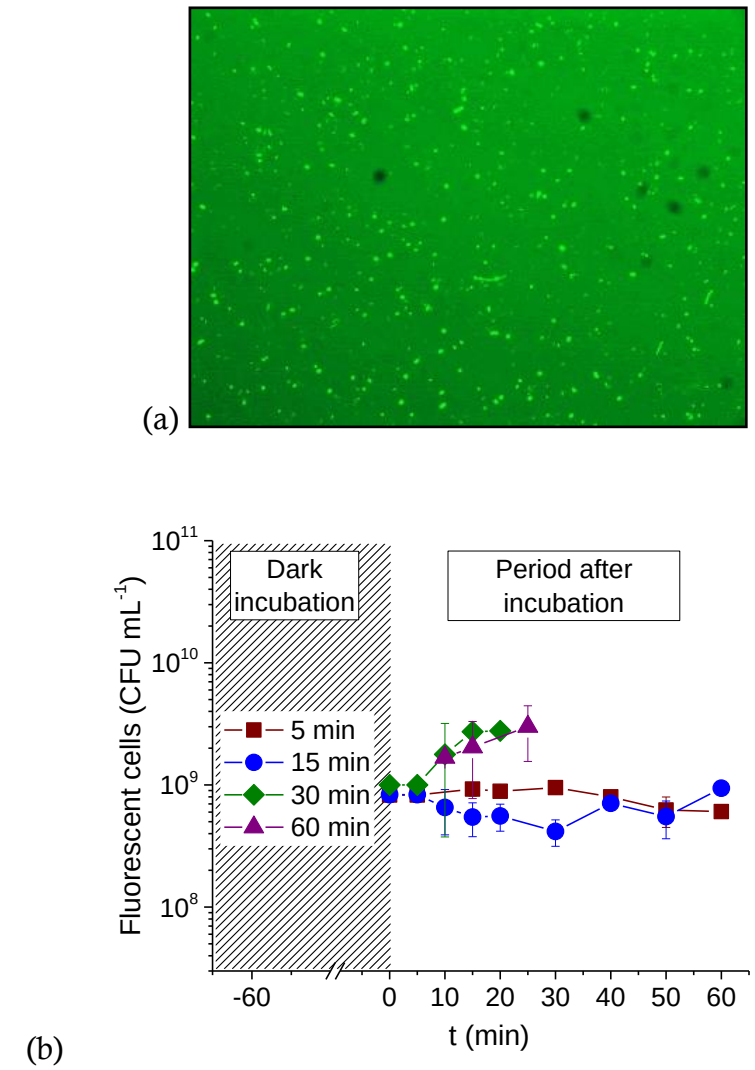

Figure 4.6. Unaltered *E. coli* sample loaded with 10 μM DCFH and incubated at 37 °C in the dark: (a) 40x fluorescence microscope photograph of 15 min of incubation; (b) fluorescent *E coli* cells counts incubated for 5, 15, 30, and 60 min over a post incubation period (0 – 60 min).

An incubation time between 5 and 15 min was found ideal for this protocol, because it gives a stable measurement over time of unmodified ROS. For this work, it was selected 15 min of incubation, which avoids long incubation periods and guarantee stable fluorescent measurement by successful DCFH diffusion and ROS-reaction inside cells.

4.5 Proposed protocol for intracellular ROS detection

Several aspects of the protocol to detect the intracellular ROS formed during the exposure of cells to solar radiation were investigated. Finally, a protocol was proposed and it is summarized in Figure 4.7. It consists on:

1. Hydrolysis of DCFH-DA: the probe is used in the hydrolysed form (DCFH) that is obtained from the reaction of DCFH-DA with NaOH removing the diacetate groups of the probe molecule. This step avoids the natural hydrolysis by the cellular esterases that could be altered by solar light.

2. Bacterial load with DCFH: immediately after the chemical hydrolysis, DCFH is added to the cellular suspension under assessment. In the case of the evaluation of ROS formed by the induction of solar radiation, the addition of the probe has to be done necessarily after the cellular irradiation to avoid the formation of photo-products that could interfere in the fluorescence detection.

3. Incubation: after the addition of the probe to cells, they are incubated 15 min at 37 ºC. This incubation time has demonstrated to be enough to permit the reaction between the probe and the intracellular ROS. In addition, set a period of time between the cellular load and the fluorescent measurement permits to standardize the detection and to obtain all the samples in the same conditions.

4. ROS detection: the measurement of intracellular ROS is done by the detection of the fluorescent emission of the DCF product that is formed from the reaction between DCFH and the internal ROS. Flow cytometry method was selected for the fluorescence detection. It is a sensitive technique that amplifies the fluorescence signal so it is able to detect slight differences on ROS levels, unlike others techniques as the fluorescence microscopy. In addition, the equipment is specifically designed for cellular analysis. In this sense, other equipment as the fluorimeter presents problems with the noise-

signal due to the light scattering generated by cells that act as particles in suspension.

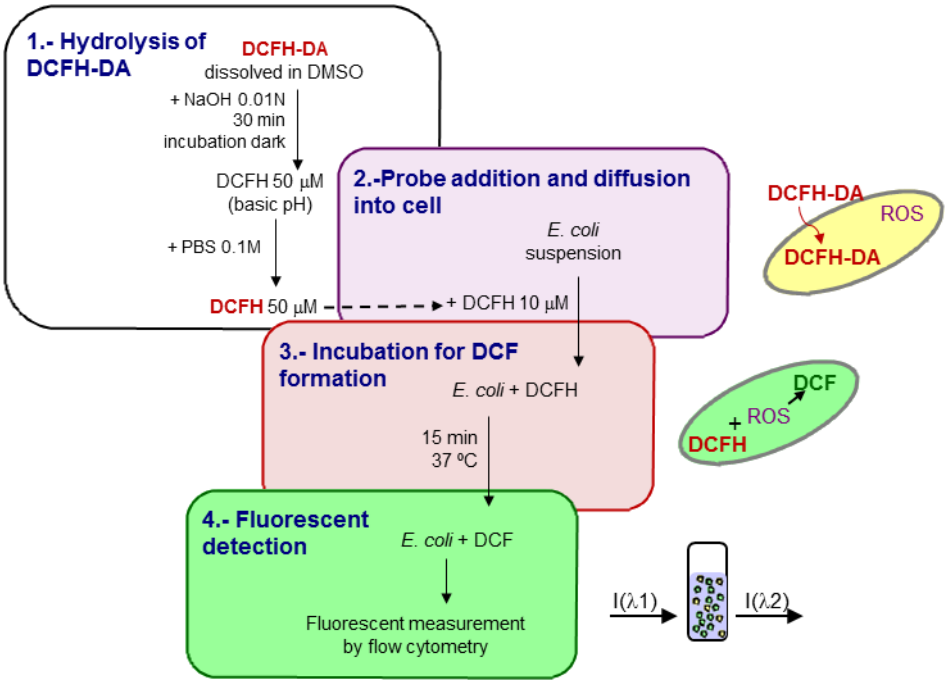

Figure 4.7. General scheme of the proposed protocol for ROS detection in *E. coli* cells exposed to natural sunlight using DCFH-DA previously hydrolysed.

4.6 Flow cytometry method

In order to check the bacterial protocol loaded with the probe DCFH some previous analysis were done: negative control, blank and positive controls with unaltered *E. coli* cells. Data analysis provided by the flow cytometer was reported in Figure 4.8. In the figure, it is shown the distribution of cells due to the scattering (forward and side) and the fluorescence intensity that is represented in the histograms in terms of FITC-A.

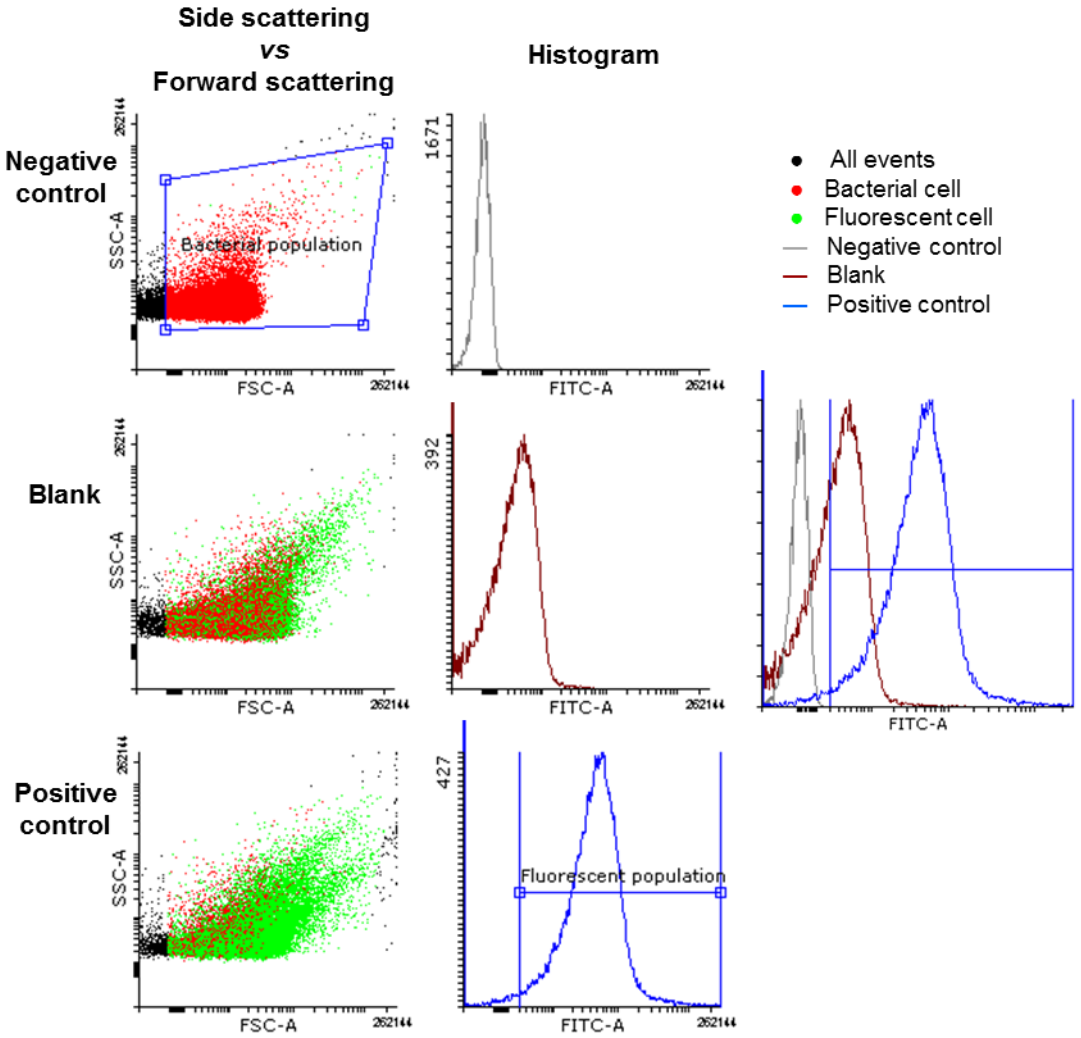

Figure 4.8. Flow cytometry analysis of negative control (cells), blank (cells with probe) and positive control (cells with H_2O_2 and probe).

The negative control consisted in an unaltered *E. coli* suspension sample of 10^6 CFU mL^{-1} without any probe. The equipment provided data of the scattering of all the events detected by the sensors (black points in Figure 4.8). It was selected the region of the graph considered as the bacterial population (red in Figure 4.8), discarding the extreme points. Hereinafter, the measurements were set on 50 000 events or bacterial cells passing through the equipment.

The blank sample consisted in the bacterial suspension loaded with the DCFH and incubated 15 min. It was observed in the histogram that a large number of cells had larger fluorescent intensity than negative control. DCFH may be

provided some background fluorescence signal and also it could react with the natural intracellular ROS generated by the respiratory cellular process. It evidences the necessity of run a blank sample before the measurement of each sample under assessment.

The positive control sample consisted on bacterial suspension cells exposed for 10 minutes in dark to H_2O_2 (0.3 mM) and then loaded with 10 μM DCFH and incubated according to the above protocol. It was observed a displacement of the curve in the histogram due to an increase of the fluorescent intensity emitted cells. This result shows that the H_2O_2 added to bacterial suspension was diffused inside cells and then it reacted with the probe that emits a high fluorescence signal.

4.7 Validation of DCFH protocol using H_2O_2 as positive control

The validation of the protocol proposed (Figure 4.7) was done with bacteria cells exposed to oxidative stress of added H_2O_2. Bacterial suspension cells (10^8 CFU mL^{-1}) were exposed for 10 minutes in dark to several concentrations of H_2O_2 (0, 0.1, 0.5, 0.75, 1, and 1.5 mM). Then, the samples were taken and loaded with 10 μM DCFH, incubated and measured in the flow cytometer according to the above protocol.

Figure 4.9 shows the FITC-A average value of the 50 000 cells reaching detector. The fluorescence intensity increased linearly with added H_2O_2. This result shows that the whole protocol works without any limitation in the flow cytometer, as well as H_2O_2 diffusion into cells was correctly happening. The calibration curve has a good linear response in the range of tested concentrations. In addition, the high resolution of the equipment is clear, as FITC-A values were lower than 100.

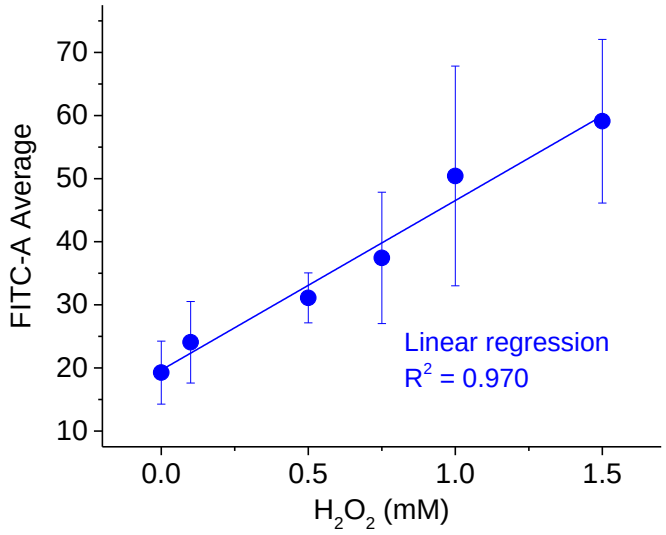

Figure 4.9. Fluorescent signal measured by flow cytometry of *E. coli*-DCFH samples exposed to different concentrations of H_2O_2.

4.8 Bacterial intracellular ROS formation during solar exposure

The aforementioned protocol developed in this work was done with the objective of obtaining experimental evidences about the intracellular ROS formation during the exposure of *E. coli* cells to solar radiation. In line with this aim, specific solar water disinfection experiments were performed within isotonic water in 200 mL-batch reactors under natural sunlight, where each water sample was simultaneously evaluated for viable *E. coli* counts (by standard plate counting method) and ROS determination (by flow cytometry). Correlated results from both techniques are shown in Figure 4.10. According to counting method results, *E. coli* concentration as a function of solar exposure time showed the typical SODIS inactivation curve [Sichel *et al.*, 2007a; Ubomba-Jaswa *et al.*, 2009a], with a small shoulder for the first 30 min followed by a close to linear decay until reaching the detection limit (not counted colonies) at 180 min. The well-known physical parameters that may affect the bacteria viability during solar exposure like temperature and solar radiation were also monitored. Water temperature varied from 20 to 27 °C along the experiment so thermal effects were discarded as factor of stress over bacteria. Solar UVA irradiance measured

with the portable UVA radiometer, increased from 12.7 W m^{-2} (t = 0 min) to 36.1 W m^{-2} (t = 155 min), and then remained almost constant up to the end of the experiment. Samples were taken every 30 min over 4 hours (four replicates).

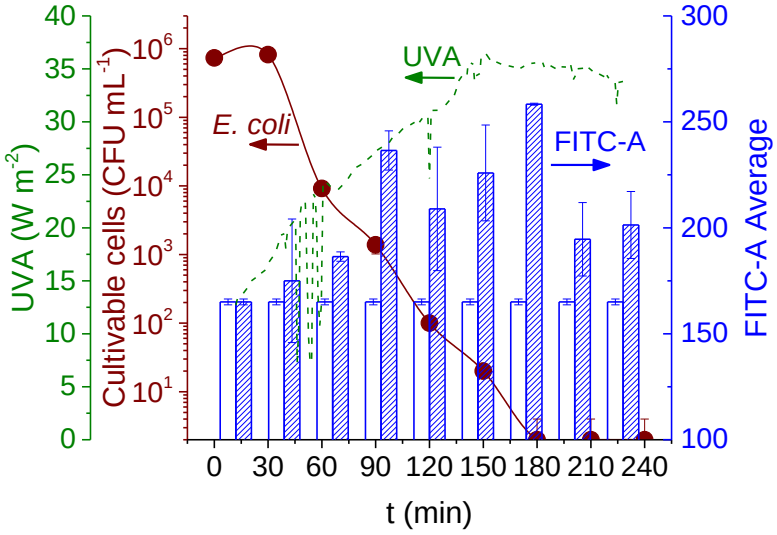

Figure 4.10. Solar water disinfection under natural sunlight within isotonic water in 200 mL-batch reactor. Inactivation curve of *E. coli* (-●-), UVA irradiance (---), normalized FITC-A (▨) and reference FITC-A value for control samples (▭).

On other hand, each flow cytometric measurement of the irradiated bacterial samples (Figure 4.10) was done against one control sample containing bacteria not exposed to solar radiation and treated with the same DCFH-DA protocol (blank sample). This was used as a reference of ROS baseline against solar induced ROS measurements in irradiated samples. Baseline fluctuation of blank samples' FITC-A was used as a reference to normalize the signal of irradiated cells; results of normalized FITC-A are shown in Figure 4.10. A significant increase in FITC-A for samples exposed to times longer than 60 min of solar radiation was observed; after 60 min the higher level of FITC-A remained nearly constant until the end of the experiment. It was expected to observe a constant increase of the fluorescence signal with the exposure time; however, experimental results showed fluctuations in the fluorescence signal among the samples, and especially high at the sample time 90 and 180 min. There is not knowledge about physiological and/or biological aspect of the bacteria on these

specific points, which may help to explain this high fluorescence signal. In addition, the fact of no constant increment of fluorescence signal with the time avoids establishing a quantitative and direct correlation between viable cell count and ROS fluorescence signal.

At view of the results obtained, it can be concluded that an uncertain level of solar induced-ROS is produced after a certain time period of solar exposure. It is also important to note that the addition of the probe after the irradiation makes it to react with stable ROS mainly, so that the signal attributed to less stable ROS could be missing in this protocol, such as $O_2^{\bullet-}$, $HO^{\bullet}$ or $ROO^{\bullet}$. Therefore, the increment on fluorescence signal could be attributed to the most stable ROS, like H_2O_2, formed during solar exposure at intracellular level, which was detected using the new DCFH protocol proposed in this work.

The results of this work show for the first time an experimental evidence of the accumulation of intracellular stable ROS in *E. coli* during solar irradiation. This is clear evidence that oxidative stress increase during the action of natural solar radiation. Previous reported studies on the bactericidal mechanism of SODIS showed indirect evidence that ROS are the main cause of bacterial inactivation, while the present contribution reports on new evidence of ROS generation over the basal levels.

Molecular techniques for investigating intracellular mechanisms of SODIS have been explored mostly from the genetic point of view. These studies demonstrated that DNA damages can modify ROS and SOS responses in bacteria. Some contributions use mutagenicity and genetic approaches to identify UVA radiation effects on bacteria cells. Webb and Brown demonstrated that irradiation with either broad-spectrum UVA or monochromatic wavelengths in the UVA can cause specific damages to DNA in *E. coli* K-12 AB2480 [Webb and Brown, 1982]. Eisenstark studied the DNA mutations due to UVA in *E. coli*. They assessed an experimental correlation between intracellular ROS and UVA and concluded that hydrogen peroxide resulted to be generated by the irradiation of tryptophan with UVA, providing at least one pathway for generation of ROS

by UVA [McCormick *et al.*, 1976]. In addition, specific UV-mutations observed were responsible for the increase in the flux of $HO^{\bullet}$ radicals [Hoerter *et al.*, 1989] and $O_2^{\bullet -}$ action [Knowles and Eisenstark, 1994]. Moreover, UVA radiation was proven to block SOS responses to DNA damages in *E. coli* that could result in cells inactivation [Turner and Eisenstark, 1984].

The generation of intracellular ROS is promoted by the absorption of light of endogenous chromophores. In this sense, experiments with mutants *E. coli katF* gene (hydroperoxidase II) suggested that porphyrin components of the respiratory chain may act as endogenous photosensitisers [Tuveson and Sammartano, 1986]. Also, it was found that cytochrome overproducing strains (cloned *cydA* and *cydB* genes) were sensitive to broad-band UVA radiation [Sammartano and Tuveson, 1987]. Berney and co-workers investigated the effect of artificial sunlight on *E. coli* using flow cytometry and viability stains to monitor six cellular functions: efflux pump activity, membrane potential, membrane integrity, glucose uptake activity, total ATP concentration and culturability. They observed at different solar flux values that efflux pump activity and ATP synthesis decreased significantly, the loss of membrane potential, glucose uptake activity and culturability, and the cytoplasmic membrane of bacterial cells became permeable [Berney *et al.*, 2006a].

Oxygen has been also investigated since early as one of the key factors affecting SODIS process, since it is the inducer of ROS generation and oxidative stress in aerobic bacteria under UVA or sunlight [Webb and Brown, 1979]. Oxygen has been identified as a requirement for efficient inactivation of faecal bacteria under sunlight showing that efficiency of *Enterococcus faecalis* inactivation was faster in air-equilibrated water than in anaerobic conditions [Reed, 1997]; even more, the extent of inactivation during illumination was directly related to the dissolved oxygen content of the water [Khaengraeng and Reed, 2005]. Beyond this, Mani *et al.* investigated *E. coli* disinfection by SODIS process using plate count method under aerobic conditions and ROS-neutralized ambient with sodium pyruvate supplemented medium. Cultivable population from ROS-neutralized

conditions was slightly higher than those in air [Mani *et al.*, 2006]. This result indicated that a fraction of the cells become sub-lethally injured during sunlight exposure since they were unable to grow aerobically.

As mentioned before, genetic studies strongly suggested the photo-generation of ROS in bacteria exposed to NUV, and therefore to sunlight. According to Imlay, ROS are continuously formed in *E. coli* through the adventitious autoxidation of its redox enzymes; their accumulation is controlled by superoxide dismutases, peroxidases and catalases [Imlay, 2015]. Under not stressed environment, the balance of these ROS is in equilibrium so bacteria are viable and stable. Superoxide dismutase avoids the accumulation of $O_2^{\bullet-}$ in bacteria converting it to H_2O_2 that is then removed by catalase. UVA radiation has a detrimental effect to these enzymes [Idil *et al.*, 2013], thus permitting higher accumulation of $O_2^{\bullet-}$ [Chen and Schopfer, 1999]. Microorganisms are vulnerable to elevated levels of intracellular ROS and it is considered one of the main pathways of bacterial inactivation during solar exposure.

4.9 Conclusions of chapter 4

The general protocol reported in literature for the detection of the intracellular ROS was demonstrated to be not suitable to be applied for the purpose of solar irradiated bacteria cells due to the photo-sensitivity of the probe DCFH-DA. A new protocol for intracellular ROS detection in solar irradiated *E. coli* in water was proposed in this chapter. The most significant novelty of this new protocol is the use of hydrolysed DCFH-DA prior to contact with the bacteria and the set an incubation time of 15 min at 37 ºC. The results shown in this chapter clearly demonstrated that the proposed protocol permits the diffusion of the probes into the cells and the detection of intracellular ROS in *E. coli*.

The new method was validated using flow cytometry and H_2O_2 as positive control for generation of intracellular ROS in *E. coli*. It was observed a linear correlation between the H_2O_2 added to the bacterial suspension and the

fluorescent cells showing the accuracy of the methodology proposed to ROS detection in *E. coli*.

It can be highlighted that this modified protocol for intracellular ROS detection proposed and validated for *E. coli* may be used for other bacteria, to investigate the influence of other stress factors, with the advantage of having a fast response and a high capability of detecting low levels of ROS, due to the fast reactivity of the hydrolysed probe and the high sensitivity of flow cytometry, respectively.

Finally, the proposed protocol was used for the first time for detecting an excess of intracellular ROS generated during solar water disinfection in *E. coli* regarding to the basal levels of ROS. After 60 min of sunlight exposure, a significant increase in the fluorescence signal was observed. Therefore, it was demonstrated the intracellular ROS photo-generation in *E. coli* due to the sunlight exposure.

CHAPTER 5

MECHANISTIC MODEL OF SOLAR WATER DISINFECTION: EFFECT OF SOLAR UVA

5 MECHANISTIC MODEL OF SOLAR WATER DISINFECTION: EFFECT OF SOLAR UVA

In this chapter, a kinetic modelling approach of the SODIS process is presented. The model attempts to describe the mechanisms by which the Gram negative bacteria *E. coli* presented in water are inactivated when exposed to sunlight in a reasonably simplified way. The model considers that bacterial inactivation is mainly due to the oxidative stress of ROS generated under sunlight inside cells. It takes into account the intracellular reactions of generated ROS and the photo-inactivation of catalase (CAT) and superoxide dismutase (SOD) due to UVA range as part of the complex disinfection mechanisms of SODIS. The kinetics of CAT photo-inactivation under solar radiation was experimentally determined. The values for the rest of the model parameters considered in this work were estimated using experimental data of bacterial concentration in clear water obtained during solar disinfection experiments performed under controlled conditions of solar irradiance and temperature. This model is capable to describe the time profile of the species involved in the process, including the intracellular ROS and enzymes, and the concentration of bacteria in water as well.

5.1 Light parameters calculation

The bacterial inactivation due to solar water disinfection is commonly attributed to the UV range. Although UVB can cause DNA damages resulting from the direct absorption of light, it is not considered the main lethal agent for microorganisms in SODIS due to the low percentage of UVB that reaches Earth's surface (around 3 % of UV range) [Sinha and Häder, 2002]. Therefore, the range of the solar spectrum that is expected to be most harmful to the bacterial viability is the UVA. The estimation of the light parameters needed to develop the mechanistic model of bacterial inactivation by SODIS was done as an approximation using the averaged value in the UVA range (320 – 400 nm).

The reactor chosen to run the experiments was an open vessel with a diameter big enough to consider a one-dimensional light transport. The reactor used was the 700 mL-batch reactor, described in chapter 3. Considering the low optical density of the system and the geometrical characteristics of the photo-reactor and the solar simulator lamp, the local volumetric rate of photon absorption (LVRPA, e^a) can be considered constant in the entire photo-reactor. Assuming that optical properties of bacteria are constant during the process, LVRPA can be also considered constant over time. It is considered that sunlight is absorbed by some intracellular endogenous species in the reactor; as it is explained below, CAT, SOD and NADH are the species considered in the model. e^a values for each compound i can be estimated using the equation (1.50). The solution of that equation was done as an approximation using the averaged values of the light parameters (i.e. $\kappa_{i,\lambda}$ and G_λ) in the UVA ($\overline{\kappa}_i$ and $\overline{G}$). $\overline{\kappa}_i$ was determined as the product of the specific absorption coefficient averaged in the UVA range $\overline{\kappa}_i^*$, and the concentration of the compound i, $[i]$:

$$\overline{\kappa}_i = \overline{\kappa}_i^* \cdot [i] \tag{5.1}$$

The averaged incident radiation $\overline{G}$ (Einstein s^{-1} m^{-2}), could be estimated from the incident radiation in UVA range set in the solar lamp I_{UVA}, in terms of W m^{-2}, the

photon energy averaged in the UVA range $\overline{E_p}$ (J photon^{-1}) and the Avogadro number N_A (photon Einstein^{-1}):

$$\overline{G} = \frac{I_{\mathrm{UVA}}}{\overline{E_p} \cdot N_A} \tag{5.2}$$

5.2 Catalase solar photo-inactivation

5.2.1 Catalase activity: definition of parameters

Catalase activity is measured by following the reaction rate of H_2O_2 decomposition. Although the exact mechanism of catalase-accelerated H_2O_2 decomposition remains unclear, it is known that its kinetic is not Michaelis-Menten. One of the most accepted mechanisms is the proposed by Tao *et al.* [Tao *et al.*, 2009]:

$$E + \mathrm{H_2O_2} \xrightarrow{k_i} I + \mathrm{H_2O} \tag{5.3}$$

$$\mathrm{H_2O_2} + I \xrightarrow{k_{ii}} E + \mathrm{H_2O} + \mathrm{O_2} \tag{5.4}$$

where E is the initial catalase state and I the intermediate compound formed. At steady state, the rates of the two steps are equal, $k_i[E][\mathrm{H_2O_2}] = k_{ii}[I][\mathrm{H_2O_2}]$. Taking into account that the total concentration of catalase $[E_0]$ remains constant, i.e., $[E_0] = [E] + [I]$, the previous expression leads to $[E] = \frac{k_{ii}}{k_i + k_{ii}}[E_0]$.

Then, the reaction rate of H_2O_2 decomposition R, becomes:

$$\begin{aligned} R = \frac{\mathrm{d}[\mathrm{H_2O_2}]}{\mathrm{d}t} &= -k_i[E][\mathrm{H_2O_2}] - k_{ii}[I][\mathrm{H_2O_2}] = -2k_i[E][\mathrm{H_2O_2}] \\ &= -\frac{2k_i k_{ii}}{k_i + k_{ii}}[E_0][\mathrm{H_2O_2}] = -k[E_0][\mathrm{H_2O_2}] = k^*[\mathrm{H_2O_2}] \end{aligned} \tag{5.5}$$

where k is the apparent kinetic constant of the overall reaction and k^* is the specific apparent kinetic constant.

For a better understanding of the catalase activity measurement, it is necessary to define some parameters:

- Catalase activity is measured by *units* (U) that is defined as the number of μmol of H_2O_2 decompound by the own catalase under assessment in one minute (μmol min^{-1}).
- The reaction rate of H_2O_2 decomposition R, is also known as the catalase specific volumetric activity A_v, that is measured in terms of activity *units* per litre (U L^{-1}), which are equivalent to reaction rate units (μM min^{-1}). This parameter could be determined by equation (5.5). The value of R (or A_v) increases at higher values of catalase and H_2O_2 concentration ($R = -k\,[E_0]\,[H_2O_2]$).
- The specific mass activity of catalase A_m, is measured in terms of activity *units* per mass unit (U mg^{-1}). The value of A_m is function of the H_2O_2 concentration used in the measurement while it is independent of catalase concentration used.
- The apparent kinetic constant of the reaction k, is measured in terms of $M^{-1}\,s^{-1}$. k is an intrinsic value of the reaction, so it is independent of the concentrations of H_2O_2 or catalase used in the measurement.
- The specific apparent kinetic constant of the reaction k^*, is measured in terms of s^{-1} ($k^* = k\,[E_0]$). The value of the k^* is a function of the catalase concentration.

5.2.2 Estimation of active catalase concentration

Several catalase activity measurements were performed in order to determine the optimal concentration of both species for the protocol used in this work. H_2O_2 concentration ranged from 10 to 100 mM and CAT from 5 to 70 mg L^{-1} (all experiments are listed in Table 5.1). Absorbance curves obtained in all cases were similar to those shown in Figure 5.1, which represents the absorbance measured for 50 mM of H_2O_2 at different concentrations of CAT. At the beginning of the reaction, it was observed a rapid decay in the absorbance that

indicates the disappearance of H_2O_2. Then, the absorbance remained constant or even increased slightly due to the formation of O_2 bubbles that interfered the measurements. The obtained kinetic constant are summarized in Table 5.1. The averaged values were $k = (2 \pm 1) \cdot 10^5$ M^{-1} s^{-1} and $k^* = (2 \pm 1) \cdot 10^{-2}$ s^{-1} that is concordance with previously reported kinetics values [Seaver and Imlay, 2001a].

Table 5.1. Parameters of the decomposition reaction of H_2O_2 catalysed by CAT: concentrations, slope of regression A_{240nm} *vs* t, A_v, A_m, k and k^*.

CAT (mg L^{-1})	H_2O_2 (mM)	Slope (min^{-1})	A_v (μM min^{-1})	A_m (U mg^{-1})	k (M^{-1} s^{-1})	k^* (s^{-1})
5	10	0.285	6546	1309	$5.40 \cdot 10^5$	$1.09 \cdot 10^{-2}$
10	10	0.499	11450	1145	$4.72 \cdot 10^5$	$1.91 \cdot 10^{-2}$
30	10	0.975	22362	745	$3.07 \cdot 10^5$	$3.73 \cdot 10^{-2}$
50	10	1.110	25459	509	$2.10 \cdot 10^5$	$4.24 \cdot 10^{-2}$
70	10	1.722	39495	564	$2.33 \cdot 10^5$	$6.58 \cdot 10^{-2}$
5	20	0.288	6612	1322	$2.73 \cdot 10^5$	$5.51 \cdot 10^{-3}$
10	20	0.537	12326	1233	$2.54 \cdot 10^5$	$1.03 \cdot 10^{-2}$
30	20	1.554	35642	1188	$2.45 \cdot 10^5$	$2.97 \cdot 10^{-2}$
50	20	1.320	30275	606	$1.25 \cdot 10^5$	$2.52 \cdot 10^{-2}$
70	20	2.658	60963	871	$1.80 \cdot 10^5$	$5.08 \cdot 10^{-2}$
5	50	0.509	11674	2335	$1.93 \cdot 10^5$	$3.89 \cdot 10^{-3}$
10	50	1.150	26374	2637	$2.18 \cdot 10^5$	$8.79 \cdot 10^{-3}$
30	50	3.393	77821	2594	$2.14 \cdot 10^5$	$2.59 \cdot 10^{-2}$
50	50	4.239	97225	1944	$1.60 \cdot 10^5$	$3.24 \cdot 10^{-2}$
70	50	4.806	110229	1575	$1.30 \cdot 10^5$	$3.67 \cdot 10^{-2}$
5	70	0.512	11750	2350	$1.38 \cdot 10^5$	$2.80 \cdot 10^{-3}$
10	70	1.625	37280	3728	$2.20 \cdot 10^5$	$8.88 \cdot 10^{-3}$
30	70	3.520	80725	2691	$1.59 \cdot 10^5$	$1.92 \cdot 10^{-2}$
50	70	4.848	111193	2224	$1.31 \cdot 10^5$	$2.65 \cdot 10^{-2}$
70	70	6.018	138028	1972	$1.16 \cdot 10^5$	$3.29 \cdot 10^{-2}$
5	100	0.536	12303	2461	$1.01 \cdot 10^5$	$2.05 \cdot 10^{-3}$
10	100	1.270	29117	2912	$1.20 \cdot 10^5$	$4.85 \cdot 10^{-3}$
30	100	4.710	108028	3601	$1.49 \cdot 10^5$	$1.80 \cdot 10^{-2}$
50	100	6.147	140986	2820	$1.16 \cdot 10^5$	$2.35 \cdot 10^{-2}$
70	100	10.470	240138	3431	$1.42 \cdot 10^5$	$4.00 \cdot 10^{-2}$

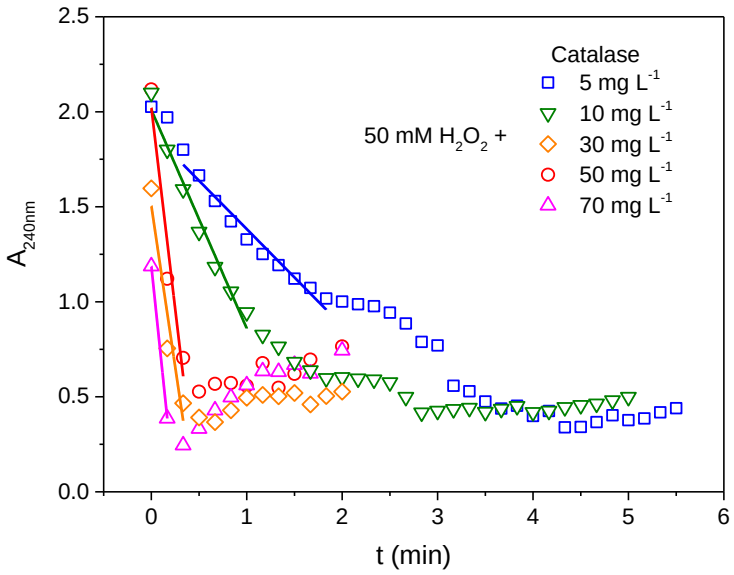

Figure 5.1. Absorbance at 240 nm versus time profile during the decomposition of H_2O_2 (50 mM) catalysed by CAT (different concentrations: 5, 10, 30, 50 and 70 mg L^{-1}).

Figure 5.2 shows the decomposition rate of H_2O_2 or in other words, the catalase specific volumetric activity, A_m. The higher concentration of H_2O_2 and CAT, the higher reaction rate was observed as expected by equation (5.5). Experimental results showed that high concentrations of both the enzyme (50 and 70 mg L^{-1}) and the substrate (70 and 100 mM) led to very rapid reactions that generated a great amount of bubbles and revealed uncertain absorbance values. In addition, reactions with 10 and 20 mM of H_2O_2 reached to low reaction rates even with high amounts of CAT. Therefore, 50 mM of H_2O_2 was selected as the optimal concentration to perform the catalase activity measurements.

Further measurements were performed in order to obtain the correlation between CAT activity and CAT concentration. The activity was measured using different concentrations of enzyme (5, 10, 20, 30 and 40 mg L^{-1}) and 50 mM of H_2O_2. The detection limit for CAT concentration was 3 mg L^{-1}; below that value the reaction is too slow so that the activity of CAT could not be measured. Linear regression of experimental results (Figure 5.3) permitted to determine the concentration of CAT (mg L^{-1}) equivalent to a specific activity of the enzyme A_v (U L^{-1}).

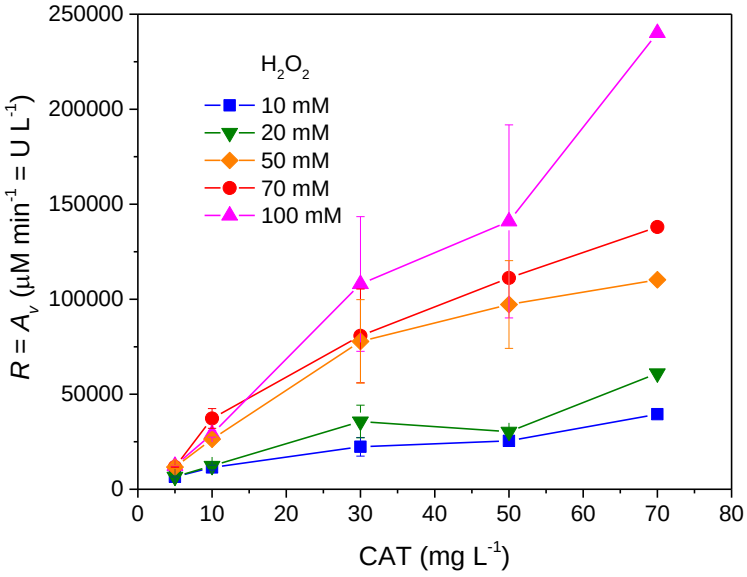

Figure 5.2. Reaction rate (R) of H_2O_2 decomposition (or catalase activity, A_v) at different concentrations of enzyme and substrate.

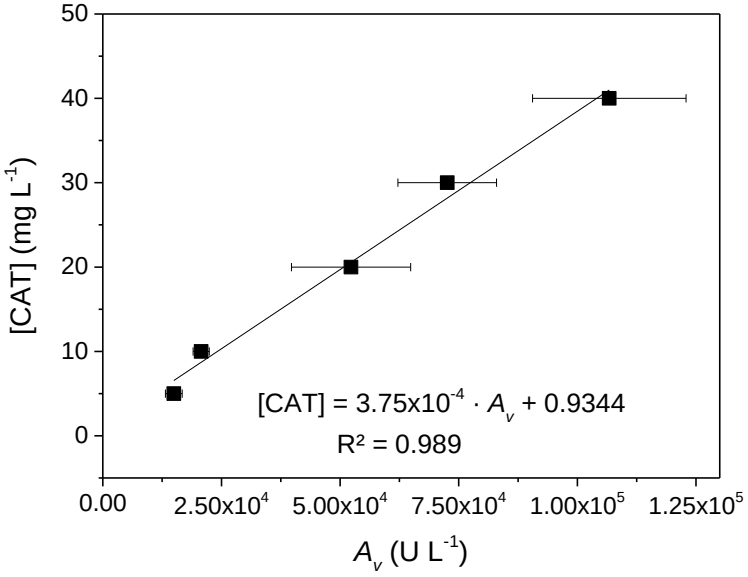

Figure 5.3. Correlation of the catalase concentration [CAT] and its volumetric activity A_v, in the range of 5 – 40 mg L^{-1}. Standard deviation of A_v is represented by error bars.

5.2.3 Kinetic catalase solar photo-inactivation

Solar irradiated catalase experiments were performed in the solar simulator system within the 700 mL-batch reactor under different irradiance values (30, 40 and 50 W m^{-2} of UVA) and an initial concentration of CAT of 30 mg L^{-1}. Catalase activity during solar exposure is represented in Figure 5.4 (a). The results demonstrated that the catalase activity was reduced when exposed to sunlight. Catalase photo-inactivation followed a first order kinetics with respect CAT concentration and the light density (LVRPA) according to the following equation:

$$r_{CAT} = \frac{d[CAT]}{dt} = k_{CAT} \cdot [CAT] \cdot e^{a}_{CAT} \quad (5.6)$$

e^{a}_{CAT} estimation was done by equation (1.50). The catalase absorbance was measured by a spectrophotometer in the UVA range at different catalase concentrations, and then the specific absorption coefficient calculated was $\overline{\kappa}^{*}_{CAT} = 2.6 \cdot 10^{5}\ M^{-1}\ cm^{-1}$.

In the experiments of catalase photo-inactivation, although the activity was reduced, the concentration of CAT did not change along radiation time. Therefore, [CAT] can be considered as the concentration of the "active catalase" in the equation (5.6). This concentration can be estimated by the correlation curve between CAT-concentration and CAT-activity (Figure 5.3).

Using the expression of LVRPA (equation (1.50)) and integrating equation (5.6) from time t = 0 (initial concentration of catalase, $[CAT]_0$) to a time t (catalase concentration [CAT]):

$$\frac{1}{[CAT]} = \frac{1}{[CAT]_0} + k_{CAT} \cdot \overline{\kappa}^{*}_{CAT} \cdot \overline{G} \cdot t \quad (5.7)$$

Equation (5.7) gives the expression of a linear equation, whose slope is equal to the kinetic constant of CAT photo-inactivation. Figure 5.4 (b) shows the linear fits of the three experiments at different irradiance values and the regression by least squares method of the experimental data. Following this, the value for k_{CAT} was determined as $1.5 \cdot 10^7$ cm^3 Einstein^{-1}.

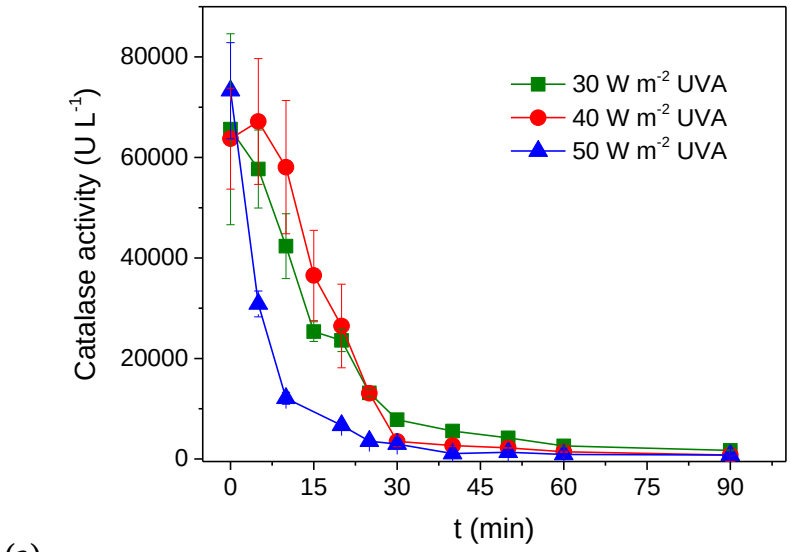

(a)

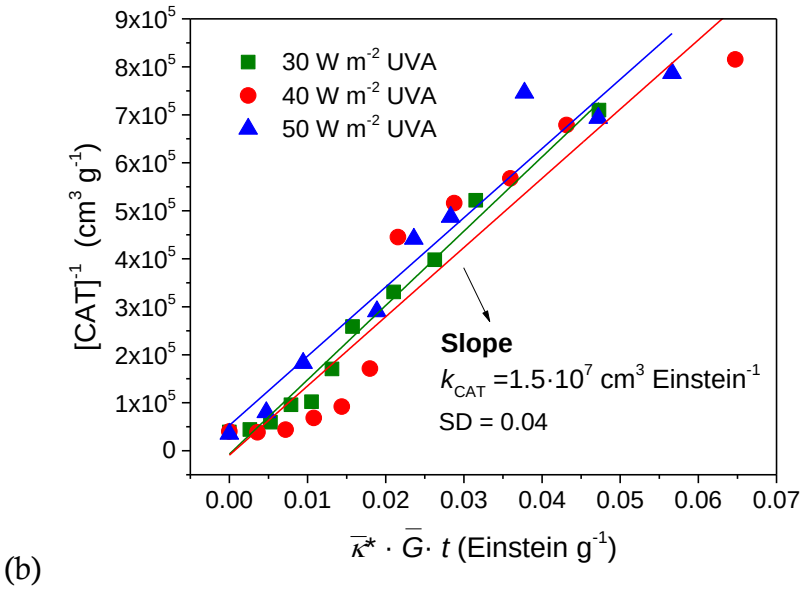

(b)

Figure 5.4. (a) Photo-inactivation of catalase in distilled water at 30, 40 and 50 W m^{-2} of UVA and (b) regression to determine the kinetic constant parameter.

5.3 Kinetic solar disinfection model

The proposed SODIS mechanism is based on three assumptions:

i) ROS are formed inside cells as a consequence of the biochemical routes of metabolism where oxygen plays an important role. Under aerobic conditions it could be considered that intracellular oxygen concentration is almost equivalent to extracellular oxygen [Imlay and Fridovich, 1991]. O_2 acts as final acceptor of electrons in the so-called electron transport chain (ETC). It is the final and most important step of cellular respiration since the energy needed in the cell to conduct any activity is generated. During the ETC, several redox reactions occur and the electrons flux obtained from donor molecules such as NAD^+, $NADP^+$, flavoprotein, quinone or hemo groups will be used to generate energy, which is stored in the cell as ATP [Seaver and Imlay, 2004]. Although redox process is conducted with high efficiency, a little percentage of free electrons interact with the intracellular O_2 to reduce it prematurely to $O_2^{\bullet-}$, and then to other ROS. Under sunlight radiation, the generation of $O_2^{\bullet-}$ is increased by the excitation of some photosensitiziers [Tanaka *et al.*, 2006; Giannakis *et al.*, 2016].

ii) Bacteria have a series of regulation mechanisms to control the toxic levels of ROS naturally formed inside cells. SOD reduces $O_2^{\bullet-}$ to H_2O_2 and then CAT reduce H_2O_2 to water. Nevertheless, solar radiation may alter the activity of these enzymes [Eisenstark, 1998].

iii) The balance of the intracellular ROS and their regulation by enzymes is altered when bacterial suspensions are exposed to sunlight, leading to inactivation of bacterial cells through a process in which recovery by the cell defence mechanisms can also take place.

Rigorous description of all involved biochemical routes is far beyond the possibilities of the kinetic description of the global SODIS process. The simplified model that is presented in this work captures the essential steps of the global process. It is considered as an optimal compromise between the fundamental description of the process and the simplicity model's requirements

for engineering purposes. Table 5.2 summarizes the reaction steps considered in the mechanism (ROS formation, ROS recombination, enzymes photo-inactivation, etc.) that will be explained later.

Table 5.2. Proposed SODIS mechanism of *E. coli* inactivation based on the photo-generation of intracellular ROS and the photo-inactivation of CAT and SOD enzymes.

Step	Reaction		Rate	Kinetic constant ($M^{-1}s^{-1}$)
Internal ROS formation	$O_2 + e^- \rightarrow O_2^{\bullet -}$	(5.8)	$k_1[O_2][e^-]$	[a] $2 \cdot 10^{10}$
	$O_2 + e^- \xrightarrow{h\nu,\ NADH} O_2^{\bullet -}$	(5.9)	$k_2[O_2][e^-]e^a_{NADH}$	
	$O_2^{\bullet -} + H^+ \xrightarrow{SOD} \frac{1}{2}H_2O_2 + \frac{1}{2}O_2$	(5.10)	$k_3[O_2^{\bullet -}][SOD]$	[b] 10^9
	$Fe^{2+} + H_2O_2 \rightarrow Fe^{3+} + HO^- + HO^{\bullet}$	(5.11)	$k_4[Fe^{2+}][H_2O_2]$	[c] 70
	$Fe^{3+} + H_2O \xrightarrow{h\nu} Fe^{2+} + HO^{\bullet} + H^+$	(5.12)	$k_5[Fe^{3+}][H_2O]\ e^a_{Fe3+}$	
ROS recombination	$H_2O_2 + HO^{\bullet} \rightarrow HO_2^{\bullet} + H_2O$	(5.13)	$k_6[H_2O_2][HO^{\bullet}]$	[d] $2.7 \cdot 10^7$
	$HO_2^{\bullet} \rightarrow \frac{1}{2}H_2O_2 + \frac{1}{2}O_2$	(5.14)	$k_7[HO_2^{\bullet}]^2$	[e] $8.3 \cdot 10^5$
H_2O_2 decomposition	$H_2O_2 \xrightarrow{CAT} \frac{1}{2}O_2 + H_2O$	(5.15)	$k_8[H_2O_2][CAT]$	[f] $9 \cdot 10^5$
Enzymes photo-inactivation	$CAT \xrightarrow{h\nu} CAT_i$	(5.16)	$k_9[CAT]e^a_{CAT}$	$1.5 \cdot 10^7$ $cm^3Einstein^{-1}$ **(this work)**
	$SOD \xrightarrow{h\nu} SOD_i$	(5.17)	$k_{10}[SOD]e^a_{SOD}$	
Cell damages caused by ROS	$OM_{red} + HO^{\bullet} \rightarrow OM_{ox}$	(5.18)	$k_{11}[HO^{\bullet}]$	
	$OM_{red} + O_2^{\bullet -} \rightarrow OM_{ox}$	(5.19)	$k_{12}[O_2^{\bullet -}]$	
Bacteria inactivation	$B_v \xrightarrow{HO^{\bullet}, O_2^{\bullet -}} B_i$	(5.20)	$k_{13}[HO^{\bullet}][O_2^{\bullet -}][B_v]$	

B_v: viable bacteria
B_i: inactivated bacteria
OM_{red}: organic matter reduced
OM_{ox}: organic matter oxidized
[a] Gort and Imlay, 1998; [b] Abreu and Cabelli, 2010; [c] Imlay, 2003; [d] Buxton *et al.*, 1988; [e] Gallard and De Laat, 2000; [f] Tao et *al.*, 2009.

5.3.1 Internal ROS formation

Under solar irradiation, the natural formation of ROS inside cells is accelerated by photosensitizers that are excited to high energy levels and donates an electron to oxygen, thus reducing it. Although there are several endogenous photosensitizers such flavins or quinons, NADH is one of the main photosensitizers that promotes the $O_2^{\bullet-}$ formation from oxygen molecule [Chen and Schopfer, 1999]. The redox cycle NADH/NAD^+ that is accomplished under UV exposure takes the following steps [Tanaka *et al.*, 2006; Joubert *et al.*, 2004]:

(i) NADH is photo-excited to $^3NADH^*$ that is quickly oxidized to $NADH^{\bullet+}$.

$$NADH \xrightarrow{h\nu} {}^3NADH^* \rightarrow NADH^{\bullet+} + e^- \tag{5.21}$$

(ii) $NADH^{\bullet+}$ forms an intermediate compound $NAD^{\bullet}$, that in presence of oxygen, is oxidized to NAD^+ reducing the oxygen to superoxide radical.

$$\left.\begin{aligned} NADH^{\bullet+} &\rightarrow NAD^{\bullet} + H^+ \\ NAD^{\bullet} + O_2 &\rightarrow NAD^+ + O_2^{\bullet-} \end{aligned}\right\} NADH^{\bullet+} + O_2 \rightarrow NAD^+ + H^+ + O_2^{\bullet-} \tag{5.22}$$

(iii) To complete the redox cycle, NAD^+ is reduced to NADH again.

$$NAD^+ + H^+ + 2e^- \rightarrow NADH \tag{5.23}$$

These reactions are the intermediate steps of the global reaction of superoxide formation induced by sunlight, as summarized in reaction (5.9). This reaction and reaction (5.8) that occurs naturally during cell respiration process, are responsible for the formation of $O_2^{\bullet-}$ in the cells when are exposed to sunlight. The kinetic constant of the reaction (5.8) was previously reported while the one of (5.9) was not determined experimentally. The reaction rate was introduced in the model using k_2 as an unknown parameter, e^a_{NADH} was determined using $\overline{\kappa}^*_{NADH}$ value previously reported as equal to 6220 $M^{-1}cm^{-1}$ [Nakamaru-Ogiso *et al.*, 2010], and a constant NADH concentration of 250 μM [Kishko *et al.*, 2012]. The concentration of molecular oxygen was considered equivalent to extracellular oxygen that is the dissolved oxygen in water, 210 μM [Imlay,

2003]. Taking into account that the reaction rate of $O_2^{\bullet-}$ in steady state is 5.7 μM s^{-1} [Imlay and Fridovich, 1991], and considering that is formed mainly via reaction (5.8), the concentration of electrons could be estimated as $1.35 \cdot 10^{-6}$ μM.

Imlay and co-workers studied the natural generation of intracellular $O_2^{\bullet-}$ in *E. coli* and determined that the reaction rate of the endogenous formation of $O_2^{\bullet-}$ from O_2 (reaction (5.8)) is 5 μM s^{-1} [Imlay and Fridovich, 1991; Gort and Imlay, 1998]. Nevertheless, the concentration of this radical at steady state was determined to be significantly low (10^{-10} M) due to the action of SOD, which transforms it into H_2O_2 in the presence of H^+ (reaction (5.10)). *E. coli* contains two cytoplasmic SOD enzymes, with manganese- and iron- as cofactors (MnSOD and FeSOD) and a single periplasmatic SOD enzyme, copper, zinc-cofactor type (CuZnSOD) [Imlay, 2008]. Viglino and co-workers studied the kinetics of CuSOD reaction [Viglino *et al.*, 1986]. Other researchers completed the mechanism of SOD by the observation of a burst phase and a zero-order phase in MnSOD [Abreu and Cabelli, 2010]. The proposed mechanism was expressed by the redox cycle of the cofactor:

$$Mn^{3+}SOD\left(OH^-\right) + O_2^{\bullet-} + H^+ \xrightarrow{k} Mn^{2+}SOD\left(H_2O\right) + O_2 \qquad (5.24)$$

$$Mn^{2+}SOD\left(H_2O\right) + O_2^{\bullet-} + H^+ \xrightarrow{k'} Mn^{3+}SOD\left(OH^-\right) + H_2O_2 \qquad (5.25)$$

where *k* and *k'* are the kinetic constants of each semi-reaction. The resulting reaction is expressed as reaction (5.10), with a kinetic constant considered equivalent to the limiting reaction kinetic constant. The citoplasmatic SOD concentration in *E. coli* was determined to be 20 μM [Imlay, 2008].

Intracellular H_2O_2 generates $HO^{\bullet}$ by Fenton like reactions ((5.11) and (5.12)) that is the one of the species that can directly damage biomolecules [Imlay, 2008]. Iron takes part in these reactions as a catalyst due to Fe^{2+} is oxidized to Fe^{3+} and then reduced again to its initial state. The reduction of iron is a spontaneous reaction that is accelerated by UV and visible light becoming (5.12) the limiting reaction of the internal photo-Fenton process. The iron that catalyses these

reactions is called "free iron", referring to the iron that is not incorporated into enzymes or iron-storage proteins. Bound iron can be released from enzyme co-factors such iron-sulfur cluster by ROS, specifically by superoxide radicals or hydrogen peroxide, or even from nucleic acids, proteins and lipids. *E. coli* contains approximately 20 μM of Fenton-active ferrous iron [Imlay, 2003].

Due to the high reactivity of ROS, several ROS recombination reactions occur. Contributions from Buxton, Gallard and co-workers collect a large list of ROS reactions [Buxton *et al.*, 1988; Gallard and De Laat, 2000]. From the kinetics point of view reactions (5.13) and (5.14) are two of the most representative ROS recombination reactions that have been used in other photo-oxidative models [Zalazar *et al.*, 2007; Flores *et al.*, 2012].

5.3.2 H_2O_2 decomposition

SOD controls the concentration of $O_2^{\bullet-}$ at low levels in natural conditions, although it also generates H_2O_2 at a rate of 15 μM s^{-1} [Seaver and Imlay, 2004]. Taking into account that levels above 1 μM are substantially toxic [Imlay, 2008], cells require a defensive mechanism against H_2O_2. In most of the microorganisms H_2O_2 is scavenged by peroxidases and catalase. The primary scavenger in *E. coli* is the alkylhydroperoxide reductase (Ahp) that is so effective that the concentration of H_2O_2 at the steady-state does not exceed 20 nM [Imlay, 2008]. Nevertheless, levels of H_2O_2 higher than 100 nM cause the activity of Ahp to top out. Then, CAT is strongly induced, becoming the primary scavenging enzyme.

When bacterial suspension is exposed to solar radiation, H_2O_2 content is expected to be higher than 100 nM so that CAT is considered the primary scavenging enzyme while Ahp action can be neglected. The decomposition mechanism of H_2O_2 by CAT is a very complex process that is not known in complete detail due to the variety of interactions between catalase and H_2O_2, $HO^{\bullet}$ and $HO_2^{\bullet}$ [Bergmeyer, 1983]. One of the most accepted mechanisms is that

Fe^{3+} acts as electron source, forming a Fe-intermediate [Tao *et al.*, 2009] according to:

$$Fe^{3+}CAT + H_2O_2 \xrightarrow{k} O{=}Fe^{4+}CAT + H_2O \quad (5.26)$$

$$O{=}Fe^{4+}CAT + H_2O_2 \xrightarrow{k'} Fe^{3+}CAT + H_2O + O_2 \quad (5.27)$$

where k and k' are the kinetic constants of each semi-reaction. The resulting reaction is expressed as (5.15) in Table 5.2, whose kinetic constant is considered the same as the one corresponding to the limiting reaction. Catalase at steady-state in *E. coli* was determined as 92 μM [Seaver and Imlay, 2001a; 2001b].

5.3.3 Enzymes inactivation by UVA light action

Enzymes are also affected by solar light [Youn *et al.*, 1995; Idil *et al.*, 2003]. SOD and CAT are macromolecular biological catalysts whose activity decreases under the action of UV radiation. Moreover, the concentration of intracellular ROS, such as $O_2^{\bullet-}$ and H_2O_2, may change during the solar exposure of bacteria cells. Reactions (5.16) and (5.17) represent the photo-inactivation of both enzymes. Bosshard and co-workers found evidences of the reduction of catalase activity during SODIS treatment [Bosshard *et al.*, 2010]. To our knowledge there is not any reported research of the photo-inactivation kinetics of these enzymes. In this study, photo-inactivation of catalase was experimentally evaluated under the same conditions as for solar water disinfection tests, to determine the kinetic parameter of the reaction (5.16), which resulted to be $1.5 \cdot 10^7$ cm^3 $Einstein^{-1}$. The reaction rate of the photo-inactivation of SOD (reaction (5.17)) was introduced in the model using k_{10} as an unknown parameter and e^a_{SOD} determined using the $\overline{\kappa}^*_{SOD}$ value previously reported of 800 $M^{-1}cm^{-1}$ [Jackson *et al.*, 2004].

5.3.4 Internal oxidative damages leading to cells inactivation

Generally, ROS are capable to oxidize the organic matter and constituent components in cells. Scientific community generally agreed that all the reactive

species photo-generated by UVA are source of injury and precursors of cells inactivation. Nevertheless, there is no experimental evidence that identify ROS, and beyond that which type of ROS, as main responsible for solar disinfection although the most commonly attributed species are hydroxyl radicals, superoxide radicals, hydrogen peroxide and singlet oxygen [Tyrrell and Keyse, 1990; Spuhler *et al.*, 2010; McGuigan *et al.*, 2012]. A complete solar water disinfection model should include all ROS that can oxidize cells components and lead to the disruption of the cellular metabolism and to a later cell inactivation. This simplified model considers only the two most oxidative ROS, i.e. $HO^{\bullet}$ or $O_2^{\bullet-}$, as a simplification of the several existing sources of intracellular oxidative stress. Reactions (5.18) and (5.19) refer those attacks to several intracellular targets that are encompassed in the term OM_{red} as the organic matter that is susceptible to be oxidized by $HO^{\bullet}$ or $O_2^{\bullet-}$.

Proteins can be the main target of ROS during SODIS due to an increase in protein carboxylation at the first stage of irradiation [Bosshard *et al.*, 2010] that is followed by an accumulation of proteins' aggregates after longer periods of solar irradiation. The damaged proteins during solar exposure are enzymes involved in translation, transport, transcription, glycolysis, DNA-repair, respiration, protein folding and ATP synthesis [Fernández-Ibáñez *et al.*, 2016]. In general, an accumulation of several damages provoked by ROS is necessary to induce cell death. Bacteria with intermediate levels of damage would be still able to growth in a suitable culture medium or specific growth conditions. The macroscopic reaction of bacterial inactivation can be considered as activated or mediated by the intracellular ROS according to reaction (5.20). Therefore, the mass balance of viable bacteria could be expressed in terms of the concentration of bacteria in water and the reaction rate is dependent on the intracellular concentrations of $HO^{\bullet}$ and $O_2^{\bullet-}$ (see Table 5.2). The units of the apparent kinetic constant k_{13} are $M^{-2}\ s^{-1}$, which refer to the bacterial cell volume while the reaction rate of the bacteria inactivation ($d[B_v]/dt = -k_{13}[HO^{\bullet}][O_2^{\bullet-}][B_v]$) is expressed in terms of CFU $mL^{-1}\ s^{-1}$, referring to the reactor volume.

5.4 Estimation of model parameters

5.4.1 Kinetic modelling

Mass balance for each species involved in the process can be solved for a single cell volume to obtain the profiles of concentration of ROS and enzymes versus the treatment time. Although $O_2^{\bullet -}$ and H_2O_2 are capable to inactivate iron-sulfur cluster and release iron, this release from cluster can be neglected and free iron can be considered constant during the process. The concentrations *in vivo* of the oxidants are so low ($O_2^{\bullet -}$ and H_2O_2) and the reduction reaction of bound iron is so slow that the predicted half-time for this reaction is higher than 10 h, far too long to be physiologically relevant [Woodmansee and Imlay, 2002]. Finally, the profiles of concentration in a single cell are derived by applying the kinetic micro steady-state approximation for concentration of iron (Fe^{2+} and Fe^{3+}) and radicals ($O_2^{\bullet -}$, $HO^{\bullet}$ and $HO_2^{\bullet}$) inside a bacterial cell:

Iron balances in a single cell:

$$\frac{d\left[Fe^{2+}\right]}{dt} = -\frac{d\left[Fe^{3+}\right]}{dt} = -k_4\left[Fe^{2+}\right]\left[H_2O_2\right] + k_5\left[Fe^{3+}\right]\left[H_2O\right]e^a_{Fe^{3+}} \approx 0 \qquad (5.28)$$

$$k_4\left[Fe^{2+}\right]\left[H_2O_2\right] = k_5\left[Fe^{3+}\right]\left[H_2O\right]e^a_{Fe^{3+}} \qquad (5.29)$$

Superoxide radicals balance in a single cell:

$$\frac{d\left[O_2^{\bullet -}\right]}{dt} = k_1\left[O_2\right]\left[e^-\right] + k_2\left[O_2\right]\left[e^-\right]e^a_{NADH} - k_3\left[O_2^{\bullet -}\right]\left[SOD\right] - k_{12}\left[O_2^{\bullet -}\right] \approx 0 \qquad (5.30)$$

$$\left[O_2^{\bullet -}\right] = \frac{\gamma_1 + \gamma_2 \cdot e^a_{NADH}}{k_3\left[SOD\right] + k_{12}} \qquad (5.31)$$

Hydroxyl radicals balance in a single cell:

$$\frac{\mathrm{d}\left[\mathrm{HO}^{\bullet}\right]}{\mathrm{d}t} = -k_6\left[\mathrm{H_2O_2}\right]\left[\mathrm{HO}^{\bullet}\right] - k_{11}\left[\mathrm{HO}^{\bullet}\right] + k_4\left[\mathrm{Fe}^{2+}\right]\left[\mathrm{H_2O_2}\right] + \\ + k_5\left[\mathrm{Fe}^{3+}\right]\left[\mathrm{H_2O}\right]e^{a}_{\mathrm{Fe}^{3+}} \approx 0 \tag{5.32}$$

$$\left[\mathrm{HO}^{\bullet}\right] = \frac{2\gamma_3\left[\mathrm{H_2O_2}\right]}{k_6\left[\mathrm{H_2O_2}\right] + k_{11}} \tag{5.33}$$

Hydroperoxyl radicals balance in a single cell:

$$\frac{\mathrm{d}\left[\mathrm{HO}_2^{\bullet}\right]}{\mathrm{d}t} = k_6\left[\mathrm{H_2O_2}\right]\left[\mathrm{HO}^{\bullet}\right] - k_7\left[\mathrm{HO}_2^{\bullet}\right]^2 \approx 0 \tag{5.34}$$

$$\left[\mathrm{HO}_2^{\bullet}\right] = \sqrt{\frac{k_6}{k_7}\left[\mathrm{H_2O_2}\right]\left[\mathrm{HO}^{\bullet}\right]} \tag{5.35}$$

where

$$\gamma_1 = k_1\left[\mathrm{O_2}\right]\left[\mathrm{e}^{-}\right]$$
$$\gamma_2 = k_2\left[\mathrm{O_2}\right]\left[\mathrm{e}^{-}\right] \tag{5.36}$$
$$\gamma_3 = k_4\left[\mathrm{Fe}^{2+}\right]$$

Hydrogen peroxide is a compound that cannot be considered in a micro steady state inside the bacterial cell. The rate expression of H_2O_2 is obtained by:

$$\frac{\mathrm{d}\left[\mathrm{H_2O_2}\right]}{\mathrm{d}t} = \frac{1}{2}k_3\left[\mathrm{O}_2^{\bullet-}\right]\left[\mathrm{SOD}\right] + \frac{1}{2}k_7\left[\mathrm{HO}_2^{\bullet}\right]^2 - k_4\left[\mathrm{Fe}^{2+}\right]\left[\mathrm{H_2O_2}\right] + \\ - k_6\left[\mathrm{H_2O_2}\right]\left[\mathrm{HO}^{\bullet}\right] - k_8\left[\mathrm{H_2O_2}\right]\left[\mathrm{CAT}\right] \tag{5.37}$$

Introducing equations (5.31), (5.33) and (5.35) into (5.37), the hydrogen peroxide rate results to be:

$$\frac{\mathrm{d}\left[\mathrm{H_2O_2}\right]}{\mathrm{d}t} = \frac{1}{2}\cdot\frac{k_3\left[\mathrm{SOD}\right]\left(\gamma_1+\gamma_2\cdot e^a_{\mathrm{NADH}}\right)}{k_3\left[\mathrm{SOD}\right]+k_{12}} - \frac{\gamma_3\cdot k_6\left[\mathrm{H_2O_2}\right]^2}{k_6\left[\mathrm{H_2O_2}\right]+k_{11}} + \\ -\left(\gamma_3+k_8\left[\mathrm{CAT}\right]\right)\left[\mathrm{H_2O_2}\right] \tag{5.38}$$

Enzymes are inactive along treatment time due to the action of solar photons. CAT and SOD are species in not-steady-state:

$$\frac{\mathrm{d}\left[\mathrm{CAT}\right]}{\mathrm{d}t} = -k_9\left[\mathrm{CAT}\right]e^a_{\mathrm{CAT}} \neq 0 \tag{5.39}$$

$$\frac{\mathrm{d}\left[\mathrm{SOD}\right]}{\mathrm{d}t} = -k_{10}\left[\mathrm{SOD}\right]e^a_{\mathrm{SOD}} \neq 0 \tag{5.40}$$

Introducing the expression of LVRPA of each compound determined by equation (1.50) into the mass balances of each enzyme ((5.39) and (5.40)) and taking into account the (5.1) for the calculation of the absorption coefficient, the following expressions are obtained:

$$\frac{\mathrm{d}\left[\mathrm{CAT}\right]}{\mathrm{d}t} = -k_9\cdot\overline{\kappa}^*_{\mathrm{CAT}}\cdot\overline{G}\cdot\left[\mathrm{CAT}\right]^2 \tag{5.41}$$

$$\frac{\mathrm{d}\left[\mathrm{SOD}\right]}{\mathrm{d}t} = -k_{10}\cdot\overline{\kappa}^*_{\mathrm{SOD}}\cdot\overline{G}\cdot\left[\mathrm{SOD}\right]^2 \tag{5.42}$$

Integrating the both equations from time $t = 0$ (initial concentrations of enzymes, $[\mathrm{CAT}]_0$ and $[\mathrm{SOD}]_0$) to an instant time t ([CAT] and [SOD]):

$$\left[\mathrm{CAT}\right] = \frac{1}{1/\left[\mathrm{CAT}\right]_0 + k_9\cdot\overline{\kappa}^*_{\mathrm{CAT}}\cdot\overline{G}\cdot t} \tag{5.43}$$

$$\left[\mathrm{SOD}\right] = \frac{1}{1/\left[\mathrm{SOD}\right]_0 + k_{10}\cdot\overline{\kappa}^*_{\mathrm{SOD}}\cdot\overline{G}\cdot t} \tag{5.44}$$

Finally, the reaction rate of the bacteria inactivation is obtained from the reaction (5.20) and the mass balance of the bacteria in the whole reactor volume:

$$\frac{d[B_v]}{dt} = -k_{13}[HO^{\bullet}][O_2^{\bullet}][B_v] \tag{5.45}$$

Introducing the expression of the $O_2^{\bullet-}$ and $HO^{\bullet}$ concentrations ((5.31) and (5.33)) into the above equation, the following expression is obtained:

$$\frac{d[B_v]}{dt} = -k_{13} \cdot \frac{2\gamma_3[H_2O_2]}{k_6[H_2O_2]+k_{11}} \cdot \frac{\gamma_1+\gamma_2 \cdot e^{a}_{NADH}}{k_3[SOD]+k_{12}} \cdot [B_v] \tag{5.46}$$

Thus, the SODIS model is able to predict the concentration of bacteria over the treatment time by solving the equation (5.46) applied to the whole water volume reactor. This differential equation must be solved simultaneously to other equations of the model as they have common variables (expressions of H_2O_2 (5.38), CAT (5.43) and SOD (5.44)). Those equations are applied to one single cell and consisted on the set of equations in Table 5.2. According to the isotropic hypothesis, the same internal reactions will occur in all cells without population, time or space preferences. Consequently, intracellular species involved in the process are behaving similar in all cells. This coupled system of equations was solved using the Dormand-Prince method as described in chapter 3.

The SODIS model presented has 13 kinetic parameters. Most of them have been previously studied by other authors and reported in literature as shown in Table 5.2. In some cases, the conditions for determining these kinetic constants are different from those found in the inner bacteria. Nevertheless, these differences may not be significant due to the species involved are most of them chemical compounds or biomolecules (CAT and SOD) that have been studied *in vivo* as reported in the scientific literature. The kinetic constant of reaction (5.16) referring to the reduction of catalase activity due to the light action has been determined experimentally in this work, as was previously explained. The proposed model eventually has five unknown parameters: γ_2 (related to the photo-generation of $O_2^{\bullet-}$), k_{10} (kinetic constant of SOD photo-inactivation), k_{11} (kinetic constant of cell's content oxidation by $HO^{\bullet}$), k_{12} (kinetic constant of cell's content oxidation by $O_2^{\bullet-}$) and k_{13} (kinetic constant of bacteria inactivation).

5.4.2 Experimental results and regression

Solar disinfection experiments within isotonic water were performed in the solar simulator system at different operational conditions: initial bacteria concentration (10^3, 10^4, 10^5, 10^6 CFU mL^{-1}) and irradiance values (25, 30 and 40 W m^{-2} of solar UVA). The results (Figure 5.5) showed that: (i) the higher dose intensity of radiation the faster bacterial inactivation and (ii) the initial concentration of bacteria does not affect to the kinetic constants. Experimental results were used for determining the SODIS model parameters by mathematical correlation between predicted model values and experimental data (Appendix A). The model parameters obtained are:

$\gamma_2 = 1.14 \cdot 10^5$ M cm^3 $Einstein^{-1}$

$k_{10} = 1.56 \cdot 10^6$ cm^3 $Einstein^{-1}$

$k_{11} = 2.04 \cdot 10^4$ s^{-1}

$k_{12} = 1.36 \cdot 10^5$ s^{-1}

$k_{13} = 8.03 \cdot 10^{15}$ M^{-2} s^{-1}

NRMSLE = 8.32 %

Figure 5.5 shows the experimental and simulated results in the different conditions. This evidences that modelled results and the optimized parameters fit satisfactorily experimental results. Even, the NRMSLE calculated for all the experiments is smaller than 10 %, which according to other works [Raes *et al.*, 2012] can be considered as an excellent regression result.

It is important to note that parameters' values obtained in this work are specifically estimated for the operational conditions of the experiments. In this sense, the kinetic parameters k_{11}, k_{12} and k_{13} were estimated using the common *E. coli* strain K-12 in stationary phase. For other microorganism or other growth state of this bacterium, the parameters could be quite different and should be estimated for the specific cell and operational conditions. Furthermore, reactor

setup is also an important factor due to it determines the inlet UVA photon flux inside bacterial cells. Consequently, the kinetic values estimated could be applied for clear waters and reactors with similar photon distribution than the used in this work.

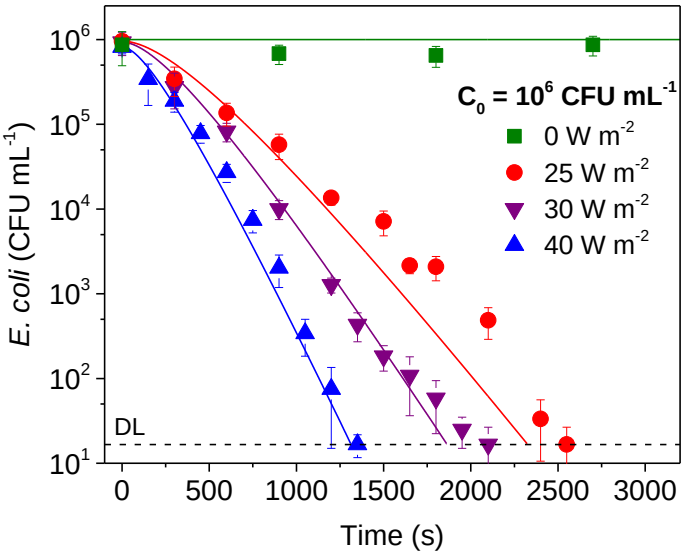

(a)

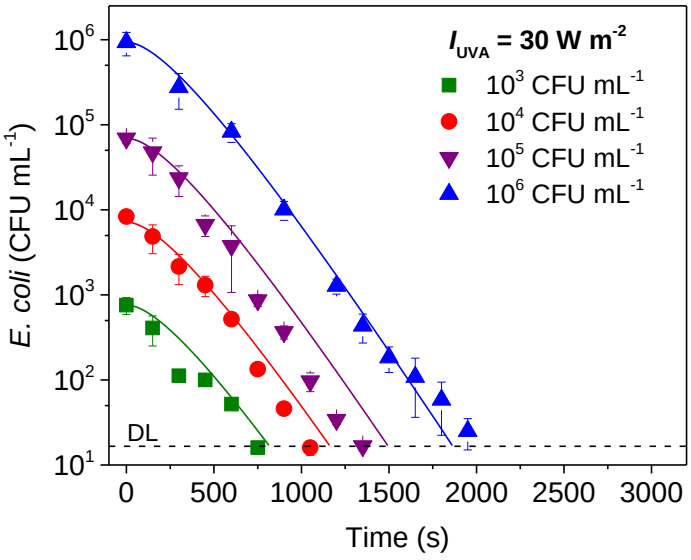

(b)

Figure 5.5. Inactivation of *E. coli* by solar water disinfection: experimental data (dots) and modelled data (lines) at (a) different UVA irradiances and (b) different initial bacteria concentration.

5.5 Modelled profiles of intracellular ROS and enzymes

This SODIS model is capable to simulate and predict the time profile of intracellular ROS during solar water disinfection. The proposed species involved in the process are $O_2^{\bullet -}$, H_2O_2, $HO^{\bullet}$ and $HO_2^{\bullet}$. The hypothesis done for mass balance equations of these species was that all the short lifetime radicals reach a micro stationary-state due to the high reactivity of the species, while H_2O_2 was considered in a non-stationary-state with possible accumulation.

Simulation runs at different irradiance values as shown in Figure 5.7. The simulation results predict that H_2O_2, $HO^{\bullet}$ and $HO_2^{\bullet}$ reach a new stationary-state in less than 10 minutes and increase their concentration up to 3-log even for an UVA irradiance of 10 W m^{-2}. The simulated behaviour of $O_2^{\bullet -}$ is apparently quite different, as a very slight increase is observed in all cases, even for high irradiance as 50 W m^{-2}. Still, this increase is 5 orders of magnitude lower than the rest of ROS species (Figure 5.7 (b), (c) and (d)). At view of these predictions, it could be assumed that the new stationary state for $O_2^{\bullet -}$ is reached much faster than the others, so fast that the plateau profile of the other graphs is not observed here. This is a result of the high rate reactions of $O_2^{\bullet -}$ consumption in the model. This is in concordance with the low relevant role of the photo-inactivation reaction of SOD, as shown by its low kinetic rate constant (k_{10} = 1.56 · 10^6 cm^3 $Einstein^{-1}$) as compared to the corresponding to catalase (k_9 = 1.5 · 10^7 cm^3 $Einstein^{-1}$).

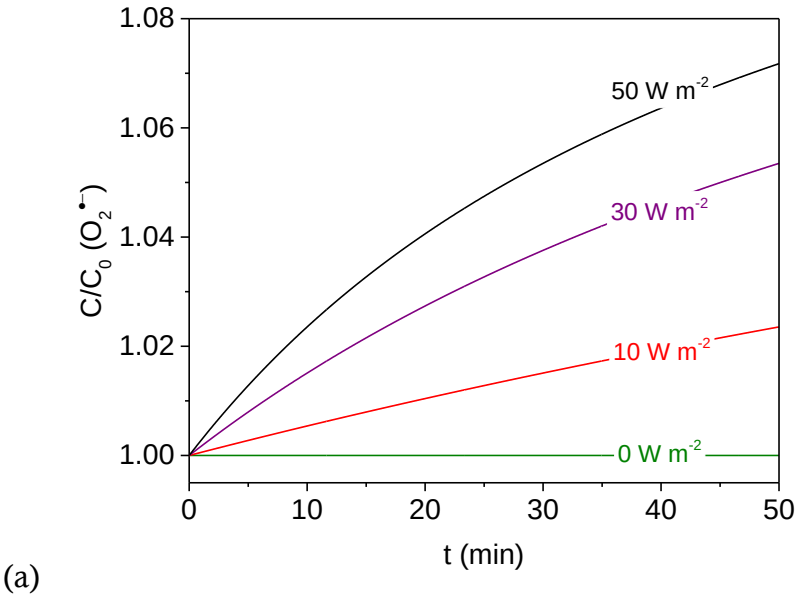

(a)

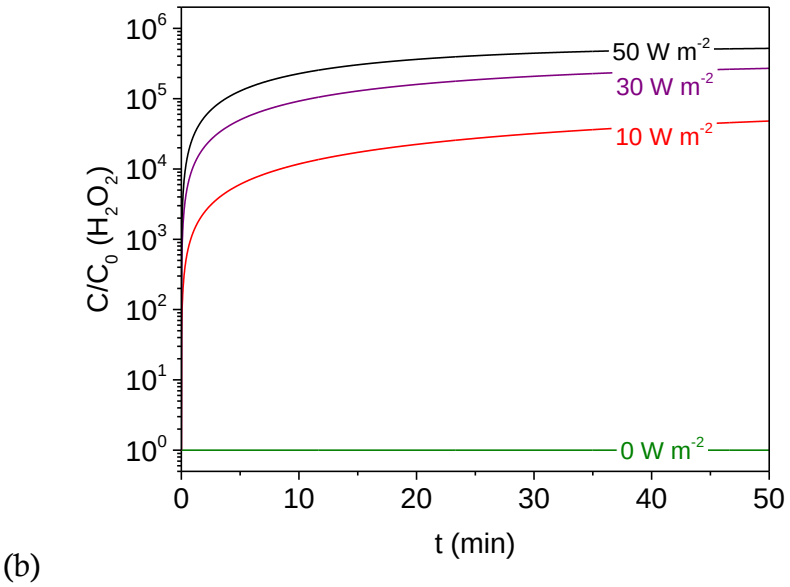

(b)

Figure 5.6. Model simulations for intracellular concentrations of (a) $O_2^{\bullet-}$, (b) H_2O_2, (c) $HO^{\bullet}$ and (d) $HO_2^{\bullet}$ in *E. coli* during 50 min of solar water disinfection treatment at 0, 10, 30 and 50 W m^{-2} of UVA irradiances.

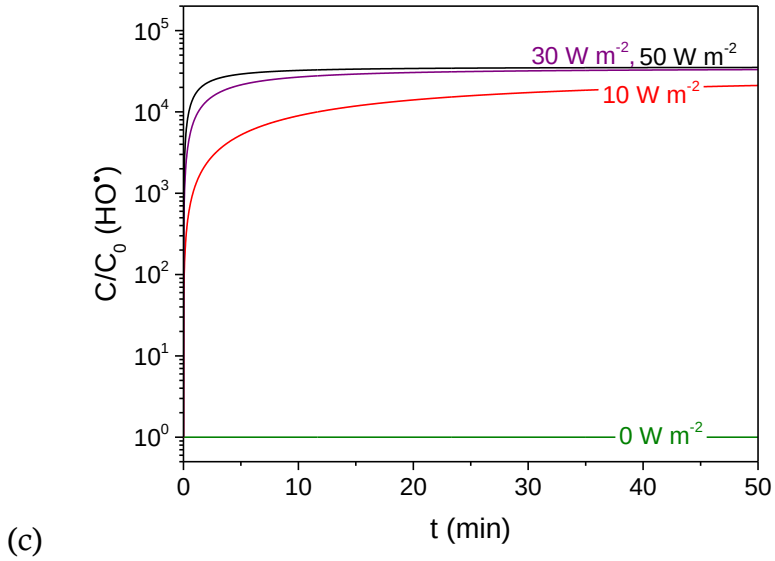

(c)

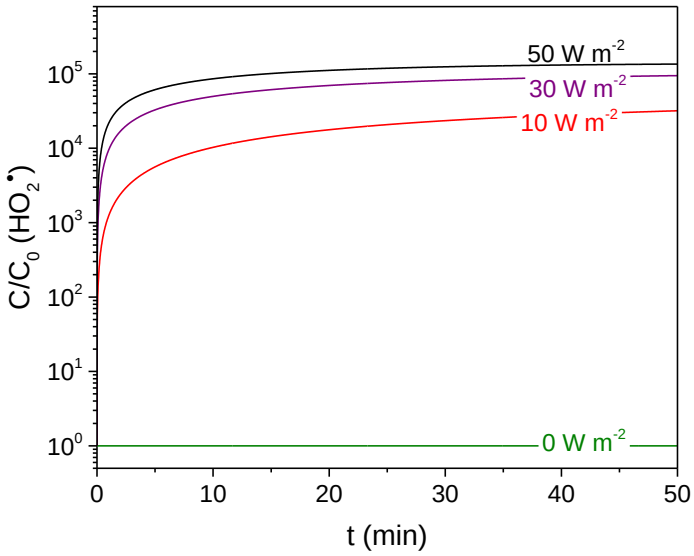

(d)

Figure 5.7. (continued) Model simulations for intracellular concentrations of (a) $O_2^{\bullet-}$, (b) H_2O_2, (c) $HO^{\bullet}$ and (d) $HO_2^{\bullet}$ in *E. coli* during 50 min of solar water disinfection treatment at 0, 10, 30 and 50 W m^{-2} of UVA irradiances.

Simulation profiles for CAT and SOD at different solar irradiances are shown in Figure 5.8. Experimental data of CAT photo-inactivation are also plotted here. The model describes accurately the experimental data obtained in the same experimental conditions. Simulations of both enzymes show, as expected, a reduction of their activity during the process. Nevertheless, SOD activity reduction is not as rapid as CAT photo-inactivation. These simulations are in

agreement with results obtained by other researchers [Idil *et al.*, 2013] that studied experimentally the effect of UVA in enzyme levels of *E. coli* in seawater. In addition, the slow SOD activity decrease permits to control the amounts of $O_2^{\bullet-}$ forming inside the cells. This fact is observed in the Figure 5.7 (a) where $O_2^{\bullet-}$ profiles show a very slight increase even at 50 W m^{-2}.

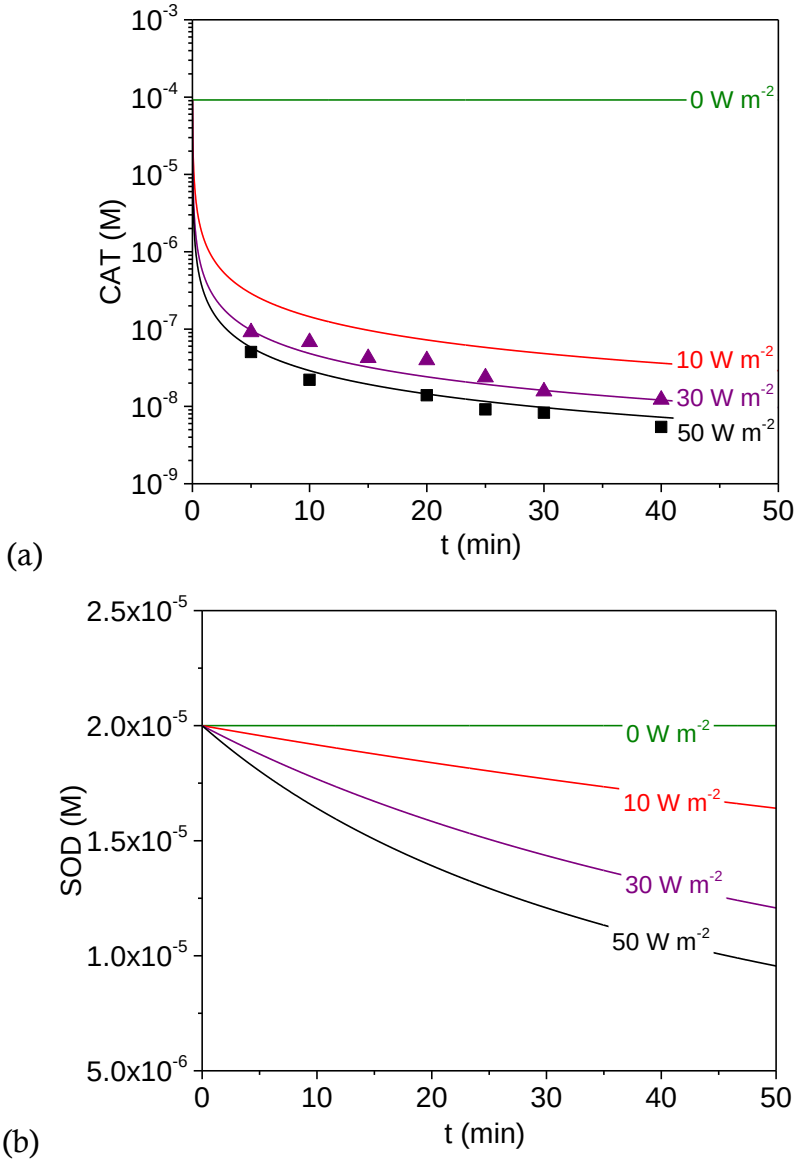

Figure 5.8. Model simulations for intracellular concentrations of (a) CAT (lines) and (b) SOD in *E. coli* during 50 min of solar disinfection treatment at 0, 10, 30 and 50 W m^{-2} of UVA irradiances. Dots in (a) represent experimental data of CAT photo-inactivation at 30 W m^{-2} (▲) and 50 W m^{-2} (■).

5.6 Conclusions of chapter 5

The presented simplified SODIS model for bacteria inactivation can be considered as an intrinsic kinetic description of solar water disinfection process and the kinetic parameters obtained could be applied for *E. coli* strain K-12 and for reactors with similar photon flux distribution.

The SODIS model summarizes the main reactions that validate mathematically experimental evidence of *E. coli* inactivation due to the solar irradiation. The model is successfully capable to reproduce the time profile of the viable bacteria concentration in clear water under different solar UVA irradiances and different initial bacterial concentrations with a normalized root mean square logarithmic error of 8.32 %. This mechanistic SODIS model is also capable to simulate the generation of intracellular ROS (i.e. $HO^{\bullet}$, H_2O_2, $O_2^{\bullet-}$, and $HO_2^{\bullet}$) and photo-inactivation of two enzymes, CAT and SOD, during SODIS.

Kinetic parameters of the reactions presented have been correlated in this work. Bacterial inactivation is introduced in the SODIS model as a reaction mediated by intracellular $HO^{\bullet}$ and $O_2^{\bullet-}$ ($k_{13} = 8.03 \cdot 10^{15}$ M^{-2} s^{-1}). Inside the cells, those attacks have been represented by the oxidation of natural organic matter by $HO^{\bullet}$ and $O_2^{\bullet-}$ ($k_{11} = 2.04 \cdot 10^{4}$ s^{-1} and $k_{12} = 1.36 \cdot 10^{5}$ s^{-1}, respectively). Although kinetics of the naturally formation of intracellular ROS was previously studied by other researchers, this work is the first attempt to determine the kinetics of the ROS formation due to the solar UVA photons' action. The photo-generation of $O_2^{\bullet-}$ is proposed as a reaction mediated by the natural photosensitizer NADH ($\gamma_2 = 1.14 \cdot 10^{5}$ M cm^3 $Einstein^{-1}$). Kinetic constant of CAT photo-inactivation was determined experimentally ($k_9 = 1.5 \cdot 10^{7}$ cm^3 $Einstein^{-1}$) and kinetic constant of SOD photo-inactivation was obtained by model regression ($k_{10} = 1.56 \cdot 10^{6}$ cm^3 $Einstein^{-1}$).

CHAPTER 6

MECHANISTIC MODEL OF SOLAR WATER DISINFECTION: SYNERGISTIC EFFECT OF SOLAR UVA AND MILD-HEAT

6 MECHANISTIC MODEL OF SOLAR WATER DISINFECTION: SYNERGISTIC EFFECT OF SOLAR UVA AND MILD-HEAT

In this chapter, the solar mild-heat effect is introduced in the mechanistic model of the inactivation of *E. coli* occurring during SODIS. Bacterial killing during solar exposure of contaminated water is attributed to the join effect of i) the UVA photons absorbed by bacteria and producing intracellular ROS that induce oxidative damages, and ii) a water mild increase of temperature that accelerates the bacterial inactivation process. The synergistic SODIS-thermal model described in this chapter is a simplified approach of the kinetic reactions that explain the synergy between UVA radiation and temperature to successfully reproduce SODIS experimental results. The main steps considering in the model are (i) the photo-induced formation of intracellular ROS from O_2 taking into account the internal thermal and photo-Fenton reactions; (ii) the thermal and photo-inactivation of CAT and SOD and (iii) the internal damages due to the action of the oxidative and thermal effects. The new model is capable to reproduce the time-profile of *E. coli* concentration in clear water at different temperatures (10 to 55 ºC) and under different solar UVA irradiances (30 to 50 W m^{-2}).

6.1 Model of dark thermal effect on the *E. coli* survival

The effect of temperature in *E. coli* viability was experimentally evaluated in the range of 10 – 55 ºC. Figure 6.1 (a) shows the experimental results of the concentration of cultivable *E. coli* exposed to different temperatures for 5 h with an initial concentration of 10^6 CFU mL^{-1}. No bacterial inactivation was observed for experiments at 10, 20 or 30 ºC. At temperature values higher than 30 ºC (from 37 to 55 ºC) the viability of the bacterial cells was negatively affected so that the higher temperature the lower viability was observed. Similar inactivation profiles were obtained with 10^3 CFU mL^{-1} of initial concentration (Figure 6.1 (b)). These results are as expected, in concordance with other results reported in literature [McGuigan *et al.*, 1998]. The objective of these experiments was to obtain the experimental data for the mathematical 'thermal dark model' fit. This model represents the *E. coli* inactivation due to the mere thermal effect.

The first signal of heat stress is the unfolded outer membrane protein in the periplasmic space, precursor of the activation of the transcription factor σ^E (encoded by *rpoE*) to start the transcription of the genes required for responding against the heat stress signal. Another signal is the unfolded cytoplasmic proteins that activate the main heat shock sigma factor σ^H [Noor, 2015]. As a result of the heat stress, the permeability and the potential of the membrane, esterase activity, intracellular pH and production of ROS increased [Baatout *et al.*, 2005]. All these injuries lead eventually to a reduction of the bacterial population in water due to the thermal effect.

The mere effect of the temperature on the bacteria viability is represented by a simplified reaction that includes all the mentioned intracellular damages resulting into the transformation of viable bacteria (B_v) to inactive bacteria (B_i):

$$B_v \xrightarrow{T} B_i \tag{6.1}$$

This model that explains the *E. coli* inactivation due to the thermal effect is represented by the equation (6.1) and it is called from now on *thermal model*.

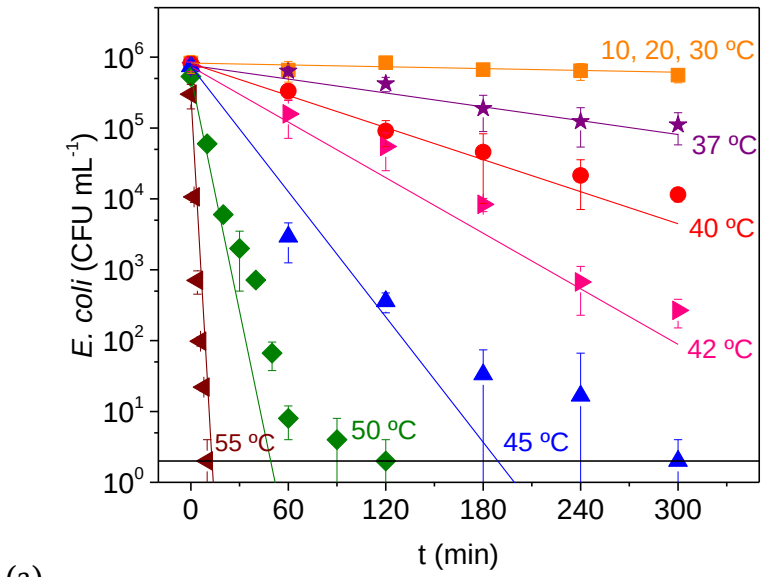

(a)

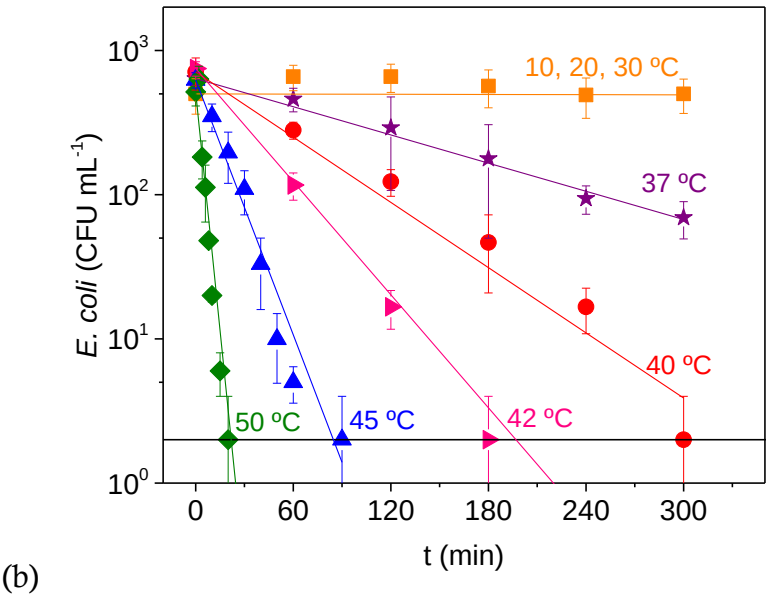

(b)

Figure 6.1. Inactivation of *E. coli* in isotonic water due to thermal effects in the dark. Experimental results (dots) and log-linear regressions (lines) with initial bacterial concentration of (a) 10^6 CFU mL^{-1} and (b) 10^3 CFU mL^{-1}.

Considering a first order kinetics for the above reaction with a kinetic constant k_T, the reaction rate is defined by equation (6.2) that if it is integrated, the equation (6.3) is obtained:

$$r_{B_v} = \frac{d[B_v]}{dt} = -k_T \cdot [B_v] \tag{6.2}$$

$$\ln\left(\frac{[B_v]}{[B_v]_0}\right) = -k_T \cdot t \tag{6.3}$$

Thus, the kinetic constant k_T for each temperature could be calculated by linear regression as the slope of the line $\ln([B_v]/[B_v]_0)$ versus t. Using experimental data (Figure 6.1), the values of k_T values at each temperature and each initial bacterial concentration were fitted. Data are shown in Table 6.1, showing that k_T is temperature dependent which correlation could be defined by Arrhenius law:

$$\ln k_T = \ln A - \frac{Ea}{R \cdot T} \tag{6.4}$$

where A is the pre-exponential factor, Ea the activation energy and R the ideal gas constant. Arrhenius parameters were determined by a linear regression showing, $\ln A = 79 \pm 3$ (A in s^{-1}), and $Ea = (23 \pm 1) \cdot 10^4$ J mol^{-1}.

Table 6.1. Kinetic thermal constant values for dark thermal inactivation of *E. coli*.

Temperature	k_T (min^{-1}) Experiments with $[B_v]_0 = 10^6$ CFU mL^{-1}	k_T (min^{-1}) Experiments with $[B_v]_0 = 10^3$ CFU mL^{-1}
10 ºC	0.0008 ± 0.0002	0.0003 ± 0.0003
20 ºC	0.0011 ± 0.0001	0.0007 ± 0.0004
30 ºC	0.0012 ± 0.0002	0.0014 ± 0.0004
35 ºC	0.0030 ± 0.0002	0.0030 ± 0.0005
37 ºC	0.0068 ± 0.0004	0.0074 ± 0.0002
40 ºC	0.0151 ± 0.0005	0.019 ± 0.002
42 ºC	0.0266 ± 0.0009	0.035 ± 0.005
45 ºC	0.048 ± 0.004	0.080 ± 0.004
50 ºC	0.182 ± 0.005	0.29 ± 0.01
55 ºC	1.25 ± 0.05	---

6.2 Model of the combined effect of UVA and mild-heat

6.2.1 *SODIS + thermal model*

The first attempt to include the effect of mild-heat in the SODIS model introduced in chapter 5 (summarized in Table 5.2), was the simple addition of reaction (6.1) (*thermal model*) to the equations of Table 5.2. The two models individually give account for cells inactivation due to the action of solar radiation (with no dependence on temperature) and temperature (in dark), respectively. This combined model is the simplest strategy to explain solar water disinfection at mild-heat temperatures reached during SODIS technique, rising typically from 25 to 55 ºC [McGuigan *et al.*, 1998]. Since it is the addition of the single effects with any consideration of extra beneficial action of temperature over SODIS, this model is called from now on *SODIS + thermal model*.

It is necessary to notice that the mass balance of viable bacteria has to be proposed for the entire reactor using reaction (6.1) of *thermal model* and the reaction (5.20) of *SODIS model*. On the contrary, the rest of the reactions of *SODIS model* are intracellular reactions and have to be used for solving the mass balance at intracellular level, for internal species in a single cell. According to the isotropic hypothesis, the same internal reactions will occur in all cells without population, time or space preferences. Consequently, the changes over time on the concentration of the intracellular species involved in the process could be considered the same in all cells. Therefore, the two following assumptions were made to solve the mass balances: (i) iron released from cluster due to oxidative stress is neglected because this reduction reaction is far too long to be physiologically relevant [Woodmansee and Imlay, 2002], and (ii) it is considered a kinetic micro steady-state approximation for intracellular iron (Fe^{2+} and Fe^{3+}) and radicals ($O_2^{\bullet -}$, $HO^{\bullet}$ and $HO_2^{\bullet}$). According to this, the mass balance of the viable bacteria is given by the following equation:

$$\frac{d[B_v]}{dt} = -k_{13}[HO^{\bullet}][O_2^{\bullet -}][B_v] - k_T[B_v] \quad (6.5)$$

The *SODIS + thermal model* should predict the *E. coli* inactivation by solar water disinfection at different temperatures by solving the equation (6.5) simultaneously with the mass balance equations of the rest of the intracellular species involved in the model, SOD, CAT, H_2O_2, $HO^{\bullet}$ and $O_2^{\bullet -}$ (equations (5.28) to (5.44) of chapter 5).

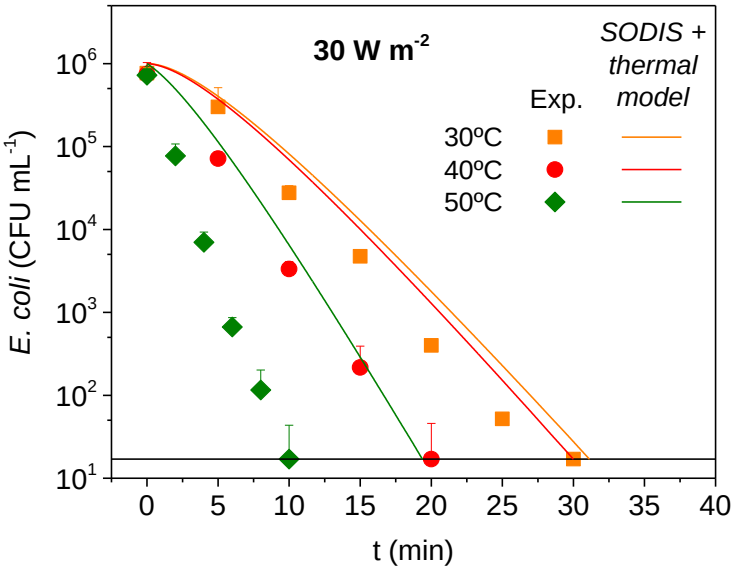

Figure 6.2. Inactivation of *E. coli* in isotonic water exposed to simulated sunlight (30 W m^{-2} of UVA) at 30, 40 and 50 ºC. Experimental results (dots) and simulation of *SODIS + thermal model* (lines).

Figure 6.2 shows the *E. coli* inactivation within isotonic water by solar water disinfection at different temperatures, 30, 40 and 50 ºC under 30 W m^{-2} of UVA radiation performed in the solar simulator system and in the 700 mL-batch reactor. The experimental results are represented (dots) together with the predictions given by the *SODIS + thermal model* (solid lines). The profiles predicted by the model are significantly lower than experimental data, underestimating the bacterial inactivation efficiency that was really observed in the SODIS experiments done at the three selected temperatures. This result

clearly suggests that the relationship between temperature and solar radiation mechanisms is much more than the mere addition of both single effects. This is clear experimental evidence about the synergistic effect between temperature and solar UVA radiation occurring during solar water disinfection process. This result is in concordance with the reported by McGuigan and coworkers, who reached the same conclusion with empirical regressions [McGuigan *et al.*, 1998].

6.2.2 Role of the thermal inactivation of CAT

Catalase is an intracellular enzyme that plays a very important role in the defensive action against cellular oxidative stress. Due to the biological nature of this protein is one of the main targets that are susceptible to be affected by temperature and solar radiation. In fact, in the *SODIS model*, the photo-inactivation of catalase enzyme is estimated to be significantly quick, CAT photo-inactivation kinetic constant was found to be 10 fold higher than SOD inactivation. The kinetics of CAT inactivation within the temperature range of 30 – 60 ºC was previously investigated [Cantemir *et al.*, 2013]. CAT thermo-inactivation was characterized by relative initial rates, increased with incubation time and with temperature.

According to this, catalase is also expected to have a key role in the *E. coli* inactivation by the synergistic effect of solar radiation and thermal increase. To analyse the importance of CAT activity in the defence mechanisms of bacteria against the oxidative stress, simulation of the *SODIS + thermal model* was run in the absence of any catalase, i.e. $[CAT]_0 = 0$. Figure 6.3 shows the predicted values for bacteria inactivation using the model *SODIS + thermal model* with $[CAT]_0 = 0$ (dashed lines). As expected, since catalase is a bacterial defensive enzyme, simulations without catalase result in a faster bacterial inactivation than with catalase (solid lines, Figure 6.3). It is also observed at 30 ºC that the inactivation profile simulated is faster than experimental *E. coli* behaviour. This fact indicates that catalase is still effective at 30 ºC, which gets to reduce the bacterial inactivation rate as shown in the experimental results at 30 ºC.

However, at 40 and 50 °C, the simulations without catalase approach better the experimental results, but they still underestimated the bacterial inactivation values experimentally measured. Thus, although catalase is a susceptible radiation target, when cells are exposed to oxidative stress, there must be other intracellular targets participating in the process and that account for an accelerated bacterial inactivation.

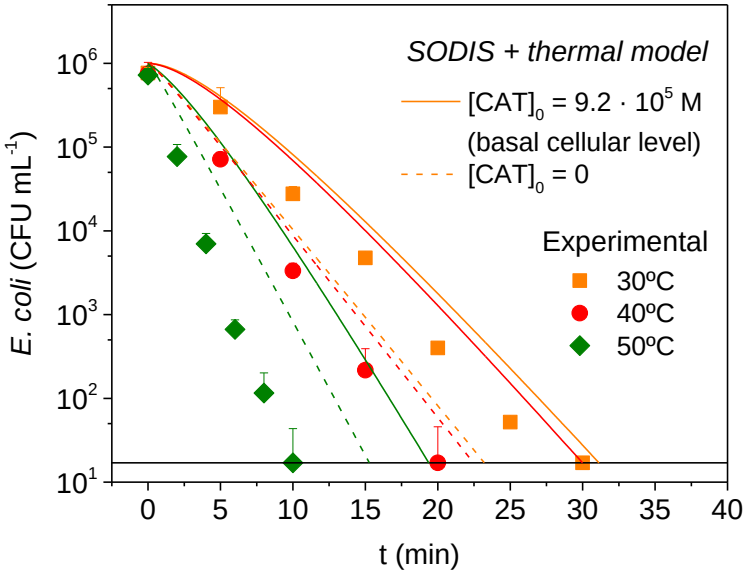

Figure 6.3. Inactivation of *E. coli* in isotonic water exposed to simulated sunlight (30 W m^{-2} of UVA) at 30, 40 and 50 °C. Experimental results (dots) and simulation of *SODIS + thermal model* (lines), with basal levels of CAT (solid lines, results from Figure 6.2) and with no CAT (dashed lines).

6.2.3 *Synergistic SODIS-thermal model*

According to previous results, it may be concluded that mild-heat improves solar disinfection efficiency and this factor must be considered as part of the solar process taking part of some intracellular reactions promoted by solar exposure, as a synergistic factor. Although CAT is a very important species in this process, it was proven that is not the only compound affected by the synergistic effect. Thus, the *SODIS + thermal model* was modified including this synergistic effect, leading to a new proposed model that predicts the behaviour of the intracellular

species and the concentration of viable bacteria when they are exposed to solar UVA radiation and taken into account the temperature factor for mild temperature values (30 to 55 ºC). The enhanced model is called from now on as *synergistic SODIS-thermal model* and is summarized by the equations in Table 6.2.

Table 6.2. *Synergistic SODIS-thermal model*: proposed mechanism for the synergistic effect between mild-heat and solar UVA photons on *E. coli*.

Reaction		Rate	Kinetic constant (M^{-1} s^{-1})	[a]Arrhenius parameters: ***A / Ea***
$O_2 + e^- \xrightarrow{T} O_2^{\bullet-}$	(6.6)	$k_1[O_2][e^-]$	$A_1 \cdot \exp\left(\frac{-Ea_1}{R \cdot T}\right)$	[b]$3.16 \cdot 10^{12}$ / $1.3 \cdot 10^4$
$O_2 + e^- \xrightarrow{h\nu, NADH, T} O_2^{\bullet-}$	(6.7)	$k_2[O_2][e^-]e^a_{NADH}$	$A_2 \cdot \exp\left(\frac{-Ea_2}{R \cdot T}\right)$	
$O_2^{\bullet-} + H^+ \xrightarrow{SOD} \frac{1}{2}H_2O_2 + \frac{1}{2}O_2$	(6.8)	$k_3[O_2^{\bullet-}][SOD]$	[c]10^9	
$Fe^{2+} + H_2O_2 \xrightarrow{T} Fe^{3+} + HO^- + HO^\bullet$	(6.9)	$k_4[Fe^{2+}][H_2O_2]$	$A_4 \cdot \exp\left(\frac{-Ea_4}{R \cdot T}\right)$	[d]$1.92 \cdot 10^9$ / $4.68 \cdot 10^4$
$Fe^{3+} + H_2O \xrightarrow{h\nu, T} Fe^{2+} + HO^\bullet + H^+$	(6.10)	$k_5[Fe^{3+}][H_2O]$ e^a_{Fe3+}	$A_5 \cdot \exp\left(\frac{-Ea_5}{R \cdot T}\right)$	
$H_2O_2 + HO^\bullet \rightarrow HO_2^\bullet + H_2O$	(6.11)	$k_6[H_2O_2][HO^\bullet]$	[b]$2.7 \cdot 10^7$	
$HO_2^\bullet \rightarrow \frac{1}{2}H_2O_2 + \frac{1}{2}O_2$	(6.12)	$k_7[HO_2^\bullet]^2$	[e]$8.3 \cdot 10^5$	
$H_2O_2 \xrightarrow{CAT} \frac{1}{2}O_2 + H_2O$	(6.13)	$k_8[H_2O_2][CAT]$	[f]$9 \cdot 10^5$	
$CAT \xrightarrow{h\nu, T} CAT_i$	(6.14)	$k_9[CAT]e^a_{CAT}$	$A_9 \cdot \exp\left(\frac{-Ea_9}{R \cdot T}\right)$	
$SOD \xrightarrow{h\nu} SOD_i$	(6.15)	$k_{10}[SOD]e^a_{SOD}$	[g]$1.56 \cdot 10^6$ cm^{-3} $Einstein^{-1}$	
$OM_{red} + HO^\bullet \rightarrow OM_{ox}$	(6.16)	$k_{11}[HO^\bullet]$	[g]$2.04 \cdot 10^4$ s^{-1}	
$OM_{red} + O_2^{\bullet-} \rightarrow OM_{ox}$	(6.17)	$k_{12}[O_2^{\bullet-}]$	[g]$1.36 \cdot 10^5$ s^{-1}	
$B_V \xrightarrow{HO^\bullet, O_2^{\bullet-}} B_i$	(6.18)	$k_{13}[HO^\bullet][O_2^{\bullet-}][B_V]$	[g]$8.03 \cdot 10^{15}$ M^{-2} s^{-1}	
$B_V \xrightarrow{T} B_i$	(6.19)	$k_{14}[B_V]$	$A_{14} \cdot \exp\left(\frac{-Ea_{14}}{R \cdot T}\right)$	$1.30 \cdot 10^{34}$ / $2.26 \cdot 10^5$ (this work)

[a] A_1 and A_4 in M^{-1} s^{-1}; A_{14} in s^{-1}; *Ea* in J mol^{-1}.
[b] Buxton *et al.*, 1988; [c] Abreu and Cabelli, 2010; [d] Farias et *al.*, 2009; [e] Gallard and De Laat, 2000; [f] Tao et *al.*, 2009; [g] determined in chapter 5.

The synergy UVA&T was included in those reactions where radiation was involved, briefly, in the photo-formation of superoxide radicals (reaction (6.7)), in the intracellular photo-Fenton process (reaction (6.10)) and in the CAT photo-

inactivation (reaction (6.14)). Thermal effect was not only included in photo-induced reactions, also temperature was incorporated in those reactions of which Arrhenius parameters were previously reported, as included in Table 6.2. Each step of the model is explained in detail below.

6.2.3.1 Intracellular ROS formation

Several ROS are formed in the interior of the cells due to the sunlight and temperature actions:

I. Superoxide radicals: The intracellular molecular oxygen is reduced to $O_2^{\bullet -}$ by electrons that come from the electron transport chain process. This reduction occurs by natural ways in the inner cells by the reaction (6.6). The thermal effect was included in the model using the Arrhenius parameters reported in other works [Buxton *et al.*, 1988]. $O_2^{\bullet -}$ is also formed by photo-inducted reduction of oxygen in presence of some photo-sensitizers as NADH [Chen and Schopfer, 1999]. This reaction is represented by the equation (6.7). Temperature was also considered in this reaction through Arrhenius parameters that are unknown, so they were taken as model's parameters (k_2 and Ea_2).

   The intracellular oxygen concentration is equivalent to extracellular oxygen [Imlay, 2003], i.e. the dissolved oxygen in water. This parameter is temperature dependent ranging from 236 to 177 μM, at 30 to 50 ºC, respectively. Nevertheless, the maximum intracellular oxygen concentration permitted for bacteria is 210 μM, in air-saturated bacteria cells [Imlay, 2003]. It was assumed that specific value for the regression of the experimental data. In the next section, it is presented an analysis of the influence of these slightly changes in the intracellular oxygen concentration due to temperature in the bacterial inactivation simulations.

II. Hydrogen peroxide: Superoxide radicals are converted to H_2O_2 in a reaction catalysed by SOD (equation (6.8)). Up to date, this reaction has been widely studied although not thermal dependence has been reported.

III. Hydroxyl radicals: $HO^{\bullet}$ are formed by thermal Fenton and photo-Fenton process that is a complex set of reactions that has high dependency on the pH and temperature. The main reactions are summarized [Farias *et al.*, 2009]:

$$Fe^{3+} + H_2O \xrightarrow{h\nu, T} Fe^{2+} + HO^{\bullet} + H^{+} \quad (6.20)$$

$$Fe^{2+} + H_2O_2 \xrightarrow{T} Fe^{3+} + HO^{-} + HO^{\bullet} \quad (6.21)$$

$$Fe^{3+} + H_2O_2 \xrightarrow{T} Fe^{2+} + H^{+} + HO_2^{\bullet} \quad (6.22)$$

$$Fe^{3+} + HO_2^{\bullet} \rightarrow Fe^{2+} + H^{+} + O_2 \quad (6.23)$$

$$Fe^{2+} + HO_2^{\bullet} + H^{+} \rightarrow Fe^{3+} + H_2O_2 \quad (6.24)$$

$$Fe^{2+} + HO^{\bullet} \rightarrow Fe^{3+} + HO^{-} \quad (6.25)$$

Farias *et al.* considered that thermal effect on the reactions (6.23) to (6.25) can be neglected, being only significant the temperature action in the reactions (6.20) to (6.22) [Farias *et al.*, 2009]. For modelling purposes, some simplifications were done:

(i) Reaction (6.22) in which hydrogen peroxide reacts with iron, was neglected because is a very slow reaction ($2 \cdot 10^{-3}$ M^{-1} s^{-1}, [Rossetti *et al.*, 2002]) in comparison with (6.21) (70 M^{-1} s^{-1}).

(ii) Reactions (6.23) and (6.24) were also neglected due to $HO_2^{\bullet}$ was not considered in this model.

(iii) From the point of view of $HO^{\bullet}$ reactivity, reaction (6.16) ($2.04 \cdot 10^{4}$ s^{-1}) is predominant over reaction (6.25) ($k_{apparent}$ = 10^{2} s^{-1} [De Laat and Gallard, 1999]); then reaction (6.25) was also neglected.

Thus, only reactions (6.20) and (6.21) were considered in this model, as in the previous *SODIS model* (chapter 5). Farias *et al.* correlated the Arrhenius parameters of these reactions in their kinetic study of the photo-Fenton

degradation of formic acid in the range of temperatures 20 to 55 ºC [Farias *et al.*, 2009]. The mentioned parameters were used in this work as is shown in Table 6.2.

IV. ROS recombination: due to the high reactivity of ROS, there are some recombination reactions to be considered. The most important ones considered in other kinetic models are the reactions (6.11) and (6.12) [Farias *et al.*, 2009; Rossetti *et al.*, 2002]. The effect of temperature in these reactions was considered negligible as previously studied by Farias and co-workers.

6.2.3.2 Hydrogen peroxide decomposition

H_2O_2 is naturally decomposed to water and oxygen by the catalytic action of CAT inside cells (reaction (6.13)). Although, temperature may affect to the catalase integrity, it has not been reported that the direct action of temperature alter significantly the H_2O_2 decomposition.

6.2.3.3 Enzymes photo-inactivation

The activity of the enzymes involved in ROS decomposition may be affected by thermal and photon action (reactions (6.14) and (6.15)). Thermal effect was included in the kinetics of CAT photo-inactivation by Arrhenius parameters. For modelling purposes, the following assumption was done: the value of k_9 estimated in *SODIS model* is valid for 25 ºC ($k_{9,25ºC}$ = 1.5 · 10^7 cm^3 $Einstein^{-1}$, chapter 5). Then, the pre-exponential factor A_9 is obtained by the following equation, resulting in only one model parameter, Ea_9:

$$A_9 = k_{9,25ºC} \cdot \exp\left(\frac{Ea_9}{R \cdot (25+273)}\right) \tag{6.26}$$

The thermal effect was not considered in SOD photo-inactivation due to SOD has fair thermal stability with a maximum activity in the range of 37 – 50 ºC [Petkar *et al.*, 2013; Zhang *et al.*, 2015], being affected only at temperature values higher than 70 ºC [Hearn *et al.*, 2001]. Also, it was previously observed that the

role of SOD compared with catalase is nearly negligible during the solar disinfection process (chapter 5).

6.2.3.4 Cellular damages and bacteria inactivation

The most reactive ROS are $HO^{\bullet}$ and $O_2^{\bullet-}$ and they are considered as the main responsible of the cellular damages by ROS in the cells. The ROS attack several intracellular targets and they are encompassed in the reactions (6.16) and (6.17) that include the oxidation of the organic matter susceptible to be oxidized (OM_{red}) by $HO^{\bullet}$ or $O_2^{\bullet-}$. In this case we have assumed that temperature has a negligible effect due to the high reactivity of ROS at this range of temperatures.

Finally, bacteria can be inactivated due to the action of either ROS (reaction (6.18)) or temperature (reaction (6.19)). The reaction (6.18) has a very high kinetic constant, and the effect of temperature in the range 10 – 55 ºC was considered negligible in relation with the reaction (6.19). The last reaction represents the cellular inactivation due to direct damages caused by temperature with no effect of light. This reaction is the same as represented by (6.1) whose Arrhenius parameters were previously determined.

Mass balance of viable bacteria has to be proposed for the entire reactor using the reactions (6.18) and (6.19). On the contrary, the rest of the reactions of Table 6.2 are intracellular reactions and have to be used to solve the mass balances of the internal species for a single cell. According to the isotropic hypothesis, the same internal reactions will occur in all cells without population, time or space preferences. Consequently, the change of the concentration of the intracellular species that are involved in the process could be considered the same in all cells. The assumptions to solve the mass balances are: (i) kinetic micro steady-state approximation for concentration of iron (Fe^{2+} and Fe^{3+}) and radicals ($O_2^{\bullet-}$, $HO^{\bullet}$ and $HO_2^{\bullet}$) inside a bacterial cell and (ii) iron released from cluster due to oxidative stress is neglected.

The iron balances in a single cell are:

$$\frac{\mathrm{d}\left[\mathrm{Fe}^{2+}\right]}{\mathrm{d}t} = -\frac{\mathrm{d}\left[\mathrm{Fe}^{3+}\right]}{\mathrm{d}t} = -k_4(\mathrm{T})\cdot\left[\mathrm{Fe}^{2+}\right]\left[\mathrm{H_2O_2}\right] + k_5(\mathrm{T})\left[\mathrm{Fe}^{3+}\right]\left[\mathrm{H_2O}\right]e^a_{\mathrm{Fe}^{3+}} \approx 0 \quad (6.27)$$

$$k_4(\mathrm{T})\cdot\left[\mathrm{Fe}^{2+}\right]\left[\mathrm{H_2O_2}\right] = k_5(\mathrm{T})\left[\mathrm{Fe}^{3+}\right]\left[\mathrm{H_2O}\right]e^a_{\mathrm{Fe}^{3+}} \quad (6.28)$$

The superoxide radical balance in a single cell is:

$$\frac{\mathrm{d}\left[\mathrm{O_2^{\bullet -}}\right]}{\mathrm{d}t} = k_1(\mathrm{T})\cdot\left[\mathrm{O_2}\right]\left[\mathrm{e^-}\right] + k_2(\mathrm{T})\left[\mathrm{O_2}\right]\left[\mathrm{e^-}\right]e^a_{\mathrm{NADH}} - k_3\left[\mathrm{O_2^{\bullet -}}\right]\left[\mathrm{SOD}\right] + \\ - k_{12}\left[\mathrm{O_2^{\bullet -}}\right] \approx 0 \quad (6.29)$$

$$\left[\mathrm{O_2^{\bullet -}}\right] = \frac{\delta_1\cdot\exp\left(\frac{-Ea_1}{R\cdot\mathrm{T}}\right) + \delta_2\cdot\exp\left(\frac{-Ea_2}{R\cdot\mathrm{T}}\right)e^a_{\mathrm{NADH}}}{k_3\left[\mathrm{SOD}\right] + k_{12}} \quad (6.30)$$

The hydroxyl radical balance in a single cell is:

$$\frac{\mathrm{d}\left[\mathrm{HO^{\bullet}}\right]}{\mathrm{d}t} = -k_6\left[\mathrm{H_2O_2}\right]\left[\mathrm{HO^{\bullet}}\right] - k_{11}\left[\mathrm{HO^{\bullet}}\right] + k_4(\mathrm{T})\left[\mathrm{Fe}^{2+}\right]\left[\mathrm{H_2O_2}\right] + \\ + k_5(\mathrm{T})\left[\mathrm{Fe}^{3+}\right]\left[\mathrm{H_2O}\right]e^a_{\mathrm{Fe}^{3+}} \approx 0 \quad (6.31)$$

$$\left[\mathrm{HO^{\bullet}}\right] = \frac{2\cdot\delta_3\cdot\exp\left(\frac{-Ea_4}{R\cdot\mathrm{T}}\right)\cdot\left[\mathrm{H_2O_2}\right]}{k_6\left[\mathrm{H_2O_2}\right] + k_{11}} \quad (6.32)$$

The hydroperoxyl radical balance in a single cell is:

$$\frac{\mathrm{d}\left[\mathrm{HO_2^{\bullet}}\right]}{\mathrm{d}t} = k_6\left[\mathrm{H_2O_2}\right]\left[\mathrm{HO^{\bullet}}\right] - k_7\left[\mathrm{HO_2^{\bullet}}\right]^2 \approx 0 \quad (6.33)$$

$$\left[\mathrm{HO_2^{\bullet}}\right] = \sqrt{\frac{k_6}{k_7}\left[\mathrm{H_2O_2}\right]\left[\mathrm{HO^{\bullet}}\right]} \quad (6.34)$$

where,

$$\begin{aligned}\delta_1 &= A_1\left[\mathrm{O_2}\right]\left[\mathrm{e^-}\right]\\ \delta_2 &= A_2\left[\mathrm{O_2}\right]\left[\mathrm{e^-}\right]\\ \delta_3 &= A_4\left[\mathrm{Fe^{2+}}\right]\end{aligned} \tag{6.35}$$

The hydrogen peroxide is a compound that cannot be considered in a micro steady state inside the bacterial cell. The rate expression of H_2O_2 is obtained by:

$$\begin{aligned}\frac{\mathrm{d}\left[\mathrm{H_2O_2}\right]}{\mathrm{d}t} = \frac{1}{2}k_3\left[\mathrm{O_2^{\cdot-}}\right][\mathrm{SOD}] + \frac{1}{2}k_7\left[\mathrm{HO_2^{\cdot}}\right]^2 - k_4(\mathrm{T})\left[\mathrm{Fe^{2+}}\right]\left[\mathrm{H_2O_2}\right] + \\ - k_6\left[\mathrm{H_2O_2}\right]\left[\mathrm{HO^{\cdot}}\right] - k_8\left[\mathrm{H_2O_2}\right][\mathrm{CAT}]\end{aligned} \tag{6.36}$$

Introducing (6.30), (6.32) and (6.34) in (6.36), the final expression for hydrogen peroxide concentration over the time is:

$$\begin{aligned}\frac{\mathrm{d}\left[\mathrm{H_2O_2}\right]}{\mathrm{d}t} = \frac{1}{2}\cdot\frac{k_3\cdot\left[\delta_1\cdot\exp\left(\frac{-Ea_1}{R\cdot\mathrm{T}}\right)+\delta_2\cdot\exp\left(\frac{-Ea_2}{R\cdot\mathrm{T}}\right)\cdot e^a_{\mathrm{NADH}}\right][\mathrm{SOD}]}{k_3[\mathrm{SOD}]+k_{12}} + \\ -\frac{\delta_3\cdot\exp\left(\frac{-Ea_4}{R\cdot\mathrm{T}}\right)\cdot k_6\left[\mathrm{H_2O_2}\right]^2}{k_6\left[\mathrm{H_2O_2}\right]+k_{11}} - \left(\delta_3\cdot\exp\left(\frac{-Ea_4}{R\cdot\mathrm{T}}\right)+k_8[\mathrm{CAT}]\right)\left[\mathrm{H_2O_2}\right]\end{aligned} \tag{6.37}$$

The enzymes are inactive over treatment time due to the photon action. Among this, CAT and SOD are species in not steady state:

$$\frac{\mathrm{d}[\mathrm{CAT}]}{\mathrm{d}t} = -k_9(\mathrm{T})[\mathrm{CAT}]e^a_{\mathrm{CAT}} \neq 0 \tag{6.38}$$

$$\frac{\mathrm{d}[\mathrm{SOD}]}{\mathrm{d}t} = -k_{10}[\mathrm{SOD}]e^a_{\mathrm{SOD}} \neq 0 \tag{6.39}$$

Introducing the expression of LVRPA of CAT and SOD determined by the equation (1.50) and (5.1) in the above expressions, the following formulas are obtained:

$$\frac{\mathrm{d}[\mathrm{CAT}]}{\mathrm{d}t} = -k_9(\mathrm{T}) \cdot \overline{\kappa}^{*}_{\mathrm{CAT}} \cdot \overline{G} \cdot [\mathrm{CAT}]^2 \tag{6.40}$$

$$\frac{\mathrm{d}[\mathrm{SOD}]}{\mathrm{d}t} = -k_{10} \cdot \overline{\kappa}^{*}_{\mathrm{SOD}} \cdot \overline{G} \cdot [\mathrm{SOD}]^2 \tag{6.41}$$

Integrating these equations from time $t = 0$ (initial concentrations of enzymes, $[\mathrm{CAT}]_0$ and $[\mathrm{SOD}]_0$) up to an instant time t ([CAT] and [SOD]):

$$[\mathrm{CAT}] = \frac{1}{1/[\mathrm{CAT}]_0 + A_9 \cdot \exp\left(\frac{-Ea_9}{R \cdot \mathrm{T}}\right) \cdot \overline{\kappa}^{*}_{\mathrm{CAT}} \cdot \overline{G} \cdot t} \tag{6.42}$$

$$[\mathrm{SOD}] = \frac{1}{1/[\mathrm{SOD}]_0 + k_{10} \cdot \overline{\kappa}^{*}_{\mathrm{SOD}} \cdot \overline{G} \cdot t} \tag{6.43}$$

Finally, the reaction rate of the bacteria inactivation is obtained from the mass balance of the bacteria in the reactor:

$$\frac{\mathrm{d}[\mathrm{B_v}]}{\mathrm{d}t} = -k_{13}[\mathrm{HO^{\bullet}}][\mathrm{O_2^{\bullet -}}][\mathrm{B_v}] - k_{14}(\mathrm{T})[\mathrm{B_v}] \tag{6.44}$$

The reaction rate of the bacteria inactivation (CFU $\mathrm{mL^{-1}\ s^{-1}}$) is referred to the reactor volume while the apparent kinetic constant k_{13} ($\mathrm{M^{-2}\ s^{-1}}$) is referred to the bacterial cell volume. This is due to that viable bacterial reaction rate in water is dependent on the intracellular concentrations of $\mathrm{HO^{\bullet}}$ and $\mathrm{O_2^{\bullet -}}$.

Introducing the expression of the radicals' concentration and reorganizing terms, the following expression is obtained:

$$\frac{\mathrm{d}[\mathrm{B_v}]}{\mathrm{d}t} = -\left(\begin{array}{l} \dfrac{2 \cdot \left[\delta_1 \cdot \exp\left(\dfrac{-Ea_1}{R \cdot \mathrm{T}}\right) + \delta_2 \cdot \exp\left(\dfrac{-Ea_2}{R \cdot \mathrm{T}}\right) \cdot e^{a}_{\mathrm{NADH}} \right]}{\left(k_6[\mathrm{H_2O_2}] + k_{11}\right) \cdot \left(k_3[\mathrm{SOD}] + k_{12}\right)} \cdot \\ \cdot \delta_3 \cdot \exp\left(\dfrac{-Ea_4}{R \cdot \mathrm{T}}\right) \cdot k_{13}[\mathrm{H_2O_2}] + A_{14} \cdot \exp\left(\dfrac{-Ea_{14}}{R \cdot \mathrm{T}}\right) \end{array} \right) [\mathrm{B_v}] \tag{6.45}$$

Finally, to simulate the change over time of the bacterial concentration or the internal species concentrations, it is necessary to solve simultaneously the differential equations that define the concentration of viable bacteria (equation (6.45)), H_2O_2 (6.37) and enzymes (6.42), (6.43). To do so, the three model-parameters (A_2, Ea_2 and Ea_9) are correlated minimizing the NRMSLE with the experimental data (MATLAB® code used is in Appendix B). The experimental results used for this regression were obtained from the disinfection experiments performed at different temperatures (30, 40 and 50 °C) at 30 W m^{-2} of solar UVA in the simulator system within isotonic water in the 700 mL-batch reactor (Figure 6.4). Values obtained from the regression are:

$Ea_2 = 3.76 \cdot 10^3$ J mol^{-1}

$A_2 = 7.07 \cdot 10^{21}$ cm^3 $Einstein^{-1}$ M^{-1}

$Ea_9 = 5.31 \cdot 10^4$ J mol^{-1}

NRMSLE = 8.79 %

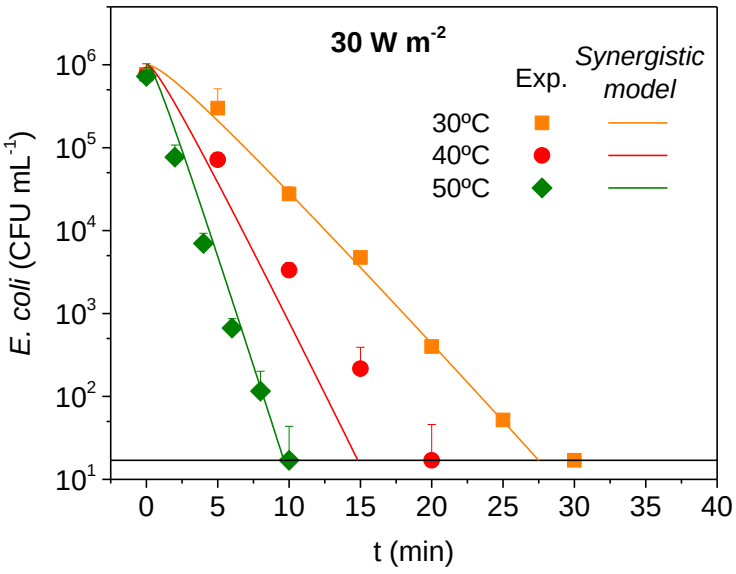

Figure 6.4. Inactivation of *E. coli* in clear water exposed to simulated sunlight (30 W m^{-2} of UVA) at 30, 40 and 50 °C. Experimental results (dots) and simulation of *synergistic SODIS-thermal model* (lines).

Figure 6.4 shows the experimental and modelled results in the different evaluated conditions. This evidences that the obtained model using the optimized parameters fits satisfactorily experimental results. The NRMSLE of the experiments of 30 and 50 ºC are smaller than 10 % (4.2 and 4.9 %, respectively) that means an excellent regression. In the experiment of 40 ºC, the regression describes a slight faster inactivation than the experimental results, just 5 minutes. Nevertheless, the NRMSLE of the experiment at 40 ºC is lower than 20 % (17.3 %), so the regression could be considered good [Raes *et al.*, 2012].

It is important to note that parameters' values obtained are specifically estimated for the operational conditions of the experiments of in this work, i.e. type of microorganism and growth phase, reactor setup that determine the inlet UVA and water matrix that could interfere in UVA absorption.

6.3 Effect of the intracellular oxygen in the *synergistic SODIS-thermal model*

To simplify the data fitting analysis, the intracellular O_2 concentration was considered independent of T and set on 210 μM (section 6.2.3.1). Then, the thermal effect on intracellular O_2 was considered, observing little differences in the simulation results at the three selected temperatures (Figure 6.5).

The final treatment time differ less than 3 minutes in the evaluated temperature range. Therefore, it can be concluded that although the temperature affects the intracellular oxygen concentration, this influence is negligible from the bacterial inactivation point of view.

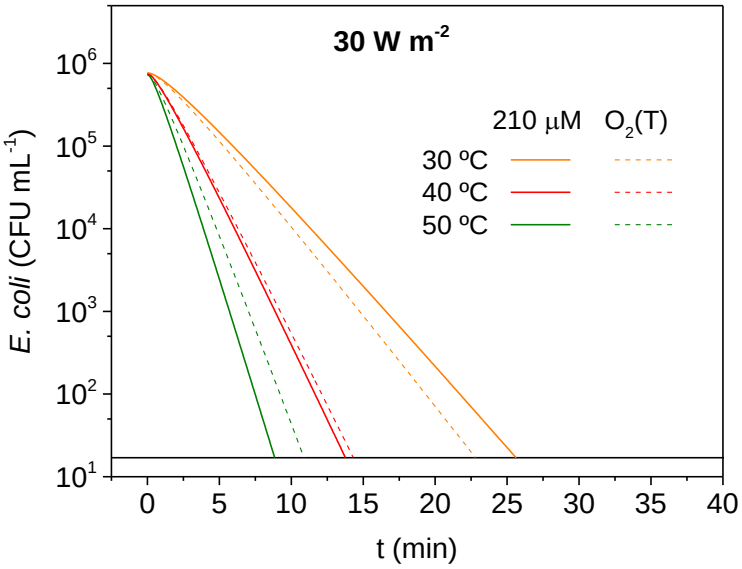

Figure 6.5. *Synergistic SODIS-thermal model* simulations of *E. coli* inactivation with a basal concentration of O_2 of 210 µM and different values of O_2 concentration determined by the T (236, 202 and 177 µM, for 30, 40 and 50 ºC, respectively).

6.4 Validation of the *synergistic SODIS-thermal model*

This mechanistic model was obtained by regression with experimental data of the inactivation of *E. coli* by simulated sunlight at different temperatures and 30 W m^{-2} of UVA. The validation of the proposed model was developed under different irradiances and in two different scenarios: (i) keeping the water temperature constant and (ii) increasing the temperature during the solar water disinfection process to simulate the real conditions of the SODIS process.

Figure 6.6 shows the experimental and the simulated data of *E. coli* inactivation at different irradiances values. The experiments represented in Figure 6.6 (a) were performed at a constant temperature of 30 ºC while experiments of Figure 6.6 (b) were carried out with variable temperature ramped from 35 – 40 ºC to 30 – 50 ºC. In the second case, the temperature was introduced in the model code in MATLAB® as a polynomial equation (time dependent). It is observed that model data fit accurately the experimental results, with a NRMSLE for each experiment less than 10 %.

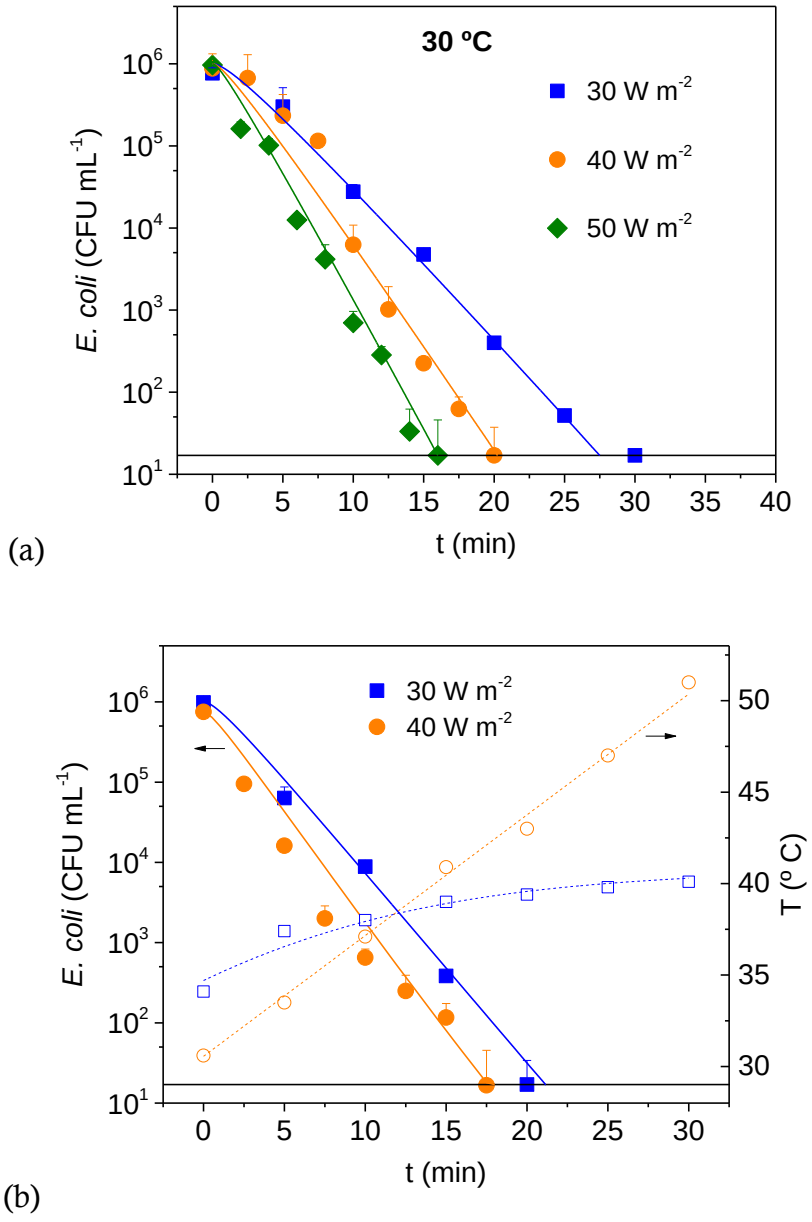

Figure 6.6. Inactivation of *E. coli* in isotonic water exposed to simulated sunlight at constant irradiance values of 30, 40 and 50 W m^{-2} of UVA. Experimental (dots) and modelled by the *synergistic SODIS-thermal model* (lines) results of *E. coli* inactivation (closed dots and solid lines) and temperature (open dots and dashed lines) conducted at (a) constant temperature of 30 °C and (b) temperature increases.

The *synergistic SODIS-thermal model* describes satisfactorily the *E. coli* inactivation results obtained during the exposure of the bacterial suspension to simulated sunlight at different constant irradiances (ranged from 30 to 50 W m^{-2} of UVA) and different temperature values (ranged from 30 to 50 °C that is the typically

values in real SODIS applications). The model was validated for constant values of water temperature (Figure 6.6 (a)) and for increasing values of temperature (following the SODIS temperature profile) during the process (Figure 6.6 (b)).

6.5 Conclusions of chapter 6

The model of the synergistic effect between mild temperature and solar UVA radiation for SODIS described for *E. coli* inactivation in isotonic water is a considerable advance for the knowledge on the mechanisms underpinning solar water disinfection. Temperature effect has been included in a SODIS mechanistic model, to explain the well-recognized synergistic effect between water temperature and UVA radiation during solar water disinfection. The new SODIS model is capable to reproduce successfully the time-profile of viable bacterial concentration over treatment time under different irradiances and temperatures. The synergistic effect was included in the model by means of the temperature dependence of the kinetic constants. The Arrhenius parameters for the photo-generation of $O_2^{\bullet-}$ by the reduction from oxygen (Ea_2 = 3.76 · 10^3 J mol^{-1}, A_2 = 7.07 · 10^{21} cm^3 $Einstein^{-1}$ M^{-1}) and the CAT photo-inactivation (Ea_9 = 5.31 · 10^4 J mol^{-1}, A_9 = 3.05 · 10^{16} cm^3 $Einstein^{-1}$) were determined. This mechanistic approach of the synergistic effect between optical and thermal effects over bacterial suspensions will permit to use it to predict results for real SODIS conditions where irradiation and water temperature change through time, to model new concepts of SODIS reactors and to optimize their disinfection performance in terms of final disinfection result and total volume of water treated.

CHAPTER 7

VALIDATION OF SOLAR WATER DISINFECTION MODEL IN SOLAR REACTORS UNDER REAL FIELD CONDITIONS

7 VALIDATION OF SOLAR WATER DISINFECTION MODEL IN SOLAR REACTORS UNDER REAL FIELD CONDITIONS

In this chapter, the mechanistic model presented in chapter 6 has been validated in several solar reactors under real field conditions. The *synergistic SODIS-thermal model* was used to describe the inactivation profile of *E. coli* with different weather conditions under natural sunlight using isotonic and well water in the 2 L-PET batch reactor. Irradiance and temperature were significantly variable depending on the local climate conditions, influencing the solar disinfection treatment. The effect of water turbidity in the range of 5 to 300 NTU was evaluated using artificial (kaolin) and natural (red soils) agents. The averaged incident radiation in the reactor volume was calculated by solving the Radiative Transfer Equation (RTE) using a 2-dimensional 2-directional Discrete Ordinate Method (2D-2D DOM). Different reactor designs were also used to validate the model with different materials (polycarbonate, borosilicate and methacrylate) and different volumes ranged from 2 to 22.5 L. The synergistic SODIS-thermal model was proven to be capable to predict the *E. coli* inactivation times-profiles at real conditions of changing irradiance, temperature and turbidity in several reactor configurations.

7.1 Incident radiation determination

7.1.1 General considerations of natural sunlight

The parameters of the mechanistic models developed in chapters 5 and 6 were obtained with experimental data obtained in the solar simulator system. The reactor design (700 mL-batch reactor) and the source of light were used to permit the selection of irradiance set point as the incident radiation inside the reactor. The light reached directly the water surface and it could be considered homogenous radiation in the entire photo-reactor due to the reactor dimensions (large diameter and small optical thickness).

The objective of this chapter is to validate the synergistic SODIS-thermal model under real sunlight. The 700 mL-batch reactor used for the development of the model was discarded to use under natural sunlight because some shadows regions were generated in the water surface due to the walls of the reactor and the sun position. The 2 L-PET batch reactor was selected for the experiments run in this chapter since is the most widely used reactor in SODIS applications.

The effect of the solar radiation angle is represented in Figure 7.1 that shows a scheme of the rays and the optical path length of a 2 L-PET batch reactor. Considering that the reactor is located in the north-south orientation, in the Figure 7.1 (a) is represented the effect of the azimuthal angle that does not affect to the total incident radiation that could be considered independent on the radiation angle during the day. In the Figure 7.1 (b), it is observed the effect of the altitude angle and how it affects to the incident radiation. This angle and hence the incident radiation is dependent on the date.

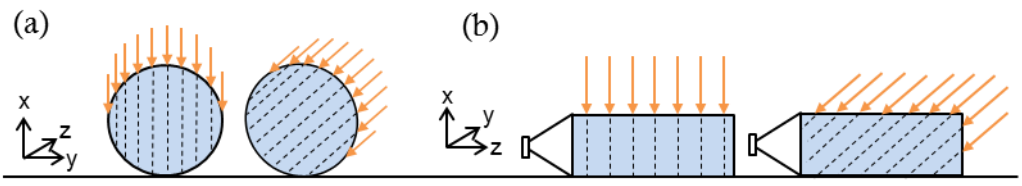

Figure 7.1. Scheme of the solar radiation rays in a 2 L-PET reactor.

Independently on the radiation angle, a pyranometer located horizontally measures the incident irradiance in a horizontal surface that is considered equal to the incident radiation in the walls of the photo-reactor, $I_{0,w}$. Then, the irradiance in the inner walls I_0 could be estimated using the material transmittance value, T:

$$I_0 = I_{0,w} \cdot T \tag{7.1}$$

In systems containing clear water, it is assumed that water absorption is neglected. Among this, I_0 is homogeneous inside the entire photo-reactor.

Nevertheless, in turbid waters, the suspended particles scatter the radiation, modifying the inlet irradiance value and decreasing the UVA light available to solar disinfection. The radiation profiles and local values of the incident radiation in every position of the reactor can be calculated by solution of the Radiative Transfer Equation (RTE), as described in next sections for the 2 L-PET batch reactor.

7.1.2 Incident radiation in turbid water in the 2 L-PET reactor

For turbid water, the incident radiation decreases due to the scattering of the particles in suspension. The RTE has been used for determining the radiation balance inside the photo-reactor available for the SODIS process. The geometry of the 2 L-PET batch reactor has been considered to define the boundary conditions.

7.1.2.1 Geometry simplification

In the Cartesian geometry, let consider the position of the reactor as is shown in Figure 7.2 (a) in which X is the direction of the incoming radiation. Some assumptions and simplifications are must be considered:

- The radiation incident in the photo-reactor, $I_{0,w}$, could be assumed to be perpendicular to the reactor wall and it can be represented by the irradiance on the horizontal plane, i.e. the Earth surface.

- The irradiance in the inner wall is obtained by the equation (7.1).
- The irradiance is considered constant in the Z direction. Henceforth, the problem is simplified to two dimensions (x,y).
- The optical path length of the reactor regarding the incidence direction of the incoming rays depends on the position (x,y) as is shown in the Figure 7.2 (b). In order to simplify the solution of the RTE, an equivalent optical path length is considered. The geometry of the reactor is assumed to be a parallelepiped as the one shown in the Figure 7.2 (c).

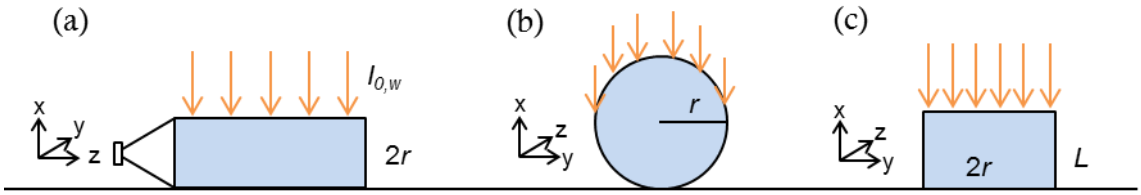

Figure 7.2. Scheme view of the 2 L-PET batch reactor (a) XZ plane, (b) XY plane and (c) XY plane of the parallelepiped approximation.

The equivalent optical path length distance of the entire circumference is equal than the semi-circumference of radius *r*. Let consider a distance *x* from the centre with an optical path length *L* (Figure 7.3), and applying the Pythagoras theorem:

$$L = 2 \cdot \sqrt{r^2 - x^2} \tag{7.2}$$

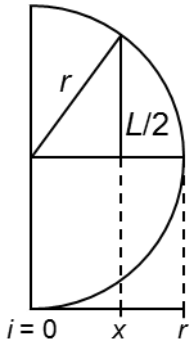

Figure 7.3. Scheme of a semi-circumference of radius *r* and an optical path length of *L* at a distance *x* from the centre.

The equivalent optical path length is obtained from the following equation whose solution is developed in Table 7.1:

$$< L >= \frac{\int_0^r L(x)\,\mathrm{d}x}{\int_0^r \mathrm{d}x} \tag{7.3}$$

Table 7.1. Mathematical solution of the equivalent optical path length of the 2 L-PET batch reactor.

Introducing equation (7.2) into (7.3)	$< L >= \frac{\int_0^r 2\cdot\sqrt{r^2-x^2}\,\mathrm{d}x}{\int_0^r \mathrm{d}x} = \frac{2\cdot r\cdot\int_0^r \sqrt{1-\left(\frac{x}{r}\right)^2}\,\mathrm{d}x}{\int_0^r \mathrm{d}x}$	(7.4)
Change of variable	$\frac{x}{r}=\sin t \quad \rightarrow \quad t=\arcsin\left(\frac{x}{r}\right)$ $\mathrm{d}x = r\cdot\cos t\,\mathrm{d}t$	(7.5)
Applying the change of variable to the integral of equation (7.4)	$\int\sqrt{1-\left(\frac{x}{r}\right)^2}\,\mathrm{d}x = \int\sqrt{1-\sin^2 t}\cdot r\cdot\cos t\,\mathrm{d}t = r\int\cos^2 t\,\mathrm{d}t = r\cdot I$	(7.6)
Integration by parts	$u=\cos t \quad \rightarrow \quad \mathrm{d}u=-\sin t\,\mathrm{d}t$ $\mathrm{d}v=\cos t\,\mathrm{d}t \quad \rightarrow \quad v=\sin t$	(7.7)
Applying integration by parts method to the integral I (equation (7.6))	$I=\sin t\cdot\cos t+\int\sin^2 t\,\mathrm{d}t=\sin t\cdot\cos t+\int\left(1-\cos^2 t\right)\mathrm{d}t=$ $=\sin t\cdot\cos t+t-\int\cos^2 t\,\mathrm{d}t=\sin t\cdot\cos t+t-I \quad\Rightarrow$ $2I=\sin t\cdot\cos t+t \;\Rightarrow\; I=\frac{\sin t\cdot\cos t+t}{2}$	(7.8)
Introducing equation (7.8) into (7.6) and applying the change of variable of (7.5)	$\int\sqrt{1-\left(\frac{x}{r}\right)^2}\,\mathrm{d}x = r\cdot\frac{\sin t\cdot\cos t+t}{2} = r\cdot\frac{\left(\frac{x}{r}\right)\cdot\sqrt{1-\frac{x^2}{r^2}}+\arcsin\left(\frac{x}{r}\right)}{2}$	(7.9)
Introducing equation (7.9) into (7.4)	$< L >= \frac{r^2\left[\left(\frac{x}{r}\right)\cdot\sqrt{1-\frac{x^2}{r^2}}+\arcsin\left(\frac{x}{r}\right)\right]_0^r}{[x]_0^r} = \frac{\pi}{2}\cdot r$	(7.10)

7.1.2.2 Light model definition

The RTE describes the macroscopic conservation law of the energy streaming in the direction of propagation Ω. The irradiance in every system point $I_{\lambda,\Omega}$, could be obtained from the RTE expressed in two-dimensional Cartesian coordinates:

$$\mu\frac{\partial I_{\lambda,\Omega}(x,y)}{\partial x}+\eta\frac{\partial I_{\lambda,\Omega}(x,y)}{\partial y}=-(\kappa_\lambda+\sigma_\lambda)\cdot I_{\lambda,\Omega}(x,y)+ \\ +\frac{\sigma_\lambda}{2\pi}\cdot\int_{\Omega'=2\pi}p(\Omega'\rightarrow\Omega)\cdot I_{\lambda,\Omega'}(x,y)\,\mathrm{d}\Omega' \tag{7.11}$$

where, μ and η are the direction cosines of Ω with respect to the (x,y) axes, κ_λ and σ_λ are the absorption and scattering coefficients, respectively and p (Ω'→Ω) is the phase function that describes the scattering distribution.

In this work, a 2-dimensional 2-directional discrete ordinate method (DOM) has been applied to solve the RTE. This method has been used firstly in the neutron transport theory [Lee, 1962; Duderstadt and Martin, 1979] but it has been also applied to solve the RTE in other works [Romero *et al.*, 1997; Marugán *et al.*, 2006]. The DOM permits to transform the integro-differential equation RTE into a system of algebraic equations that can be solved by computation by the discretization of the systems in small cells. The RTE is defined as an algebraic equation that has to be solved for every cell.

Figure 7.4 represents the discretization of the reactor determined by N_X and N_Y (number of divisions of X and Y axis) and M (number of divisions of the radiation direction, i.e. M = 8 in Figure 7.4). L_X is the equivalent optical path length obtained by the equation (7.10) and L_Y the diameter of the batch reactor. The number of divisions of the radiation M, determined the values of the direction cosines, μ and η, as is shown in Figure 7.4: μ takes positives values in the quadrants I and IV and negatives in the quadrants II and III, while η takes positives values in the quadrants I and II and negatives in the quadrants III and IV.

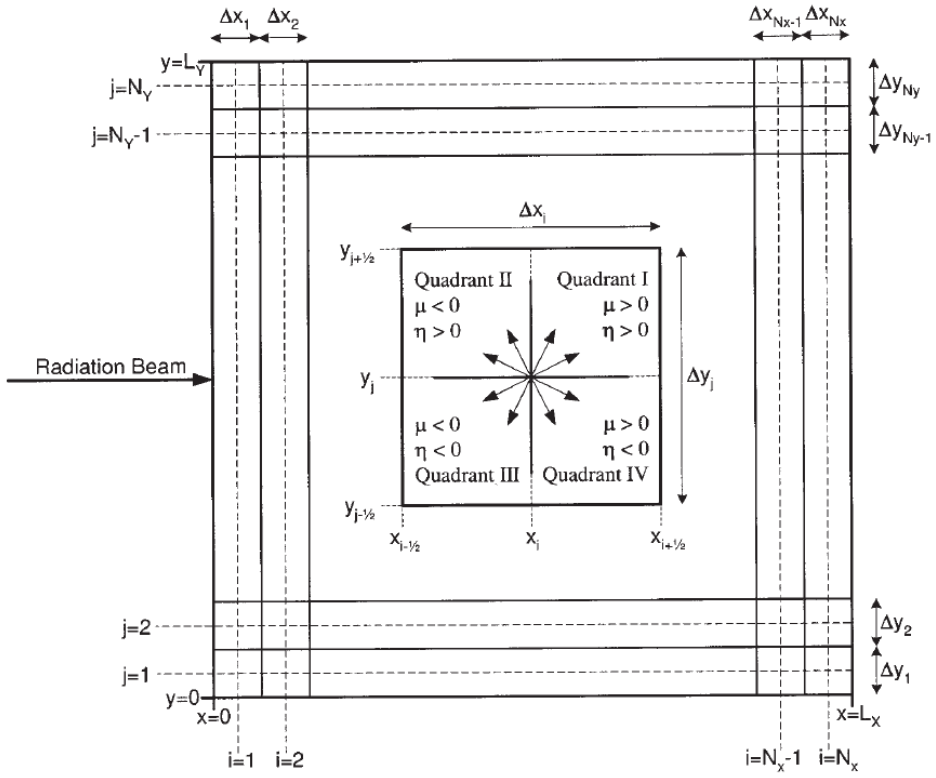

Figure 7.4. Spatial mesh for the 2-dimensional, 2-directional discretization of the equivalent parallelepiped 2 L-PET batch reactor [Marugán *et al.*, 2006].

The RTE applied to the cell *i,j* permits to obtain the monochromatic radiation at every light direction *m*:

$$I_{i,j,m} = \frac{2\Delta y_j |\mu_m|}{D} \cdot I_{i\pm 1/2,j,m} + \frac{2\Delta x_i |\eta_m|}{D} \cdot I_{i,j\pm 1/2,m} + \frac{S_{i,j,m}\Delta x_i \Delta y_j}{D} \tag{7.12}$$

where

$$D = 2\Delta y_j |\mu_m| + 2\Delta x_i |\eta_m| + (\kappa_\lambda + \sigma_\lambda)\Delta x_i \Delta y_j \tag{7.13}$$

$$S_{i,j,m} = \frac{\sigma_\lambda}{2\pi} \cdot \int_{\Omega'=2\pi} p(\Omega' \to \Omega) \cdot I_{i,j,m} d\Omega' \tag{7.14}$$

The source term *S* is the corresponding to the in-scattering contribution and it could be obtained using the Gaussian quadrature [Duderstadt and Martin, 1979]:

$$S_{i,j,m} = \frac{\sigma_\lambda}{2\pi} \cdot \sum_{n=1}^{N} \omega_n \cdot p_{nm} \cdot I_{i,j,m} \tag{7.15}$$

where ω_n is the Gaussian quadrature weighting factor.

The radiation intensity in the cell-edges could be obtained according to the symmetric diamonds difference relations:

$$I_{i,j,m} = \frac{1}{2} \cdot \left(I_{i+1/2,j,m} + I_{i-1/2,j,m} \right) \tag{7.16}$$

$$I_{i,j,m} = \frac{1}{2} \cdot \left(I_{i,j+1/2,m} + I_{i,j-1/2,m} \right) \tag{7.17}$$

Finally, the incident radiation that is available inside the entire photo-reactor is obtained:

$$\overline{G} = 2\pi \cdot \int_{2\pi} I(x,y)\, \mathrm{d}\Omega \tag{7.18}$$

7.1.2.3 Light model solution

The solution of the light model was developed through MATLAB® software. The code is presented in the Appendix C. Previously, some assumptions were done:

- Isotropic scattering, which means that all direction contributions are equally distributed. In this case, the phase function takes the value 1.
- Light scattering is due to kaolin or red soils particles added to the water while absorption is due to the bacteria cells. The absorbance spectrum of solutions with different concentration of kaolin, red soils and bacteria were measured to estimate their optical properties. The kaolin and red soils specific scattering coefficient σ^* were found to be 0.00278 and 0.00292 cm^{-1} NTU^{-1}, respectively (data averaged for UVA range). The absorption coefficient resulted to be 0.0059 cm^{-1} for a bacterial solution of 10^6 CFU mL^{-1} (UVA-averaged).

- 200 divisions in x and y ($N_X = N_Y = 200$) and 36 directions of each quadrant ($M = 144$) were considered. The discrete S_{16} approximation was used to obtain the values of ω_m, μ_m and η_m as shown in Figure 7.5 [Lee, 1962].

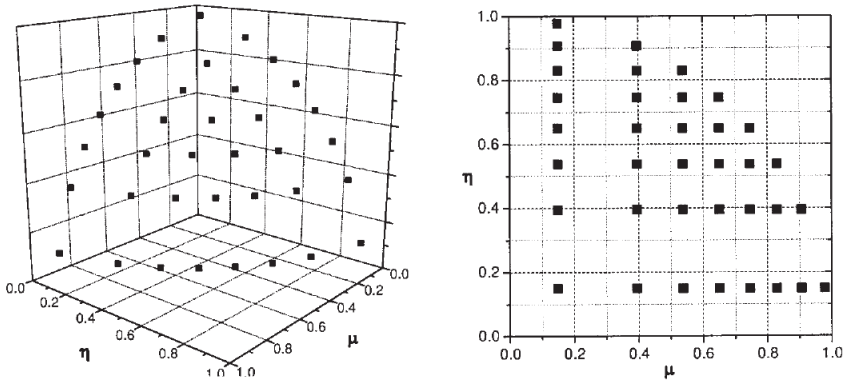

Figure 7.5. Director cosines values used for the solution of the light model by DOM [Marugán *et al.*, 2006].

The problem to solve is determined the following boundary conditions:

- Direct inlet radiation at $x = 0$ (direction $\mu = 1$) obtained from equation (7.1).
- Walls semi-transparent with any back-scattering but with some absorption and forward scattering, which means null inlet radiation at $x = L_X$ (directions of quadrants II and III, $\mu < 0$), $y = 0$ (quadrants I and II, $\eta > 0$) and $y = L_Y$ (quadrants III and IV, $\eta < 0$).

Figure 7.6 shows the steps to solve the light model of the 2 L-PET batch reactor. Firstly, it is solved from the cell corner in which boundary conditions are known: from the point $(x,y) = (1,1)$ and the quadrant I direction. Then, (i) cell-centred intensity is calculated by (7.12) from the known inlet values and (ii) outlet values of the cell-edges from the diamonds differences relations by (7.16) and (7.17). For the estimation of cell-centred intensity, it is required the source term value that depends on the cell-centred intensities, so it is necessary to initialize this value and then, to do iterations until the S calculated from equation (7.15) coincide with the value used.

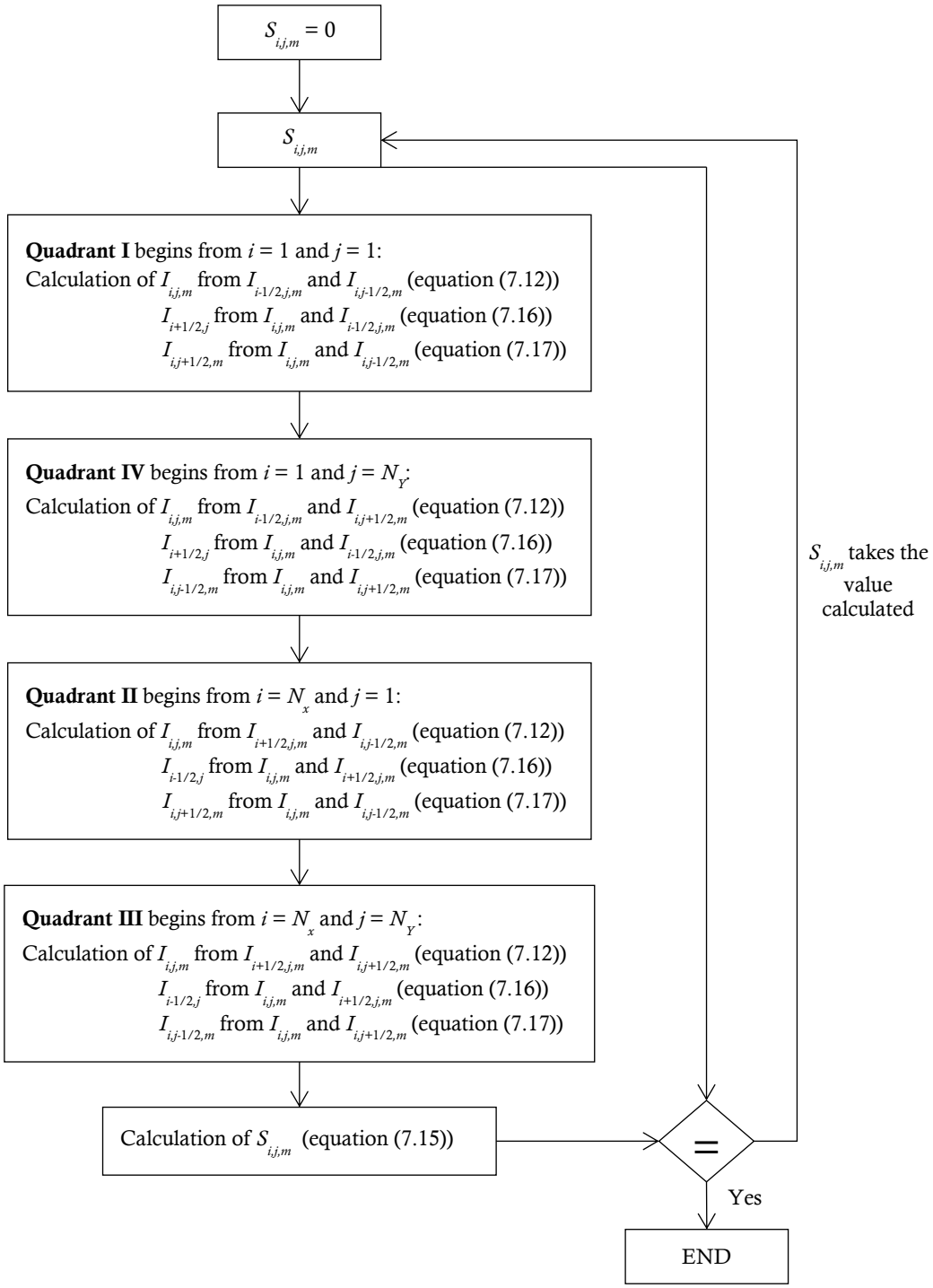

Figure 7.6. Algorithm for the RTE solution applied to the 2 L-PET batch reactor.

7.2 Comparison of the experimental and modelled data

The experiments conducted in different type of reactors, within different water matrixes and different weather conditions were performed in order to validate the synergistic SODIS-thermal model developed in the previous chapter. The input parameters of the model are:

- Initial bacterial concentration: determined experimentally by the standard plate counting method.
- Water temperature: data was monitored every 30 or 60 minutes during the experiments and introduced in the model as a function on time (polynomial of second-order).
- Inlet irradiance: UVA data was monitored every 1 min during the experiments and introduced in the model as a vector parameter. The UVA value was corrected due to the turbidity effect by the corrector factor, *f*:

$$f = \frac{\overline{G}}{I_0} \tag{7.19}$$

  The corrector factor takes the value of 1 in clear waters. For the experiments with kaolin, the loss of turbidity has been taken into account due to the high precipitation of the compound. In this case, *f* value was introduced in the model as a function on time.

In the Appendix D, it is shown an example of the MATLAB® code used for the simulations of the experiments performed under real sunlight.

7.2.1 Climate conditions effect

The climate condition is one of the most important factors for bacteria inactivation efficiency as it determines the incident irradiance and water temperature. Solar water disinfection was performed within isotonic water in the 2 L-PET batch reactor in consecutive days. Figure 7.7 (a) shows the results of experiments conducted in sunny days with similar irradiance values but with water temperature values slightly different.

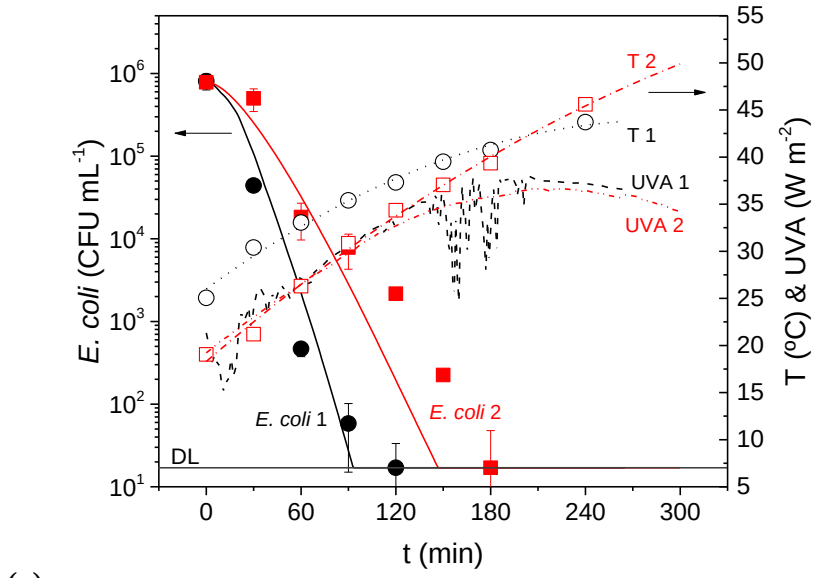

(a)

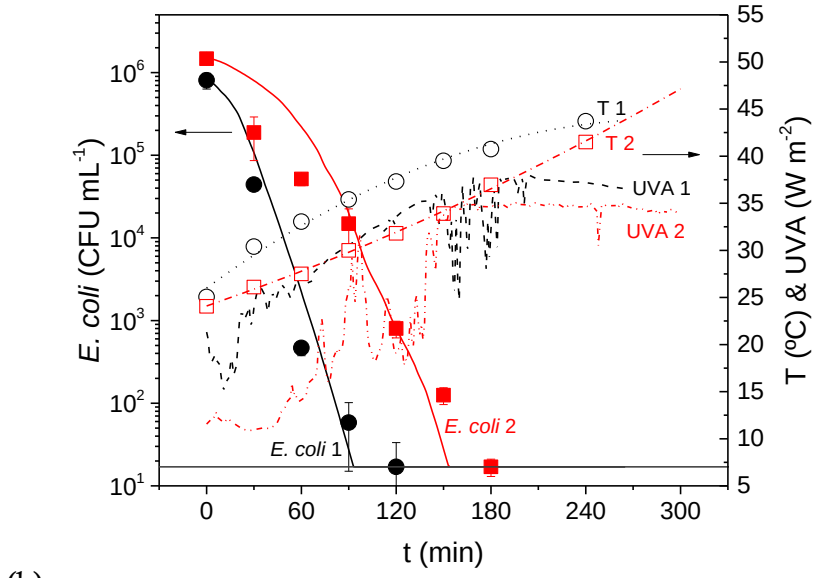

(b)

Figure 7.7. Experimental (dots) and simulated by synergistic SODIS-thermal model (lines) SODIS results under natural sunlight within isotonic water in 2 L-PET batch reactor with different climate conditions: (a) different water temperature values (experiment 1 – higher temperature, in black and circles; experiment 2 – lower temperature, in red and squares) and (b) different irradiance values (experiment 1 – sunny day, in black and circles; experiment 2 – cloudy day, in red and squares).

It is observed that the experiment with higher temperature (experiment 1) presents a faster bacterial inactivation as it was expected due to the influence of the temperature in the SODIS process. In the graph, the modelled predictions are also plotted, which fit satisfactorily (11.6 and 16.5 % of NRMSLE for each experiment) the experimental results. Figure 7.7 (b) show two experiments conducted at different conditions of irradiance, taken place in a sunny and in a cloudy day, respectively. The experiment 2 (cloudy conditions) resulted in an inactivation rate lower than experiment 1 (sunny), but in both cases the synergistic SODIS-thermal model presented good predictions for the bacterial profile (11.6 and 14.1 % of NRMSLE for each experiment).

The comparison between experimental and modelled results becomes a very important implications for SODIS application: the synergistic SODIS-thermal model is capable to describe the *E. coli* inactivation in isotonic water in the most commonly used containers, i.e. PET bottles, under natural sunlight that means varying values of irradiance and water temperature.

7.2.2 Well water

The most common application of SODIS is the disinfection of natural waters for drinking purposes. Well water has been used as the natural water matrix in this work. The physical characteristic of the well water is quite similar to the isotonic water since the turbidity is very low (< 2 NTU) and it could be considered as clear water. The main differences in the chemical composition is the high content of carbonates and the presence of some organic matter in the well water (Table 3.1). Carbonates are always in competition with oxidation by hydroxyl radicals and other oxidizing species acting as scavenger of radicals and slowing down the inactivation rate [Fernández-Ibáñez *et al.*, 2009]. On the contrary, the organic matter could have different effects: on the one hand it could be used by the bacteria cells as nutrients decreasing the efficiency of the disinfection process, but also some specific matter could act as photosensitizer generating radicals and enhancing the SODIS efficiency. Therefore, these chemicals effects are not

considered in this work, and the synergistic SODIS-thermal model is directly applied to well waters without any kinetic modification.

Figure 7.8 shows the *E. coli* inactivation in well water within the 2 L-PET batch reactor and the prediction of the synergistic SODIS-thermal model for two different climate conditions (sunny and cloudy). It is observed that the model describes the inactivation accurately with a NRMSLE of 13.46 % and 12.2 %, respectively.

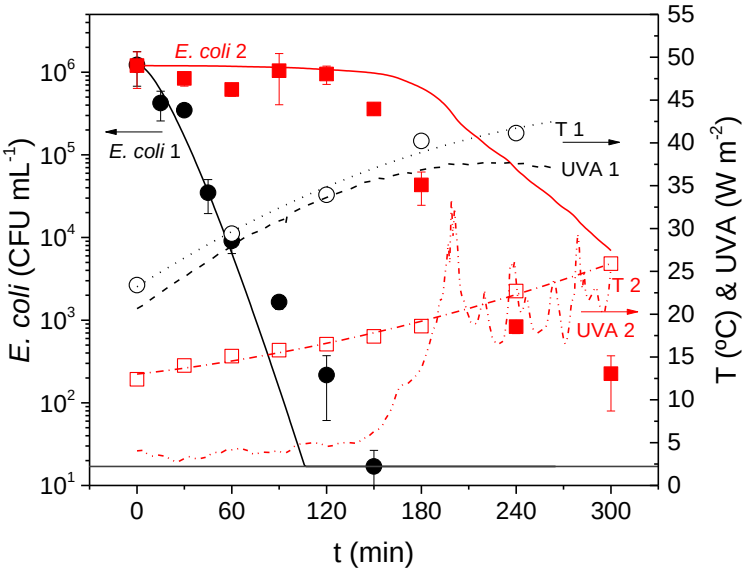

Figure 7.8. Experimental (dots) and simulated by synergistic SODIS-thermal model (lines) SODIS results under natural sunlight within clear well water in 2 L-PET batch reactor with different climate conditions (experiment 1 – sunny day, in black and circles; experiment 2 – cloudy day, in red and squares).

Therefore, although the model was developed for isotonic water, it could be also applied for well water mainly due to absence of turbidity that permits to light to penetrate within the entire photo-reactor. The result has a very interesting implication due to the model could be used for estimate the *E. coli* inactivation within natural clear waters, such as well water, in both sunny and cloudy conditions.

7.2.3 Turbidity effect

Turbidity effect was evaluated to determine the influence of the photon depletion generated by the solid particles scattering. The solution of the light model for the 2 L-PET batch reactor containing a well water solution of 5, 100 and 300 NTU (red soils) provides the profile of the incident radiation in the reactor (Figure 7.9 (a)). It decreases along the reactor in the light radiation propagation (X axis) due to a screening effect that inhibits the penetration of photons in the reactor. Then, the incident radiation available for the disinfection was estimated as the averaged of the radiation at each point (equation (7.18)) and the turbidity corrector factor (equation (7.19)) was included in the synergistic SODIS-thermal model.

In Figure 7.9 (b) the bacterial inactivation profiles for different turbidity values (0, 5, 100 and 300 NTU) are shown. There is a clear inactivation rate decrease with the increase in turbidity attributed to the reduction of photons available for the disinfection process. It is observed that synergistic SODIS-thermal model fits accurately the *E. coli* inactivation profiles within turbid waters ranged from 5 to 300 NTU in sunny conditions. Cloudy conditions were also evaluated but any bacterial reduction was observed with 100 and 300 NTU water (data no shown). The model was also capable to predict these disinfection results.

Finally, the effect of the type of particles present in water was analysed using kaolin as another source of turbidity. The model used to simulate the light depletion in the kaolin solution had the same assumptions as for the case of red soils; i.e. turbid agent particles are the responsible for the in- and out-scattered of light in the water. This effect is included in the light model calculation by the specific scattering coefficient value of kaolin solution. For this, experiments were performed at 100 NTU in well water in the 2 L-PET batch reactor in similar climate conditions. Figure 7.10 shows the results of the inactivation of these experiments and the model predictions of both cases (kaolin and red soils). It could be observed that the predictions fit satisfactorily the experimental results of SODIS performed in turbid waters using different types of particles. Both experiments present a NRMSLE lower than 14 %.

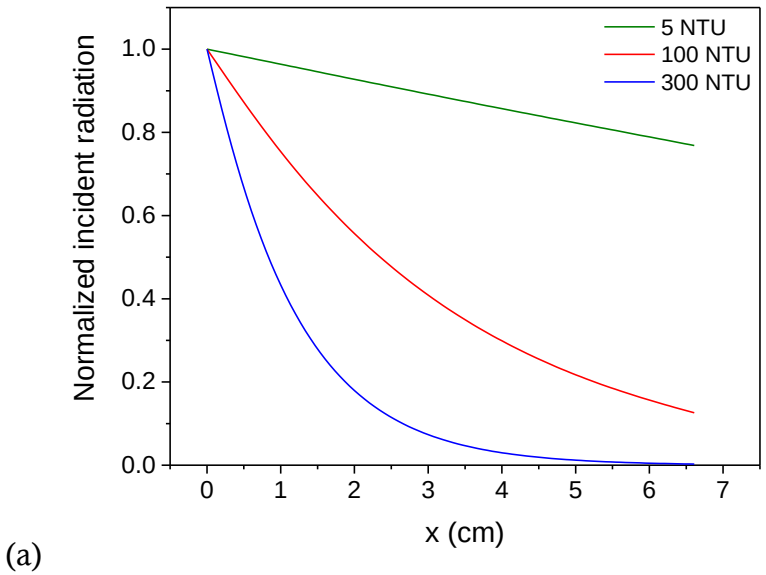

(a)

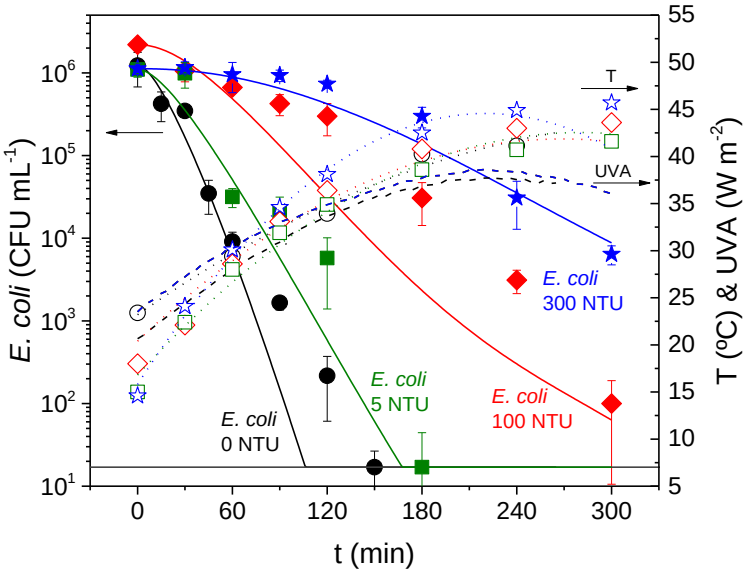

(b)

Figure 7.9. Analysis of the turbidity effect generated by red soils within well water in 2 L-PET batch reactor: (a) normalized incident radiation profile in the radiation direction for 5, 100, and 300 NTU solutions and (b) experimental (dots) and simulated by synergistic SODIS-thermal model (lines) SODIS results for 0 (in black and circles), 5 (in green and squares), 100 (in red and diamonds) and 300 NTU (in blue and stars). Experimental data was previously reported [Ubomba-Jaswa, 2009b].

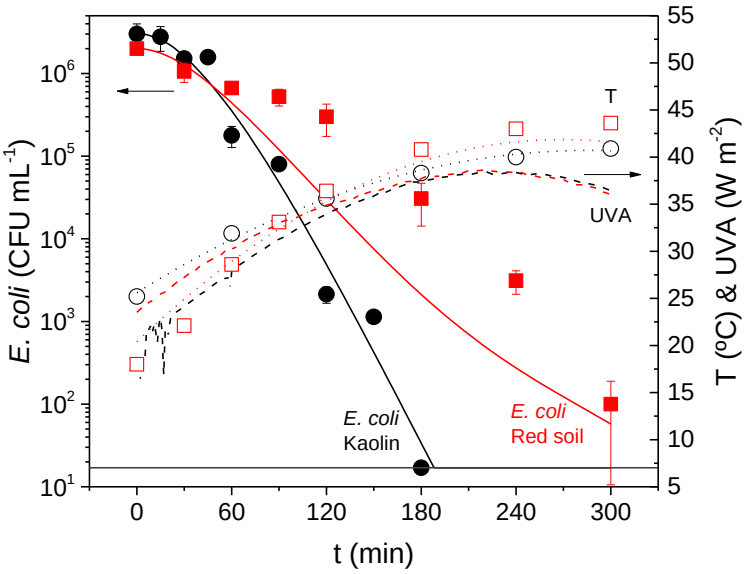

Figure 7.10. Experimental (dots) and simulated by synergistic SODIS-thermal model (lines) SODIS results under natural sunlight within 100 NTU well water in 2 L-PET batch reactor with: kaolin (in black and circles) and red soils (in red and squares). Experimental data of the red soils was previously reported [Ubomba-Jaswa, 2009b].

7.2.4 Reactor design and materials effect

Different reactors have been presented as promising design for SODIS applications. In this section, several reactors were tested to evaluate the efficiency of the synergistic SODIS-thermal model under natural sunlight. The reactors characteristics were described in chapter 3 (section 3.5.3) and they could be classified in two groups: (i) batch reactors with CPC and (ii) without CPC.

In the reactors without CPC mirror, as it was explained previously for the 2 L-PET, the radiation angle does not affect to the optical path length (Figure 7.2). The same conclusion is achieved for reactors with CPC: the light reflected by the mirror is distributed throughout the receiving tube so that the entire circumference of the receiving photo-reactor is homogeneously illuminated (Figure 7.11). Therefore, the same simplifications performed for clear waters for 2 L-PET reactors, are considered for the rest of the reactors tested in this work, so the incident radiation is estimated by the equation (7.1).

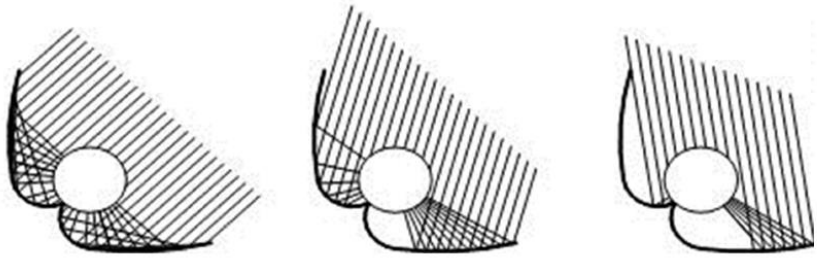

Figure 7.11. Scheme of the solar radiation rays depending on the angle that impact on to a CPC photo-reactor [Blanco, 2002].

Several experiments were performed under similar weather conditions (inlet graph of Figure 7.12) in clear well water. In the Figure 7.12 it is observed that the synergistic SODIS-thermal model predicts accurately the *E. coli* inactivation using different kind of reactors (different transmittances and volume): 20 L-BS (T = 90 %), 2.5 L-BS, 2 L-PET (52 %), 19 L-PC (33 %) and 22.5 L-MC (19 %). The treatment time is highly dependent on the reactor-material, since the BS permits higher inlet irradiance available to the SODIS reactions than MC.

Different diameter tubes were tested for the same reactor configuration and material. The 2.5 L-BS batch reactor has an external diameter of 5 cm while the 20 L-BS has 20 cm. The simulations in both cases were done without taking into account the geometry of the reactor; only temperature and inlet irradiance were used as input model parameters. The irradiance was estimated equally with any geometrical consideration; it was calculated with equation (7.1) and a turbidity corrector factor of 1 (clear water). The fact that both inactivation modelled profiles fit accurately the experimental disinfection, reveal that the diameter does not affect to the incident radiation in the photo-reactor. These results were expected because in clear waters the absorption or scattering of light was considered negligible, so that the sunlight rays do not suffer any direction deviation along the diameter of the photo-reactor independently of the optical path length (reactor diameter). Nevertheless, the reactor diameter could affect to the water temperature, raising faster in photo-reactors with smaller diameters. The influence of the diameter in the water thermal increase and therefore in the

E. coli disinfection rate has to be taken into account in those cases in which the temperature measurements are limited.

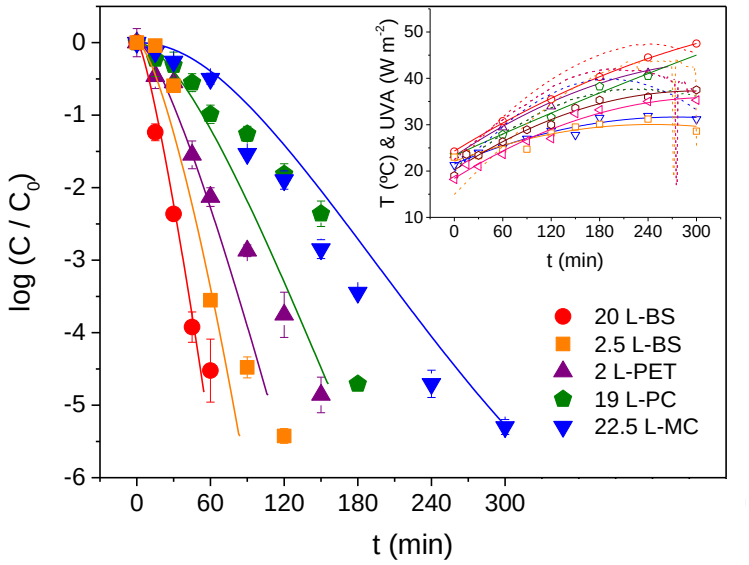

Figure 7.12. Experimental (dots) and simulated by synergistic SODIS-thermal model (lines) SODIS results under natural sunlight within clear well water in different photo-reactors: 20 L-BS (in red and circles), 2.5 L-BS (in orange and squares), 2 L-PET (in purple and up triangles), 19 L-PC (in green and pentagons) and 22.5 L-MC (in blue and down triangles); in the main graph it is plotted the *E. coli* reduction and in the inlet graph, the temperatures (opened dots and solid lines) and the UVA irradiance (dashed lines). Experimental data for 22.5 L-MC and 2.5 L-BS were previously reported [Ubomba-Jaswa *et al.*, 2010; Navntoft *et al.*, 2008].

Additionally, the synergistic SODIS-thermal model was also evaluated under cloudy conditions in a CPC reactor. The experimental and predicted results for the *E. coli* inactivation are shown in the Figure 7.13. It is observed that the model described successfully the inactivation in both cases, with a NRMSLE of 6.1 in the sunny experiment and 10.9 % in the cloudy experiment. It could be observed that the modelled inactivation curve for the experiment performed in the cloudy day suffers a change in the tendency at approximately 90 min because at this moment the simulated inactivation rate decreases due to the pronounced drop in the irradiance values from 13 to 7 W m^{-2}.

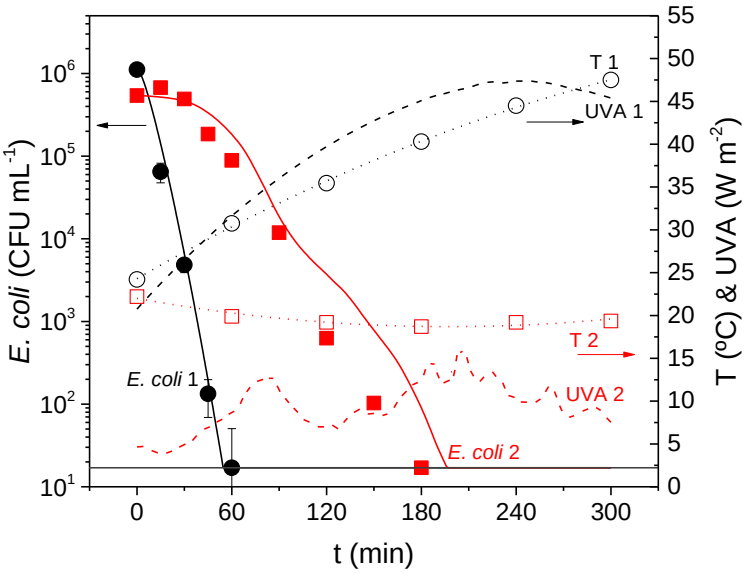

Figure 7.13. Experimental (dots) and simulated by synergistic SODIS-thermal model (lines) SODIS results under natural sunlight in well water in a 20 L-BS batch reactor with different climate conditions (experiment 1 – sunny day, in black and circles; experiment 2 – cloudy day, in red and squares).

The validation of the synergistic SODIS-thermal model in all the tested reactor configurations in this work for sunny and cloudy conditions has promising implications. The incident radiation in every reactor could be estimated directly by the transmittance of the material (equation (7.1)) and it could be considered homogeneous for clear water with no dependency of the diameter of the reactor. This conclusion is especially important in the field of reactor design: the synergistic SODIS-thermal model could be used as a tool for the estimation of the treatment time of new reactors just including the transmittance of the reactor material, the inlet irradiance and the water temperature. The last parameter could be estimated by the model of Sukkasi and Akamphon. They developed a heat-transfer model to estimate the water temperature contained in PET bottles and LDPE (low-density polyethylene) bags exposed to sunlight [Sukkasi and Akamphon, 2013]. The same procedure could be applied to determine the water temperature in other reactors with different transmittance and configurations.

7.3 Conclusions of chapter 7

The synergistic SODIS-thermal model developed in this work (chapter 6) has been validated under real sunlight and different operational conditions. The model was proven to be suitable for clear (isotonic and well water) and turbid waters ranged 5 to 300 NTU (kaolin or red soils), different volumes ranged 2 to 22.5 L and different photo-reactors materials (borosilicate, methacrylate, polyethylene terephthalate and polycarbonate). The model was also validated for different weather conditions (cloudy and sunny days) determining variations of irradiance and water temperature. The real scenario of changing parameters has been introduced in the synergistic SODIS-thermal model as time-dependent parameters (not constants parameters). The light depletion due to the turbidity was modelled solving the RTE by the DOM in a 2-dimension system.

The validation of the synergistic SODIS-thermal model has an important impact in the reactor design field. The model capability to provide treatment times to inactive the bacterial load of contaminated water is a key parameter to estimate the treated volume in batch systems. This information could be used to automatize the SODIS operation in the developing countries where the process normally is applied.

CHAPTER 8
THESIS IMPLICATIONS

8 THESIS IMPLICATIONS

This thesis encompasses the know-how of diverse areas such as microbiological techniques, kinetic modelling and engineering SODIS applications. The SODIS mechanistic model of this thesis was developed mainly (i) to increase the scientific knowledge related with the SODIS process and to understand how the interactions between solar radiation and the bacterial cells lead to their inactivation and (ii) to predict the efficiency of new photo-reactor prototypes without the necessity of built them and test them experimentally. Although a number of contributions show the efforts done in reactor design for SODIS applications to overcome some important drawbacks of the actual SODIS deployment, there is still not any inexpensive tailor-made reactors for efficient SODIS performance to conduct solar water disinfection in a reasonable time

(less than 5 – 8 hours) at large scale for further implementation in developing countries or isolated communities.

The main objective of this thesis is related with the application of the synergistic SODIS-thermal model to real field conditions, nevertheless other important findings were obtained in the microbiology area. In chapter 4, a protocol to detect the intracellular ROS photo-generated during the bacterial exposure to sunlight was proposed. This protocol overcomes the limitations of the ROS-probe (the DCFH-DA) to be exposed to solar light and reduces the incubation time of the bacteria cells loaded with the probe that permits to detect the maximal amount of photo-generated intracellular ROS. This protocol can be used for other bacteria, to investigate the influence of other stress factors, with the advantage of having a fast response and a high capability of detecting low ROS levels due to the fast reactivity of the hydrolysed probe and the high sensitivity of flow cytometry, respectively.

In addition, the study reported in chapter 4 has an important experimental discovery. The protocol of intracellular ROS detection was applied to cells added with different concentrations of H_2O_2 up to 1.5 mM, and it was observed a linear dependency between the additions of H_2O_2 and the signal corresponding to the internal generated ROS. This measurement is a clear experimental evidence of the H_2O_2 diffusion into cells when the reagent is added to a bacterial suspension. This also confirmed the hypothesis accepted in literature on H_2O_2 diffusion through the cell wall enhancing the solar water disinfection with additions of H_2O_2 to the contaminated water [Sichel *et al.*, 2009; Spuhler *et al.*, 2010; Polo-López *et al.*, 2011].

In chapters 5, 6 and 7, for the first time a kinetic mechanistic model of the solar water disinfection is proposed which is based on the intracellular photo-generation of ROS and the photo-inactivation of enzymes induced by the synergistic effect between solar radiation and solar mild-heat temperatures reached during SODIS. This is a great advance in the SODIS knowledge and in the photo-reactor design since it could be used as a tool to predict the efficiency

of new reactors prototypes. The synergistic SODIS-thermal model proposed is capable to estimate the inactivation time of *E. coli* under different weather conditions using the following input modelling parameters:

- Initial bacterial concentration and the bacterial reduction desired that depends on the bacterial load of the contaminated water and the standard requirements established in the guidelines for safe HWTS.
- Water temperature that is dependent on the infrared radiation and changing over the solar exposure. The water temperature varies with the location and the season. Typical values measured in the PSA in summer vary from 25 to 50 ºC (with temperature increments of 20 ± 5 ºC) meanwhile typical values in winter ranged between 15 and 25 ºC (increments of 10 ± 5ºC).
- Incident radiation depends obviously on the climate conditions, but also on the type of reactor and the water turbidity. The photo-reactor materials absorb part of the UVA light decreasing the incident radiation in the interior of the reactor. Also, the water turbidity affects the radiation available for SODIS process. In this thesis, a light transport model was developed for a PET bottle containing particulate matter, by solving the RTE. The same calculation procedure can be applied for other type of reactors. In the case of clear waters, the incident irradiance could be assumed to be homogeneous in the photo-reactor independent of the volume (in the range from 2 to 22.5 L) or diameter of the tube (5 – 200 mm).

For SODIS applications, the **treatment time** is of great importance because the process purpose is to obtain drinking water and it is necessary to assure that the treated water satisfy the drinking requirements. In general, the treatment time have to be enough safe to reduce the microbial load of the contaminated water to a lower level of the infective dose (ID) [WHO, 2011a]. The ID is defined as the minimal number of pathogens that causes an infection in the host. The ID of *E. coli* is quite large, is in the range 10^5 – 10^8 organisms [Kothary and Babu, 2001]. A standard classification of a treatment quality is given by the WHO that establishes a basis for assessment performance for the disinfection treatment and

assumes a maximum protective level when at least a 4-log reduction of bacteria, 5-log reduction of viruses and 4-log reduction of protozoa are achieved [WHO, 2011b; WHO, 2014].

Due to the importance of the treated water quality since the final purpose is drinking, it is advisable to add an extra treatment time to the predicted time to warrantee the desired level of disinfection. Other researchers have also used the concept of 'extra time' to guarantee complete disinfection and no re-growth, i.e. post-treatment bacterial recover. Rincón and Pulgarín defined the 'effective disinfection time' as the time required for total inactivation of bacteria without re-growth in a subsequent dark period referenced at 48 h [Rincón and Pulgarín, 2004]. The estimation of this extra time permits to obtain a 'safe time', t_{safe} that is defined as the sufficient treatment time to assure that the desired inactivation level (i.e. 4-log or 5-log reduction) has been achieved:

$$t_{safe} = t_{model} + 0.2 \cdot t_{model} + 30 \quad (8.1)$$

where t_{model} is the time predicted by the model to reach a certain inactivation. Times are expressed in terms of minutes. The t_{safe} proposed is to be determined using the synergistic SODIS-thermal model for the SODIS experiments in which a 5-log reduction was achieved. This logarithmic reduction value was previously proven to be sufficient to prevent any bacterial regrowth during the following 48 h after the solar water exposure [Ubomba-Jaswa *et al.*, 2009a].

The equation (8.1) was obtained taking into account the model predictions and experimental times errors. The error associated to the model predictions was explained in previous chapters and it has been assumed to be acceptable only when it was lower than 20 % [Raes *et al.*, 2012]. This value has been assumed as the maximum error of the model and it has been considered as the extra time to be conservative because the final end-use is drinking water. An additional time of 30 minutes was added to the model prediction time due to the following reasons:

- The synergistic SODIS-thermal model was developed based on experiments conducted in the solar simulator (chapters 5 and 6) in which large number of samples was analysed to obtain the model kinetic constants. To do so, samples were taken every 5 minutes.
- The experiments with photo-reactors under real sunlight were conducted to evaluate the model capability. In these cases, water samples were taken less frequently due to the experimental procedure applied to solar reactors, with a sampling of 30 minutes. Due to the impossibility of on-line measurements (or more frequent sampling times) of the bacterial concentration, it is not possible to determine the exact exposure time for which the detection limit (DL) was achieved. So, to be conservative in the estimations, it has been assumed this interval of 30 minutes as the maximum error of the experimental inactivation time at pilot scale.

The application of this equation gives valuable and practical information about the safe inactivation time as the solar exposure time required to disinfect water at a safe level. As it was described in chapter 7, the validation of the synergistic SODIS-thermal model was done with experimental results obtained with different reactor designs (2 L-PET, 2.5 L-BS, 20 L-BS, 22.5 L-MC and 19 L-PC batch reactors), two types of water (isotonic and well water), various turbidity values (from 5 to 300 NTU), and different weather conditions (irradiance and water temperature). Table 8.1 shows the experimental, modelled and safe times obtained for each experiment conducted under different operational conditions. Two different inactivation limits, 5- and 4-LRV (log reduction values) were considered. The 5-LRV is the safe time required to achieve the DL (17 CFU mL^{-1}) while the 4-LRV is the time necessary to satisfy the WHO requirements of 4-log bacterial reduction (highly protective measure) for HWTS. Model simulations were performed for a maximum treatment time of 5 hours. For all the experiments where the 4-LRV was not reached in this time (represented by a hyphen in the table) due to a number of factors (i.e. the sky cloudiness, the high turbidity of the water, the small transmittance of the photo-reactor wall material, etc.), the SODIS process is not recommend.

Table 8.1. Characteristics of SODIS experiments ($C_0 = 10^6$ CFU mL^{-1}) and the experimental, modelled and safe 5- and 4-LRV, considered in this work.

Reactor	Water	Turb. (NTU)	T (ºC)[a]	I (W m^{-2})[a]	LRV ≥ 5 (min)[b]			LRV ≥ 4 (min)[b]		
					Exp.	Mod.	Safe	Exp.	Mod.	Safe
2 L-PET	IW	0	35.6	31.9	120	94	143	90	83	130
2 L-PET	IW	0	31.7	31.8	180	147	206	150	130	186
2 L-PET	IW	0	31.5	26.3	180	154	215	150	139	197
2 L-PET	IW	5[d]	31.0	35.8	180	128	184	120	112	164
2 L-PET	IW	5[d]	17.7	11.5	-	-	-	-	-	-
2 L-PET	IW	100[d]	33.1	35.8	300	299	389	240	233	310
2 L-PET	IW	100[d]	17.6	11.5	-	-	-	-	-	-
2 L-PET	IW	300[d]	34.7	35.8	-	-	-	240	217	290
2 L-PET	IW	300[d]	18.9	11.5	-	-	-	-	-	-
2 L-PET[c]	WW	0	31.7	46.3	90	57	98	60	57	98
2 L-PET[c]	WW	0	33.7	45.7	90	58	100	90	58	100
2 L-PET[c]	WW	0	34.9	31.5	120	95	144	120	95	144
2 L-PET	WW	0	33.6	33.0	150	107	158	120	92	140
2 L-PET	WW	0	21.3	11.5	240	287	374	240	268	352
2 L-PET	WW	5[d]	32.8	34.4	180	168	232	150	143	202
2 L-PET	WW	5[d]	19.2	14.8	-	-	-	-	-	-
2 L-PET	WW	100[e]	35.3	33.3	180	189	257	150	155	216
2 L-PET	WW	100[d]	34.4	34.4	-	-	-	300	252	332
2 L-PET	WW	100[d]	17.2	11.5	-	-	-	-	-	-
2 L-PET	WW	300[d]	19.0	11.5	-	-	-	-	-	-
2.5 L-BS	WW	0	25.5	29.4	60	61	103	60	57	98
2.5 L-BS	WW	0	32.2	32.6	90	54	95	60	43	82
2.5 L-BS	WW	0	26.7	34.5	120	84	131	60	68	112
20 L-BS	WW	0	37.1	39.6	60	55	96	45	48	87
20 L-BS	WW	0	26.4	30.0	120	75	120	90	71	115
20 L-BS	WW	0	19.9	16.6	120	92	140	120	86	133
20 L-BS	WW	0	24.5	19.3	150	99	149	120	87	134
20 L-BS	WW	0	20.9	20.2	150	147	206	90	118	172
20 L-BS	WW	0	19.8	9.4	210	197	266	180	185	252
22.5 L-MC	IW	0	34.4	35.0	240	242	320	180	191	259
22.5 L-MC	WW	0	31.4	35.9	300	267	350	240	226	301
22.5 L-MC	WW	0	27.1	34.5	300	300	390	240	238	316
22.5 L-MC	WW	0	27.3	37.6	300	300	390	240	260	342
22.5 L-MC	WW	0	23.1	29.7	-	-	-	300	275	360
22.5 L-MC	WW	0	22.9	32.6	-	-	-	-	-	-
22.5 L-MC	WW	0	22.9	26.9	-	-	-	-	-	-
22.5 L-MC	WW	0	17.5	24.6	-	-	-	-	-	-
22.5 L-MC	WW	0	15.7	19.9	-	-	-	-	-	-
19 L-PC	WW	0	33.1	31.5	120	136	193	120	136	193
19 L-PC	WW	0	32.4	33.0	180	156	217	180	138	196
19 L-PC	WW	0	22.6	11.7	-	-	-	-	-	-

WW = well water; IW = isotonic water; (-) indicated that log-reduction was not achieved.
PET = polyethylene terephthalate; BS = borosilicate; MC = methacrylate; PC = polycarbonate.

[a] Averaged values during 5 h. The model input parameters used were the instantaneous values.
[b] LRV (log reduction value) = time required to achieved a certain microbial reduction.
[c] Experiments started with 10^5 CFU mL^{-1}.
[d] Turbidity with red soils. Experimental data were previously reported [Ubomba-Jaswa, 2009b].
[e] Turbidity generated with kaolin.

In the Table 8.1 all experiments considered for the model validation were also analysed to determine the safe time, being higher than experimental inactivation time, which guarantees that the inactivation desired have been reached. This observation is easily detected in the Figure 8.1 where each dot represents the inactivation time for every experiment of the Table 8.1 to reach a 5-log reduction (Figure 8.1 (a)) and a 4-log reduction (Figure 8.1 (b)). The blue dots show the experimental time (Y axis) corresponding to the inactivation time predicted by the model (X axis) while the green dots show the safe time (Y axis) calculated for each experiment from the equation (8.1). It is observed that for all the experiments analysed, the recommended treatment time for safe water or safe time (green dots) is higher than the experimental time (blue dots), which means that the safe time determination is well established for a wide variety of realistic conditions of SODIS, including all types of solar reactors (with several photo-reactor materials), water turbidity, bacterial load, and weather variations. Therefore, the proposed synergistic SODIS-thermal model for this variety of real conditions and the equation (8.1) permit to obtain a quite realistic and protective required treatment time to achieve a certain protective level of intervention for drinking water using SODIS in several solar reactors.

Therefore, as previously discussed, the safe time is a suitable parameter to estimate the disinfection efficacy of new reactors for SODIS. It could be also used for reactor design in order to compare the new prototypes proposed under certain operational conditions. Nevertheless, when the reactor is installed and is operating in the field the most commonly used parameter for the comparison of solar water treatments is the 'UVA dose' [Ubomba-Jaswa *et al.*, 2009a; Keogh *et al.*, 2015; Polo *et al.*, 2015] that encompasses the treatment time and the irradiance values. It is defined as the solar UVA energy delivered onto the system (J m^{-2}) and it could be obtained by integration of UVA solar irradiance I_{UVA}, (W m^{-2}) over a given period of time dt, (s).

$$Dose_{UVA} = \int I_{UVA} \mathrm{d}t \tag{8.2}$$

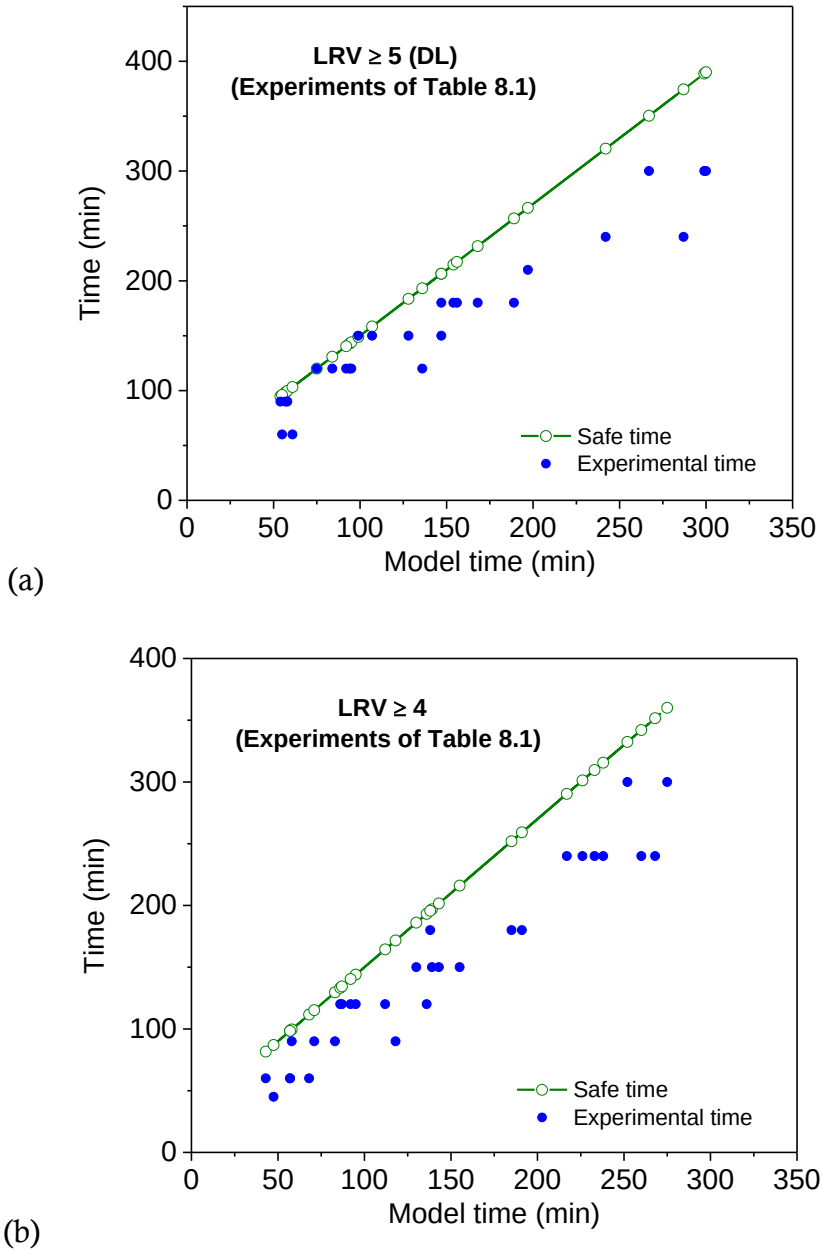

Figure 8.1. Experimental, modelled and safe inactivation time of several SODIS experiments (see Table 8.1). (a) LRV ≥ 5 (time to reach DL) and (b) LRV ≥ 4 (time to accomplish the WHO requirements for HWTS quality).

In the same line of the definition of a 'safe time', it could be defined a 'safe UVA dose' as the minimal UVA dose required to assure the desired inactivation. The Figure 8.2 shows the averaged doses required to achieve a 5 and a 4-log reduction of *E. coli* for the different conditions tested in this work. The UVA

doses presented in this graph are the averaged values of the experiments listed in Table 8.1 that were conducted in different weather conditions. The water temperature differences between the experiments induce some differences between the UVA requirements for a certain operational condition (type of reactor and turbidity). These differences are represented in the graphs by the error bars (standard deviation).

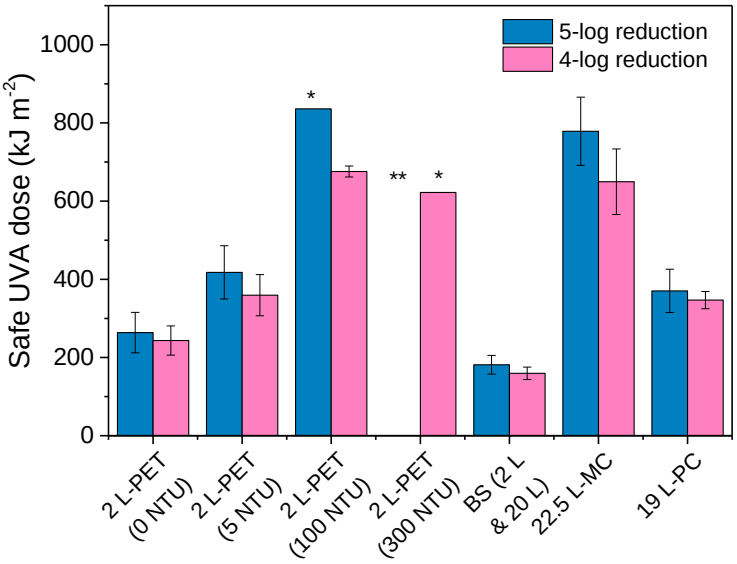

*Data of a single experiment (no standard deviation).
**5-log reduction was not reached.
In the experiments presented in this graph, the turbidity was generated by red soils.
The group '2 L-PET (0 NTU)' includes the experiments within IW and WW. Two sample t test (IW, WW) concluded no significant differences between the two groups (Microsoft Excel, $\alpha = 0{,}05$).
The group 'BS (2 L & 20 L)' includes the two type of reactors (t test concluded no significant differences between the groups).

Figure 8.2. 'Safe UVA dose' required to reach 5 and 4-log reduction of *E. coli*. The averaged values are presented in columns and the standard deviation in error bars (data from Table 8.1).

The 'safe UVA dose' presented in the Figure 8.2 corresponds to the experiments listed in Table 8.1. The results were grouped by type of reactor and water turbidity. The estimated 'safe UVA dose' for a 4 or 5-LRV by solar water disinfection was determined for clear water in 2 L-PET, 2 L-BS, 20 L-BS, 22.5 L-MC and 19 L-PC, and also for turbid water in 2 L-PET batch reactors with 5,

100 and 300 NTU. In the graph, the 'safe UVA dose' for the 2 L-BS and 20 L-BS are presented together, since no significant difference was observed between the two groups (two sample t test by Microsoft Excel, α = 0.05). This fact can be attributed to the model assumptions, which neglected the effects of light absorption and scattering in clear waters and therefore the inlet radiation is only dependent on the transmittance of the photo-reactor material (in this case is borosilicate glass), meanwhile it is independent on reactor diameter and therefore on the volume of the reactor.

The 'UVA dose' parameter has been largely used to determine the final point of the treatment, even to commercial purposes. As an example, it can be cited the solar UV device developed by Helioz GmbH (Austria). It has been developed and commercialized the WADI device for indicating when the operation of a solar water disinfection container has reached the dose for a complete or a certain log-decrease on bacterial inactivation, as for in PET bottles is shown in the Figure 8.3 [Helioz GmbH website]. The WADI product is a solar UV measurement device that is recording the UV dose during the SODIS process. Once the process is completed, according to the WHO microbiological criteria, a smiley face on the WADI confirms that the water is safe to drink.

The synergistic SODIS-thermal model developed in this thesis could be used in a similar way as the WADI device but not only considering the irradiance parameter (UVA dose), but also including the thermal effect on the water disinfection. Monitoring irradiance and water temperature during the SODIS process, the model could provide the time or UVA dose required to achieve a certain bacterial reduction, indicating the moment to stop the process when the water is ready for drinking.

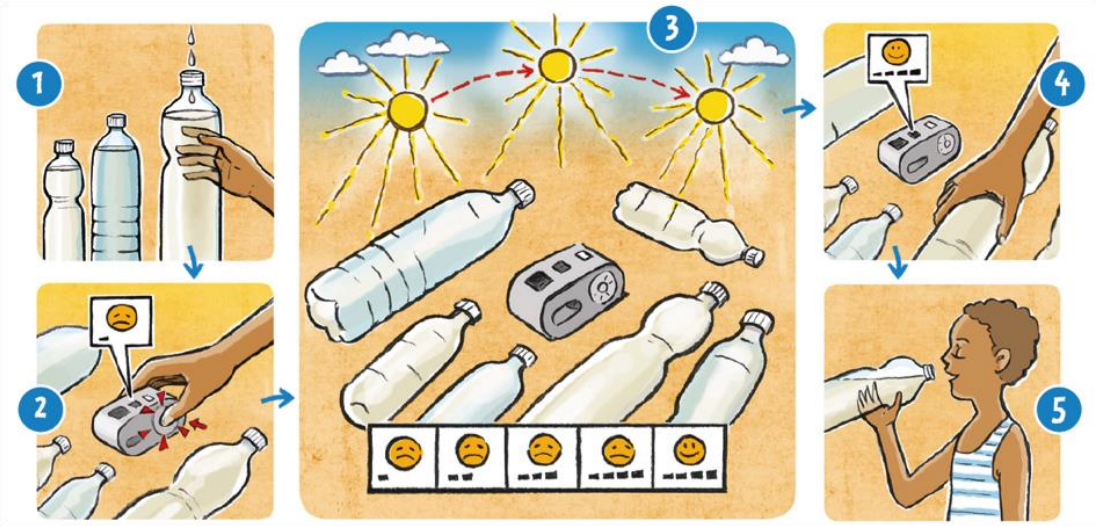

Figure 8.3. Scheme of the application of WADI device: (1) fill PET bottles; (2) exposure to the sun and press WADI reset button; (3) wait for some hours during SODIS; (4) to stop the exposure when a smiley face appears on the WADI display and (5) water is ready for consumption [Helioz GmbH website].

The synergistic SODIS-thermal model developed in this work has promising applications for large scale photo-reactors with clear implications in the design and optimization of SODIS reactors which will permit to enhance reactors efficiency and to increase treated water output. Nevertheless, there are some other parameters that affect the SODIS efficiency and that could be further included in the developed SODIS-model to cover other potential complex scenarios:

- Nature of microorganism: the model was developed for the inactivation of *E. coli* in stationary phase since it is the most used faecal microorganism indicator in a number of research contributions. The model could be also applied for other bacteria cells or other growth stages of this bacterium. For this purpose it is necessary to obtain previously some kinetic constants for the specified bacteria (k_{11}, k_{12} and k_{13} of chapter 5 and A_{14} and Ea_{14} of chapter 6). Other pathogens, like viruses or protozoa, will obviously behave differently under the action of sunlight. Therefore, other intracellular mechanisms will have to be proposed to attempt a similar mechanistic model based on microbiological facts.

- Dissolved oxygen (DO): the level of dissolved oxygen in the water is an important factor in the ROS generation during the solar process [Reed, 1997; Kadir and Nelson, 2014]. In the presented model the amount of DO could be included by the modification of the intracellular oxygen concentration in bacteria (in chapters 5, 6 and 7). Previously, it is necessary to study the real effect of the DO in water in the bacterial cells behaviour.

- Water physicochemical characteristics: the presence of inorganic or organic matter has been observed to modify the efficiency of SODIS [Sichel *et al.*, 2007c; Polo-López *et al.*, 2011]. The lack of ions in water increases the osmotic pressure within the bacteria weakening the cell membranes; while elevated amounts of ions could limit the effect on the SODIS process by ROS scavenging or photo-absorption. The effect of the organic matter in water is not so obvious. On one hand, the organic matter could act as light screen reducing the incident radiation in the photo-reactor and it could also contribute as source of nutrient with beneficial effects for bacterial cells. On the other hand, some specific natural organic matter could act as photo-sensitizers promoting the generation of ROS in water and enhancing the disinfection. These effects have not been taken into account in this model, but they could be included for its application for complex water matrixes.

- Recirculation-reactors: the effect of water recirculation has a negative effect on bacterial inactivation since the intermittent exposure to solar radiation is detrimental for the solar disinfection efficiency as the cells are given a chance to switch on self-defense mechanisms during the dark period and hence are more resistant to sunlight when they are re-illuminated again after dark periods [Ubomba-Jaswa *et al.*, 2009a]. In the presented model, the 'dark-recirculation' effect has not been considered in the disinfection mechanisms, so this model could not be applied to recirculation-reactors. The models developed by Velez-Colmenares to explain the bacteria photo-reactivation by sunlight could be useful for modelling the effect of recirculation during SODIS process [Velez-Colmenares, 2011].

- Water temperature estimation: in the presented model the water temperature was included manually using experimental data. Nevertheless, the water temperature could be estimated from irradiance values with rigorous models of heat-transfer. In the literature, there are some models that describe the water temperature fluctuations contained in PET bottles and LDPE bags (low-density polyethylene) exposure to sunlight [Sukkasi and Akamphon, 2013]. A similar procedure could be applied to develop models that will be capable to predict the water temperature in different photo-reactor with higher diameters, more transparent materials or other enhancements like the use of solar mirrors (CPC).

- Wavelength: the bacterial inactivation by solar water disinfection technique is wavelength-dependant [Santos *et al.*, 2013]; in general, the bacterial sensitivity is higher at shorter wavelengths, being UVB and UVA more efficient than visible. In this work only the contribution of the complete UVA range was considered using averaged values in the UVA range, without consideration of the differences between the several components of the UVA spectrum neither the contribution of UVB nor visible light into the bacterial inactivation. The specific effect of each wavelength and the potential synergies between them are still unknown at solar irradiance levels, and it could be an interesting research line for future advances in this topic.

  In line with this, an experimental study during an abroad research stay of 3 months in the Nanotechnology and Integrated BioEngineering Centre (NIBEC) of Ulster University (UK) under the supervision of Prof. J. A. Byrne was carried out. This work was focused on study the effect of every wavelength on the bacterial inactivation under solar radiation exposure, to investigate the specific and synergistic contributions of several wavelengths to SODIS efficiency in the UVA, UVB and visible spectra. Nevertheless, the results obtained were not conclusive and further investigation is still required to elucidate clearly the wavelength contribution to the solar water disinfection.

A monochromatic irradiation source (Horiba, Jobin Yvon FL-1039/40) was used to irradiate the water samples with a narrow wavelength band of 20 nm approximately. The wavelength values tested were 310, 315, 320 and 325 nm with irradiance intensity similar to the solar radiation, 1.8 ± 0.1 W m^{-2} (inlet Figure 8.4 (a)). Figure 8.4 (a) shows the *E. coli* behaviour under the exposure of the monochromatic light. The DL (2-log reduction) was reached after 5 hours of exposure at 310 nm. Above this wavelength no significant bacterial reduction was observed, the bacterial profile at 315, 320 and 325 nm was similar. The graph only shows the *E. coli* concentration time variation under exposure at 315 nm.

In addition, the study of the combination of two monochromatic lights was performed in order to find out the occurrence of synergies between the different wavelengths. Nevertheless, no synergy was observed in the tests conducted (310 + 325 nm, 310 + 340 nm, 310 + 365 nm).

The contribution of each spectral range was also studied separately with a Spectral Energy solar simulator (1000 W xenon lamp and LPS 256 SM power supply) and different optical filters to provide the desired range of the solar spectrum (inlet Figure 8.4 (b)). Figure 8.4 (b) shows that only UVA or only visible radiation has no bactericidal effect. It was observed that although the UV irradiance exposure in the experiment with the full spectra (24.7 W m^{-2} of UV) is twice the UV irradiance of the experiment with only UV light (11.6 W m^{-2}), the time required to reach the DL was quite similar. As mentioned before, more investigation has to be done in this matter to have conclusive results.

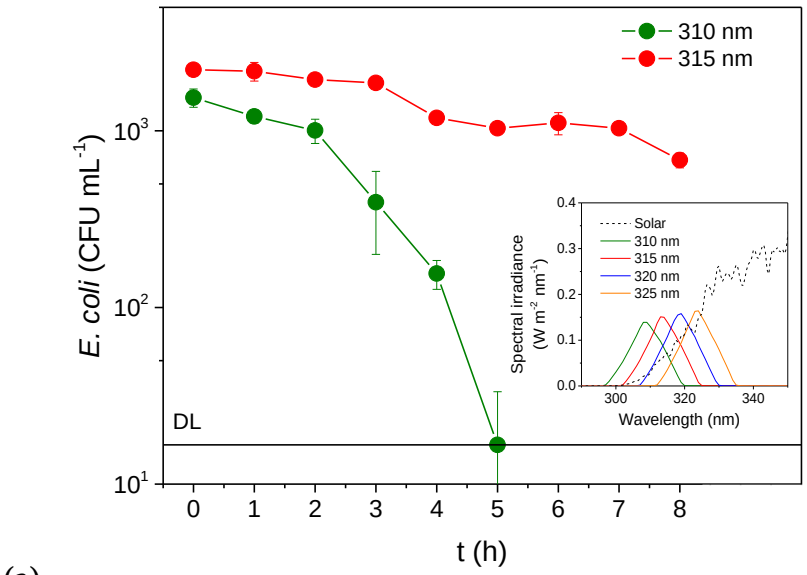

(a)

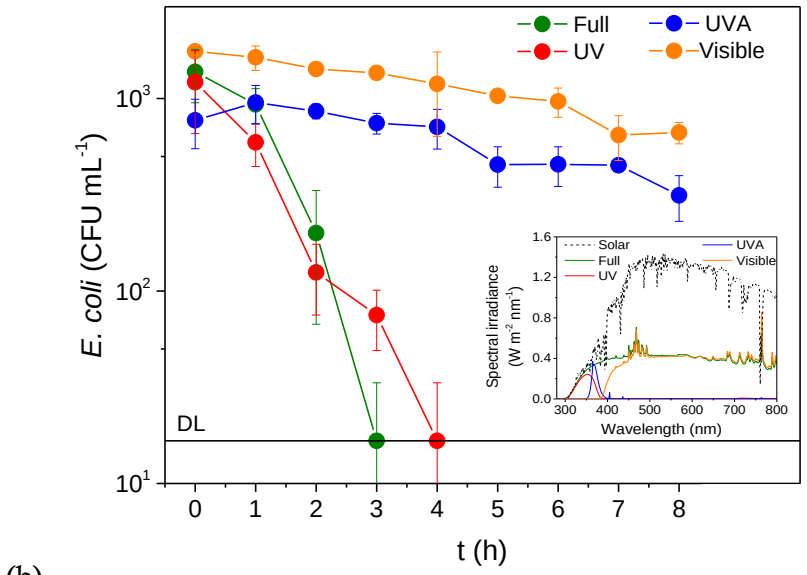

(b)

Figure 8.4. Inactivation of *E. coli* and spectral irradiance of the different experiments performed with the comparison of the solar spectrum (inlet graph). (a) Bacterial inactivation by the exposure of monochromatic light (20 nm of broadband) and (b) polychromatic light.

CHAPTER 9
CONCLUSIONS

9 CONCLUSIONS

1. For the first time, this work shows an experimental evidence of the accumulation of intracellular stable photo-generated ROS in *E. coli* during solar water disinfection. This is a clear proof that oxidative stress was increased during the action of natural solar radiation.

2. A novel protocol for intracellular ROS detection has been proposed and validated for *E. coli* using several fluorimetric techniques. The main novelty of this protocol consisted on the use of hydrolysed DCFH-DA, commonly used for photo-dynamic therapy. This protocol can be used to investigate other oxidative stress factors in bacteria with a fast response profile and high capability for detecting low levels of ROS using flow cytometry.

3. The SODIS model proposed in this work is the first attempt to summarize the main reactions that validate mathematically experimental evidence of *E. coli* inactivation due to the exposure to solar radiation. The model is successfully capable to reproduce the time profile of the concentration of viable bacteria in clear water under different solar irradiances and different initial bacterial concentrations. The mechanistic model is also capable to simulate the change of intracellular ROS and enzymes during SODIS process.

4. The main intracellular bacterial reactions that occur in parallel during *E. coli* inactivation have been proposed for this model, and the determined the kinetic parameters of those reactions have been determined. The naturally formation of intracellular ROS under solar irradiation was previously studied by other researchers, but this work is the first attempt to determine the kinetic of the ROS formation due to the action of solar UVA radiation.

5. The SODIS model proposed in this work considers the attacks of the radicals $HO^{\bullet}$ and $O_2^{\bullet-}$ to diverse intracellular organic targets radicals as the main lethal agent. The bacterial inactivation has been conceptualized as a reaction mediated by those radicals, and its kinetic constant was determined by model regression.

6. Although catalase and superoxide dismutase are the main natural protection agents against the accumulation of internal ROS in cells, the UVA action induces the inactivation of both enzymes. In this work, the kinetic constant of the catalase photo-inactivation was experimentally determined for the first time, while the photo-inactivation of superoxide dismutase was determined by model regression. It was observed that the photo-inactivation of the catalase was significantly much quicker than the superoxide dismutase.

7. The model that considers the synergistic effect between solar mild heating and solar UVA radiation for SODIS presented in this work is a considerable advance for the field of solar water disinfection over the previously proposed SODIS model, described for *E. coli* inactivation in clear water. Up to now, this is the only work where the thermal effect has been included in a SODIS mechanistic model, to explain the well-recognized synergistic effect between water temperature and UV radiation during solar water disinfection. The *synergistic SODIS-thermal model* developed in this work is capable to reproduce successfully the time profile of viable bacterial concentration over treatment time under different irradiances and temperatures.

8. The synergistic SODIS-thermal model was proven to be capable to describe the *E. coli* inactivation during the SODIS process in real field conditions including clear water (isotonic and well water), increasing values of irradiance and water temperature, cloudy and sunny days in PET bottles, (the widely used SODIS container or reactor).

9. The synergistic SODIS-thermal model using the incident radiation value estimated by a light transport model, can predict the *E. coli* inactivation in turbid waters (5 – 300 NTU) in PET bottles and in other photo-reactor designs at different scales, with different diameters and materials.

10. The synergistic SODIS-thermal model here proposed, developed and validated has been also proposed as a tool for photo-reactors design and for prediction of SODIS efficiency under several conditions. The predicted inactivation times by the model were used to define a 'safe time' and 'safe UVA dose' which gives an estimation of the time or UVA dose required to assure the complete disinfection (or up to a certain level of bacterial reduction) for drinking water.

CHAPTER 10
REFERENCES

10 REFERENCES

Abdelsalam S. A., Korayem A. M., Elsherbini E. A. M. Abdel-Aal A.-A. A., Mohamed D. S., Photosensitizing Effects of Hematoporphyrin Dihydrochloride against the Flesh Fly *Parasarcophaga argyrostoma* (Diptera: Sarcophagidae). *Florida Entomologist*, 97(4) (2014) 1662–1670.

Abreu I. A., Cabelli D. E., Superoxide dismutases - a review of the metal-associated mechanistic variations. *Biochimica et Biophysica Acta*, 1804 (2010) 263–274.

Acra A., Karahagopian Y., Raffoul Z., Dajani R., Disinfection of oral rehydration solutions by sunlight. *The Lancet*, 2(8206) (1980) 1257–1258.

Adolfsen K. J., Brynildsen M. P., A Kinetic Platform to Determine the Fate of Hydrogen Peroxide in *Escherichia coli*. *PLoS Computational Biology*, 11 (11) (2015) e1004562.

Afanas'ev I. B., Reactivity of superoxide ion, in *Superoxide ion: chemistry and biological Implications* Vol. I, Chapter 4, CRC Press, Florida, United States (1989).

Alfano O. M., Negro A. C., Cabrera M. I., Cassano A. E., Scattering Effects Produced by Inert Particles in Photochemical Reactors. 1. Model and Experimental Verification. *Industrial & Engineering Chemistry Research*, 34 (1995) 488–499.

Arif T., Krelin Y., Shoshan-Barmatz, V., Reducing VDAC1 expression induces a non-apoptotic role for pro-apoptotic proteins in cancer cell differentiation. *Biochimica et Biophysica Acta – Bioenergetics*, 1857(8) (2016) 1228–1242.

Augusto O., Miyamoto S., Oxygen Radicals and Related Species, in: *Principles of Free Radical Biomedicine,* Vol. 1 (eds Pantopoulos K., Schipper H. M.), Chapter II, Lady Davis Institute for Medical Research, Montreal (2011).

Baatout S., de Boever P., Mergeay M., Temperature-induced changes in bacterial physiology as determined by flow cytometry. *Annals of Microbiology*, 55 (2005) 73–80.

Baliza D. P., Caixeta F., de Resende Von Pinho É. V., da Cunha R. L., Carvalho Martins D., Veiga Franco da Rosa S. D., Physiological quality of coffee seeds produced under different levels of solar radiation and maturation stages. *Revista Brasileira de Sementes*, 34(3) (2012) 416–423.

Bartosz G., Use of spectroscopic probes for detection of reactive oxygen species. *Clinica Chimica Acta*, 368 (2006) 53–76.

Beltrán-Heredia J., Sánchez-Martín J., Improvement of water treatment pilot plant with Moringa oleifera extract as flocculant agent. *Environmental Technology*, 30(6) (2009) 525–534.

Bergmeyer H. U., Enzymes 1: oxidoreductases, transferases, in: *Methods of Enzymatic Analysis*, Vol. 3, 3rd ed., VCH Publ., Weinheim, (1983) 274–277.

Berney M., Weilenmann H. U., Egli T., Flow-cytometric study of vital cellular functions in *Escherichia coli* during solar disinfection (SODIS). *Microbiology*, 152(6) (2006a) 1719–1729.

Berney M., Weilenmann H.-U., Simonetti A., Egli T., Efficacy of solar disinfection of *Escherichia coli*, *Shigella flexneri*, *Salmonella Typhimurium* and *Vibrio cholera*. *Journal of Applied Microbiology*, 101 (2006b) 828–836.

Blanchard J. L., Wholey W.-Y., Conlon E. M., Pomposiello P. J., Rapid Changes in Gene Expression Dynamics in Response to Superoxide Reveal SoxRS-Dependent and Independent Transcriptional Networks. *PLoS ONE,* 2 (11) (2007) e1186.

Blanco J., Desarrollo de colectores solares sin concentración para aplicaciones fotoquímicas de degradación de contaminantes persistentes en agua. PhD Thesis Doctoral, (2002). University of Almería.

Borde P., Elmusharaf K., McGuigan K. G., Keogh M. B., Community challenges when using large plastic bottles for Solar Energy Disinfection of Water (SODIS). *BMC Public Health*, 16:931 (2016) 1–8.

Bosshard F., Riedel K., Schneider T., Geiser C., Bucheli M., Egli T., Protein oxidation and aggregation in UVA-irradiated *Escherichia coli* cells as signs of accelerated cellular senescence. *Environmental Microbiology*, 12(11) (2010) 2931–2945.

Brownell S. A., Chakrabarti A. R., Kaser F. M., Connelly L. G., Peletz R. L., Reygadas F., Lang M. J., Kammen D. M., Nelson K. L., Assessment of a low-cost, point-of-use, ultraviolet water disinfection technology. *Journal of Water and Health*, 6(1) (2008) 53–65.

Brucato A., Rizzuti L., Simplified Modeling of Radiant Fields in Heterogeneous Photoreactors. 2. Limiting "Two-Flux" Model for the Case of Reflectance Greater Than Zero. *Industrial & Engineering Chemistry Research*, 36 (1997) 4748–4755.

Brucato A., Cassano A. E., Grisafi F., Montante G., Rizzuti L., Vella G., Estimating Radiant Fields in Flat Heterogeneous Photoreactors by the Six-Flux Model. *AIChE Journal*, 52(11) (2006) 3882–3890.

Buxton G. V., Greenstock C. L., Helman W. P., Ross A. B., Critical review of rate constants for reactions of hydrated electrons, hydrogen atoms and hydroxyl radicals ($^{\bullet}OH/^{\bullet}O^{-}$) in aqueous solution. *Journal of Physical and Chemical Reference Data,* 17 (1988) 513–886.

Byrne J. A., Fernández-Ibáñez P. A., Dunlop P. S. M., Alrousan D. M. A., Hamilton J. W. J., Photocatalytic Enhancement for Solar Disinfection of Water: A Review. *International Journal of Photoenergy*, 798051 (2011) 1–12.

Cabrera A., Combinación de Fotocatálisis Solar con Biorreactores de Membrana para el Tratamiento de Aguas Tóxicas. Modelado del Proceso Foto-Fenton como Herramienta de Diseño y Optimización. PhD Thesis, (2013). University of Almería.

Cai H., Dikalov, S., Griendling K. K., Harrison D. G., Detection of Reactive Oxygen Species and Nitric Oxide in Vascular Cells and Tissues, in *Vascular Biology Protocols* (eds. Sreejayan N., Ren J.), Chapter 20, Humana Press, Totowa, New Jersey, (2007).

Cantemir A. R., Raducan A., Puiu M., Oance D., Kinetics of thermal inactivation of catalase in the presence of additives. *Process Biochemistry*, 48(3) (2013) 471–477.

Cassano A. E., Martin C. A., Brandi R. J., Alfano O. M., Photoreactor Analysis and Design: Fundamentals and Applications. *Industrial & Engineering Chemistry Research*, 34 (1995) 2155–2201.

Cassano A. E., Alfano O. M., Reaction engineering of suspended solid heterogeneous photocatalytic reactors. *Catalysis Today*, 58 (2000) 167–197.

Chen S. X., Schopfer P., Hydroxyl-radical production in physiological reactions. *European Journal of Biochemistry*, 260(3) (1999) 726–735.

Chick H., An investigation into the laws of disinfection. *The Journal of Hygiene*, 8 (1908) 92–158.

Chignell C. F., Sik R. H., A photochemical study of cells loaded with 2',7'-dichlorofluorescin: implications for the detection of reactive oxygen species generated during UVA irradiation. *Free Radical Biology & Medicine*, 34(8) (2003) 1029–1034.

Crow J. P., Dichlorodihydrofluorescein and Dihydrorhodamine 123 Are Sensitive Indicators of Peroxynitrite in Vitro: Implications for Intracellular Measurement of Reactive Nitrogen and Oxygen Species. *NITRIC OXIDE: Biology and Chemistry*, 1(2) (1997) 145–157.

De Laat J., Gallard H., Catalytic Decomposition of Hydrogen Peroxide by Fe(III) in Homogeneous Aqueous Solution: Mechanism and Kinetic Modeling. *Environmental Science and Technology*, 33 (1999) 2726–2732.

Dikalov S. I., Harrison D. G., Methods for Detection of Mitochondrial and Cellular Reactive Oxygen Species. *Antioxidants & Redox Signaling*, 20(2) (2012) 372–382.

Djaman O., Outten F. W., Imlay J. A., Repair of Oxidized Iron-Sulfur Clusters in *Escherichia coli*. *The Journal of Biological Chemistry*, 279(43) (2004) 44590–44599.

Downes A., Blunt T. P., Researches on the effect of light upon bacteria and other organisms. *Proceedings of the Royal Society*, 28 (1877) 488–500.

Duderstadt J. J., Martin W. R., Chapter 8. Numerical Methods in Transport Theory. *Transport Theory*, New York, Wiley (1979).

Eisenstark A., Bacterial gene products in response to near-ultraviolet radiation. *Mutation Research*, 422 (1998) 85–95.

EPA (United States Environmental Protection Agency), 2011 Edition of the Drinking Water Standards and Health Advisories. 820-R-11-002 (2011).

Fan L. T., Argoti A., Nonlinear stochastic model for bacterial disinfection: analytical solution and Monte Carlo simulation. *Industrial & Engineering Chemistry Research*, 51 (2012) 1697–1702.

Farias J., Albizzati E. D., Alfano O. M., Kinetic study of the photo-Fenton degradation of formic acid. Combined effects of temperature and iron concentration. *Catalysis Today*, 144 (2009) 117–123.

Farr S. B., Kogoma T., Oxidative Stress Responses in *Escherichia coli* and *Salmonella typhimurium*. *Microbiological reviews*, 55(4) (1991) 561–585.

Fernández-Ibáñez P., Sichel C., Polo-López M. I., de Cara-García M., Tello J. C., Photocatalytic disinfection of natural well water contaminated by *Fusarium solani* using TiO_2 slurry in solar CPC photo-reactors. *Catalysis Today*, 144 (2009) 62–68.

Fernández-Ibáñez P., Byrne J. A., Polo-López M. I., Dunlop P. S. M., Karaolia P., Fatta–Kassinos D., Chapter 3. Solar photocatalytic disinfection of water, in *Photocatalysis: Applications*, RSC Energy and Environment Series No. 15 (2016) 72–91.

Flores M. J., Brandi R. J., Cassano A. E., Labas M. D., Chemical disinfection with H_2O_2 - The proposal of a reaction kinetic model. *Chemical Engineering Journal*, 198-199 (2012) 388–396.

Foucaud L., Wilson M. R., Brown D. M., Stone V., NanoImpactNet Scientific Protocol. Dichlorofluorescein (DCFH) oxidation assay, in *The European Network on the Health and Environmental Impact of Nanomaterials* (eds. Clift, K., Clift, M. J. D.) (2010).

Gallard H., De Laat J., Kinetic modelling of Fe(III)/H_2O_2 oxidation reactions in dilute aqueous solution using atrazine as a model organic compound. *Water Research*, 34 (2000) 3107–3116.

Gerschman R., Gilbert D. L., Nye S. W., Dwyer P., Fenn W. O., Oxygen poisoning and X-irradiation - a mechanism in common. *Science*, 119 (1954) 623–626.

Giannakis S., Polo-López M. I., Spuhler D., Sánchez-Pérez J. A., Fernández-Ibáñez P., Pulgarin C., Solar disinfection is an augmentable, in situ-generated photo-Fenton reaction–Part 1: A review of the mechanisms and the fundamental aspects of the process. *Applied Catalysis B: Environmental*, 199 (2016) 199–223.

Gill L. W., McLoughlin O. A., Solar Disinfection Kinetic Design Parameters for Continuous Flow Reactors. *Journal of Solar Energy Engineering*, 129(1) (2007) 111–118.

Gomes A., Fernandes E., Lima J. L. F. C., Fluorescence probes used for detection of reactive oxygen species. *Journal of Biochemical and Biophysical Methods*, 65 (2005) 45–80.

Goodsell D. S., The molecular perspective: ultraviolet light and pyrimidine dimmers. *Oncologist*, 6 (2001) 298–299.

Gort A. S., Imlay J. A., Balance between Endogenous Superoxide Stress and Antioxidant Defenses. *Journal of Bacteriology*, 180(6) (1998) 1402–1410.

Haider H., Ali W., Haydar S., Tesfamariam S., Sadiq R., Modeling exposure period for solar disinfection (SODIS) under varying turbidity and cloud cover conditions. *Clean Technologies and Environmental Policy*, 16 (2014) 861–874.

Hansberg W., Biología de las especies de oxígeno reactivas, in *Mensaje Bioquímico*, Vol XXVI (eds. Cea A., del Arenal I. P., Riveros H., Vázquez-Contreras E.), ISSN-0188-137X (2002).

He Y.-Y., Häder D.-P., UV-B-induced formation of reactive oxygen species and oxidative damage of the cyanobacterium *Anabaena* sp.: protective effects of ascorbic acid and *N*-acetyl-L-cysteine. *Journal of Photochemistry and Photobiology B*, 66 (2002) 115–124.

Hearn A. S., Stroupe M. E., Cabelli D. E., Lepock J. R., Tainer J. A., Nick H. S., Silverman D. N., Kinetic Analysis of Product Inhibition in Human Manganese Superoxide Dismutase. *Biochemistry*, 40 (2001) 12051–12058.

Helali S., Polo-López M. I., Fernández-Ibáñez P., Ohtani B., Amano F., Malato S., Guillard C., Solar photocatalysis: A green technology for *E. coli* contaminated water disinfection. Effect of concentration and different types of suspended catalyst. *Journal of Photochemistry and Photobiology A: Chemistry*, 276 (2014) 31–40.

Helioz GmbH website. Description of WADI device. Available on: https://www.helioz.org/overview.php (reviewed on May 2017).

Herrera G., Martinez A., Blanco M., O'Connor J.-E., Assessment of *Escherichia coli B* With Enhanced Permeability to Fluorochromes for Flow Cytometric Assays of Bacterial Cell Function. *Cytometry*, 49 (2002) 62–69.

Hijnen W. A. M., Beerendonk E. F., Medema G. J., Inactivation credit of UV radiation for viruses, bacteria and protozoan (oo)cysts in water: A review. *Water Research*, 40(1) (2006) 3–22.

Hoerter J., Eisenstark A., Touati D., Mutations by near-ultraviolet radiation in *Escherichia coli* strains lacking superoxide dismutase. *Mutation Research/Fundamental and Molecular Mechanisms of Mutagenesis*, 215(2) (1989) 161–165.

Hom L. W., Kinetics of chlorine disinfection in an ecosystem. *ASCE Journal of the Sanitary Engineering Division*, 98 (1972) 183–194.

Idil O., Darcan C., Ozen T., Ozkanca R. The effect of UV-A and various visible light wavelengths radiations on expression level of *Escherichia coli* oxidative enzymes in seawater. *Jundishapur Journal of Microbiology*, 6(3) (2013) 230–236.

Imlay J. A., Pathways of oxidative damage. *Annual Review of Microbiology*, 57 (2003) 395–418.

Imlay J. A., Cellular defenses against superoxide and hydrogen peroxide. *Annual Review of Biochemistry*, 77 (2008) 4.1–4.22.

Imlay J. A., Diagnosing oxidative stress in bacteria: not as easy as you might think. *Current Opinion in Microbiology,* 24 (2015) 124–131.

Imlay J. A., Chin S. M., Linn S., Toxic DNA Damage by Hydrogen Peroxide Through the Fenton Reaction in Vivo and in Vitro. *Science*, 240 (1988) 640–642.

Imlay J. A., Fridovich I., Assay of metabolic superoxide production in *Escherichia coli*. *The Journal of Biological Chemistry*, 266(11) (1991) 6957–6965.

Imlay J. A., Fridovich I., Suppression of oxidative envelope damage by pseudoreversion of a superoxide dismutase-deficient mutant of *Escherichia coli*. *Journal of Bacteriology*, 174 (1992) 953–961.

Imlay J. A., Hassett D. J., Oxidative and Nitrosative Stress Defence Systems in *Escherichia coli* and *Pseudomonas aeruginosa*: A Model Organism of Study Versus a Human Opportunistic Pathogen, in *Stress Response in Pathogenic Bacteria* (ed. Kidd S.), Chapter 1, CAB International, Cambridge (2011).

Imoberdorf G. E., Taghipour F., Keshmiri M., Mohseni M., Predictive radiation field modeling for fluidized bed photocatalytic reactors. *Chemical Engineering Science*, 63 (2008) 4228–4238.

Jackson T. A., Karapetian A., Miller A.-F., Brunold T. C., Spectroscopic and computational studies of the azide-adduct of Manganese Superoxide Dismutase: definitive assignment of the ligand responsible for the low-temperature thermochromism. *Journal of the American Chemical Society*, 126 (2004) 12477 – 12491.

Jensen J. N., Disinfection model based on excess inactivation sites: implications for linear disinfection curves and the Chick-Watson dilution coefficient. *Environmental Science & Technology*, 44 (2010) 8162–8168.

Joubert F., Fales H. M., Wen H., Combs C. A., Balaban R. S., NADH enzyme-dependent fluorescence recovery after photobleaching (ED-FRAP): applications to enzyme and mitochondrial reaction kinetics, in vitro. *Biophysical Journal*, 86 (2004) 629–645.

JoVE Science Education Database. General Laboratory Techniques. Introduction to Fluorescence Microscopy. JoVE, Cambridge, MA, doi: 10.3791/5040 (2016).

Kadir K., Nelson K. L., Sunlight mediated inactivation mechanism of *Enterococcus faecalis* and *Escherichia coli* in clear water versus waste stabilization pond water. *Water Research*, 50 (2014) 307–317.

Kalyanaraman B., Darley-Usmar V., Davies K. J. A., Dennery P. A., Forman H. J., Grisham M. B., Mann G. E., Moore K., Roberts II L. J., Ischiropoulos H., Measuring reactive oxygen and nitrogen species with fluorescent probes: challenges and limitations. *Free Radical Biology & Medicine*, 52 (2012) 1–6.

Karlsson M., Kurz T., Brunk U. T., Nilsson S. E., Frennesson, C. I., What does the commonly used DCF test for oxidative stress really show? *Biochemical Journal*, 428 (2010) 183–190.

Keane D. A., McGuigan K. G., Fernández-Ibáñez P., Polo-López M. I., Byrne J. A., Dunlop P. S. M., O'Shea K., Dionysiou D. D., Pillai S. C., Solar photocatalysis for water disinfection: materials and reactor design. *Catalysis Science & Technology*, 4 (2014) 1211–1226.

Keogh M. B., Castro-Alférez M., Polo-López M. I., Fernández-Calderero I., Al-Eryani Y. A., Joseph-Titus C., Sawant B., Dhodapkar R., Mathur C., McGuigan K. G., Fernández-Ibáñez P., Capability of 19-L polycarbonate plastic water cooler containers for efficient solar water disinfection (SODIS): Field case studies in India, Bahrain and Spain. *Solar Energy*, 116 (2015) 1–11.

Khaengraeng R., Reed R. H., Oxygen and photoinactivation of *Escherichia coli* in UVA. *Journal of Applied Microbiology*, 99(1) (2005) 39–50.

Kiehl J. T., Trenberth K. E., Earth's Annual Global Mean Energy Budget. *Bulletin of the American Meteorological Society*, 78 (2) (1997) 197–208.

Kishko I., Harish B., Zayats V., Reha D., Tenner B., Beri D., Gustavsson T., Ettrich R., Carey J., Biphasic kinetic behavior of *E. coli* WrbA, an FMN-dependent NAD(P)H:quinone oxidoreductase. *PLoS ONE,* 7(8) (2012) 1–10.

Knowles R. L., Eisenstark A., Near-ultraviolet mutagenesis in superoxide dismutase-deficient strains of *Escherichia coli*. *Environmental Health Perspectives*, 102(1) (1994) 88–94.

Koppenol W. H., The chemistry of peroxynitrite, a biological toxin. *Quimica Nova*, 21(3) (1998) 326–331.

Korshunov S., Imlay J. A., Detection and Quantification of Superoxide Formed within the Periplasm of *Escherichia coli*. *Journal of Bacteriology,* 188(17) (2006) 6326–6334.

Kothary M. H., Babu U. S., Infective dose of foodborne pathogens in volunteers: A review. *Journal of Food Safety*, 21(1) (2001) 49–68.

Kramer B., Muranyi P., Effect of pulsed light on structural and physiological properties of *Listeria innocua* and *Escherichia coli*. *Journal of Applied Microbiology*, 116(3) (2013) 596–611.

Labas M. D., Brandi R. J., Martín C. A., Cassano A. E., Kinetics of bacteria inactivation employing UV radiation under clear water conditions. *Chemical Engineering Journal*, 121 (2006) 135–145.

Labas M. D., Zalazar C. S., Brandi R. J., Cassano A. E., Reaction kinetics of bacteria disinfection employing hydrogen peroxide. *Biochemical Engineering Journal*, 38 (2008) 78–87.

Labas M. D., Brandi R. J., Zalazar C. S., Cassano A. E., Water disinfection with UVC radiation and H_2O_2. A comparative study. *Photochemical & Photobiological Sciences*, 8 (2009) 670–676.

Lee C. E., The discrete Sn approximation to transport theory. Los Alamos Scientific Laboratory Report LA-2595, (1962).

Li Puma G., Khor J. N., Brucato A., Modeling of an Annular Photocatalytic Reactor for Water Purification: Oxidation of Pesticides. *Environmental Science and Technology*, 38 (2004) 3737–3745.

Lo L.-C., Chu C.-Y., Development of highly selective and sensitive probes for hydrogen peroxide. *Chemical Communications*, (2003) 2728–2729.

Loewen P. C., Hengge-Aronis R., The role of the sigma factor σ^S (KatF) in bacterial global regulation. *Annual Reviews in Microbiology*, 48 (1994) 53–80.

Malato S., Fernández-Ibáñez P., Maldonado M. I., Blanco J., Gernjak W., Decontamination and disinfection of water by solar photocatalysis: Recent overview and trends. *Catalysis Today,* 147 (2009) 1–59.

Mani S. K., Kanjur R., Bright Singh I. S., Reed R. H., Comparative effectiveness of solar disinfection using small-scale batch reactors with reflective, absorptive and transmissive rear surfaces. *Water Research*, 40(4) (2006) 721–727.

Marugán J., van Grieken R., Alfano O. M., Cassano A. E., Optical and Physicochemical Properties of Silica-Supported TiO_2 Photocatalysts. *AiChe Journal*, 52(8) (2006) 2832–2843.

Marugán J., van Grieken R., Sordo C., Cruz C., Kinetics of the photocatalytic disinfection of *Escherichia coli* suspensions. *Applied Catalysis B: Environmental*, 82 (2008a) 27–36.

Marugán J., van Grieken R., Cassano A. E., Alfano O. M., Intrinsic kinetic modeling with explicit radiation absorption effects of the photocatalytic oxidation of cyanide with TiO_2 and silica-supported TiO_2 suspensions. *Applied Catalysis B: Environmental*, 85 (2008b) 48–60.

Marugán J., van Grieken R., Pablos C., Satuf M. L., Cassano A. E., Alfano O. M., Rigorous kinetic modelling with explicit radiation absorption effects of the photocatalytic inactivation of bacteria in water using suspended titanium dioxide. *Applied Catalysis B: Environmental*, 102 (2011) 404–416.

Massé E., Gottesman S., A small RNA regulates the expression of genes involved in iron metabolism in *Escherichia coli*. *Proceedings of the National Academy of Sciences of the United States of America*, 99 (2002) 4620–4625.

McCord J. M., Fridovich I., Superoxide dismutase an ezymic function for erythrocuprein (hemocuprein). *The Journal of Biological Chemistry*, 244 (1969) 6049–55.

McCormick J. P., Fisher J. R., Pachlatko J. P., Eisenstark A., Characterisation of a cell-lethal product from the photooxidation of tryptophan: hydrogen peroxide. *Science*, 191 (1976) 468–669.

McGuigan K. G., Joyce T. M., Conroy R. M., Gillespie J. B., Elmore-Meegan M., Solar disinfection of drinking water contained in transparent plastic bottles: characterizing the bacterial inactivation process. *Journal of Applied Microbiology*, 84 (1998) 1138–1148.

McGuigan K. G., Conroy R. M., Mosler H. J., du Preez M., Ubomba-Jaswa E., Fernández-Ibáñez P., Solar water disinfection (SODIS): A review from bench-top to roof-top. *Journal of Hazardous Materials*, 235–236 (2012) 29–46.

Messner K. R., Imlay J. A., The Identification of Primary Sites of Superoxide and Hydrogen Peroxide Formation in the Aerobic Respiratory Chain and Sulfite Reductase Complex of *Escherichia coli*. *The Journal of Biological Chemistry*, 274(15) (1999) 10119–10128.

Messner K. R., Imlay J. A., Mechanism of Superoxide and Hydrogen Peroxide Formation by Fumarate Reductase, Succinate Dehydrogenase, and Aspartate Oxidase. *The Journal of Biological Chemistry*, 277(45) (2002) 42563–42571.

Meulemans C. C. E., The Basic Principles of UV–Disinfection of Water. *Ozone: Science & Engineering*, 9 (1987) 299–314.

Moss S. H., Smith K. C., Membrane damage can be a significant factor in the inactivation of *Escherichia coli* by near-ultraviolet radiation. *Photochemistry and Photobiology*, 33 (1981) 203–210.

Nakamaru-Ogiso E., Kao M.-C., Chen H., Sinha S. C., Yagi T., Ohnishi T., The membrane subunit NuoL(ND5) is involved in the indirect proton pumping mechanism of *Escherichia coli* Complex I. *The Journal of Biological Chemistry*, 285(50) (2010) 39070 – 39078.

Nalwanga R., Quilty B., Muyanja C., Fernández-Ibáñez P., McGuigan K. G., Evaluation of solar disinfection of *E. coli* under Sub-Saharan field conditions using a 25 L borosilicate glass batch reactor fitted with a compound parabolic collector. *Solar Energy*, 100 (2014) 195–202.

Navntoft C., Ubomba-Jaswa E., McGuigan K. G., Fernández-Ibáñez P., Effectiveness of solar disinfection using batch reactors with non-imaging aluminium reflectors under real conditions: Natural well-water and solar light. *Journal of Photochemistry and Photobiology B: Biology*, 93 (2008) 155–161.

Ndabigengesere A., Narasiah K. S., Quality of water treated by coagulation using Moringa oleifera seeds. *Water Research*, 32(3) (1998) 781–791.

NHMRC, NRMMC (National Health and Medical Research Council, National Resource Management Ministerial Council). Australian Drinking Water Guidelines Paper 6 National Water Quality Management Strategy, version 3.3 Updated November 2016. (2011).

Noor R., Mechanism to control the cell lysis and the cell survival strategy in stationary phase under heat stress. *SpringerPlus,* 4 (2015) 1–9.

NWP (Netherlands Water Partnership), Smart Disinfection Solutions Smart Solutions (2010), ISBN/EAN: 978 94 6022 101 9.

Park S., You X., Imlay J.A., Substantial DNA damage from submicromolar intracellular hydrogen peroxide detected in Hpx-mutants of *Escherichia coli*. *Proceedings of the National Academy of Sciences of the United States of America*, 102 (2005) 9317–9322.

Petkar M. B., Pillai M. M., Kulkarni A. A., Bondre S. H., Rao K. R. S. S., Purification and characterization of superoxide dismutase isolated from sewage isolated *E. coli*. *Journal of Microbial & Biochemical Technology*, 5 (4) (2013) 102–106.

Polo D., García-Fernández I., Fernández-Ibáñez P., Romalde J. L., Solar water disinfection (SODIS): Impact on hepatitis A virus and on a human Norovirus surrogate under natural solar conditions. *International Microbiology*, 18 (2015) 41–49.

Polo-López M. I., García-Fernández I., Oller I., Fernández-Ibáñez P., Solar disinfection of fungal spores in water aided by low concentrations of hydrogen peroxide. *Photochemical and Photobiological Sciences*, 10(3) (2011) 381–388.

Pomposiello P. J., Bennik M. H. J., Demple B., Genome-Wide Transcriptional Profiling of the *Escherichia coli* Responses to Superoxide Stress and Sodium Salicylate. *Journal of Bacteriology*, 183(13) (2001) 3890–3902.

Raes D., Steduto P., Hsiao T. C., Fereres E., Chapter 2. Users Guide, in *AquaCrop Version 4.0*, FAO, Land and Water Division, Rome, Italy, (2012).

Rastogi R. P., Singh S. P., Häder D.-P., Sinha R. P., Detection of reactive oxygen species (ROS) by the oxidant-sensing probe 2',7'-dichlorodihydrofluorescein diacetate in the cyanobacterium *Anabaena variabilis* PCC 7937. *Biochemical and Biophysical Research Communications*, 397 (2010) 603–607.

Reed R. H., Solar inactivation of faecal bacteria in water: the critical role of oxygen. *Letters in Applied Microbiology*, 24 (1997) 276–280.

Rincón A.-G., Pulgarín C., Bactericidal action of illuminated TiO_2 on pure *Escherichia coli* and natural bacterial consortia: post-irradiation events in the dark and assessment of the effective disinfection time. *Applied Catalysis B: Environmental*, 49 (2004) 99–112.

Romero L. R., Alfano O. M., Cassano A. E., Cylindrical photocatalytic reactors. Radiation absorption and scattering effects produced by suspended fine particles in an annular space. *Industrial & Engineering Chemistry Research*, 36 (1997) 3094–3109.

Rosa G., Clasen T., Estimating the scope of household water treatment in low- and medium-income countries. *The American Journal of Tropical Medicine and Hygiene*, 82(2) (2010) 289–300.

Rossetti G. H., Albizzati E. D., Alfano O. M., Decomposition of Formic Acid in a Water Solution Employing the Photo-Fenton Reaction. *Industrial & Engineering Chemistry Research*, 41 (2002) 1436–1444.

Ryter S. W., Tyrrell R. M., Singlet molecular oxygen ($^1O_2$): a possible effector of eukaryotic gene expression. *Free Radical Biology & Medicine*, 24(9) (1998) 1520–1534.

Sammartano L. J., Tuveson R. W., *Escherichia coli* strains carrying the cloned cytochrome d terminal oxidase complex are sensitive to near-UV inactivation. *Journal of Bacteriology*, 169 (1987) 5304–5307.

Santos A. L., Oliveira V., Baptista I., Henriques I., Gomes N. C. M., Almeida A., Correia A., Cunha A., Wavelength dependence of biological damage induced by UV radiation on bacteria. *Archives of Microbiology*, 195 (2013) 63–74.

Schultz B. E., Chan S. I., Thermodynamics of electron transfer in *Escherichia coli* cytochrome bo_3. *Proceedings of the National Academy of Sciences of the United States of America*, 95 (1998) 11643–11648.

Seaver L. C., Imlay J. A., Alkyl hydroperoxide reductase is the primary scavenger of endogenous hydrogen peroxide in *Escherichia coli*. *Journal of Bacteriology*, 183(24) (2001a) 7173–7181.

Seaver L. C., Imlay J. A., Hydrogen peroxide fluxes and compartmentalization inside growing *Escherichia coli*. *Journal of Bacteriology*, 183(24) (2001b) 7182–7189.

Seaver L. C., Imlay J. A., Are respiratory enzymes the primary sources of intracellular hydrogen? *The Journal of Biological Chemistry*, 279(47) (2004) 48742–48750.

Severin B. F., Suidan M. T., Engelbrecht R. S., Kinetic modeling of U.V. disinfection of water. *Water Research*, 17(11) (1983) 1669–1678.

Shiklomanov I. A., World fresh water resources, in: *Water in crisis: A guide to the world's fresh water resources*, (ed. Gleick P. H.), Oxford University Press, New York, (1993) 13–24.

Sichel C., Tello J., de Cara M., Fernández-Ibáñez P., Effect of UV solar intensity and dose on the photocatalytic disinfection of bacteria and fungi. *Catalysis Today*, 129 (2007a) 152–160.

Sichel C., de Cara M., Tello J., Blanco J., Fernández-Ibáñez P., Solar photocatalytic disinfection of agricultural pathogenic fungi: *Fusarium* species. *Applied Catalysis B: Environmental*, 74 (2007b) 152–160.

Sichel C., Blanco J., Malato S., Fernández-Ibáñez P., Effects of experimental conditions on *E. coli* survival during solar photocatalytic water disinfection. *Journal of Photochemistry and Photobiology A: Chemistry*, 189 (2007c) 139–246.

Sichel C., Fernández-Ibáñez P., de Cara M., Tello J., Lethal synergy of solar UV-radiation and H_2O_2 on wild *Fusarium solani* spores in distilled and natural well water. Water Research 43(7) (2009) 1841–1850.

Sinha R. P., Häder D.-P., UV-induced DNA damage and repair: a review, *Photochemical and Photobiological Sciences*, 1 (2002) 225–236.

Sobota J. M., Imlay J. A., Iron enzyme ribulose-5-phosphate 3-epimerase in *Escherichia coli* is rapidly damaged by hydrogen peroxide but can be protected by mangenese. *Proceedings of the National Academy of Science of the United States of America*, 108 (2011) 5402–5407.

Solic M., Krstulovic N., Separate and combined effects of solar radiation, temperature, salinity, and pH on the survival of faecal coliforms in seawater. *Marine Pollution Bulletin*, 24 (8) (1992) 411–416.

Spasiano D., Marotta R., Malato S., Fernández-Ibáñez P., Di Somma I., Solar photocatalysis: Materials, reactors, some commercial, and pre-industrialized applications. A comprehensive approach. *Applied Catalysis B: Environmental*, 170–171 (2015) 90–123.

Spuhler D., Rengifo-Herrera J. A., Pulgarin C., The effect of Fe^{2+}, Fe^{3+}, H_2O_2 and the photo-Fenton reagent at near neutral pH on the solar disinfection (SODIS) at low temperatures of water containing *Escherichia coli* K12. *Applied Catalysis B: Environmental*, 96 (2010) 126–141.

Sukkasi S., Akamphon S., Heat-transfer modeling as a design tool for improving solar water disinfection (SODIS) containers. *Clean Technologies and Environmental Policy*, 16(8) (2013) 1773–1780.

Tanaka M., Ohkubo K., Fukuzumi S., DNA cleavage by UVA irradiation of NADH with dioxygen via radical chain processes. *The Journal of Physical Chemistry A*, 110 (2006) 11214–11218.

Tang B., Zhang L., Zhang L.-L., Study and application of flow injection spectrofluorimetry with a fluorescent probe of 2-(2-pyridil)-benzothiazoline for superoxide anion radicals. *Analytical Biochemistry*, 326 (2004) 176–182.

Tao Z., Raffel R. A., Souid A.-K., Goodisman J., Kinetic studies on enzyme-catalyzed reactions: oxidation of glucose, decomposition of hydrogen peroxide and their combination. *Biophysical Journal*, 96 (2009) 2977–2988.

Tortora G. J., Funke B. R., Case L. C., Microbiology: An Introduction. 9th edition. Pearson International Edition, San Francisco, (2007).

Trenberth K. E., Stepaniak D. P., The flow of energy through the earth's climate system. *Quartely Journal of the Royal Meteorological Society*, 130 (2004) 2677–2701.

Turner M. A., Eisenstark A., Near-ultraviolet radiation blocks SOS responses to DNA damage in *Escherichia coli*. *Molecular Genetics and Genomics*, 193(1) (1984) 33–37.

Tuveson R. W., Sammartano L. J., Sensitivity of hema mutant *Escherichia coli* cells to inactivation by near-UV light depends on the level of supplementation with delta-aminolevulinic-acid. *Photochemistry and Photobiology*, 43 (1986) 621–626.

Tyrrell R. M., Keyse S. M., New trends in photobiology the interaction of UVA radiation with cultured cells. *Journal of Photochemistry and Photobiology B: Biology*, 4 (1990) 349–361.

Ubomba-Jaswa E., Navntoft C., Polo-López M. I., Fernandez-Ibáñez P., McGuigan K. G., Solar disinfection of drinking water (SODIS): an investigation of the effect of UV-A dose on inactivation efficiency. *Photochemical & Photobiological Sciences*, 8 (2009a) 587–595.

Ubomba-Jaswa E., A Study of the Genotoxic Implications and Enhancement Technologies for Solar Disinfection (SODIS) of Drinking Water. PhD Thesis, (2009b). Royal College of Surgeons in Ireland.

Ubomba-Jaswa E., Fernández-Ibáñez P., Navntoft C., Polo-López M. I., McGuigan K. G., Investigating the microbial inactivation efficiency of a 25 L batch solar disinfection (SODIS) reactor enhanced with a compound parabolic collector (CPC) for household use. *Journal of Chemical Technology and Biotechnology*, 85 (2010) 1028–1037.

Unden G., Steinmetz P. A., Degreif-Dünnwald P., The aerobic and anaerobic respiratory chain of *Escherichia coli* and *Salmonella enterica*: Enzymes and energetics. *EcoSal Plus*, 6(1) (2014) 1–37.

UNESCO, The United Nations World Water Development Report 2015: Water for a Sustainable World. Paris, (2015).

Varghese S., Wu A., Park S., Imlay K. R. C. , Imlay J. A., Submicromolar hydrogen peroxide disrupts the ability of Fur protein to control free-iron levels in *Escherichia coli*. *Molecular Microbiology*, 64(3) (2007) 822–830.

Vatansever F., de Melo W. C. M. A., Avci P., Vecchio D., Sadasivam M., Gupta A., Chandran R., Karimi M., Parizotto N. A., Yin R., Tegos G. P., Hamblin M. R., Antimicrobial strategies centered around reactive oxygen species – bactericidal antibiotics, photodynamic therapy, and beyond. *FEMS Microbiology Reviews*, 37 (2013) 955–989.

Velez-Colmenares J., Estudio de los procesos de reactivación de los microorganismos fecales irradiados por luz ultravioleta. PhD Thesis, (2011). University of Cádiz.

Viglino P., Scarpa M., Coin F., Rotilio G., Rigo A., Oxidation of reduced Cu, Zn superoxide dismutase by molecular oxygen. A kinetic study. *Biochemical Journal*, 237 (1986) 305–308.

Visick J., Clarke S., RpoS- and OxyR-independent induction of HPI catalase at stationary phase in *Escherichia coli* and identification of *rpoS* mutations in common laboratory strains. *Journal of Bacteriology*, 179(13) (1997) 4158–4163.

Wang L., He H., Yu Y., Sun L., Liu S., Zhang C., He L., Morphology-dependent bactericidal activities of Ag/CeO_2 catalysts against *Escherichia coli*. *Journal of Inorganic Biochemistry*, 135 (2014) 45–53.

Watson H. E., A note on the variation of the rate of disinfection with change in the concentration of the disinfectant. *The Journal of Hygiene*, 8 (1908) 536–542.

Webb R. B., Brown M. S., Action spectra for oxygen-dependent and independent inactivation of *Escherichia coli*-Wp2s from 254-nm to 460-nm. *Photochemistry and Photobiology*, 29 (1979) 407–409.

Webb R. B., Brown M. S., Genetic damage in *Escherichia coli* K12 AB2480 by broad spectrum near ultraviolet radiation. *Science*, 215 (1982) 991–993.

Wegelin M., Canonica S., Mechsner K., Fleischmann T., Pesaro F., Metzler A., Solar water disinfection: scope of the process and analysis of radiation experiments. *Journal of Water Supply: Research and Technology - AQUA*, 43 (3) (1994) 154–169.

WHO/SDE/WSH, Managing Water in the Home: Accelerated Health Gains from Improved Water Supply, Department of Protection of the Human Environment WHO Geneva, (ed M. D. Sobsey) (2002).

WHO, Guidelines for drinking-water quality - Fourth edition. WHO Library Cataloguing-in-Publication Data, ISBN 978 92 4 154815 1 (2011a).

WHO, Evaluating household water treatment options: health-based targets and microbiological performance specifications. WHO Library Cataloguing-in-Publication Data, ISBN 978 92 4 154822 9 (2011b).

WHO, WHO International Scheme to Evaluate Household Water Treatment Technologies Harmonized Testing Protocol: Technology Non-Specific, (2014).

WHO/UNICEF, Progress on Sanitation and Drinking Water – 2015 update and MDG assessment. WHO Library Cataloguing-in-Publication Data, ISBN 9 789241 509145 (2015).

WHO Global Health Observatory visualizations. Water, sanitation and hygiene, (2016a) *online*. Available on: http://apps.who.int/gho/data/node.wrapper.ENVWATSAN?lang=en (reviewed on May 2017).

WHO Media Centre, Drinking-water. Fact sheet, (2016b) *online*. Available on: http://www.who.int/mediacentre/factsheets/fs391/en/ (reviewed on May 2017).

WHO, Results of Round I of the WHO International Scheme to Evaluate Household Water Treatment Technologies. WHO Library Cataloguing-in-Publication Data, ISBN 978 92 4 150994 7 (2016c).

Winterbourn C. C., The biological chemistry of hydrogen peroxide. *Methods in Enzymology*, 528 (2013) 3–25.

Winterbourn C. C., Kettle A. J., Radical–radical reactions of superoxide: a potential route to toxicity. *Biochemical and Biophysical Research Communications*, 305 (2003) 729–736.

Woodmansee A. N., Imlay J. A., Reduced Flavins Promote Oxidative DNA Damage in Non-respiring *Escherichia coli* by Delivering Electrons to Intracellular Free Iron. *The Journal of Biological Chemistry*, 277(37) (2002) 34055–34066.

Youn H.-D., Yim Y.-I, Kim K., Hah Y. C., Kang S.-O., Spectral characterization and chemical modification of catalase-peroxidase from *streptomyces* sp. *The Journal of Biological Chemistry*, 270(3) (1995) 13740–13747.

Zacarías S. M., Vaccari M. C., Alfano O. M., Irazoqui H. A., Imoberdorf G. E., Effect of the radiation flux on the photocatalytic inactivation of spores of *Bacillus subtilis*. *Journal of Photochemistry and Photobiology A: Chemistry*, 214 (2010) 171–180.

Zalazar C. S., Labas M. D., Brandi R. J., Cassano A. E., Dichloroacetic acid degradation employing hydrogen peroxide and UV radiation. *Chemosphere,* 66 (2007) 281–286.

Zhang M., Shi J., Jiang L., Modulation of mitochondrial membrane integrity and ROS formation by high temperature in *Saccharomyces cerevisiae*. *Electronic Journal of Biotechnology*, 18 (2015) 202–209.

Zhou X., Li Z., Lan J., Yan Y., Zhu N., Kinetics of inactivation and photoreactivation of *Escherichia coli* using ultrasound-enhanced UV-C light-emitting diodes disinfection. *Ultrasonics Sonochemistry*, 35 (2017) 471–477.

CHAPTER 11
APPENDIXES

Appendix A. Modelling of solar water disinfection (effect of solar UVA) using MATLAB® software

In chapter 5 (*Mechanistic model of solar water disinfection: effect of solar UVA*), it is presented the equations to solve the model at different experimental conditions of irradiance and initial bacteria concentration. The parameters search and the simulations were done by MATLAB® software.

It was created one excel file ("SODIS.xls") with the experimental data and five MATLAB® files: "MODEL.m", "Objective.m", "Sequential_search.m", "Monte_Carlo_search.m" and "Optimization.m", which content is presented below:

"SODIS.xls":

Table A.1. Sheet "t" of the excel file "SODIS.xls".

0	0	0	0	0	0
300	300	150	150	150	150
600	600	300	300	300	300
900	900	450	450	450	450
1200	1200	600	600	600	600
1350	1500	750	750	750	750
1500	1650	900		900	900
1650	1800	1050		1050	1050
1800	2100	1200			1200
1950	2400	1350			1350
2100	2550				

Table A.2. Sheet "Bu" of the excel file "SODIS.xls".

933333	958333	816667	758	7167	69300
276458	343958	340833	408	3542	47700
82500	136250	188750	112	2117	23600
10033	57500	78333	100	1308	6670
1275	13583	27125	52	556	3780
433	7148	7417	17	148	867
183	2154	2025		46	367
108	2088	342		17	97
58	488	75			34
25	33	17			17
17	17				

Table A.3. Sheet "I" of the excel file "SODIS.xls".

30	25	40	30	30	30

This excel file contains three sheets: "t", "Bu" and "I" that are the experimental data of time (s), bacteria concentration (CFU mL^{-1}) and UV irradiance (W m^{-2}), respectively. Each column is one experiment. The data is presented in the Tables A.1, A2 and A.3.

"MODEL" code:

```
%%%%%%%%%%%%%%%%%%%%%%%%%%%%%%%%
% MODEL OF SOLAR DISINFECTION %
%%%%%%%%%%%%%%%%%%%%%%%%%%%%%%%%

%The equations are defined with normalized concentrations of each species.
%The model has 5 model parameters that is given in the vector "k".
%The conditions simulated (irradiance and initial bacterial concentration)
%is given in the first raw of the matrixes "B_matrixexcel" and
%"irradiance_matrixexcel" in which each column is one experimental
%condition.
%The output matrix "result" has 7 columns: time(s), bacteria(CFU·mL-1), CAT
%(M), SOD (M), H2O2(M),O2.-(M) and HO.(M).

function result=MODEL(k,exp)

global B_matrixexcel irradiance_matrixexcel f


%%Experimental conditions of simulation
%---------------------------------------

Binicial=B_matrixexcel(1,exp);
irradiance=irradiance_matrixexcel(exp);

%%Constants
%---------------------------------------

iron=2e-5;        %M
oxig=2e-4;        %M
elect=1.35e-12;   %M
NADH=2.5e-4;      %M

SOD0=2e-5;        %M
CAT0=9.2e-5;      %M
perox0=2e-8;      %M

k1=2e10;          %M-1·s-1
k3=1e9;           %M-1.s-1
k4=70;            %M-1·s-1
k6=2.7e7;         %M-1·s-1
k7=8.3e5;         %M-1·s-1
k8=9e5;           %M-1·s-1
k9=1.56e7;        %cm3·Einstein-1

gamma1=k1*oxig*elect;  %M·s-1
gamma3=k4*iron;        %s-1
```

```
%%Irradiance
%---------------------------------------

Ep=6.626e-34*3e8/350e-9;     %h·c/lambda_average (J·photon-1)
NA=6.022e23;                 %photon·Einstein-1
G=irradiance/(Ep*NA)*1e-4;   %Einst/(cm2·s)

kCAT_spec=267718;            %M-1·cm-1
kSOD_spec=800;               %M-1·cm-1
kNADH_spec=6220;             %M-1·cm-1

kNADH=kNADH_spec*NADH;       %cm-1
eNADH=kNADH*G;               %Einst/(cm3·s)


%%Model parameters
%---------------------------------------

gamma2=k(1)*f(1);       %cm3·Einst-1·M
k10=k(2)*f(2);          %cm3·Einstein-1
k11=k(3)*f(3);          %s-1
k12=k(4)*f(4);          %s-1
k13=k(5)*f(5);          %s-1


%%Model equations
%---------------------------------------

%xN(1)=peroxN
%XN(2)=BN

superox0 =  ( gamma1 + gamma2*eNADH )/( k3*SOD0 + k12 );
hidrox0 = ( 2*gamma3*perox0 )/( k6*perox0 + k11);

CATN=@(t) 1./( 1 + k9*kCAT_spec*G*CAT0*t );
SODN=@(t) 1./( 1 + k10*kSOD_spec*G*SOD0*t );

superoxN=@(t) (k3*SOD0 + k12) ./ ( k3*SOD0*SODN(t) + k12) ;
hidroxN=@(t,xN) xN(1)*( k6*perox0+k11 ) ./ ( k6*xN(1)*perox0 + k11);

dperoxN=@(t,xN) 1/(2*perox0) * k3*SOD0*SODN(t)*(gamma1+gamma2*eNADH ) /
(k3*SOD0*SODN(t)+k12 ) - gamma3*k6*perox0*xN(1)^2 / (k6*perox0*xN(1)+k11) -
(gamma3 + k8*CAT0*CATN(t) )*xN(1) ;
dBN=@(t,xN) -k13*hidrox0*hidroxN(t,xN).*superox0*superoxN(t).*xN(2) ;

funcion=@(t,xN)[dperoxN(t,xN);dBN(t,xN)];


%%Solve differential equations
%---------------------------------------

xN0=[1;1];
t_modelo=(0:1:3000)';
[t,xN]=ode45(funcion,t_modelo,xN0);

peroxN=xN(:,1);
B=Binicial*xN(:,2);
B( B<17 ) = 17; %Detection limit for bacteria = 17

result=zeros(3001,7); %%columns = time, bacteria, CAT, SOD, H2O2, O2.-, HO.

for i=1:3001
    result(i,1)=t(i);
    result(i,2)=B(i);
```

```
    result(i,3)=CAT0*feval(CATN,i-1);
    result(i,4)=SOD0*feval(SODN,i-1);
    result(i,5)=perox0*peroxN(i);
    result(i,6)=superox0*feval(superoxN,i-1);
    result(i,7)=hidrox0*feval(hidroxN,i-1,xN(i));
end

end
```

"Objective" code:

```
%%%%%%%%%%%%%%%%%%%%%%%%%%%%%%%%%%%%%%%%%%%%%%%%
% CALCULATION OF THE OBJECTIVE FUNCTION %
%%%%%%%%%%%%%%%%%%%%%%%%%%%%%%%%%%%%%%%%%%%%%%%%

%It is calculated the NRMSLE (objective function) of all the experiments (6
%in total), comparison between the experimental data and simulated data.
%Experimental data is given the matrix "B_matrixexcel" and %"t_matrixexcel"
%in which each column is one experimental condition.
%Model simulated data is calculated with "MODEL" function using de model
%parameters of the vector "k".


function NRMSLE = Objective(k)

global num_exp n_pts B_matrixexcel t_matrixexcel

NRMSLE_exp=zeros(num_exp,1);
format long


%%NRMSLE for experiment "v"
%---------------------------------------

for v=1:num_exp

    %Experimental data of the experiment "v"
    n_pts_exp=n_pts(v);
    B_experimental=zeros(n_pts_exp,1);
    t_experimental=zeros(n_pts_exp,1);
    for i=1:n_pts_exp
        B_experimental(i)=B_matrixexcel(i,v);
        t_experimental(i)=t_matrixexcel(i,v);
    end

    %Simulated data of experiment "v"
    result=MODEL(k,v);
    t_model=result(:,1);
    B_model=result(:,2);

    %Simulated data of experiment "v" at sampling times
    B_calc=zeros(n_pts(v),1);
    for i=1:n_pts(v)
        idx = t_model==t_experimental(i);
        B_calc(i)=B_model(idx,1);
    end

    %NRMSLE experiment "v"
    NRMSLE_exp(v)=sqrt(1/n_pts(v) * sum( ( log10(B_calc(:)+1)-
log10(B_experimental(:)+1) ) .^2 )  )  / ( sum( log10(B_experimental(:)) ) /
n_pts(v) ) *100;

end
```

```
%%NRMSLE for all the experiments
%--------------------------------------

NRMSLE=sum(NRMSLE_exp)/num_exp;

end
```

"Sequential search" code:

```
%%%%%%%%%%%%%%%%%%%%%
% SEQUENTIAL SEARCH %
%%%%%%%%%%%%%%%%%%%%%

%The model has 5 parameters. This program test one parameter (k) taken
%values from 1 to 10^20 changing the order of magnitude in each test
%(21 simulations). The rest of parameters are given the value of 1.
%The output matrix "cost" saves all the combinations tested with its
%error. In the first column is saved the NRMSLE and in the next columns,
%the model parameters.
%Experimental data is given in an excel file "SODIS.xls".

clear all
clc

global  num_exp n_pts B_matrixexcel irradiance_matrixexcel t_matrixexcel f

t_matrixexcel=xlsread('SODIS.xls','t');
B_matrixexcel=xlsread('SODIS.xls','Bu');
irradiance_matrixexcel=xlsread('SODIS.xls','I');

n_pts=[11 11 10 6 8 10]; %number of samples of each experiment
num_exp=6;

num_cts=5;
f=[1 1 1 1 1];

k=1; %%parameter that is tested in the program

vectork=ones(1,num_cts);    %vector with the model parameters
cost=zeros(21,num_cts+1);   %matrix that will save NRMSLE and the constants


for i=1:21

    vectork(1,k)=10^(i-1);

    NRMSLE=Objective(vectork);

    %Save in "cost" matrix the error and constants
    cost(i,1)=NRMSLE;
    for j=1:num_cts
        cost(i,j+1)=vectork(1,j);
    end
end
```

"Monte_Carlo_search" code:

```
%%%%%%%%%%%%%%%%%%%%%%
% MONTE CARLO SEARCH %
%%%%%%%%%%%%%%%%%%%%%%

%A combination of parameters model are used to the simulations and it is
%tested by the calculation of the NRMSLE.
%Parameters are chosen randomly in a defined interval.
%Experimental data is given in an excel file "SODIS.xls".


clear all
clc

global  num_exp n_pts B_matrixexcel irradiance_matrixexcel t_matrixexcel f


%%Experimental data
%---------------------------------------

t_matrixexcel=xlsread('SODIS.xls','t');
B_matrixexcel=xlsread('SODIS.xls','Bu');
irradiance_matrixexcel=xlsread('SODIS.xls','I');

n_pts=[11 11 10 6 8 10]; %number of samples of each experiment
num_exp=6;


%%Model parameters intervals definition
%---------------------------------------

num_cts=5;

%Define three searching intervals for each constant
%rkas(i,:)=[X1 X2 X3 X4]
%Interval 1 = [X1 X2]
%Interval 2 = [X2 X3]
%Interval 3 = [X3 X4]

rkas(1,:)=[0.1 1.71 29.2 500];     %gamma2
rkas(2,:)=[0.1 1.71 29.2 500];     %k10
rkas(3,:)=[0.1 1.71 29.2 500];     %k11
rkas(4,:)=[0.1 1.71 29.2 500];     %k12
rkas(5,:)=[0.1 1.71 29.2 500];     %k13

f=[1e6 1e6 1e5 1e5 1e16];


%%Random parameters generation
%---------------------------------------

iter=50;

matrik=zeros(iter,num_cts); %save all the parameters combinations created
interval=zeros(num_cts,2);

for j=1:iter
    %Choose randomly one of the three intervals
    for i=1:num_cts
    a=rand;
        if a>=0.33 && a<=0.66
            interval(i,:)=[rkas(i,2) rkas(i,3)];
```

```
        else if a<0.33
                interval(i,:)=[rkas(i,1) rkas(i,2)];
            else %%a>0.66;
            interval(i,:)=[rkas(i,3) rkas(i,4)];
            end
        end
    end
    %Create a random parameter inside the interval chosen
    a=rand(num_cts,1);
    rk=zeros(num_cts,1);
    for i=1:num_cts
        rk(i,1)=a(i,1)*(interval(i,2)-interval(i,1))+interval(i,1);
    end
    matrik(j,:)=rk';
end


%%Model simulation
%--------------------------------------

cost=zeros(iter,num_cts+1);  %matrix that will save NRMSLE and the constants
improved=0;                  %index that indicate the number of iterations
that have been improved
min=ones(1,10)*1e20;         %vector that will save the 10 best NRMSLE
pos_min=zeros(1,10);         %vector that will save the number of "iter" of
the 10 best NRMSLE

for j=1:iter

    %Error calculation of cts of the iteration "j"
    NRMSLE=Objective(matrik(j,:));

    %Save in "cost" matrix the error and constants
    cost(j,1)=NRMSLE;
    for i=1:num_cts
        cost(j,i+1)=matrik(j,i);
    end

    %Save in "min" and "pos_min" the 10 best combinations of constants and
    %update "improved" number
    if cost(j,1)<=min(10)
        for i=1:10
            if cost(j,1)<=min(i)
                p=10;
                    for m=i:9
                        min(p)=min(p-1);
                        pos_min(p)=pos_min(p-1);
                        p=p-1;
                    end
                min(i)=cost(j,1);
                pos_min(i)=j;
                    if i==1
                        improved=improved+1;
                    end
               break
            end
        end
    end


    sprintf('Left %d iterations to finish the program \n', iter-j)
    sprintf('The actual minimum is %f \n',min(1))
    sprintf('The number of improvements until now is %d \n',improved)
end
```

```
%%Best combination of parameters
%---------------------------------------

kbest=zeros(1,num_cts);
for i=1:num_cts
    kbest(i)=cost(pos_min(1),i+1);
end

t=zeros(3001,num_exp);
B=zeros(3001,num_exp);
CAT=zeros(3001,num_exp);
SOD=zeros(3001,num_exp);
perox=zeros(3001,num_exp);
superox=zeros(3001,num_exp);
hidrox=zeros(3001,num_exp);


for v=1:num_exp

    result=MODEL(kbest,v);

    t(:,v)=result(:,1);
    B(:,v)=result(:,2);
    CAT(:,v)=result(:,3);
    SOD(:,v)=result(:,4);
    perox(:,v)=result(:,5);
    superox(:,v)=result(:,6);
    hidrox(:,v)=result(:,7);


    %Graph
    subplot(2,3,v)
    semilogy(t_matrixexcel(:,v),B_matrixexcel(:,v),'r*',t(:,v),B(:,v),'b-');
    axis([0 3000 1e0 1e6])
    %legend ('Experimental','Model')
    xlabel('Time (s)')
    ylabel('Bacteria (CFU/mL)')

end
```

"Optimization" code:

```
%%%%%%%%%%%%%%%%%%%%%%%%%%%%
% PARAMETERS OPTIMIZATION %
%%%%%%%%%%%%%%%%%%%%%%%%%%%%

%A nonlinear regression is performed to minimize the objective function.
%Experimental data is given in an excel file "SODIS.xls".
%Parameter values for initiate the regression is given in the vector
%"k_ini" and "f" as the best results obtained in the Monte Carlo search.
%Output vector "k" gives the optimizated values of the parameters.
%Simulation results of the 6 experimental conditions tested are saved in
%the matrixes "t", "B", "CAT", "SOD", "perox", "superox" and "hidrox". Each
%column is correspondent to one experimental condition.


clear all
clc

global t_matrixexcel B_matrixexcel irradiance_matrixexcel n_pts num_exp f
```

```
%%Experimental data
%---------------------------------------

t_matrixexcel=xlsread('SODIS.xls','t');
B_matrixexcel=xlsread('SODIS.xls','Bu');
irradiance_matrixexcel=xlsread('SODIS.xls','I');

n_pts=[11 11 10 6 8 10]; %number of samples of each experiment
num_exp=6;


%%Nonlinear regression
%---------------------------------------

% Initial values of k and contraints intervals LB < k < UB:
k_ini = [1 1 2 1 8];
f=[1e5 1e6 1e4 1e5 1e15];
LB=[0.1 0.1 0.1 0.1 0.1];
UB=[10 10 10 10 10];

% Objective function minimization
options=optimset('Display','iter','Algorithm','interior-point');
[k,NRMSLE,exitflag,info,lambda,grad,hessian]=fmincon('Objective',k_ini,[],[]
,[],[],LB,UB,[],options);

format long
k
NRMSLE
err = sqrt(diag(inv(hessian)));


%%Best combination of parameters
%---------------------------------------

t=zeros(3001,num_exp);
B=zeros(3001,num_exp);
CAT=zeros(3001,num_exp);
SOD=zeros(3001,num_exp);
perox=zeros(3001,num_exp);
superox=zeros(3001,num_exp);
hidrox=zeros(3001,num_exp);

for v=1:num_exp

    result=MODEL(kbest,v);

    t(:,v)=result(:,1);
    B(:,v)=result(:,2);
    CAT(:,v)=result(:,3);
    SOD(:,v)=result(:,4);
    perox(:,v)=result(:,5);
    superox(:,v)=result(:,6);
    hidrox(:,v)=result(:,7);


    %Graph
    subplot(2,3,v)
    semilogy(t_matrixexcel(:,v),B_matrixexcel(:,v),'r*',t(:,v),B(:,v),'b-');
    axis([0 3000 1e0 1e6])
    %legend ('Experimental','Model')
    xlabel('Time (s)')
    ylabel('Bacteria (CFU/mL)')

end
```

Implementation:

Firstly, the sequential search was run by writing "Sequential_search" in the command window of MATLAB®. The program was run several times changing the value of k (1, 2, 3, 4 and 5) being the rest of the parameters in each run equal to 1. Then, the program was again run making different combinations of the parameters using orders of magnitude obtained as the best in the previous runs.

Secondly, the parameters Monte Carlo search was run by writing "Monte_Carlo_search" in the command window. The program was run several times to reach different combinations of parameters that deal to a NRMSLE < 10 %. The interval of searching was defined using the order of magnitude for each parameter obtained in the previous step.

Finally, a nonlinear regression was performed by writing "Optimization" in the command window. The initial values of the parameters used were those obtained in the Monte Carlo search.

Appendix B. Modelling of solar water disinfection (synergistic effect of solar UVA and mild-heat) using MATLAB® software

In the chapter 6 (*Mechanistic model of solar water disinfection: synergistic effect of solar UVA and mild-heat*), it is presented the equations to solve the *synergistic SODIS-thermal* model at different experimental conditions of irradiance, temperature and initial bacteria concentration. The parameters search and the simulations were done by MATLAB® software with the same procedure explained above.

It was created one excel file ("SODIS_T.xls") with the experimental data and five MATLAB® files: "MODEL_T.m", "Objective_T.m", "Sequential_search_T.m", "Monte_Carlo_search_T.m" and "Optimization_T.m". Their content is very similar than the files developed for the previous model. In the files "Sequential_search_T.m", "Monte_Carlo_search_T.m" and "Optimization_T.m", it was included a new *global* variable (*temperature_matrixexcel*) and the number of experiments, points and constants were changed:

```
temperature_matrixexcel=xlsread('SODIS_T.xls','Temp');

n_pts=[7 5 7]; %number of samples of each experiment
num_exp=3;

num_cts=3;
```

The "MODEL.m" was suffered more modifications; the complete code is written below:

```
%%%%%%%%%%%%%%%%%%%%%%%%%%%%%%%%%%
% MODEL OF SOLAR DISINFECTION %
%%%%%%%%%%%%%%%%%%%%%%%%%%%%%%%%%%

function result=MODEL_T(k,exp)

global  B_matrixexcel irradiance_matrixexcel temperature_matrixexcel f


%%Experimental conditions of simulation
%---------------------------------------

Binicial=B_matrixexcel(1,exp);
irradiance=irradiance_matrixexcel(exp);
T=temperature_matrixexcel(exp);
```

```
%%Constants
%---------------------------------------

iron=2e-5;        %M
oxig=2e-4;        %M
elect=1.35e-12;   %M
NADH=2.5e-4;      %M

SOD0=2e-5;        %M
CAT0=9.2e-5;      %M
perox0=2e-8;      %M

R=8.314;          %J·K-1·mol-1

A1=3.16e12;       %M-1.s-1
Ea1=1.3e4;        %J·mol-1
k3=1e9;           %M-1.s-1
A4=1.92e9;        %M-1.s-1
Ea4=4.676e4;      %J·mol-1
k6=2.7e7;         %M-1·s-1
k7=8.3e5;         %M-1·s-1
k8=9e5;           %M-1·s-1
k10=1.56e6;       %cm3·Einstein-1
k11=2.04e4;       %s-1
k12=1.36e5;       %s-1
k13=8.03e15;      %M-2·s-1
A14=1.3e34;       %s-1
Ea14=225614;      %J·mol-1

delta1=A1*oxig*elect;  %M·s-1
delta3=A4*iron;        %s-1


%%Irradiance
%---------------------------------------

Ep=6.626e-34*3e8/350e-9;    %h·c/lambda_average (J·photon-1)
NA=6.022e23;                %photon·Einstein-1
G=irradiance/(Ep*NA)*1e-4;  %Einst/(cm2·s)

kCAT_spec=267718;           %M-1·cm-1
kSOD_spec=800;              %M-1·cm-1
kNADH_spec=6220;            %M-1·cm-1

kNADH=kNADH_spec*NADH;      %cm-1
eNADH=kNADH*G;              %Einst/(cm3·s)


%%Model parameters and boundary conditions
%-----------------------------------------

Ea2=k(1)*f(1);         %J·mol-1
A2=k(2)*f(2);          %cm3·Einstein-1·M-1
Ea9=k(3)*f(3);         %J·mol-1

delta2=A2*oxig*elect;  %cm3·Einst-1·M

k9_25C=1.5e7;                       %cm3·Einst-1
A9=k9_25C*exp(Ea9/(R*(25+273)));    %cm3·Einst-1
```

```
%%Model equations
%---------------------------------------

%xN(1)=peroxN
%XN(2)=BN

superox0 =  delta1*exp(-Ea1/(R*T)) /( k3*SOD0 + k12 );
hidrox0 = ( 2*delta3*exp(-Ea4/(R*T))*perox0 )/( k6*perox0 + k11 );

CATN=@(t)1./(1+A9*exp(-Ea9/(R*T))*kCAT_spec*G*CAT0*t);
SODN=@(t)1./(1+k10*kSOD_spec*SOD0*G*t);

superoxN=@(t) (1+ delta2/delta1*exp(-(Ea2-Ea1)/(R*T))*eNADH) * ( k3*SOD0 +
k12 ) ./ ( k3*SOD0*SODN(t) + k12 );
hidroxN=@(xN,t)xN(1)*( k6*perox0 + k11 ) ./ ( k6*xN(1)*perox0 + k11);

dperoxN=@(t,xN) k3*SOD0/(2*perox0)*SODN(t)*(delta1*exp(-
Ea1/(R*T))+delta2*exp(-Ea2/(R*T))*eNADH) / (k3*SOD0*SODN(t)+k12) -
delta3*exp(-Ea4/(R*T))*k6*perox0*xN(1)^2 / (k6*perox0*xN(1)+k11) -
(delta3*exp(-Ea4/(R*T)) + k8*CAT0*CATN(t) )*xN(1) ;
dBN=@(t,xN) -k13*hidrox0*hidroxN(t,xN).*superox0*superoxN(t).*xN(2) +
A14*exp(-Ea14/(R*T))*xN(2) ;

funcion=@(t,xN)[dperoxN(t,xN);dBN(t,xN)];

%%Solve differential equations
%---------------------------------------

xN0=[1;1];
t_modelo=(0:1:3500)';
[t,xN]=ode45(funcion,t_modelo,xN0);

peroxN=xN(:,1);
B=Binicial*xN(:,2);
B( B<17 ) = 17; %Detection limit for bacteria = 17

result=zeros(3501,7); %%columns = time, bacteria, CAT, SOD, H2O2, O2.- and
HO.

for i=1:3501
    result(i,1)=t(i);
    result(i,2)=B(i);
    result(i,3)=CAT0*feval(CATN,i-1);
    result(i,4)=SOD0*feval(SODN,i-1);
    result(i,5)=perox0*peroxN(i);
    result(i,6)=superox0*feval(superoxN,i-1);
    result(i,7)=hidrox0*feval(hidroxN,i-1,xN(i));
end

end
```

The "SODIS_T.xls" excel file contains four sheets: "t", "Bu", "I" and "Temp" that are the experimental data of time (s), bacteria concentration (CFU mL^{-1}), UV irradiance (W m^{-2}) and temperature (ºC), respectively. The data is presented in the next tables:

Table A.4. Sheet "t" of the excel file "SODIS_T.xls".

0	0	0
300	300	120
600	600	240
900	900	360
1200	1200	480
1500		600
1800		720

Table A.5. Sheet "Bu" of the excel file "SODIS_T.xls".

766667	750000	725000
300000	71667	77000
27625	3333	7000
4750	217	667
400	17	116
52		26
17		17

Table A.6. Sheet "I" of the excel file "SODIS_T.xls".

30	30	30

Table A.7. Sheet "Temp" of the excel file "SODIS_T.xls".

30	40	50

Appendix C. Modelling of incident radiation for turbid waters within the 2 L-PET batch reactor using MATLAB® software

In chapter 7 (*Validation of solar water disinfection model in solar reactors under real field conditions*), it is presented the equations to solve the radiative transfer equation by the discrete ordinate method for the 2-dimensions, 2-directions problem of the 2 L-PET batch reactor. The iteration method described in Figure 7.6 was developed by MATLAB® software.

It was created two MATLAB® files: "Quadrature.m" and "Light_model.m". Their content is presented below:

"Quadrature.m":

```
function [Mc,M,cosine,w]=Quadrature

% S16 DISCRETE APPROXIMATION
%%%%%%%%%%%%%%%%%%%%%%%%%%%%%%%%

    N = 16;           % doble of number of cosines
    M = N*(N+2) / 2 ; % semi-sphere directions
    Mc= M / 4;        % quadrants directions

    wd = [ 1; 2; 3; 4; 4; 3; 2; 1;
           2; 5; 6; 7; 6; 5; 2;
           3; 6; 8; 8; 6; 3;
           4; 7; 8; 7; 4;
           4; 6; 6; 4;
           3; 5; 3;
           2; 2;
           1 ];           % weight distribution [Lee,1962]

    iw =  [ 0.04551160;
            0.03977459;
            0.03004615;
            0.02733194;
            0.02328516;
            0.01862861;
            0.01763140;
            0.01534259 ]; % weight [Lee,1962]

    n =  [ 0.97752522;
           0.90676470;
           0.82999331;
           0.74535599;
           0.64978629;
           0.53748385;
           0.39440532;
           0.14907120 ]; % cosines [Lee,1962]


% MATRIX OF COSINES
%%%%%%%%%%%%%%%%%%%%%%
```

```
    cosine=zeros(M,2); % mu in column 1; eta in column 2
    w=zeros(M,1);

        % QUADRANT 1 (mu>0 and eta>0)
        dir=1;
        for i=1:N/2
            for j=1:i
            cosine(dir,1)=n(i);
            cosine(dir,2)=n(N/2-j+1);
            w(dir)=iw(wd(dir));
            dir=dir+1;
            end
        end

        % QUADRANT 2 (mu<0 and eta>0)
        for i=1:Mc
            cosine(dir,1)=-cosine(i,1);
            cosine(dir,2)=cosine(i,2);
            w(dir)=w(i);
            dir=dir+1;
        end

        % QUADRANT 3 (mu<0 and eta<0)
        for i=1:Mc
            cosine(dir,1)=-cosine(i,1);
            cosine(dir,2)=-cosine(i,2);
            w(dir)=w(i);
            dir=dir+1;
        end

        % QUADRANT 4 (mu>0 and eta<0)
        for i=1:Mc
            cosine(dir,1)=cosine(i,1);
            cosine(dir,2)=-cosine(i,2);
            w(dir)=w(i);
            dir=dir+1;
        end

    %NORMALIZATION

    w = w / 4;  % sum of the weight of the M direction = 1
```

“Light_model.m”:

```
%%INITIAL DATA
%%%%%%%%%%%%%%%%%%%%%%%%%%%%%%%%%%%%%%%%%%%%%%%

% Incident radiation
q0w=100; % Wm-2sr-1  %% reference flux


% Water characteristics
kappa=5.9e-3;        %cm-1      %%bacteria absorption for 1e6 CFUmL-1
sigma_sp=2.78e-3;    %cm-1NTU-1 %%kaolin specific scattering
%sigma_sp=2.92e-3;   %cm-1NTU-1 %%red soil specific scattering
C=100;               %NTU       %%turbidity
sigma=sigma_sp*C;    %cm-1      %%scattering kaolin or red soils
beta=kappa+sigma;    %cm-1      %extinction coefficient


% Reactor characteristics
T = 0.52;    %transmittance
```

```
r = 8.5/2;   %cm %% radius
LX = pi/2*r; %cm %% equivalent path length
LY = 2*r;    %cm %% diameter

q0=T*q0w; % Wm-2sr-1  %% flux


% Mesh size
NX=200;
NY=NX;
DX=L/NX; %discrete increment of x
DY=H/NY; %discrete increment of y

[Mc,M,cosine,w]=Quadrature;


% Initialization and boundary conditions
I=zeros(NY,NX,M);        % three dimensional matrix I(y,x,m)
Imasi=zeros(NY,NX+1,M);  % three dimensional matrix I(y,x+1/2,m)
Imasj=zeros(NY+1,NX,M);  % three dimensional matrix I(y+1/2,x,m)
S=zeros(NY,NX,M);        % three dimensional matrix S(y,x,m)

Imasi(:,1,1)     = q0 / (  cosine(1,1)   *  w(1)   *2*pi) / NY /2 ;  %direct
radiation distributed in direction 1 of quadrant 1
Imasi(:,1,3*Mc+1)= q0 / (cosine(3*Mc+1,1)*w(3*Mc+1)*2*pi) / NY / 2;  %and
quadrant 4 (to assure X symetry)

iter_max=500;
tol=0.00001;

iter=1;
err=tol+1;


% MESH SOLUTION
%%%%%%%%%%%%%%%%%%%%%%%%%%%%%%%%%%%%%%%%%%%%%%%

while(iter<=iter_max && err>tol)

    % FORWARD: Calculation of I with mu>0 (quadrants 1 and 4)

    % Quadrant 1 from left-bottom corner
    for j=NY:-1:1 % from element at y=1 (last matrix-row) to y=NY
        for i=1:NX
            for m=1:Mc
                m1 = 0*Mc + m;
                D = 2*DY*abs(cosine(m1,1)) + 2*DX*abs(cosine(m1,2)) +
beta*DX*DY;
                I (j,i,m1) =  2*DY*abs(cosine(m1,1))/D * Imasi(j,i,m1) +
2*DX*abs(cosine(m1,2))/D * Imasj(j+1,i,m1) + S(j,i,m1)*DX*DY/D;
                Imasi (j,i+1,m1) = 2* I(j,i,m1) - Imasi(j,i,m1);
                if Imasi(j,i+1,m1)<0
                    Imasi(j,i+1,m1)=0;
                end
                Imasj (j,i,m1) = 2* I(j,i,m1) - Imasj(j+1,i,m1);
                if Imasj(j,i,m1)<0
                    Imasj(j,i,m1)=0;
                end
            end
        end
    end

    % Quadrant 4 from left-top corner
    for j=1:NY    % from element at y=NY (first matrix-row) to y=1
```

```
        for i=1:NX
            for m=1:Mc
                m4 = 3*Mc + m;
                D = 2*DY*abs(cosine(m4,1)) + 2*DX*abs(cosine(m4,2)) +
beta*DX*DY;
                I (j,i,m4) =  2*DY*abs(cosine(m4,1))/D * Imasi(j,i,m4) +
2*DX*abs(cosine(m4,2))/D * Imasj(j,i,m4) + S(j,i,m4)*DX*DY/D;
                Imasi (j,i+1,m4) = 2* I(j,i,m4) - Imasi(j,i,m4);
                if Imasi(j,i+1,m4)<0
                    Imasi(j,i+1,m4)=0;
                end
                Imasj (j+1,i,m4) = 2* I(j,i,m4) - Imasj(j,i,m4);
                if Imasj(j+1,i,m4)<0
                    Imasj(j+1,i,m4)=0;
                end
            end
        end
    end


    % BACK: Calculation of I with mu<0 (quadrants 2 and 3)

    % Quadrant 2 from right-bottom corner
    for j=NY:-1:1 %from element at y=1 (last matrix-row) to y=NY
        for i=NX:-1:1
            for m=1:Mc
                m2 = 1*Mc + m;
                D = 2*DY*abs(cosine(m2,1)) + 2*DX*abs(cosine(m2,2)) +
beta*DX*DY;
                I (j,i,m2) =  2*DY*abs(cosine(m2,1))/D * Imasi(j,i+1,m2) +
2*DX*abs(cosine(m2,2))/D * Imasj(j+1,i,m2) + S(j,i,m2)*DX*DY/D;
                Imasi (j,i,m2) = 2* I(j,i,m2) - Imasi(j,i+1,m2);
                if Imasi(j,i,m2)<0
                    Imasi(j,i,m2)=0;
                end
                Imasj (j,i,m2) = 2* I(j,i,m2) - Imasj(j+1,i,m2);
                if Imasj(j,i,m2)<0
                    Imasj(j,i,m2)=0;
                end
            end
        end
    end

    % Quadrant 3 from right-top corner
    for j=1:NY    % from element at y=NY (first matrix-row) to y=1
        for i=NX:-1:1
            for m=1:Mc
                m3 = 2*Mc + m;
                D = 2*DY*abs(cosine(m3,1)) + 2*DX*abs(cosine(m3,2)) +
beta*DX*DY;
                I (j,i,m3) =  2*DY*abs(cosine(m3,1))/D * Imasi(j,i+1,m3) +
2*DX*abs(cosine(m3,2))/D * Imasj(j,i,m3) + S(j,i,m3)*DX*DY/D;
                Imasi (j,i,m3) = 2* I(j,i,m3) - Imasi(j,i+1,m3);
                if Imasi(j,i,m3)<0
                    Imasi(j,i,m3)=0;
                end
                Imasj (j+1,i,m3) = 2* I(j,i,m3) - Imasj(j,i,m3);
                if Imasj(j+1,i,m3)<0
                    Imasj(j+1,i,m3)=0;
                end
            end
        end
    end
```

```
    % SOURCE TERM CALCULATION
    Scalc=zeros(NY,NX,M);

    for j=1:NY
        for i=1:NX
            for m=1:M
                for cont=1:M
                    Scalc(j,i,m)=Scalc(j,i,m)+I(j,i,cont)*w(cont);
                end
                Scalc(j,i,m) = Scalc(j,i,m)*sigma / (2 * pi);
            end
        end
    end


    err=max(max(max(abs(S-Scalc)))) % iteration error

    S=Scalc;
    iter=iter+1
end


% ENERGY BALANCE
%%%%%%%%%%%%%%%%%%%%%%%%%%%%%%%%%%%%%%%%%%%%%%%%

%INPUTS

% Input in X0 qmu+(0)
Input_X0=0;
    % Quadrant 1
    for m=1:Mc
        m1=0*Mc+m;
        for j=1:NY
            Input_X0=Input_X0+Imasi(j,1,m1)*abs(cosine(m1,1))*w(m1)*2*pi;
        end
    end
    % Quadrant 4
    for m=1:Mc
        m4=3*Mc+m;
        for j=1:NY
            Input_X0=Input_X0+Imasi(j,1,m4)*abs(cosine(m4,1))*w(m4)*2*pi;
        end
    end


% Input in XL qmu-(L)
Input_XL=0;
    % Quadrant 2
    for m=1:Mc
        m2=1*Mc+m;
        for j=1:NY
            Input_XL=Input_XL+Imasi(j,NX+1,m2)*abs(cosine(m2,1))*w(m2)*2*pi;
        end
    end
    % Quadrant 3
    for m=1:Mc
        m3=2*Mc+m;
        for j=1:NY
            Input_XL=Input_XL+Imasi(j,NX+1,m3)*abs(cosine(m3,1))*w(m3)*2*pi;
        end
    end
```

```
% Input in Y0 qeta+ (0)
Input_Y0=0;
    % Quadrant 1
    for m=1:Mc
        m1=0*Mc+m;
        for i=1:NX

Input_Y0=Input_Y0+Imasj(NY+1,i,m1)*abs(cosine(m1,2))*w(m1)*2*pi;
        end
    end
    % Quadrant 2
    for m=1:Mc
        m2=1*Mc+m;
        for i=1:NX
            Input_Y0=Input_Y0+Imasj(NY+1,i,m2)*abs(cosine(m2,2))*w(m2)*2*pi;
        end
    end


% Input in YL qeta- (L)
Input_YL=0;
    % Quadrant 3
    for m=1:Mc
        m3=2*Mc+m;
        for i=1:NX
            Input_YL=Input_YL+Imasj(1,i,m3)*abs(cosine(m3,2))*w(m3)*2*pi;
        end
    end
    % Quadrant 4
    for m=1:Mc
        m4=3*Mc+m;
        for i=1:NX
            Input_YL=Input_YL+Imasj(1,i,m4)*abs(cosine(m4,2))*w(m4)*2*pi;
        end
    end

Input=Input_X0+Input_XL+Input_Y0+Input_YL;



% OUTPUTS

% Output in XL qmu+(L)
Output_XL=0;
    % Quadrant 1
    for m=1:Mc
        m1=0*Mc+m;
        for j=1:NY

Output_XL=Output_XL+Imasi(j,NX+1,m1)*abs(cosine(m1,1))*w(m1)*2*pi;
        end
    end
    % Quadrant 4
    for m=1:Mc
        m4=3*Mc+m;
        for j=1:NY

Output_XL=Output_XL+Imasi(j,NX+1,m4)*abs(cosine(m4,1))*w(m4)*2*pi;
        end
    end
```

```
% Output in X0 qmu-(0)
Output_X0=0;
    % Quadrant 2
    for m=1:Mc
        m2=1*Mc+m;
        for j=1:NY
            Output_X0=Output_X0+Imasi(j,1,m2)*abs(cosine(m2,1))*w(m2)*2*pi;
        end
    end
    % Quadrant 3
    for m=1:Mc
        m3=2*Mc+m;
        for j=1:NY
             Output_X0=Output_X0 +
Imasi(j,1,m3)*abs(cosine(m3,1))*w(m3)*2*pi;
        end
    end


% Output in YL qeta-(L)
Output_YL=0;
    % Quadrant 1
    for m=1:Mc
        m1=0*Mc+m;
        for i=1:NX
             Output_YL=Output_YL+Imasj(1,i,m1)*abs(cosine(m1,2))*w(m1)*2*pi;
        end
    end
    % Quadrant 2
    for m=1:Mc
        m2=1*Mc+m;
        for i=1:NX
             Output_YL=Output_YL+Imasj(1,i,m2)*abs(cosine(m2,2))*w(m2)*2*pi;
        end
    end


% Output in Y0 qeta+(0)
Output_Y0=0;
    % Quadrant 3
    for m=1:Mc
        m3=2*Mc+m;
        for i=1:NX
            Output_Y0 =
Output_Y0+Imasj(NY+1,i,m3)*abs(cosine(m3,2))*w(m3)*2*pi;
        end
    end
    % Quadrant 4
    for m=1:Mc
        m4=3*Mc+m;
        for i=1:NX
            Output_Y0 =
Output_Y0+Imasj(NY+1,i,m4)*abs(cosine(m4,2)*w(m4))*2*pi;
        end
    end

Output=Output_X0+Output_XL+Output_Y0+Output_YL;

Balance = Input-Output;
```

```
% INCIDENT RADIATION ESTIMATION
%%%%%%%%%%%%%%%%%%%%%%%%%%%%%%%%%%%%%%%%%%%%%

G=zeros(NY,NX);

for j=1:NY
    for i=1:NX
        for m=1:M
            G(j,i) = G(j,i) + I(j,i,m)*w(m)*2*pi;
        end
    end
end

G_x = sum(G,1);  % radiation profile in X axis
G_Media = mean(G_x);

f = G_Media / q0;  % corrector factor
```

Appendix D. Simulation of SODIS under real sunlight using the synergistic SODIS-thermal model with MATLAB® software

In chapter 7 (*Validation of solar water disinfection model in solar reactors under real field conditions*), it is presented the comparison of experimental and modelled inactivation data of *E. coli* due to SODIS under real field conditions. In this appendix, the MATLAB® code for one of these experiments is developed, in a file named "Model_simulation.m". The simulation presented is the corresponding to the experiment performed in 2 L-PET batch reactor within well water and kaolin (100 NTU). In an excel file named "Experiment_data" is introduced the irradiance, sampling time and bacterial enumeration of the experiment, separately in sheets (without headlines):

Table A.8. Column 1: sheet "time"; column 2: sheet "UV" of the excel file "Experiment_data.xls".

0	18.19
60	18.03
120	16.24
…	…
18000	36.40

(*) The table has been broken. It has 301 rows in total.

Table A.9. Column 1: sheet "t"; column 2: sheet "bacteria" of the excel file "Experiment_data.xls".

0	3.01E+06
900	2.78E+06
1800	1.52E+06
2700	1.58E+06
3600	1.78E+05
5400	8.00E+04
7200	2.14E+03
9000	1.14E+03
10800	1.70E+01

"Model_simulation.m":

```
clear all
clc

%Reading experimental data
%---------------------------------------
t_experimental=xlsread('Experiment_data.xls','t');
B_experimental=xlsread('Experiment_data.xls','bacteria');
n_ptos=9;

t=xlsread('Experiment_data','time');
UV=xlsread('Experiment_data','UV');
Binicial=B_experimental(1);                %CFU/mL
T=@(t)-5.098E-08*t^2 + 1.755E-03*t + 2.986E+02; %K

irradiance=@(t)UV(round(t/60+1),1);

Twall=0.52;
f=@(t)4.2389E-06*t + 4.8000E-01; %turbidity
factor=@(t) Twall * f(t);


%Model kinetic constants
%---------------------------------------
iron=2e-5;        %M
oxig=2e-4;        %M
elect=1.35e-12;   %M
NADH=2.5e-4;      %M

SOD0=2e-5;        %M
CAT0=9.2e-5;      %M
perox0=2e-8;      %M

kabsCAT=267718;   %M-1·cm-1
kabsSOD=800;      %M-1·cm-1

k3=1e9;           %M-1·s-1
k6=2.7e7;         %M-1·s-1
k8=9e5;           %M-1·s-1

k10=1.56e6;       %cm3·Einstein-1
k11=2.04e4;       %s-1
k12=1.36e5;       %s-1
k13=8.03e15;      %M-2·s-1

%Arrhenius constants
%---------------------------------------
R=8.314;          %J·K-1·mol-1

A1=3.16e12;       %M-1·s-1
Ea1=1.3e4;        %J·mol-1
Ea2=3.76e3;       %J·mol-1
A4=1.92e9;        %M-1·s-1
Ea4=4.676e4;      %J·mol-1
Ea9=5.31e4;       %J·mol-1
A14=1.3e34;       %s-1
Ea14=225614;      %J·mol-1

k2_25C=1.55e21;   %cm3·Einst-1·M-1
k9_25C=1.5e7;     %cm3·Einst-1

A2=k2_25C*exp(Ea2/(R*(25+273)));   %cm3·Einst-1·M-1
```

```
A9=k9_25C*exp(Ea9/(R*(25+273)));  %cm3·Einst-1

delta1=A1*oxig*elect; %M·s-1
delta2=A2*oxig*elect; %cm3·Einst-1·M
delta3=A4*iron;       %s-1



%Irradiance
%---------------------------------------
Ep=6.626e-34*3e8/350e-9;    %h·c/lambda_average (J·photon-1)
NA=6.022e23;                %photon·Einstein-1
G=@(t) factor(t)*irradiance(t)/(Ep*NA)*1e-4;  %Einst/(cm2·s)

kCAT_spec=267718;           %M-1·cm-1
kSOD_spec=800;              %M-1·cm-1
kNADH_spec=6220;            %M-1·cm-1

kNADH=kNADH_spec*NADH;      %cm-1
eNADH=@(t) kNADH*G(t);              %Einst/(cm3·s)


%Model equations
%---------------------------------------

%xN(1)=peroxN
%XN(2)=BN

superox0 =  delta1*exp(-Ea1/(R*T(1))) /( k3*SOD0 + k12 );
hidrox0 = ( 2*delta3*exp(-Ea4/(R*T(1)))*perox0 )/( k11 + k6*perox0 );

CATN=@(t)1./(1+A9*exp(-Ea9./(R*T(t)))*kabsCAT.*G(t)*CAT0.*t);
SODN=@(t)1./(1+k10*kabsSOD*SOD0*G(t).*t);

superoxN=@(t)(1+ delta2/delta1*exp(-(Ea2-Ea1)./(R*T(t))).*eNADH(t)) * (
k3*SOD0 + k12 ) ./ ( k3*SOD0*SODN(t) + k12 );
hidroxN=@(t,xN) xN(1)*( k11 + k6*perox0 ) ./ ( k11+ k6*xN(1)*perox0 );

dperoxN=@(t,xN) k3*SOD0/(2*perox0)*SODN(t).*(delta1*exp(-
Ea1./(R*T(t)))+delta2*exp(-Ea2./(R*T(t))).*eNADH(t)) ./
(k3*SOD0*SODN(t)+k12) - delta3*exp(-Ea4./(R*T(t)))*k6*perox0.*xN(1)^2 ./
(k11+k6*perox0*xN(1)) - (delta3*exp(-Ea4./(R*T(t))) + k8*CAT0*CATN(t)
).*xN(1) ;
dBN=@(t,xN) -k13*hidrox0*hidroxN(t,xN).*superox0*superoxN(t).*xN(2) +
A14*exp(-Ea14./(R*T(t))).*xN(2) ;

funcion=@(t,xN)[dperoxN(t,xN);dBN(t,xN)];

%Model solution
%---------------------------------------
xN0=[1;1];
t_modelo=t;
[t,xN]=ode45(funcion,t_modelo,xN0);

B=Binicial*xN(:,2);
B( B<17 ) = 17; %DL=17
peroxN=xN(:,1);

siz=size(t);
rows=siz(1);
result=zeros(rows,9); %%columns = time, bacteria, CAT, SOD, H2O2, O2.-, HO.,
temperature, irradiance
for i=1:rows
    time=t(i);
```

```
    bacteriaN=xN(i);
    result(i,1)=time;
    result(i,2)=B(i);
    result(i,3)=CAT0*CATN(time);
    result(i,4)=SOD0*SODN(time);
    result(i,5)=perox0*peroxN(i);
    result(i,6)=superox0*superoxN(time);
    result(i,7)=hidrox0*hidroxN(time,bacteriaN);
    result(i,8)=T(time);
    result(i,9)=irradiance(time);
end

%NRMSLE calculation
%----------------------------------------

%Model values at sampling time
Bc_calc=zeros(n_ptos,1);
for i=1:n_ptos
    idx = t==t_experimental(i);
    Bc_calc(i)=B(idx,1);
end

%NRMSLE
NRMSLE_exp=sqrt(1/n_ptos * sum( ( log10(Bc_calc(:)+1)-
log10(B_experimental(:)+1) ) .^2 )  )  / ( sum( log10(B_experimental(:)) ) /
n_ptos ) *100

%Graph
%----------------------------------------

figure
semilogy(t_experimental,B_experimental,'r*',result(:,1),result(:,2),'r-');
axis([0 18000 1e1 5e6])
xlabel('Time (s)')
ylabel('Bacteria (CFU/mL)')
```


9 788478 347780